Hybrid Testing of an Aerial Refuelling Drogue

Bolien, Mario

Award date:
2018

Awarding institution:
University of Bath

Hybrid Testing of an Aerial Refuelling Drogue

Mario Bolien

A thesis submitted to the University of Bath in accordance with the requirements for the award of the degree of Doctor of Philosophy in the Faculty of Engineering and Design.

University of Bath
Department of Mechanical Engineering
Bath, BA2 7AY
United Kingdom

January 2018

COPYRIGHT

Signature of Author and Date .....

Mario Bolien

AUTHORSHIP

I declare that the work in this thesis was carried out in accordance with the requirements of the University's Regulations and Code of Practice for Research Degree Programmes and that it has not been submitted for any other academic award. Except where indicated by specific reference in the text, the work is the candidates own work. Any views expressed in the dissertation are those of the author.

Signature of Author and Date .....

Mario Bolien

To my mother and father who taught me how to care and reason,
and to Sandra who has put it all together and more...

Hybrid Testing of an Aerial Refuelling Drogue

Mario Bolien

Abstract

Hybrid testing is an emerging technique for system emulation that uses a transfer system composed of actuators and sensors to couple physical tests of a critical component or substructure to a numerical simulation of the remainder of a system and its complete operating environment. The realisation of modern real-time hybrid tests for multi-body contact-impact problems often proves infeasible due to *(i)* hardware with bandwidth limitations and *(ii)* the unavailability of control schemes that provide satisfactory force and position tracking in the presence of sharp non-linearities or discontinuities.

Where this is the case, the possibility of employing a pseudo-dynamic technique remains, enabling tests to be conducted on an enlarged time scale thus relaxing both bandwidth and response time constraints and providing inherent loop stability. Exploiting the pseudo-dynamic technique, this thesis presents the development of *Robotic Pseudo-Dynamic Testing* (RPsDT), a dedicated method that specifically targets the realisation of hybrid tests for multi-body contact-impact problems using commercial off-the shelve (COTS) industrial robotic manipulators. The RPsDT method is evaluated in on-ground studies of air-to-air refuelling (AAR) maneuvers with probe-hose-drogue systems where the critical contact and coupling phase is tested pseudo-dynamically with full-scale refuelling hardware while the flight regime is emulated in simulation.

It is shown that the RPsDT method can faithfully reproduce the dominant contact-impact phenomena between probe and drogue while minor discrepancies result from the absence of rate-dependant damping in the force feedback measurements. In combination with full-speed robot controlled contact tests, reliable estimates for impact forces, strain distributions and drogue responses to off-centre hits are obtained providing extensive improvements over current predictive capabilities for the in-flight behaviour of refuelling hardware and it is concluded that the technique shows great promise for industrial applications.

Keywords: hybrid testing - hardware-in-the-loop - pseudo-dynamic testing - RPsDT - virtual validation - system verification - contact dynamics - air-to-air refuelling

Acknowledgements

First and foremost, I would like to thank my supervisors, Dr. Jonathan L. du Bois and Dr. Pejman Iravani, whose guidance has been instrumental in the realisation of this thesis.

I am also grateful to the Engineering and Physical Sciences Research Council and Cobham Mission Systems for their financial support throughout my studies.

At the University of Bristol, I would like to thank Dr. Tom Richardson for a productive collaboration including the provision of the facilities in the Department of Aerospace Engineering for the duration of my experimental work.

At the University of Bath, my thanks go to peers and colleagues too numerous to name who have contributed to valuable discussions and an enjoyable work environment. Worthy of special mention is the practical instrumentation support I received of Robin Harris and Stephen Coombes.

Outside of the University, I am indebted to my parents, partner, brothers and friends for being a source of motivation and support over the course of my PhD.

Contents

List of Figures

List of Tables

Acronyms

AAAR	Autonomous Air-to-Air Refuelling
AAR	Air-to-Air Refuelling
ASTRAEA	Autonomous Systems Technology Related Airborne Evaluation & Assessment
COTS	Commercial off-the-Shelve
DOF	Degree of Freedom
HiL	Hardware-in-the-Loop
I\O	Input\Output
MHiL	Mechanical Hardware-in-the-Loop
MiL	Model-in-the-Loop
PLC	Programmable Logic Controller
PsD	Pseudo-Dynamic
RCP	Rapid Control Prototyping
RMR	Robotic Relative Motion Facility
RTDS	Real-Time Dynamic Substructuring
RTHT	Real-Time Hybrid Testing
R&D	Research & Development
SiL	Sensor-in-the-Loop
TCP	Transmission Control Protocol
UAV	Unmanned Aerial Vehicle
UDP	User Datagram Protocol
VDD	Variable Drag Drogue

Chapter 1

Introduction

1.1 Research Background

Performance assessments, system response identification and validation of mechanical hardware are integral parts of product development cycles in engineering and are of equivalent importance to the underlying component design. Thorough pre-operational testing under realistic conditions allows early identification of design flaws in complex systems, thereby reducing the likelihood of incurring unforeseen cost and loss of time due to modifications or cycle iterations at progressed design or manufacturing stages. Especially in the aerospace industry, where component failure can have severe consequences for equipment and personnel, pre-operational testing is a widely used measure for risk mitigation and is extensively performed prior to initial system commissioning and flight testing.

Traditional methods for pre-operational testing are either simulation-based or purely experimental. Both techniques have their own benefits and drawbacks. While it is often more cost and time efficient to perform system simulations, they can suffer from structural or parameter-induced model uncertainties leading to unrepresentative simulation results. By contrast, experimental tests generally allow the examination of systems and components with entirely unknown characteristics but the realisation can be challenging, especially when the operational environment is complex and a realistic laboratory reproduction demanding.

In places where pure simulation cannot achieve satisfactory results because aspects of a system are unknown or hard to model, and experimental studies are infeasible for

technical, logistical or financial reasons, hybrid testing methods can be applied. Hybrid testing describes a class of emerging techniques that seek the synergistic integration of both numeric simulation and experimental testing to harness individual benefits from either method where appropriate. To this end, a system under investigation is split, *i.e.* hybridised, into separate synthetic and physical domains which constitute numeric simulations and experimental tests of specific system substructures respectively. An interface, commonly termed the 'transfer system', is employed to link corresponding degree-of-freedoms (DOF) across both domains with the objective of imposing the interface dynamics computed by the simulation at every time step directly onto the physical test specimen. In turn, the measured response from the hardware specimen is fed back to close the simulation loop and is taken into account in the computation of the subsequent simulation states. Time-marching these states with an appropriate integration algorithm results in a mixed numerical-physical test, *i.e.* a hybrid test.

The core benefit of hybrid techniques for pre-operational testing lies in the flexible division of system parts and components into the numerical and physical substructures. This allows a critical element of a system to be tested experimentally with the remainder accounted for in simulation. In this way, high confidence predictions can be obtained for the dynamics of the complete system while test logistics and financial expenditure are kept to a minimum. Consequently, the hybrid approach is of special interest for complex systems that are hard to study with either numeric simulations or experimental tests; one such example being probe-hose-drogue systems in air-to-air refuelling (AAR) which are the subject of investigation in this thesis.

Preflight tests of probe-hose-drogue systems set stringent requirements for a realistic reproduction of the operational coupling and hose response characteristics. In particular, the modelling of the contact dynamics between probe and drogue pushes simulative methods to their limits while a complete laboratory reproduction of a flight regime, if at all possible, can only be achieved at prohibitive cost. From these challenges results the motivation to study the operational behaviour of probe-hose-drogue systems in a hybrid test. In collaboration with Cobham Mission Systems [1], the primary stakeholder and funding body of this research project, specialising (amongst other applications in the defence market) in the design and development of probe-drogue AAR equipment, this thesis investigates the feasibility of realising such tests by integrating a relative motion facility comprised of industrial robots into a simulation loop. To this end, the robots are equipped with refuelling hardware and conduct the contact phase of the manoeuvre experimentally, while a simulation computes the flight paths of the tanker and receiver aircraft and accounts for aerodynamics effects.

Achieving reliable tests in this form would enable the repeatable generation of performance data for aerial refuelling systems at early design stages, thus raising the prospect of reduced time-to-market and substantial cost savings in the development cycle. On the other hand, key challenges are centred around the test implementation: While the hybrid testing technique has been proven to be an effective method for the study of continuous systems predominantly based on highly responsive hydraulic actuation, here, vastly discontinuous contact events that set high bandwidth requirements are to be studied with conventional industrial robotic manipulators which have high latencies and low controller update rates. This thesis seeks to address these challenges.

The chapter proceeds with an introduction to the AAR technology followed by a description of modern aerial refuelling hardware with focus on Cobham's probe-hose-drogue systems and effects governing the dynamics in the hook-up space of AAR manoeuvres. This is followed by a discussion of current pre-flight test methods for AAR systems based on which the research aims and objectives are defined. The chapter closes with an outline of the thesis structure and the author's contributions.

1.2 Air-to-Air Refuelling and Significance of the Technology

AAR is the process of in-flight fuel transfer from a tanker aircraft to a receiver aircraft with the primary motivation of increasing the receiver aircraft's flight persistence, *i.e.* endurance, range and mission time. Amongst further incentives for AAR is the ability to launch from short runways with low take-off weight and prospects of increased fuel economy for long distance travel [2].

The benefits of AAR have led to a rapid introduction of the technology to armed forces around the globe where AAR operations have become a routine in strategic military manoeuvres. Modern systems cater for a wide range of requirements and can provide in-flight refuelling capability for a variety of aircraft types. These extend beyond the classical scenario, where fuel is off-loaded to bombers and fighter jets from either specially designed refuelling aircraft or modified transport planes, and also include buddy-buddy systems for refuelling between combat aircraft and special solutions for helicopters. Thus, AAR enables armed forces to maintain cost-effective and highly versatile air-fleets.

AAR is currently not prevalent in the civil domain and an introduction is unlikely.

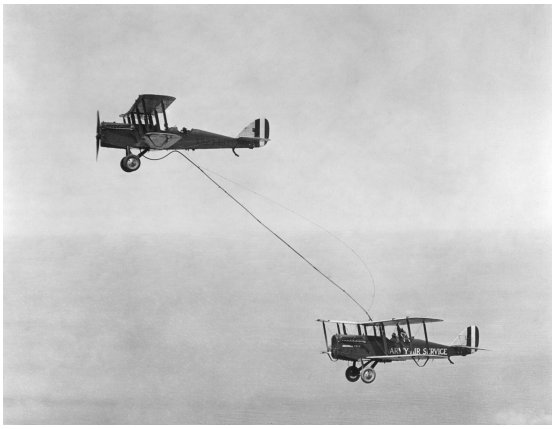

Figure 1.1: Early AAR manoeuvre performed by Capt. Lowell H. Smith and Lt. John P. Richter, at Rockwell Field, California, June 1923. They stayed in the air four days using DeHaviland airplanes. (U.S. Air Force photo) [6]

While potential improvements to fuel consumption for long distance travel and reduced emissions may be an economic driver [2], a lack of technology acceptance from the passenger side as well as prospective complications in the event of hijacking of passenger aircraft with AAR capability, are factors which currently prevent the introduction of this technology to the civil aviation sector.

By contrast, a major trend goes towards AAR of Unmanned Aerial Vehicles (UAV) also known as Autonomous Air-to-Air Refuelling (AAAR). As opposed to manned aviation, the endurance of UAV is almost solely dependent on the amount of fuel that can be carried and not affected by factors such as pilot fatigue. Consequently, AAAR has the potential to enable UAV to stay airborne for the duration of entire maintenance cycles. While AAAR is a recent field of research, the first successful flight tests have already been reported in 2007 [3]. Subsequent joint ventures between government and industry such as ASTRAEA (Autonomous Systems Technology Related Airborne Evaluation & Assessment) [4] aimed at opening civil airspace to unmanned aircraft systems have further backed the development of AAAR technology [5].

Arguably, the first recognisable demonstration of AAR took place in 1923 when gasoline was offloaded from one US Army Air Service air plane to another through a rubber hose with manually operated valves at both ends [9]. The method used was very crude: Co-pilots of the tanker and receiver aircraft dangled and grabbed the hose respectively (Figure 1.1). Today, Boeing's flying boom (Figure 1.2a)) and Cobham's probe-drogue systems (Figure 1.2b) are the dominant AAR systems in operation. The flying boom uses a rigid telescoping tube that an operator on the tanker aircraft guides into a

a)

b)

Figure 1.2: AAR systems. a) Flying boom refuelling system in operation. Royal Australian Air Force completes the first fuel transfer with the air refuelling boom from a RAAF KC-30A Multi Role Tanker Transport to a U.S. Air Force F-35A Lightning II on Sept. 25, 2015, at Edwards Air Force Base, California. (Lockheed Martin courtesy photo/ Jonathan Case) [7] b) Probe-Drogue refuelling system in operation. USAF KC-135 using Mk32B hose-drogue pods refuelling a pair of British Tornado GR4s over Iraq in 2003. The wing pods allow for use of the centreline refuelling boom. (U.S. Air Force photo/ SSgt. Suzanne M. Jenkins) [8]

receptacle typically located on top of the receiver aircraft. Throughout this procedure the boom is aerodynamically stabilised and controllable by flaps. By contrast, a drogue is an entirely passive mechanism. Attached to a flexible hose, the drogue is trailed behind the tanker aircraft and the pilot of the receiver aircraft manoeuvres its probe centrally into the drogues funnel. This latches a mechanical coupling and allows the off-loading of fuel to begin.

Both systems have their own advantages and drawbacks. These are thoroughly outlined in [10] and have been concisely summarised in tabular form (Table 1.2) by Thomas et al. [11]. The scope of this thesis is restricted to probe-hose-drogue systems which are examined in more detail throughout the subsequent section.

Flying boom	Probe and drogue
Larger size, weight and cost	Light and compact
Restricted to unary servicing	Multiple systems operable on one tanker, simultaneous servicing possible
Controllable via flaps	Passive, more susceptible to aerodynamic disturbances
Can use a boom-drogue adapter to refuel probe-mounted receivers	Restricted to probe mounted receivers
Not suitable for refuelling helicopters	Low speed drogue can be used to refuel helicopters
Workload is shared between receiver pilot and boom controller	Substantial pilot workload required to capture the drogue

Table 1.1: Comparison of flying boom and probe-drogue system as per Thomas et al. [11]

1.3 Probe-Hose-Drogue AAR Systems

The hardware in probe-drogue AAR systems fundamentally comprises the refuelling pod including the hose-drum unit, drogue and reception coupling as well as the receiver probe. In the following, the components are described individually.

1.3.1 Hose-Drum-Unit

The HDU extends and retracts the refuelling hose through which fuel is transferred to the receiver aircraft. It is contained in either wing or fuselage mounted refuelling pods. The reel is commonly hydraulically actuated. An integrated fuel boost pump provides fuel transfer capabilities in the range from 1500lbs/min to 2000lbs/min, though deviations may exist. The refuelling pods additionally accommodate the hydraulic pumps, fire detection and suppression systems as well as provisions for jettison, hose guillotine and emergency sealing. The pods are either operated with aircraft power or via self-powered ram air turbines.

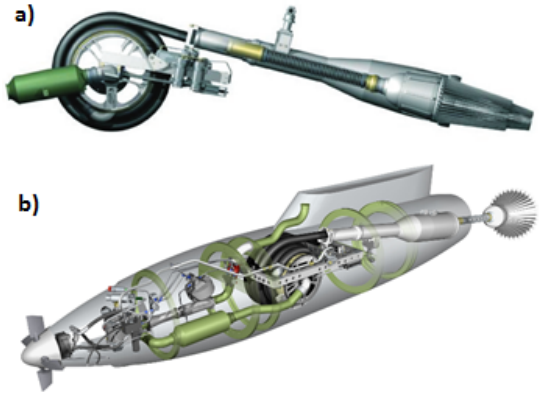

Figure 1.3: HDUs by Cobham. (a) Side view. (b) HDU assembly in wing-mounted refuelling pod powered by a ram air turbine. (Cobham) [12]

1.3.2 Drogue and Reception Coupling

The drogue stabilizes the hose in flight and provides a funnel to aid insertion of the receiver aircraft probe into the reception coupling located at the hose end. Drogues are built as collapsible structures which open parachute-like when submerged in an air stream and collapse again as the hose is retracted back into the refuelling pod. The main drag on the drogue is produced by the canopy, *i.e.* the webbing, at the end of the 'basket'.

a) **b)**

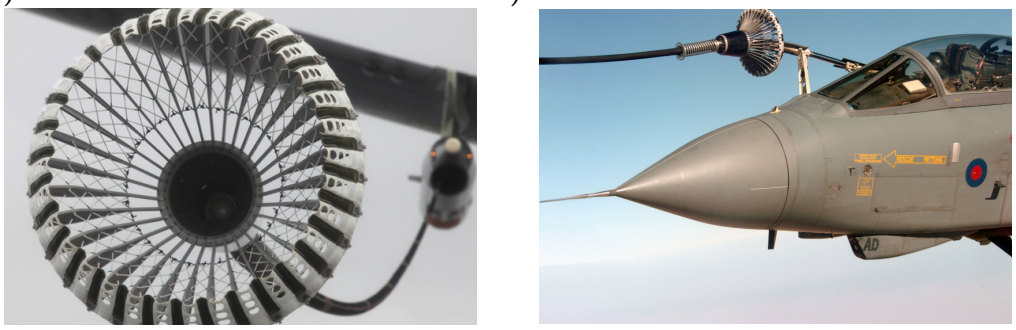

Figure 1.4: Refuelling drogues in operation. (a) Receiver cockpit view of Variable Drag Drogue trailed behind tanker. (Cobham) [13] (b) Side view of drogue. A Royal Air Force GR4 Tornado refuels off the right wing of a British VC-10 aircraft assigned to 10 Squadron 11 January, 2005, over Iraq. (U.S. Navy photo/ Mate Class 2nd Peter J. Carney) [14]

The structural rigidity of the drogue is provided by conically arranged metal ribs that are interlinked by elastics. The ribs can pivot about their respective anchor joints which are located on a common connector ring. The ring itself is fitted to a coupling that in turn connects to the hose via a ball joint allowing a small degree of relative rotation between drogue and hose. The coupling contains a fuel valve as well as a mechanical latch that is triggered when the probe's nozzle is fully inserted.

Cobham currently produce two types of drogues, Fixed Geometry and Variable Drag Drogue (VDD), covering the low and high speed flight envelopes. As the name implies, Fixed Geometry Drogues keep their shape once the hose is fully extended and are designed for a narrow flight speed range only. By contrast, VDDs decrease the drogue area with speed and operate over a larger range of flight speeds.

1.3.3 Refuelling Probe

Refuelling probes are retractable or fixed arms, typically located at the nose or fuselage of the receiver aircraft. The nozzle is located at the tip of the probe and engages with the reception coupling in the drogue's funnel. Probes can be actuated or telescopic. When the nozzle moves into the drogue's latch, it opens a fuel valve which triggers the fuel flow. A weak link connects nozzle and probe, providing a point for controlled breakage prior to the occurrence of structural damage to the probe or receiver aircraft. This functions as a safety measure for events when the probe is subjected to large radial loads while being engaged with the drogue.

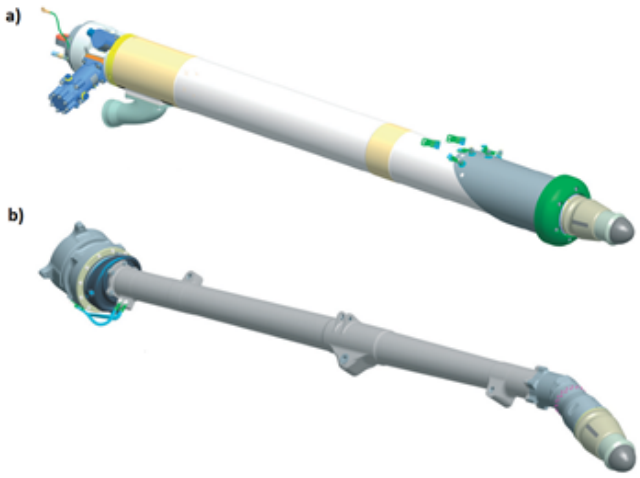

Figure 1.5: Refuelling probes by Cobham. (a) Telescopic probe. (b) Actuated probe. (Cobham) [15]

1.4 The Hook-Up Space

The dynamics in the hook-up space of AAR manoeuvres are complex. While the receiver's pilot attempts to capture the drogue with the nozzle, the relative motion between probe and drogue is affected by multiple phenomena which complicate a stable approach. These include atmospheric turbulences, tanker wake and receiver bow wave effects as well as contact induced forces. Brief individual descriptions follow.

1.4.1 Atmospheric Turbulence

The presence of atmospheric turbulences alters the airflow of the free stream and causes fluctuations in the aerodynamic forces and moments exerted onto aircraft and AAR equipment. This results in continuous perturbations of the subjected equipment around a steady state. While tankers are less sensitive to turbulence due to their high mass, the perturbations can be significant for hose, drogue and receiver aircraft.

1.4.2 Tanker Wake

Hook-up in AAR occurs in close proximity flight to the tanker aircraft where wake effects are significant. The trailing wake flow field generated by the tanker induces down-wash, vortices and turbulence. This further complicates a stable drogue approach for the receiver aircraft.

1.4.3 Receiver Bow Wave

On drogue approach, the bow wave generated around the fore-body of the receiver aircraft alters the airflow around the drogue leading to a sudden drogue disturbance. This typically results in the drogue being pushed away from the receiver aircraft on the final approach such that off-centre hits can occur or the drogue may be missed completely.

1.4.4 Contact Forces

In an ideal case, successful probe-drogue coupling results from a central drogue hit at a relative speed of 1-1.5 m/s. While the mechanical latch does not trigger at lower speeds and the docking attempt fails, higher speeds can initiate wave propagation throughout the hose. Such waves can get reflected at the refuelling pod, the fixed end, and generate violent oscillations upon return to the drogue. This phenomenon, also known as hose whip, can lead to severe equipment damage. In order to mitigate this risk, HDUs actively draw in the hose upon contact to take up slack and restore the original hose tension.

The contemporary understanding of off-centre hits and near misses is predominantly qualitative and the behaviour of the drogue in response to an off-centre hit is difficult to predict. The main reason for this lies in the nature of contact-impact dynamics which

are heavily influenced by a variety of factors including surface shapes and geometries, incidence strike angles, material properties and impact velocity [16]. In AAR these factors govern whether the contact scenario is dominated by slip of the probe towards the drogue's centre, contact losses and discontinuous impacts, drogue tipping (*i.e.* a rotational pivot motion about the ball joint), penetration of the nozzle beyond the drogue ribs or combinations of these. To date, numerical contact models rely on extensive simplifications and parametrisation that make experimental testing and validation imperative. In turn, complete experimental studies including a realistic laboratory reproduction of a flight environment are logistically infeasible for technical and financial reasons.

1.5 Research Challenges

Probe-hose-drogue systems are a mature technology, however, design changes are still day-to-day business for AAR equipment manufacturers. These target the simplification of successful contact for pilots, modifications to achieve increased aerodynamic stability, robustness, extended service life and reduced assembly weight or attempt to accommodate new aircraft configurations and alternate operating conditions in terms of refuelling speeds. In order to infer informed design decisions, a thorough understanding of the operational regime and reliable predictive capabilities for the in-service behaviour of AAR hardware are crucial. However, the complexity of both the flight regime and the contact-impact dynamics make the design of pre-flight tests a particularly difficult job.

Recent advances in the numerical analysis and simulation of probe-hose-drogue systems have been substantial. Studies including [17, 18, 19, 20] model the hose as a towed and tethered cable system in finite element or lumped parameter form, where nodal excitement accounts for structural and aerodynamic forces, and is computed according to the particular hose configuration and flight regime in each simulation step. To this end, effects governing the dynamics in the hook-up space can be individually examined, identified and described which may take the form of look-up tables from wind tunnel tests for drag coefficients and aero-moments or simplified structural analysis for hose bending. This results in a highly modular simulation environment that allows easy integration and substitution of independently validated models of varying sophistication and provides a reliable platform for the investigation of the free- and post-coupling dynamics of the hose-drogue assembly. However, the problem of modelling the contact-impact phase persists and is merely circumvented in simulation by constraining the hose

end to the motion profile of the receiver aircraft immediately upon contact meaning that instantly successful drogue capture is assumed. Thus, the critical contact and coupling phase is inherently disregarded.

In contrast to simulative approaches, only a limited number of standardized experimental pre-flight tests exist. One such example is the drop test as per MIL-PRF-81975C [21], in which a drogue and reception coupling sub-assembly is vertically suspended and released to fall onto a probe. Given that tests of this form are primarily intended to provide a common baseline for strength and endurance assessments, the knowledge gained about the underlying probe drogue contact scenarios is limited and simplifications compared to operational contact events are numerous. Hence, it is often not until expensive flight tests with complete prototypes, that equipment performance becomes evident. The risk and cost of component failure in such tests and the fact that data from different flight tests cannot be easily compared due to variations in operation conditions, give rise to a demand for realistic and repeatable pre-flight testing routines in a laboratory environment. This demand is further substantiated by trends towards AAAR where sensor and control systems have to be validated prior to first flight and technology readiness needs to be demonstrated to regulators for the opening of non-segregated airspace to UAVs.

An initial step towards addressing these needs has been made with the development of the Relative Motion Robotic Facility (RMR) at the University of Bristol [22, 23] (Figure 1.6). Also funded by Cobham Mission Systems, the RMR is a 13 degree of freedom (DOF) relative motion facility created to provide sensor in the loop (SIL) simulation support for the assessment of sensor and flight control systems in AAAR. The facility comprises two 6 DOF industrial robotic manipulators with sufficient payload to carry

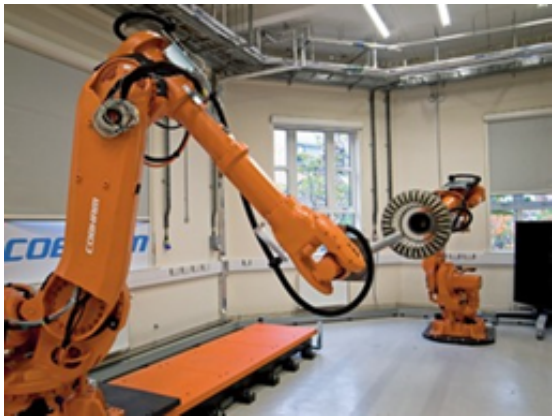

Figure 1.6: Relative Motion Robotic Facility (RMR) at University of Bristol.

refuelling equipment of actual size at the end-effectors. One robot is fitted to a linear track providing a 7th degree of freedom (DOF) and enabling accurate relative motion reproduction of AAR manoeuvres over the last 10 meters of the hook-up space.

Previous research activities at RMR have focused on the validation of vision guided schemes for drogue tracking in AAAR and rendezvous scheduling in satellite docking maneuvers [24, 25]. To this end, the latencies and controller update rates for the robotic systems were found to be sufficient to faithfully reproduce the dynamics in the pre-contact phase. In this project, the focus is shifted to the study of the critical contact and coupling phase to provide mechanical hardware-in-the-loop (HiL) capabilities through the integration of direct contact force feedback into the simulation loop. The associated increase in bandwidth requirements for the actuator system and reduced latency tolerance represent major hurdles in the realisation. The aims and objectives of this thesis follow from these challenges.

1.6 Aims, Objectives and Research Questions

Guided and underpinned by the research question which seeks to answer

'*whether it is feasible to reproduce the relevant dynamics in probe-drogue contact scenarios in a hybrid test*'

this thesis develops methods for the on-ground assessment and preflight validation of probe-hose-drogue systems with the aim to devise reliable predictive capabilities for the in-flight behaviour of the hose-drogue assembly throughout the contact and coupling phase in AAR manoeuvres. To this end, the research focuses on the development, implementation and validation of suitable hybrid testing methodology that enables the integration of robot controlled contact tests with refuelling hardware into a simulation loop of a flight regime. This is done to realise partly numerical, partly experimental tests which in combination provide predictions for the complete system dynamics that are of higher confidence than those attainable by either test modality alone, while logistical and financial efforts for the study are kept to a minimum. The research objectives further include:

- To devise and propose a hybrid testing framework for the on-ground study of contact events in AAR using conventional industrial robots.
- To develop and implement a hybrid method based on this framework.

- To validate the hybrid testing method independently and align results with flight test data where available.
- To enable the investigation of the probe-drogue contact and coupling phase in the safe, controlled and repeatable environment of a laboratory.
- To establish improved predictive capabilities for the contact-impact response of the hose-drogue assembly and inform the development of future preflight testing procedures.

1.7 Thesis Structure and Contributions

Having set the context and scope of the research work in the current chapter, the thesis continuous with a dedicated literature review of hybrid testing methods in Chapter 2. The review discusses applications and control concepts for hybrid testing methods and identifies the pseudo-dynamic method as being the most viable solution to mitigate dead-time and bandwidth restriction in conventional industrial robots in order to realise hybrid tests for the stiff and fast contact scenarios found in AAR.

Chapter 3 consists of three parts that build on one another to provide a complete description of the adopted testing methodology. The first part sets out the proposed hybrid testing framework providing a clear aim for system developments and ultimate testing procedures. Part 2 presents the *Robotic Pseudo-Dynamic Testing* (RPsDT) method and its implementation with ABB robot controllers. Part 3 discusses the integration of the contact forces from the physical test domain and presents the development and evaluation of a novel finite segment hose model for use in the numerical substructure. This model accommodates for the reel-in behaviour by varying the length of individual hose segments as opposed to modelling the process of winding the hose onto the drum.

Chapters 4 and 5 are publication-based and contain the main contributions of this thesis in terms of experimental work. The papers are preceded by an introduction that summarises and contextualises the presented work within the overarching narrative, providing continuity and cohesion. To this end, Chapter 4 presents preliminary tests that have been published throughout the development phase of the RPsDT method. These include the investigation of a 1 DOF drop test scenario detailed in a conference paper as well as a more comprehensive journal article which extends the conference paper analysis and presents a first AAR hybrid test scenario conducted at a scaled test

facility in Bath.

In chapter 5, the developments are ported to the RMR and full-scale tests are presented. These include an independent validation of the RPsDT method with AAR hardware based on a modified drop test apparatus as well as full-scale tests with off-centre hits under simulation based emulation of a flight environment. At the time of preparation of this thesis, the paper remains under review with the *AIAA Journal of Aircraft*.

Chapter 6 concludes the thesis with an overall discussion of the development work and results. Particular strengths and limitations of the RPsDT method are highlighted and proposals for future work are made.

Chapter 2

A Review of Hybrid Testing Methods

2.1 Hybrid Testing Methodology

Hybrid testing, also known as hybrid simulations, encompass a range of mixed numerical-physical techniques for the response identification, system verification and operational testing of multi physics systems (*i.e.* structures, devices, components etc.) under emulation of highly realistic in-service conditions. As indicated by the term 'hybrid', the technique seeks the combined application of simulative and experimental testing, to surpass the predictive capabilities provided by either method alone. To this end, system elements that are subject to physical testing and those that are modelled and numerically simulated can be carefully chosen, allowing time, cost and resources to be balanced against test fidelity and trustworthiness. This is particularly useful for complex systems and can aid in the realisation of tests that would otherwise not be feasible for technical or financial reasons.

On a fundamental level, hybrid tests are implemented by splitting the system at hand into a virtual/synthetic substructure where system parts and components are accounted for in numerical models, and an experimental substructure containing a physically tested hardware specimen or component. In order to study the system as a coherent entity despite the separation, the dynamics of the interface connection or interface DOFs are linked across the substructures to facilitate a seamless test execution where the states of the numerical simulation and the hardware response are mutually affected by the dynamics of the elements in opposite domains.

The nature of the substructure interface is often directly dictated by the type of component subjected to physical testing. As du Bois notes in [26], it can either rely completely on electrical connections as is the case in standard Hardware-in-the-Loop (HiL) and Sensor-in-the-Loop (SiL) tests of electronic components or incorporate a full transfer system composed of actuators and sensors as in Real-Time Hybrid Testing (RTHT) of mechanical hardware and the associated non real-time variant of pseudo-dynamic (PsD) testing. Transfer systems typically use electro-hydraulic or mechatronic actuators to physically impose the interface dynamics in terms of force or position variations onto the hardware specimen. However, in either case, the decisive feature is the closed loop that feeds back the hardware response to the corresponding simulation node (*i.e.* the interface DOF), be it on a direct electrical line or via an intermediate sensor.

Notably, it is the division and allocation of individual system parts and components into the respective substructures that provides the key advantage of hybrid techniques: It allows for flexibility in the test setup and enables individual system parts to be studied in accordance with *(i)* their criticality, *(ii)* their availability for testing as well as *(iii)* the cost and logistics for a laboratory reproduction [27]. As discussed in [26], the physical substructure would typically consist of system parts for which exact performance predictions are required or subsystems with aspects that are particularly difficult to model. On the other hand, the synthetic substructure can contain components with well known characteristics and elements that are deliberately omitted from experimental testing. Popular choices of the latter are large and distributed forces, for example of aerodynamic and hydrodynamic nature, that often cannot be reproduced experimentally due to capacity limitations or simply the lack of available testing equipment. At the opposite end of the spectrum, the substructuring principle may also be exploited for the emulation of systems requiring the total absence of specific forces throughout a test, as is the case when zero-gravity conditions are to be reproduced [28, 29, 30, 31].

The benefits of hybrid testing have made it a rapidly emerging technology that continues to receive much attention in research and development (R&D) across a variety of industry sectors. Particularly high adoption rates have been seen in civil engineering [32] and the transport sector where hybrid tests are employed to support the development process of automotive [33, 34], rail [35], and aerospace systems [36]. Reasons for introducing hybrid methods to R&D processes are as diverse as the industries they are used in but are typically driven by prospective improvements to time and cost efficiency in product validation, or revolve around the provision of enhanced risk mitigation strategies and predictive capabilities. Some examples are listed below:

- In the aerospace industry, hybrid testing lends itself as a valuable intermediate de-

risking step between basic component tests and full system flight testing [36, 37].

- In space applications, representative operating conditions (e.g. zero-gravity) are only reached once a system is fully deployed, necessitating the verification with advanced system emulation techniques prior to commissioning [38, 39].
- Obvious size and cost constraints exist for the testing of earthquake and wind excited structures such as high-rise buildings and bridges in civil engineering and hence physical tests have to focus on a critical structural part such as the damping element [32, 40] while the rest of the building is accounted for in simulation.
- In the automotive industry, the process of vehicle suspension and handling optimisation can be expedited significantly by connecting the suspension unit to an actuator that mimics the road profile and providing force feedback to a real-time simulation of the vehicle dynamics [41, 42, 43]. Thus, the time spent on iterative track testing and manual fine tuning can be greatly reduced.

From a systems and control perspective, hybrid methods can be distinguished based on the nature of the interface used to dynamically couple the experimental and numerical substructures. One possible classification for hybrid methods is proposed by the author and shown in Figure 2.1. Here, methods with mechanical and non-mechanical interface elements are separated in a first step before subsequent divisions are made on the basis of timing requirements in the test execution. Crucially, the initial step leads to a separation of hybrid methods with electrical interfaces from those incorporating an electro-hydraulic or mechatronic transfer system. Speaking in layman's terms, this is important since those methods with purely electrical interfaces are typically real-time capable as long as the simulation target can cope with the computational load to advance the simulation by one time step within the allowed interval. By contrast, a number of additional challenges arise in the real-time test execution with mechanical hardware leaving the methods in the left branch of Figure 2.1 subject to on-going research. The following sections examine the available hybrid methods on an individual basis.

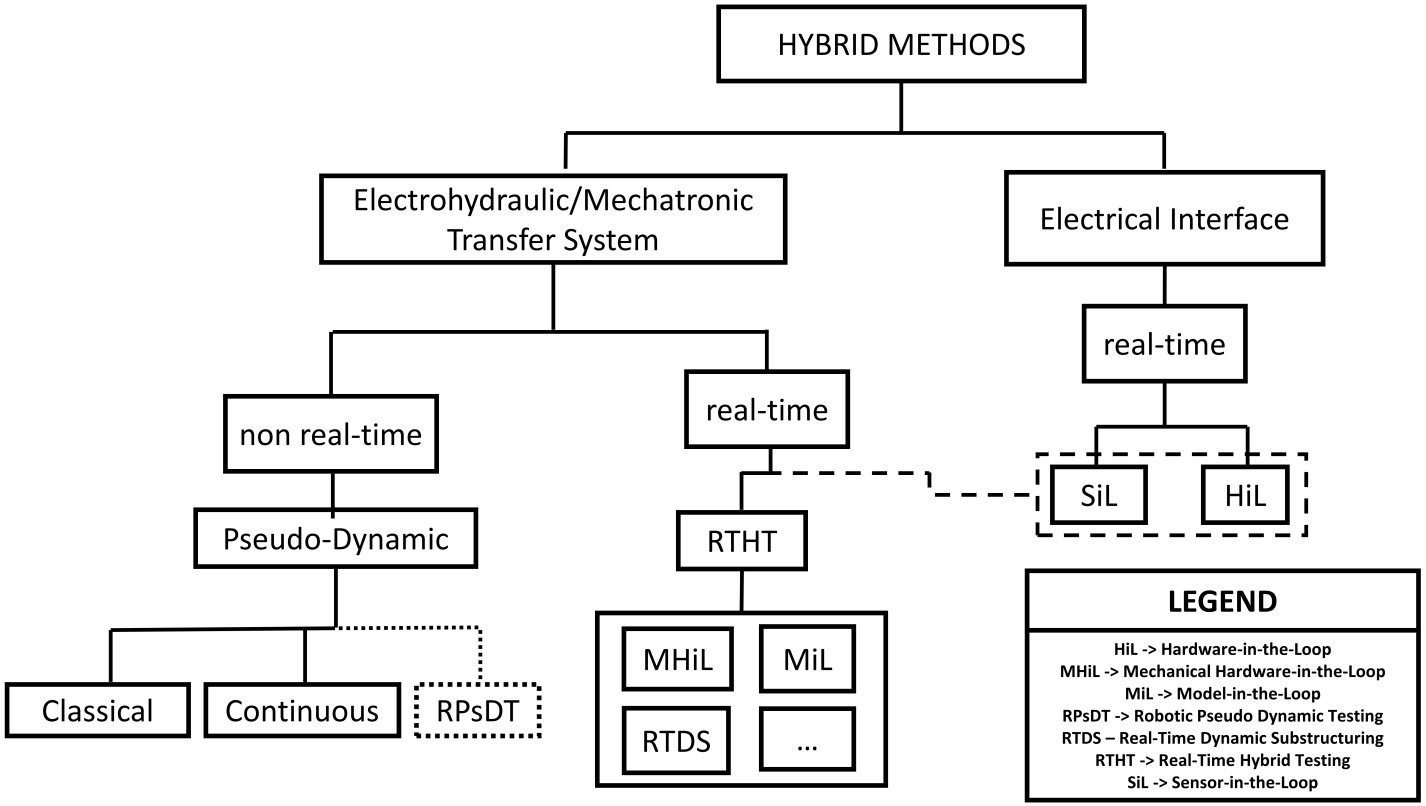

Figure 2.1: Categorisation of hybrid methods from a systems and control perspective. The dotted line illustrates where the proposed RPsDT technique resides in the overall context of contemporary hybrid methods. The dashed line denotes exceptions in the tree-based classifications for the validation of electronic sensor and controller hardware that respond to inputs generated from mechanical transfer systems as in [22, 23].

2.2 HiL & SiL Testing of Electronic Components

Although a lot of ambiguity exists in the naming conventions of hybrid methods, here the term 'Hardware-in-the-Loop' (HiL) testing is exclusively used for tests targeted at the evaluation of a physically present electronic hardware component, such as an embedded controller, by simulating the operational behaviour of connected systems and peripheral electronics that the device has to interact with in service. To this end, the substructure interface is purely electrical and the signals generated throughout the test match closely with those that the hardware would be subjected to in operation, *i.e* no significant spurious dynamics are expected to compromise the test as a consequence of system sub-structuring. Equally, this applies to most Sensor-in-the-Loop (SiL) tests that are used to assess the performance of physically present transmitters and transducers, thereby enabling the online verification of communication protocol implementations, message scheduling algorithms, data acquisition schemes and overall sensor-system integration strategies [36]. Of course, exceptions to this rule apply as indicated by the dashed line in Figure 2.1. For instance, in some cases the sensors and systems under test need to respond to inputs that are generated by a mechanical transfer system which in turn introduces significant dynamics into the test loop. An example of this are the combined SiL/HiL tests performed in [23] where robots physically reproduced the relative motion between a drogue and a receiver aircraft in order to assess the tracking performance of vision sensors and flight controllers.

In its simplest form a HiL test can be used to verify the performance of a single control unit such as a micro-controller or programmable logic controller (PLC) by connecting respective input-output (I/O) or bus interfaces to those of a real-time simulation target,

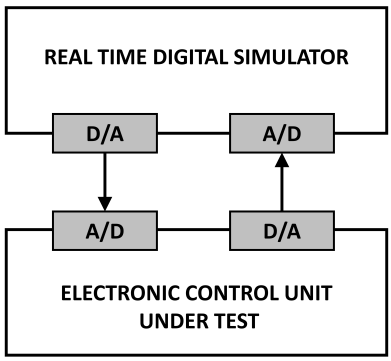

Figure 2.2: Topology of a HiL test for a single electronic control unit. The tested controller is connected to a real-time digital simulator via low voltage I/O banks.

sometimes called a 'Real-Time Digital Simulator', as schematically shown in Figure 2.2. The latter typically constitutes an industrial PC with a real-time operating system that deterministically executes deployed models of connected systems and accurately emulates their behaviour via appropriate low voltage I/O banks. An example of HiL tests based directly on this topology is outlined in [44] for the controller testing of DC-DC buck converters and DC-AC power converters and an entirely open source software based design of a HiL platform is presented in [45], detailing both the implementation and profiling of controller tests for an H-bridge inverter and boost converter.

More comprehensive setups combine HiL and SiL tests for the simultaneous validation of entire networks of electronic control units, sensors, bus- and electrical distribution systems as well as attached loads. An example of this is given by the AGCO Fendt tractor test bench depicted in Figure 2.3. Here, a numerical simulation of a tractor engine, drive train as well as power lift actuators is coupled with the physically present ECUs under test, the input devices on the human machine interface and peripheral electronic components such as lighting and signalling systems. The core of this setup is a real-time machine that simulates those inputs to the ECUs that are not available from sensors on the test bench and processes the returned actuator command signals. In this way, a comprehensive testing facility with high availability can be realised. Given that as of 2009 up to 70 electronic control units were incorporated in modern premium vehicles with an estimated 100 million object code instructions totalling 1Gbyte of embedded software [47], the transformative character the introduction of HiL testing has had on industry becomes evident. In addition, it is likely that trends towards the

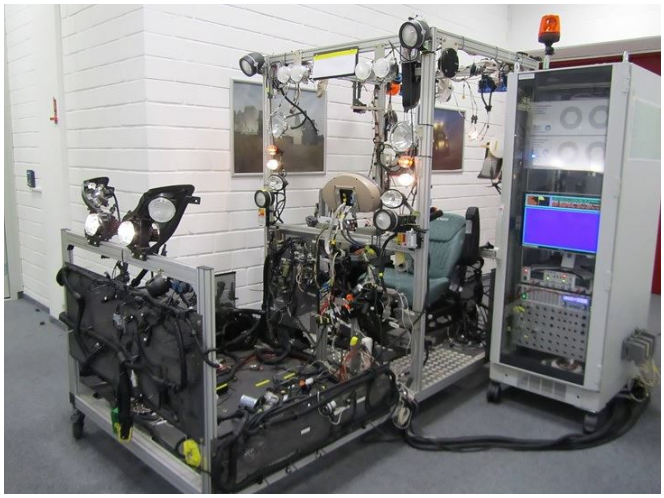

Figure 2.3: Test bench at AGCO Fendt using combined HiL and SiL to test electronic control units and peripheral electronics of a tractor. (Speedgoat GmbH) [46].

introduction of advanced driver assistance systems and increasing levels of autonomy in vehicles will further consolidate HiL and SiL as verification tools in the automotive and other sectors.

2.2.1 Challenges

Challenges in HiL testing often revolve around the real-time implementation and execution of the numerical model. For one thing, the continuous-discrete conversion at the hardware-simulator interface connection inevitably introduces a loop delay of one time-step in order to propagate signals through the numerical model which has an adverse effect on the test stability [48]. For another, both model complexity and solver parameters have to be carefully considered to ensure accuracy and convergence but avoid starving the system of computational resources.

Typically, explicit fixed-step integration algorithms are adopted (variable step solvers are unavailable for real-time execution) to ensure determinism throughout model execution and a balance between model fidelity and time-step size has to be found for a particular processor board. Problems arise when the underlying model is both complex and numerically stiff, and consequently the maximum tolerable solver step size is so small that the deadlines for advancing the model cannot be met due to limits in the available computational power. In this case, the model may have to be altered or the integration scheme needs to be further stabilised, and much contemporary attention is devoted to the latter approach [48, 49]. While dedicated integration methods have been developed and promise stability improvements at the expense of additional complexity [50, 51], simple explicit schemes like the Euler method, can immediately benefit from an analytically precomputed Jacobian for a given model structure [52]. Also, numerical stability may be affected by the state variable selection and a judicious definition based on the variation of parameters methods rather than generalised coordinates and velocities may help to avoid divergence issues [53]. Higher order methods such a Runge Kutta [54] may yield increased accuracy at the expense of higher computational load per time step but may also allow time step sizes to be relaxed which can sometimes lower the overall computational overheads. From a practical point of view a compromise between stability and computation time may also be reached by splitting the numerical model into fast and slow parts. This can be beneficial especially if the computations required to 'oversample' the fast substructre are small compared to the slower one [52].

2.3 Mechanical Hybrid Testing Methods

Whereas the previous section has focused on the testing of electronic devices and sensors, this section discusses hybrid testing of mechanical hardware by means of a mechatronic or electro-hydraulic transfer system. Despite differences in the nature of the target and interface hardware, the test topology and aim are fundamentally equivalent: The system at hand is split into a numerically simulated and an experimentally tested substructure that are in direct interaction to reproduce the dynamics of the complete system. As the name implies, the specimen in the experimental substructure of a mechanical hybrid test is an uncertain mechanical component and the test seeks to determine or verify its operational load-response characteristics as well as its influence on the dynamics of the rest of the system. To this end, the substructure interface dynamics have to be reproduced in terms of physical forces and displacements and the transfer system to do so would typically consist of displacement-controlled actuators and load transducers or force-controlled actuators and position feedback units as used in effective force testing [55]. Additional sensors can be directly fitted to the hardware specimen for the synchronised acquisition of data that does not serve as an input argument to the synthetic substructure (*e.g.* strains, operational temperatures etc.). The fundamental architecture of mechanical hybrid tests complies with Figure 2.4.

Throughout a test, the experimental specimen is subjected to a force or displacement history. The dynamics at the interface DOFs are specified by the numerical model in the synthetic substructure and imposed onto the specimen accordingly using hydraulic or electromechanical actuators. As before, the decisive test feature is the closed loop between the synthetic and experimental environment: Physical measurements of the specimen's actual response are acquired with load or displacement transducers and

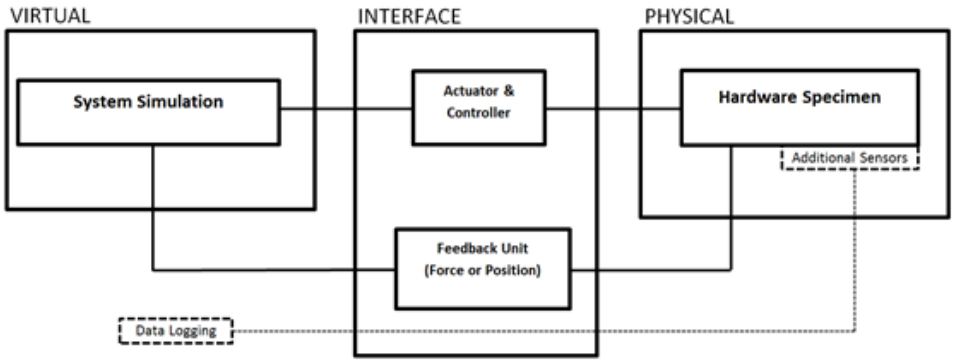

Figure 2.4: Fundamental architecture of a mechanical hybrid test.

fed back into the simulation. This way, the newly computed system states become a function of modelled and experimentally acquired data. Thus, a mechanical hybrid test effectively embeds a purely experimental test into a system simulation loop.

Major distinctions are drawn between non-real-time and real-time methods (see the left branch of Figure 2.1). While the former methods execute a test on an enlarged 'pseudo' time scale and are widely known as pseudo-dynamic (PsD) testing, here the latter are simply referred to as 'Real-Time Hybrid Testing' (RTHT) but may go by various names including '(Mechanical) Hardware-in-the-Loop' (MHIL) [26], 'Model-in-the-Loop'(MIL) [56], or for reasons of its architecture as 'Real-Time Dynamic Substructuring' (RTDS) [57]. In the following, pseudo-dynamic and real-time methods are independently reviewed.

2.3.1 Pseudo-Dynamic Testing

PsD testing is a non real-time dynamic testing technique that was developed for the assessment of structural responses to earthquakes in civil engineering [58] and was primarily intended as an alternative to the shaking table test that would typically rely on scaled models due to size and load restrictions. The PsD technique is widely said to originate from the works of Hakuno et al. in 1969 [59] (in Japanese) who attempted to conduct an early hybrid test for a single DOF cantilever structure by solving the governing equations with an analogue computer that was coupled to the structure via an actuator. Digital implementations followed in the 1970s primarily from Takanashi's work [60, 61] (with possible earlier contributions again in Japanese detailed in [62]) but hardware limitations meant that conducting the tests with realistic loading rates could not be achieved. In order to address this problem, the tests were run on an expanded time scale and the system dynamics effectively computed in simulation based on the discretised equations of motion for the tested structure. Importantly, the applied 'time scaling' had the added advantage that actuators of suitable load rating but with inadequate response speed and power rating could be used while flow requirements for hydraulic actuation and computational time limitations were vastly relaxed [58, 63].
Many good reviews of the PsD testing method exist which cover the history of development, numerous test examples, the adoption of different integration schemes and error analysis of the technique in detail beyond the scope of this section [55, 63, 64, 65]. Here, the aim is to provide a brief description of the test method in its native field, i.e. earthquake testing, to give a concise summary of the test procedure, as well as its strengths and limitations.

In civil engineering, the primary aim of a PsD test is to determine the structural response of a building to a record of ground accelerations without having to base-excite the structure dynamically. This is achieved by physically testing for the stiffness response of the structure at different building levels in a step-wise quasi-static fashion, *i.e.* incrementally at slow speeds, while a numerical model of the structure computes its dynamic response as a function of the stiffness-based restoring forces obtained from the physical test.

Consider the simplified lumped mass representation of the two story base-excited building in Figure 2.5, where the building's mass is concentrated at first and second floor in the form of m_1 and m_2 and the intermediate columns between stories have been condensed to stiffness and damping elements k_1, k_2, c_1, c_2 respectively. It can be shown that the system is governed by Eq. 2.1, where the sub- and superscripts denote the relation between the inertial reference frame 0, the base reference frame b as well as the frames 1 and 2 local to m_1 and m_2 respectively.

$$\begin{bmatrix} m_1 & 0 \\ 0 & m_2 \end{bmatrix} \begin{bmatrix} \ddot{x}_1^0 \\ \ddot{x}_2^0 \end{bmatrix} + \begin{bmatrix} (c_1 + c_2) & -c_2 \\ -c_2 & c_2 \end{bmatrix} \begin{bmatrix} \dot{x}_1^b \\ \dot{x}_2^b \end{bmatrix} + \begin{bmatrix} (k_1 + k_2) & -k_2 \\ -k_2 & k_2 \end{bmatrix} \begin{bmatrix} x_1^b \\ x_2^b \end{bmatrix} = \begin{bmatrix} 0 \\ 0 \end{bmatrix} \tag{2.1}$$

Note that the absolute displacements of masses m_1 and m_2 with respect to the inertial reference frame 0 are given as the sum of the relative displacement of the base frame to the inertial frame x_b^0 and the relative displacement of the individual masses $x_{1,2}^b$ with respect to the base frame as follows:

$$\begin{bmatrix} x_1^0 \\ x_2^0 \end{bmatrix} = \begin{bmatrix} x_b^0 \\ x_b^0 \end{bmatrix} + \begin{bmatrix} x_1^b \\ x_2^b \end{bmatrix} \tag{2.2}$$

Then double differentiation with respect to time yields

$$\begin{bmatrix} \ddot{x}_1^0 \\ \ddot{x}_2^0 \end{bmatrix} = \begin{bmatrix} \ddot{x}_b^0 \\ \ddot{x}_b^0 \end{bmatrix} + \begin{bmatrix} \ddot{x}_1^b \\ \ddot{x}_2^b \end{bmatrix} \tag{2.3}$$

and upon substitution of Eq. 2.3 into Eq. 2.1, the original motion equation becomes:

$$\begin{bmatrix} m_1 & 0 \\ 0 & m_2 \end{bmatrix} \begin{bmatrix} \ddot{x}_1^b \\ \ddot{x}_2^b \end{bmatrix} + \begin{bmatrix} (c_1 + c_2) & -c_2 \\ -c_2 & c_2 \end{bmatrix} \begin{bmatrix} \dot{x}_1^b \\ \dot{x}_2^b \end{bmatrix} + \begin{bmatrix} (k_1 + k_2) & -k_2 \\ -k_2 & k_2 \end{bmatrix} \begin{bmatrix} x_1^b \\ x_2^b \end{bmatrix} = - \begin{bmatrix} m_1 & 0 \\ 0 & m_2 \end{bmatrix} \begin{bmatrix} \ddot{x}_b^0 \\ \ddot{x}_b^0 \end{bmatrix} \tag{2.4}$$

Note that $\ddot{x}_b^0$ can be directly obtained from the ground acceleration record $\ddot{x}_{ground}$ and that this result is commonly directly stated in the literature (*e.g* [58, 63]) in compact matrix form as:

$$M\ddot{x} + C\dot{x} + Kx = M\ddot{x} + C\dot{x} + F = -M\ddot{x}_{ground} \tag{2.5}$$

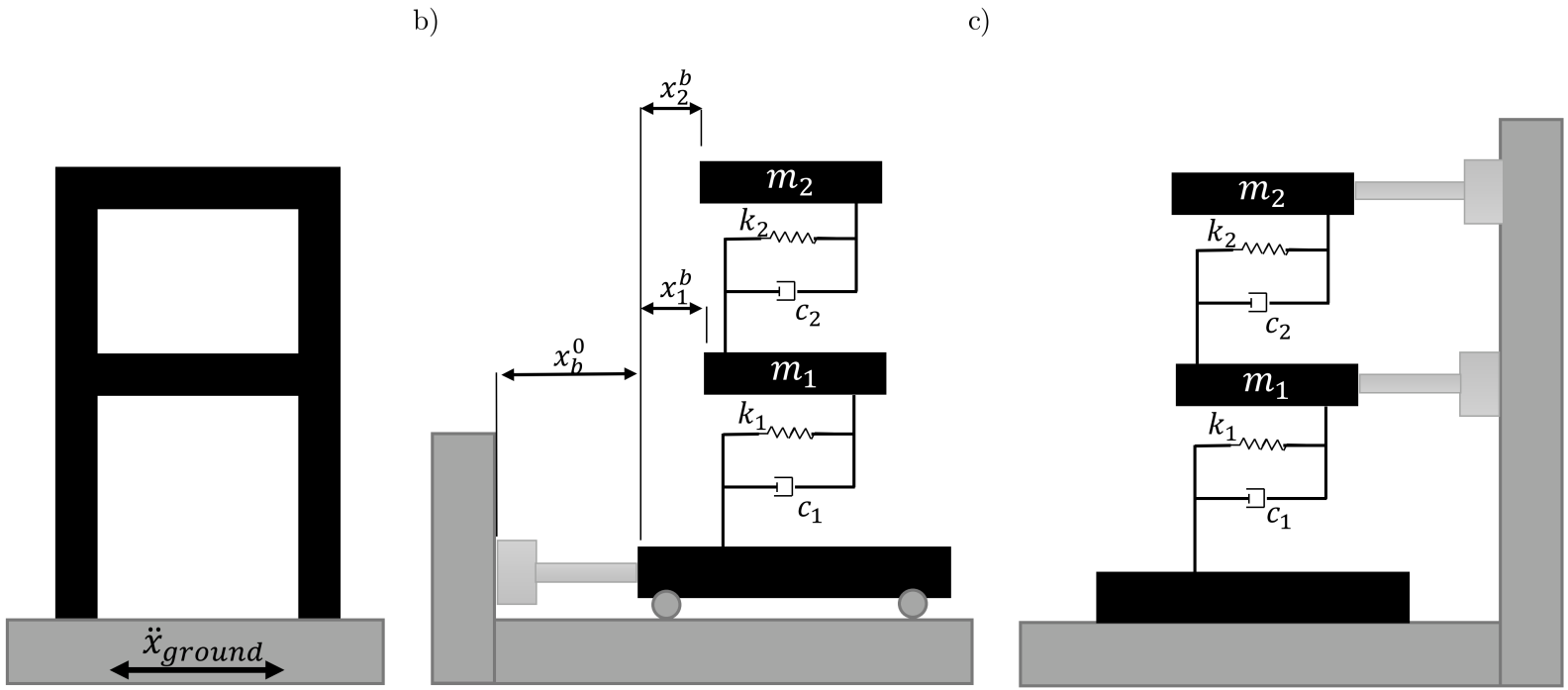

Figure 2.5: Comparison of base excitation and floor level excitation for a 2 story building. a) Original building structure subject to base excitation in an earthquake. b) Equivalent discretised model subject to base excitation in a laboratory shaking table test. c) Representation of discretised model subject to floor level excitation in a PsD test.

The short derivation above implies that base-excitation as provided by a shaking table test (Figure 2.5b)) and the excitation of individual floor levels with a fixed base are equivalent and hence the test setup in Figure 2.5c) is valid.

PsD testing exploits this principle and solves the system in Eq. 2.5 with input of the current restoring force measurements denoted F obtained as a measurement directly from the substructure in place of the stiffness forces Kx. To this end, the numerical model and physical test are directly coupled via an actuator and force sensor and the test is executed as an initial value problem according to the flow chart in Figure 2.6. At the beginning of each time-step, the current states of the structure are known and a restoring force measurement has been acquired from the physical test or is given from initial conditions. By employing a suitable integration algorithm such as the central difference method, a well-known explicit 2nd order method that has been widely used for PsD tests [58], the new states can be computed. To this end, the finite difference approximations in Eq. 2.6 and Eq. 2.7 are substituted into the governing equation in Eq. 2.5 to yield Eq. 2.8.

$$\dot{u}_i \approx \frac{u_{i+1} - u_{i-1}}{2\Delta t} \tag{2.6}$$

$$\ddot{u}_i \approx \frac{u_i - 2u_i + u_{i-1}}{\Delta t^2} \tag{2.7}$$

$$u_{i+1} \approx \left[\frac{M}{\Delta t^2} + \frac{C}{2\Delta t}\right]^{-1} \left[F_i - R_i + \frac{2M}{\Delta t^2} u_i - \left[\frac{M}{\Delta t^2} - \frac{C}{2\Delta t}\right] u_{i-1}\right] \tag{2.8}$$

Once the new nodal displacements are computed, these are slowly imposed onto the structure, allowing the actuators to settle at the target position in each step, before new restoring force measurement are taken and the cycle repeats. A ramp-hold profile is commonly employed for this purpose. Due to the quasi-static load application, the

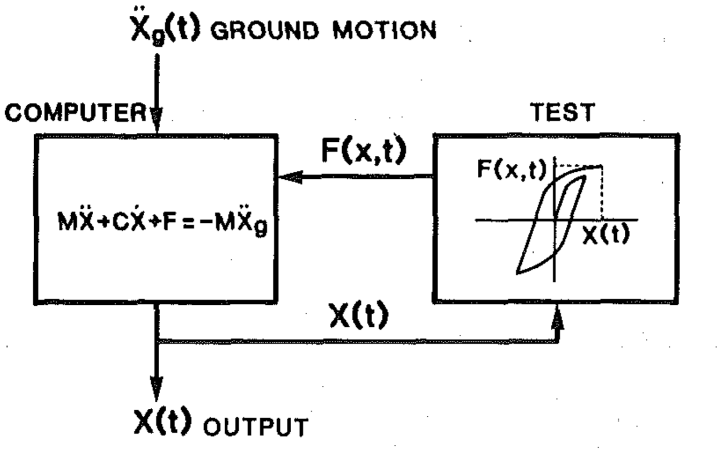

Figure 2.6: Schematic flow chart of a PsD test. Reproduced from Takanashi 1987 [63]

need for high dynamic actuator ratings and any form of real-time requirements for the simulation loop is eliminated. This, however, comes at the expense of disregarding time-dependent behaviour in the measurement of the structural response. As such, the PsD testing technique can capture non-linearity in the structural stiffness including effects of plasticity as well as structural damping and hysteresis due to loading paths dependencies. However, rate and time dependent effects in the structural response such as inertial effects, viscous damping and creep cannot be experimentally measured and must be accounted for in simulation. Additionally, problems can arise when the tested material properties differ with loading rates [66] and when significant force relaxation effects [67] occur while the actuator settles over the hold period. Both of these effects will manifest in a reduced test quality.

A 'Continuous Pseudo-Dynamic Test' is a derivative technique developed to mitigate some of the unwanted effects arising in classical PsD testing as described above. Introduced by Takanashi [68] as a 'rapid online test', in continuous PsD testing the actuator is commanded to apply the load steadily without start and stop motions and the velocity command to do so is continuously adjusted according to a predefined time scaling factor. Compared to the classical step-wise PsD test, continuous PsD testing can lead to a substantial reduction of the test duration [68, 69], however precise timing for model execution and command scheduling is required meaning that the implementation advantages of a non real-time method are effectively lost. In addition, direction changes throughout a test due to load reversals can be problematic and have been reported to result in systematic overshoots in the load application when the target position is overrun [68]. Given that such direction changes are inherent to the base excitation records in earthquake testing, simple control schemes that might be sufficient for step-wise PsD tests may not be applicable to continuous PsD testing and improvements to the control and actuation technology equivalent to those introduced for RTHT, which originates from the continuous PsD testing technique, become necessary. These are discussed as part of the next section.

Finally, distributed pseudo-dynamic testing is a further variant of the classical PsD test that exploits its non real-time character to combine tests at laboratories in different geographical locations. To this end, an event-based test architecture is created and actuator commands as well as restoring force readings are exchanged online [70]. In this way, the combined capabilities of multiple laboratories can be harnessed simultaneously. The appraoch has also been extended to distributed continuous PsD tests as reported in [71] but this requires delay mitigation and forward predictive techniques as fall back mechanisms to cope with the latencies and unpredictabilities in the scheduling of online traffic.

2.3.2 Real-Time Hybrid Testing

RTHT has evolved from the substructured PsD testing technique with the aim to excite the experimental specimen with the precise operational loading pattern that is computed by the numerical model in each time step. With forces and displacements imposed onto the experimental specimen at actual rates rather than quasi-statically, in-service conditions are expected to be more realistically replicated than in PsD tests.

Compared with HiL tests of electronic components, RTHT is more troublesome. While the same problems associated with the implementation of the real-time model and the stability of the numeric integration scheme discussed in Section 2.2.1 apply, additional challenges arise due to the introduction of the intermediate transfer system that couples both domains and converts between electrical signals and physical forces/displacements. In an ideal case, the transfer system would have unity gain on forward and feedback paths (*i.e.* instant actuator response and sensor measurement, no spurious dynamics) and given that the electrical interface signals in a HiL test can be generated to closely match the in-service conditions, no significant discrepancies arise. For RTHT, however, this is more problematic: Both, actuators and sensors inevitably introduce their own dynamics to the test loop and suffer from disturbances and measurement noise respectively. Plummer notes this deficiency, illustrates it in a schematic comparison of hybrid testing loops with perfect and imperfect transfer system (see Figure 2.7) and additionally highlights the dependence of the actuator dynamics on the coupling forces acting at the specimen attachment point [56, 72]. While in PsD tests these unwanted dynamics are vastly eliminated due to the quasi-static load application, in RTHT they are manifested in the critical real-time response and can significantly impair the quality of test results or have an immediate detrimental effect on the test stability. This is further exacerbated by the fact that the introduced discrepancies are difficult to quantify without a reliable reference model for the complete system and the existence of such a model would make the hybrid test obsolete in the first place [27].

The main causes for test instability are delays induced at the interface DOFs, be those uniform latencies or frequency dependent lags, and in the earliest RTHT experiments loop delay was shown to manifest as 'negative damping' [73] causing the response to grow unbounded when the inherent system damping is outweighed. For further information, the interested reader is pointed to Appendix A for a simple assessment of the effects of loop delays on the simulation quality using energy-based considerations. The main sources of delay in RTHT result from the *(i)* discrete-continuous conversion as discussed in Section 2.2.1, *(ii)* transducers and signal processing equipment on the

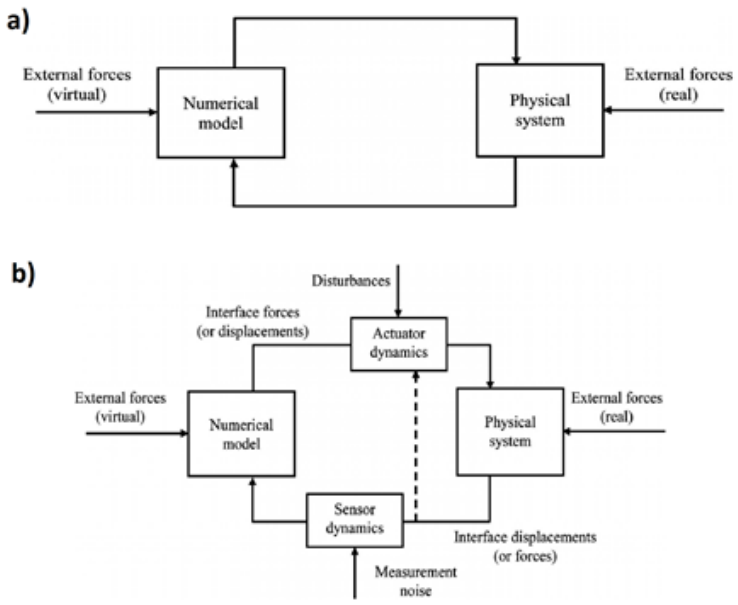

Figure 2.7: Schematic representations of real-time mechanical hybrid testing loop as per Plummer, showing (a) perfect and (b) imperfect actuator-sensor interface. Dashed line indicates the dependence of actuator dynamics on behaviour of physical system. Reproduced from [56, 72].

feedback path and *(iii)* the actuators used to excite the specimen in the first place. Given that the sensor bandwidth typically exceeds that of actuators by at least one order of magnitude [56] and measurement latencies are negligible (as for HiL tests), actuators are widely seen as the most problematic source of delay for RTHT.

Hardware vendors dedicate much effort to advance actuation technology but improvements are incremental in nature. Among all common technologies, electro-hydraulic actuation is considered the most responsive today with identified delays of 11ms and time constants of 15ms in [26] while other sources state 8ms delays as achievable for high performance systems [73]. By contrast, this compares with latencies of 20ms and rise times of up to 100ms for 6DOF industrial robotic manipulators [22]. In any case, delay mitigation strategies are necessary to guarantee both test stability and fidelity for RTHT and much recent academic attention has been devoted to this field.

Conventional approaches to RTHT use a single actuator per excited DOF on the specimen in either position or force control and fundamentally rely on a drive unit with a fast inner loop feedback controller that may well be vendor provided and pre-tuned for the specific actuator. From a control perspective, an established approach to delay mit-

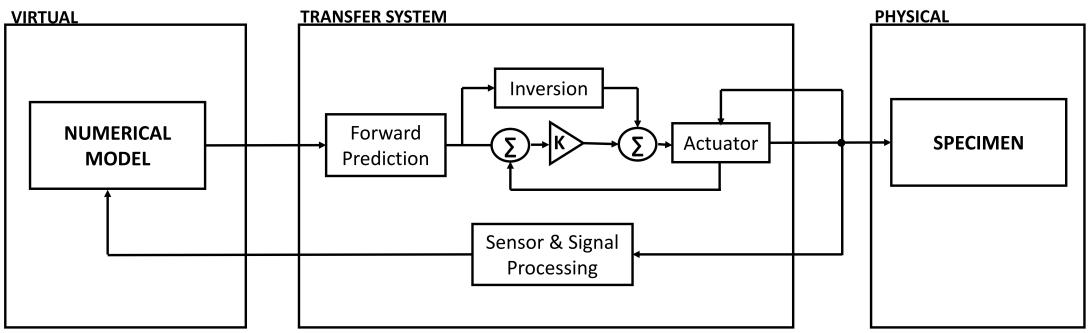

Figure 2.8: Schematic of conventional delay mitigation scheme for RTHT combining forward prediction, model inversion and fast inner loop control.

igation is to supplement this inner-loop with an outer-loop control scheme that seeks to shape the combined response of actuator and attached hardware to that demanded by the numerical simulation. To this end, popular control methods combine forward prediction algorithms and inversion schemes [26, 72, 74, 75, 76] as schematically shown in Figure 2.8. The forward-prediction projects the actuator command signal into the future based on current and previous system states, in an attempt to provide the actuator with a 'head start' and hence a possibility to compensate for uniform delays should the prediction be correct. On the other hand, inversion schemes, *i.e.* direct model inversion or inverse dynamics based approaches, can account for lags and higher order dynamics as well as non-linearity inherent to the actuator and system under test, leaving the inner loop controller with the task of taking up residual error. The main problem with this approach lies in the development of a causal and reliable inverse model in the presence of a specimen with uncertain characteristics that in turn affect the actuator dynamics as mentioned before. This is further complicated by the fact that the characteristics of the specimen may strongly depend on the operating condition and can change throughout the test while the control scheme is tuned for a single operating point.

In order to address these challenges, adaptive schemes have been introduced [77, 78, 79] and can compensate for gradually changing conditions but just like the forward prediction approach, fail to ensure accurate tracking in the presence of abrupt transitions that are typical for heavily non-linear systems. The latter are not limited to AAR maneuvers and their discontinuous contact events but are found in a variety of mechanical systems and encompass backlash in mechanisms, the sudden opening and closing of valves (*e.g* relief vales) in hydraulic systems or contact losses of tyre and road in vehicle dynamics for example. For components with linear characteristics, however, the approaches

above have proven adequate and, similar to HiL testing, led to the widespread adoption of the technique in industry where RTHT has become an important verification tool for mechanical systems and structures. Recent research on the other hand continues to focus on further refinements and addresses issues such as actuator saturation that can produce systematic undershots, lead to wind-up problems and undermine all of the control schemes mentioned above [80, 81].

2.3.3 Hybrid Tests using Robotic Actuation

Having reviewed control methods for RTHT that are tailored for and predominately implemented with hydraulic actuation in the previous section, this section shifts the focus to tests conducted with robotic manipulators and related challenges. Robot assisted hybrid tests for the pre-operational testing of complex systems is a recent field of research. Examples range from verification tests of sensor and flight controllers in the pre-contact phase of AAR operations for UAVs [22, 23, 24] to on-ground tests of satellite docking maneuvers in zero-gravity conditions [82]. Especially the kinematic versatility of industrial robots makes them an attractive choice for applications involving relative motion reproduction. In addition, industrial robots are available as commercial off-the-shelf (COTS) systems, low cost, readily equipped with accurate position feedback units and typically provide 6 or more DOF for position and orientation manipulation in 3D space. It follows from the sections above, that crucial factors in running hybrid tests of contact dynamics include *(i)* the ability of actuators to precisely manipulate the position and orientation of the colliding structure(s) in 3D space, *(ii)* sufficiently fast response times for the contact event and *(iii)* compensation for the actuator transfer dynamics. While current industrial robots satisfy the first factor, challenges arise in meeting the latter two demands, especially for high velocity impacts and particularly stiff collisions.

Industrial robots are designed to execute repetitive task in controlled environments (e.g. as part of assembly lines in factory automation) and are not intended to provide high responsiveness to external sensor measurements. The main limitations result from the inherently large link inertia and proprietary control architectures. The latter typically preclude low level access to the axis controller, thereby hindering system identification as well as the implementation of favourable RT control schemes such as impedance control [83], passivity based control [84] and model inversion schemes [26]. Low-level controller access is only available for small scale robots such as [85] which have been specifically built for the use in research laboratories but not for the industrial variants.

Commercial 'open architecture' control interfaces such as [54] that aim to provide rapid control prototyping (RCP) capability for industrial robots, essentially build on top of the high level proprietary interfaces provided by the robot vendors. Access to torque reference commands or controller parameters is not granted and only limited feedback is available which complicates system identification approaches [86]. In addition, high-level proprietary interfaces provide low controller sample rates and considerable dead times in command execution [22]. Depending on the dynamic properties of the emulated system, these factors can have a detrimental effect on the stability of the hybrid tests [87], more so when the afore mentioned delay compensation techniques such as forward prediction are not applicable due to the discontinuous nature of contact events [49].

Approaches in dealing with these limitations differ significantly. Ma et al. realised an admittance control scheme around the proprietary architecture of a KUKA industrial controller for the hybrid simulation of satellite docking manoeuvres [82]. As these manoeuvres occur at low relative speeds in the order of several centimetres per second, delay and sample rate restrictions associated with the high level robot control interface did not present a limiting factor.

Further efforts focused on gaining direct low-level robot control. Blomdell et al. [88] created an application for motion control of ABB robots which intercepts and overwrites the messages exchanged between the high level computer and the low level axis controller. This grants access to position and velocity reference and feedback signals and allows integration and processing of external sensor signals at low level and therefore high command rates. While this architecture still does not enable the implementation of direct impedance control strategies, it provides a substantial performance improvement over vendor provided interfaces.

Other approaches have circumvented the use of industrial robots completely and produced special purpose designs tailored at a particular application and control strategy. Notable efforts are the developments of parallel kinematic platforms for real-time hybrid space docking simulations [38, 39] as well as the development of a robotic facility for the emulation of contact tasks performed with space robots that cannot be operated in a 1g environment [28, 29, 30, 31]. While custom rig designs often present an optimum solution, the viability of such a design only applies to projects where the benefits substantially off-set the design and production efforts.

2.4 Comments and Critique

Hybrid testing is a promising method for the study of complex systems and given the difficult to reproduce environmental settings of an AAR manoeuvre, system hybridisation is seen as a crucial factor in enabling the preflight investigation of AAR procedures in a laboratory. To this end, it comes as a natural choice to incorporate the flight regime into a numerical simulation while capturing the critical contact dynamics between probe and drogue experimentally. In addition, this approach has the benefit of maximising the exploitation of published work on the modelling of the in-flight dynamics of the hose drogue assembly, while the complexity of contact models and inherent parameter uncertainties are avoided.

The serial link manipulators at RMR are kinematically well suited for the relative motion reproduction of probe and drogue throughout the contact and coupling phase. Shortfalls for the integration of favourable control schemes due to proprietary restrictions for ABB's native IRC5 system may be remedied in parts through adaptation of Blomdells modified architecture [89] that grants direct access to the robot's axis controller. This way, outer loop controllers with update cycles of 250Hz and 20ms latency can be implemented providing one of the most responsive systems available for industrial robots today. Nevertheless, at typical AAR contact speeds of 1.5m/s a relative penetration of 6mm would occur before a sample of the contact force has been propagated through the controller just once, followed by a further 30mm of relative penetration before the robot begins to physically react to the contact event. Given that the merits of forward predictive methods for delay mitigation cease to exist for non-linear and discontinuous events, one would simply be left with an unrepresentative crash that will likely prove detrimental to the actuators, sensors and possibly refuelling hardware. For this reason, the investigations in this thesis start from the premise that a safe and successfully conducted hybrid test of an AAR manoeuvre at RMR and facilities with similar bandwidth restrictions has to be based on the pseudo-dynamic technique for the duration of the contact and coupling phase.

The application of a pseudo-dynamic method to contact-impact problems is an unconventional choice and to the best of the author's knowledge has not been reported in the literature to date. A reason for this may be that contact phenomena are very dynamic and typically characterised by brief durations, quick increases and reductions in forces, abrupt acceleration and deceleration patterns as well as rapid energy dissipation. Consequently, the attempt to capture such high frequency content adequately in a pseudo-dynamic test may seem futile at first glance. In fact, however, the pseudo-

dynamic approach is not merely to be seen as a last resort for delay mitigation in order to stabilise the simulation loop, but behind it stands the author's hypothesis that:

'*The contact response of the drogue is preponderantly structural and dominated by its non-linear stiffness properties, while the primary form of energy dissipation is expected to result from hysteresis inherent to the ribs and interlinked elastic cord.*'

This is to say, that the contribution of rate dependent effects to the contact forces is minor and high confidence predictions for the contact and coupling dynamics are attainable despite their neglect in a pseudo-dynamic test. As an integral part in answering the research question and fulfilling the aims and objectives set out in Section 1.6, this thesis seeks to put to the test the above hypothesis in carefully designed and rigorously conducted validation experiments.

Chapter 3

Methodology

This chapter presents the development and implementation of the testing method. It comprises descriptions of the test framework, procedure, software architecture, motion control concepts as well as derivations of the models employed in the numeric substructure of the tests. The reader is advised that the contents of this chapter relate to the final test architecture and given that the development of a testing method is an iterative process, the information provided may in parts differ from or repeat contents of Chapter 4 and Chapter 5 respectively. It is judged however, that the convenience and coherency provided by the collective discussion of the methodology over the following sections outweighs the level of repetition introduced by later chapters.

3.1 Hybrid Testing Framework

The adopted framework for hybrid tests of AAR scenarios is schematically illustrated in Figure 3.1. Industrial robots equipped with 6 DOF force/torque sensors and full-scale refuelling hardware are used as a transfer system to couple a numerical simulation of a flight regime with experimental tests of probe-drogue contact scenarios in order to predict the dynamics of the complete system in realistic operating conditions. To this end, the numerical side contains simulations of the hose-drogue assembly and reel take-up mechanism as well as models for tanker and receiver aircraft and a flight regime, while the robots reproduce the relative motion of probe and drogue in each simulation step and feed back contact force measurements to close the loop. That is, the robots are effectively enslaved by a master simulation to embed an experimental contact test into a simulation loop of an AAR manoeuvre, thus ensuring that as the test advances, the

simulation states become a function of both numerically modelled and experimentally measured data. Strain gauges are fitted to the drogue ribs to allow the monitoring of induced strains throughout the test.

The chosen division of system parts and components into numerical and experimental substructures shown in Figure 3.1 reflects the argument from Section 1.5 that the most severe deficiencies lie in the modelling and simulation of the contact and coupling dynamics which consequently have to be studied experimentally, while reliable models that have been developed and validated for the continuum dynamics of the remainder of the system can be employed in the numerical substructure. Subject to the successful implementation and validation of the outlined architecture, the advantages of this hybrid approach over alternative methods for pre-operational testing are substantial:

(1) Forces and moments that develop throughout the contact- and coupling phases are based on direct measurements making simplified assumptions in numeric simulations obsolete.

(2) The need for the integration of contact models with uncertain parameters is eliminated.

(3) In contrast to a purely experimental setup, the investigation of realistic hits and drogue reactions is made possible.

Hence, the architecture in Figure 3.1 promises the quick, repeatable and inexpensive study of diverse AAR scenarios including off-centre hits and missed attempts in a controlled laboratory environment without putting equipment or personnel at significant risk. Considerations for the test implementation and execution follow in the subsequent sections.

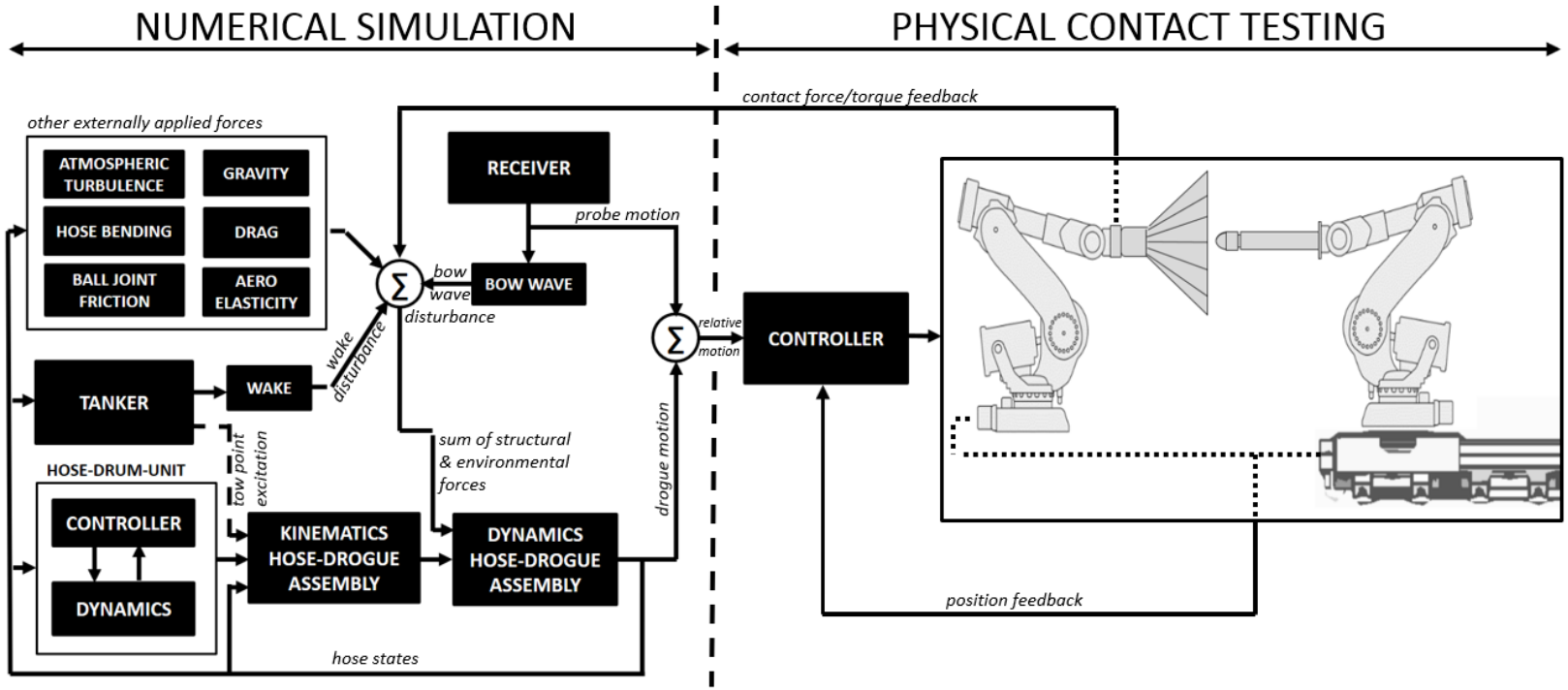

Figure 3.1: Proposed hybrid testing framework. The numerical substructure encompasses models of the flight regime, hose-drogue assembly, reel take-up mechanism as well as tanker- and receiver aircraft while industrial robots physically reproduce the contact and coupling scenarios in every time step and feed-back experimental contact force measurements to close the simulation loop.

3.2 Method & Procedure

The method follows the algorithm depicted in Figure 3.2. As opposed to classical PsD tests, actuators and substructures are not in contact continuously and data from the experimental specimen is not acquired in every time step but only throughout the contact- and near-contact phase which can be identified based on kinematic constraints in simulation. If in contact, the robot is quasi-statically moved to reproduce the relative position and orientation of the colliding structures. This strains the specimen and allows measurement of the restoring forces and moments which are then fed back into the simulation. Significantly, the demanded robot movement has to be larger than the repeatability of the robot and the time step may have to be incremented adaptively to compute a valid target pose. In a non-contact phase, the robot is kept stationary and the simulation can advance immediately without prior contact force acquisition.

Upon acquisition of the restoring force, the simulation is treated as an initial value problem: Based on the current states of the contacting structures and physically acquired force measurements from the experimental substructure, the new accelerations are computed and the new system states are obtained with a suitable integration algorithm. The cycle then repeats with the next time step.

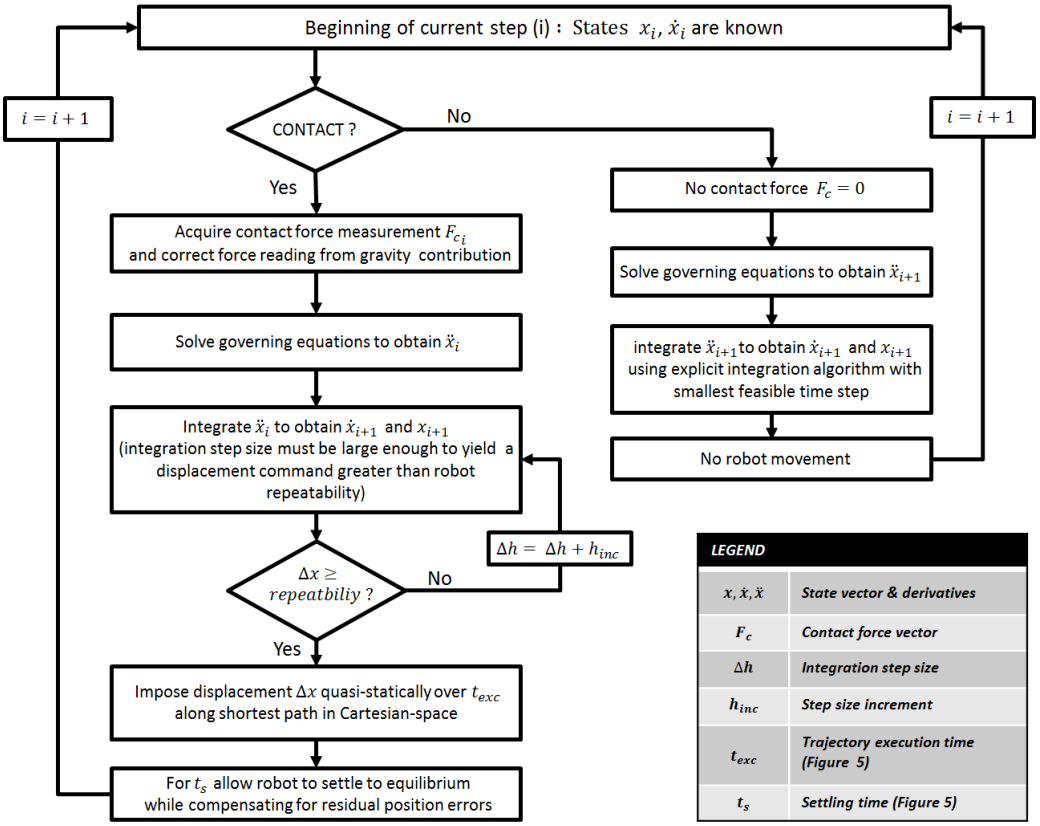

Figure 3.2: Algorithmic procedure for RPsDT of contact scenarios. Reproduced from [90]

3.3 Implementation

On a fundamental level, conducting a test according to the schematic in Figure 3.1 requires a bilateral ('full duplex') data exchange between a robot motion control unit (and attached manipulator) and a simulation environment. For a pseudo-dynamic test, real-time capability can be restricted to the robot motion controller only, while the simulation environment can be separated and executed as a standard priority task in user space with no imminent timing criticality for advancing the numerical models. In addition, the inter-process communication between both the simulation environment and the robot control unit can be kept entirely event-based (again non real-time), however precise control over the motion planing and execution throughout the contact phase is needed making the integration of bespoke trajectories a necessity.

Taking these considerations into account, the tests are implemented based on the architecture shown in Figure 3.3. Principally, the simulation environment and motion

control unit function as a designated client and server respectively. This provides a high abstraction layer and minimum dependency on system specific implementation details on either side. From an operational point of view, this structure ensures that the robot controller can be invoked (remotely if desired) on demand and commanded to execute a specified motion while the client awaits a reply (incorporating operational robot states, position and force/torque readings) that is sent upon motion completion. Using a TCP connection, the application is guarded from unpredictabilities associated with the network protocol and the data exchange is kept entirely event-based. Adopting this approach implements a master-slave hierarchy that fulfils all requirements for conducting of a classical pseudo-dynamic test. Given that the implementation is specifically tailored for robotic manipulators and intended to be used in discontinuous contact tasks that are uncommon for standard pseudo-dynamic tests, the technique is referred to as a 'Robotic Pseudo-Dynamic Testing' (RPsDT) from this point onwards.

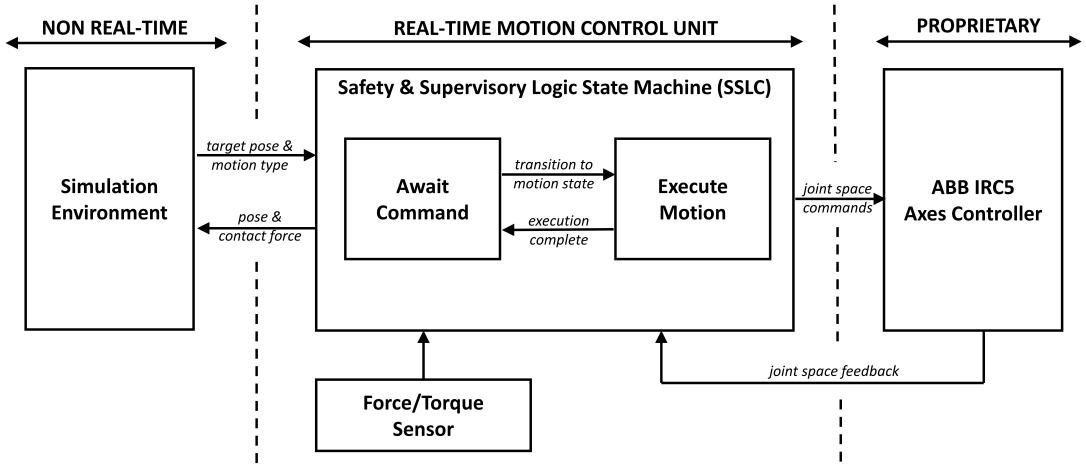

Figure 3.3: High-level RPsDT software architecture showing interaction of simulation environment, robot motion control unit and axis controller.

Reiterating that by design, the RPsDT method sets stringent requirements for the execution of the relative motion of probe and drogue throughout the contact and coupling phase, a bespoke robot control unit has been developed by the author that effectively replaces the operational software components of the standard ABB IRC5 controller throughout the tests. This enables *(i)* the precisely timed execution of bespoke trajectories, *(ii)* external force sensing and *(iii)* an open interface for integration with the simulation environment; all of which are non-trivial to achieve with modern industrial robots that rely on closed systems with proprietary architectures. On a high level, the control unit consists of a 'Safety & Supervisory Logic Controller' (SSLC) (Figure 3.3) that can be invoked to execute a range of motion types while accounting for singular-

ities or limit violations (joint position/velocity, workspace limits, force/torque limits, etc.) and providing reliable error handling and emergency halt procedures subject to the detection of such violations. The respective motion execution cases compute the desired trajectories based on the boundary conditions provided (*e.g* target pose/ target joint positions, execution/settling time) at an update rate of 250Hz and send joint level commands directly to the axis controller without any intervention from the higher level ABB system components. The forces and torques measured at the robot end-effector are made available to the controller at high update rates enabling fast reaction times in the event of a force/torque limit violation which is important to avoid equipment damage throughout the contact phases.

In order to get past the proprietary restrictions of the IRC5 system and attain the necessary freedom for application development and implementation of the control unit described above, the conventional ABB IRC5 system has been augmented based on the works of [88]. To this end, an additional task is spawned on the VXworks system of the IRC5 main computer with callbacks installed to *(i)* retrieve and forward current arm states (*i.e.* motor angles, velocities, torques etc.) for processing to an external real-time target via a real-time Ethernet connection, *(ii)* receive a reply with modified states from the real-time target within a 1ms window and *(iii)* set the modified states as new reference commands for the axis controller. Purposely, the external real-time target takes the form of a Linux machine that gains the relevant real-time capabilities on the basis of the Xenomai kernel extension/ I-pipe patch [91, 92] and RTnet driver framework [93]. The robot control unit that has been developed can be loaded and executed as a real-time kernel task on this machine for which a tool chain described in [88, 89] aides with the cross-compilation and dynamic linking in the deployment process directly from Simulink. Having a dedicated real-time machine of this type also enables the integration of external sensor signals into the robot control at high update rates and comparably low latencies again without facing any restrictions of proprietary industrial machines. Here, CAN was chosen as the initial and preferred connection type for the integration of force/ torque feedback but had to be replaced by a dedicated UDP connection at a later project stage. While this did introduce a larger delay and consequently increased reaction times of the SSLC to force/torque violations, it caused no significant performance loss for the tests.

3.4 Motion Control

The motion control unit implements a variety of motion types that can be executed when invoked externally on the basis of a predefined message protocol. Provided that the SSLC is in the 'Await Command' state (the base state), the message is parsed and an appropriate state transition initiated. The motion trajectories are computed directly upon transition to the demanded motion state (*i.e* at run-time) based on the boundary conditions extracted from individual messages. Joint level commands are then deterministically generated on this basis and sent to the axis controller every 4ms until the motion execution is completed, whereupon a transition back to the base state occurs and the robot is kept stationary to await the next command. In this manner, joint space motions subject to the definition of a joint space target position or Cartesian space target pose as well as Cartesian space motions along a direct path to the target pose can be executed either with trapezoidal velocity profiles (resulting in a linear segment with parabolic blends for the position variation) or according to 3rd order polynomial trajectories, *i.e* parabolic velocity profiles.

In addition, the realisation of more complex motion paths is made possible by interpolation based on the aforementioned fundamental motion types. To this end, the desired path has to be discretised off-line and individual 'chunks' sent to the controller in a message by message format. The motion control unit can then buffer these messages in pre-allocated memory (dynamic memory allocation is not an option for real-time systems) and execute the complex path as the seamless concatenation of the individual trajectories. In this manner, a great deal of the functionality expected from modern industrial manipulators can be implemented with a vastly open control architecture, where bespoke kinematic functions are integrated, allowing the complete control of the motion execution while computational efficiency is ensured based on the prior optimisation of these functions (by symbolic reduction) as described in [94, 95]. The latter avoids the repeated computation of equivalent terms and yields a minimum number of operations for the function evaluation in real-time.

For the execution of a motion throughout the contact phase in RPsDT (*i.e* when imposing the relative position on the specimen), it is important that the manipulation occurs along the shortest path in Cartesian space. While this implies that the 'tool' or specimen has to change position along a straight line, its orientation needs to change simultaneously along the shortest arc (on the surface of an imaginary unit sphere). These demands are satisfied by independently planned Cartesian space trajectories for 'tool' translation and orientation. In order to avoid erratic motions the position and

orientation commands follow a trapezoidal velocity profile meaning that the relative changes are predominantly imposed at constant speed, except for the necessary acceleration and deceleration phases that account for a user defined percentage of the total execution time.

Consider a motion from initial pose $\boldsymbol{x_0}, \boldsymbol{q_0}$ to target pose $\boldsymbol{x_t}, \boldsymbol{q_t}$ taking place over an execution time t_{ex} and followed by a settling time t_s for residual error compensation and restoring force acquisition, where $\boldsymbol{x_0}$ and $\boldsymbol{x_t}$ are position vectors and $\boldsymbol{q_0}$ and $\boldsymbol{q_t}$ are unit quaternions respectively. Further assume that the user specifies the acceleration and deceleration phases over the interval t_a and t_d to account for 10% of the motion time each, with constant speed being maintained over the intervening period $t_c = 0.8t_{ex}$. Then, the velocity $\boldsymbol{v_c}$ throughout the constant speed interval t_c follows from:

$$\boldsymbol{v_c} = \frac{\boldsymbol{x_t} - \boldsymbol{x_0}}{0.5t_a + t_c + 0.5t_d} \tag{3.1}$$

and nominal accelerations $\boldsymbol{a_a}$ and decelerations $\boldsymbol{a_d}$ in the intervals of duration t_a and t_d can be computed as:

$$\boldsymbol{a_a} = \frac{\boldsymbol{v_c}}{t_a}, \qquad \boldsymbol{a_d} = -\frac{\boldsymbol{v_c}}{t_d} \tag{3.2}$$

Taking a similar approach for the definition of the derivatives of the dimensionless SLERP scaling function $s(t)$ (which is subject to the bounds $s(0) = 0$ and $s(t_{ex}) = 1$ and used for the orientation interpolation as described below) yields constants equivalent to those in Equation 3.1 and Equation 3.2 respectively but for the orientation manipulation throughout the designated intervals.

$$\dot{s}_c = 0.8t_c, \qquad \ddot{s}_a = \frac{\dot{s}_c}{t_a}, \qquad \ddot{s}_d = \frac{-\dot{s}_c}{t_d} \tag{3.3}$$

Hence, the trajectories with trapezoidal velocity profiles for position and orientation variations can be obtained as linear segments with parabolic blends as follows:

For acceleration phase $t \leq t_a$:

$$\boldsymbol{x(t)} = \boldsymbol{x_0} + 0.5\boldsymbol{a_a}t^2, \qquad \boldsymbol{\dot{x}(t)} = \boldsymbol{a_a}t, \qquad \boldsymbol{\ddot{x}(t)} = \boldsymbol{a_a}$$
$$s(t) = 0.5s_at^2, \qquad \dot{s}(t) = \ddot{s}_at, \qquad \ddot{s}_t = \ddot{s}_a$$

For constant speed phase $t \leq (t_a + t_c)$:

$$t = t - t_a$$
$$\boldsymbol{x(t)} = \boldsymbol{x_0} + 0.5\boldsymbol{a_a}t_a^2 + \boldsymbol{v_c}t, \qquad \boldsymbol{\dot{x}(t)} = at, \qquad \boldsymbol{\ddot{x}(t)} = [0]$$
$$s(t) = 0.5\ddot{s}_at_a^2 + \dot{s}_ct, \qquad \dot{s}(t) = \dot{s}_c, \qquad \ddot{s}(t) = 0$$

For deceleration phase $t \leq (t_a + t_c + t_d)$:

$$t = t - t_a - tc$$

$$\boldsymbol{x(t)} = \boldsymbol{x_0} + 0.5\boldsymbol{a_a}t_a^2 + \boldsymbol{v_c}t_c + \boldsymbol{v_c}t + 0.5\boldsymbol{a_d}t^2, \qquad \boldsymbol{\dot{x}(t)} = \boldsymbol{v_c} + \boldsymbol{a_d}t, \qquad \boldsymbol{\ddot{x}(t)} = \boldsymbol{a_d}$$

$$s(t) = 0.5\ddot{s}_a t_a^2 + \dot{s}_c t_c + \dot{s}_c t + 0.5\ddot{s}_d t^2, \qquad \dot{s}(t) = \dot{s}_c + \ddot{s}_d t, \qquad \ddot{s}(t) = \ddot{s}_d$$

For settling phase $t > t_a + t_c + t_d$

$$\boldsymbol{x(t)} = \boldsymbol{x_0} + 0.5\boldsymbol{a_a}t_a^2 + \boldsymbol{v_c}t_c + \boldsymbol{v_c}t_d + 0.5\boldsymbol{a_d}t_d^2 \qquad \boldsymbol{\dot{x}(t)} = [0], \qquad \boldsymbol{\ddot{x}(t)} = [0]$$

$$s(t) = 0.5\ddot{s}_a t_a^2 + \dot{s}_c t_c + \dot{s}_c t_d + 0.5\ddot{s}_d t_d^2 = 1, \qquad \dot{s}(t) = 0, \qquad \ddot{s}(t) = 0$$

In the above, the function $s(t)$ represents a time varying scaling factor used for the Spherical Linear Interpolation (SLERP) [96] between initial and target orientation as per Equation 3.4, where $\Omega = arccos(\boldsymbol{q_0} \cdot \boldsymbol{q_t})$ describes the angle subtended by the arc of rotation. SLERP yields a Euclidean space orientation variation along the shortest arc (*i.e.* the geodesic) and is therefore incorporated in the trajectory planning mechanism for RPsDT.

$$\boldsymbol{q_i} = \left[\frac{sin(1 - s(t))\Omega}{sin(\Omega)}\right]\boldsymbol{q_0} + \left[\frac{sin(s(t)\Omega)}{sin(\Omega)}\right]\boldsymbol{q_t} \tag{3.4}$$

Corresponding joint position trajectories are subsequently computed by kinematic inversion and joint velocity commands follow simply from differentiation between the previous and current joint position commands as shown in Figure 3.4. While an analytical computation of joint velocities based on exact quaternion derivatives along the path specified by Equation 3.4 followed by inversion of the differential kinematics would be preferable, the smoothness, short time steps and low velocities for RPsDT motions mean that no significant discrepancies arise. Instead, computational time is saved while the axis position control loops are responsible for compensating the small inaccuracies.

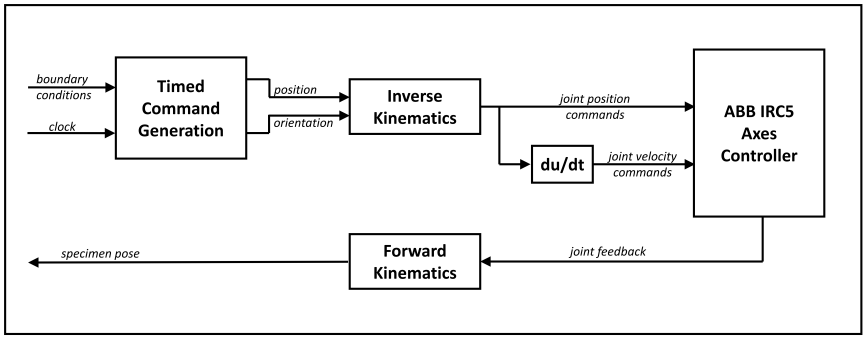

Figure 3.4: Joint space command generation from Cartesian space trajectories.

3.5 Modelling of the Hose-Drogue Assembly

This section presents the model development for use in the numerical substructure of the hybrid test. It follows the framework in Figure 3.1 and comprises a dynamic model for the hose-drogue assembly and flight regime. It is important to note that this phase of testing is primarily concerned with understanding the behaviour of the drogue itself, not the interaction of the drogue and a specific tanker/receiver combination. Hence, bow wave, wake vortices, gusts and other atmospheric disturbances are deliberately excluded from the tests and studies incorporating these effects can follow on from this work once the method has been proven. Nevertheless, the interested reader is pointed to [19, 23] for information on the modelling of these aspects.

The derivation of the hose model which is presented in the following, builds primarily on the lumped mass modelling approach described in [19]. While more sophisticated methods for the modelling of towed and tethered cable systems exist (e.g. [97]), the work in [19] has been partly validated against experimental flight data and is consequently chosen as the basis for the model development. Here, the original approach from [19] has been revised in an attempt to accommodate for the reel-in action of the HDU by uniformly shortening individual hose segments while accounting for the corresponding mass transfer effects; thereby achieving a uniform spatial resolution for individual hose segments (which increases during reel-in) throughout the entire simulation without having to model the process of winding the hose onto a drum. The underlying considerations in the development of the modified hose model are described in the following.

Consider a hose-drogue assembly represented by a finite segment model of n interlinked masses as shown in Figure 3.5a). Beginning at the hose-exit point on the refuelling pod, *i.e.* the tow point, the first $n-1$ segments represent individual hose elements as cylindrical rigid links connected by frictionless spherical joints. The mass of each link is concentrated at the link end, *i.e.* the location of the spherical joint connecting to the next hose segment. This is also the location of external load application. The lengths of all hose links can change uniformly to shorten or elongate the hose depending on the action of the *HDU* which is modelled as a separate entity that solely dictates the reel-in force, hose segment lengths and derivatives in each time step.

As opposed to current modelling approaches which reduce the drogue to a single lumped mass at the end of the hose and constrain its movement to the receiver aircraft's motion profile upon coupling, here the drogue is treated as the complete final link of the chain.

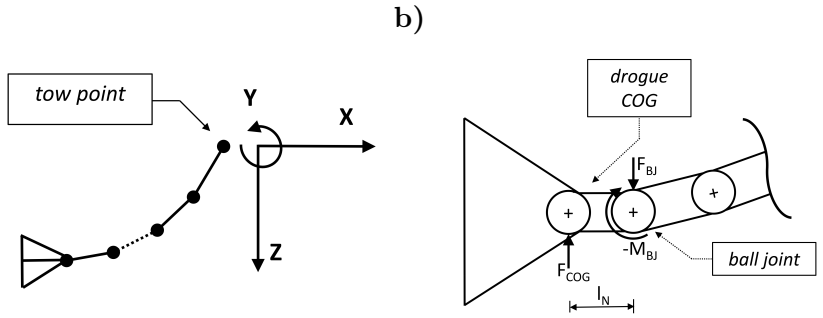

Figure 3.5: a) Structure of lumped parameter model and tow point/tanker frame assignment. b) Contact force application to drogue COG and ball joint to reproduce experimentally measured contact moment (here about negative Y-axis) on the ball joint of the hose model.

Hence, the drogue is represented as a rigid body (not just a point mass) which can change position and orientation. To this end, the second-last mass (*i.e* lump mass $n-1$) in the lumped parameter model is taken to be representative of the ball-joint while the *n-th* mass represents the drogue's COG and the length of the *n-th* link l_n corresponds with the distance from ball-joint to the drogue's COG. This results in an important advantage for the hybrid test: The contact forces and moments that develop throughout the coupling phase can be directly applied to the drogue making the assumption of instantaneous successful coupling obsolete while effects of off-centre hits and corresponding transient dynamics (such as drogue tipping) throughout the coupling phase can be accurately accounted for. Given that the measured mass and moment of inertia for the drogue is used in this configuration, the drogue's inertial properties are properly included in the numerical simulation to compensate this missing information from the expanded timescales of the PsD tests.

The application of contact forces and moments as measured from the experimental substructure is illustrated in Figure 3.5b). Significantly, contact forces acting on the drogue during the coupling phase of the maneuvers are directly applied at the ball joint, while the contact torques are applied as equivalent forces acting on ball joint and drogue COG as per Equation 3.5. In addition, the entire hose-drogue assembly is subjected to gravitational and aerodynamic loads. Viscous friction is only introduced for the ball joint, while the joints connecting individual hose links are assumed frictionless. By contrast, bending forces are applied to individual hose links and act to straighten consecutive hose elements but do not act across the ball joint onto the drogue link. These bending forces are computed from Timoshenko's beam theory as shown in [18].

$$\boldsymbol{F_n} = -\boldsymbol{F_{bj}} = \begin{pmatrix} 0 \\ -M_Z/l_n \\ M_Y/l_n \end{pmatrix} \tag{3.5}$$

The motion of all members in the hose-drogue assembly is expressed with reference to the tanker's coordinate frame which has the same orientation as the tow point frame in Figure 3.5a). The dynamics of the tanker itself are not modelled; it is assumed to be in straight, level flight at constant velocity of $200m/s$ $(720km/h)$ and altitude of $8,000m$. That is, the tanker motion is assumed undisturbed regardless of the simulated flight regime. This simplifies the analysis of the dynamics of the hose-drogue assembly by neglecting any hose-excitement induced by tanker motion. As the analysis focuses on the contact and coupling dynamics, this assumption does not present a limiting factor. The frame assignment for receiver probe and drogue complies with Figure 3.6.

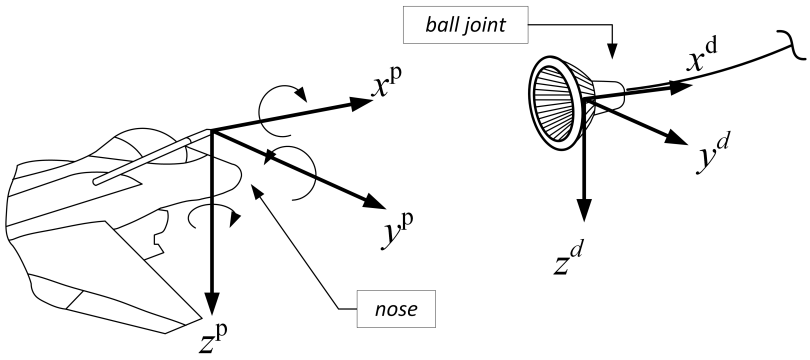

Figure 3.6: Frame assignment for probe and drogue.

3.5.1 Kinematics & Differential Kinematics

Recall that each member in the rigid body chain of the hose-drogue assembly has its reference frame located at the lumped mass position that is coincident with the spherical joint connecting to the next member down the hose. Now consider an arbitrary section of this chain, such as the system shown in Figure 3.8a), that is defined by a group of three consecutive lumped masses which are interconnected by two links. By convention, the central lumped mass is denoted with index k while indices $j = k - 1$ and $l = k + 1$ are used to describe the two lumped masses located to either side of the centre piece, *i.e.* hose upwards and hose downwards respectively. This notation is adopted throughout the following sections.

Note that, when ignoring hose twist, *i.e.* locking rotations about the X-axis of all spherical joints, the orientation of each link's reference frame with respect to the tanker follows from the Euler Y-Z rotation sequence. Thus, the orientation of the *k-th* link with respect to the tanker can be written as:

$$\boldsymbol{R_k^t} = \boldsymbol{R_{Y,\theta_{k_y}}} \boldsymbol{R_{Z,\theta_{k_z}}} \tag{3.6}$$

where $\boldsymbol{R_k^t}$ represents the rotation matrix mapping the frame of the *k-th* lumped mass with respect to the tanker's frame t and $\boldsymbol{R_{Y,\theta_{k_y}}}$ describes the rotation matrix resulting from a rotation about tanker axis Y by angle θ_{k_y}. Analogously, this applies to $\boldsymbol{R_{Z,\theta_{k_z}}}$.

The aim of this section is to provide a full description of the kinematics and differential kinematics of the hose-drogue assembly under consideration of the reel-in and pay-out action by the HDU. To this end, the HDU is treated as a separate entity with its own dynamics that solely dictates the hose length and changes in hose length which are then incorporated into the hose-drogue model. This is achieved by imposing proportional length-changes onto the individual hose-segments. Obviously, the last link of the hose-drogue model (i.e. the drogue link) is unaffected by the HDU action and remains at constant length.

Given that the hose-segment length follows from the HDU behaviour, and noting from Equation 3.6 that a system of n lumped masses is completely described by $2n$ DOF, $\theta_{k_y}, \theta_{k_z}$ *for* $k = 1, 2, ..., n$ are used as a minimal description of the hose-drogue configuration. Taking this as the origin of the derivation, the remainder of this section aims to establish expressions of the relative and absolute lumped mass positions and velocities with respect to the tanker's frame of reference.

Note that based on the frame assignment in Figure 3.5 and according to the definition in Equation 3.6, the unit vector in the X-direction of the *k-th* link, *i.e.* $\boldsymbol{n_{k_x}}$, points along the *k-th* link towards the previous, *i.e.* the *j-th* lumped mass. These unit vectors are of particular importance for the development of the equations of motion and can be written in terms of the unit vectors of the tanker frame ($\boldsymbol{n_{t_x}}, \boldsymbol{n_{t_y}}, \boldsymbol{n_{t_z}}$) as follows:

$$\boldsymbol{n_{k_x}^t} = c\theta_{k_y} c\theta_{k_z} \boldsymbol{n_{t_x}} + s\theta_{k_z} \boldsymbol{n_{t_y}} - s\theta_{k_y} c\theta_{k_z} \boldsymbol{n_{t_z}} = \begin{pmatrix} c\theta_{k_y} c\theta_{k_z} \\ s\theta_{k_z} \\ -s\theta_{k_y} c\theta_{k_z} \end{pmatrix} \tag{3.7}$$

where $s\theta_{k_{y,z}} = \sin(\theta_{k_{y,z}})$ and $c\theta_{k_{y,z}} = \cos(\theta_{k_{y,z}})$.

The absolute position of the *k-th* lumped mass in the tanker's reference frame can then

be evaluated as the sum of the preceding lumped mass position $\boldsymbol{r_j^t}$ and the relative position of the *k-th* lumped mass with respect to the *j-th* lumped mass $\boldsymbol{p_k^t}$ as given by:

$$\boldsymbol{r_k^t} = \boldsymbol{r_j^t} + \boldsymbol{p_k^t} \tag{3.8}$$

Then, from Equation 3.8, the relative position $\boldsymbol{p_k^t}$ is simply given as the product of the scalar link length l_k and the negated unit vector pointing along the *k-th* link:

$$\boldsymbol{p_k^t} = \boldsymbol{r_k^t} - \boldsymbol{r_j^t} = -l_k \boldsymbol{n_{k_x}} = l_k \begin{pmatrix} -c\theta_{k_y} c\theta_{k_z} \\ -s\theta_{k_z} \\ s\theta_{k_y} c\theta_{k_z} \end{pmatrix} \tag{3.9}$$

Thus, starting from the tow point, the individual lumped mass positions can be computed recursively and expressions for the velocities and accelerations of the lumped masses follow from differentiation:

$$\boldsymbol{v_k^t} = \boldsymbol{v_j^t} + \dot{\boldsymbol{p}}_{\boldsymbol{k}}^{\boldsymbol{t}} \tag{3.10}$$

and

$$\boldsymbol{a_k^t} = \boldsymbol{a_j^t} + \ddot{\boldsymbol{p}}_{\boldsymbol{k}}^{\boldsymbol{t}} \tag{3.11}$$

Recalling that the first $n-1$ links change length in equal proportions at equal rates to accommodate for the pay out/reel-in action of the HDU, the lumped masses along the hose have velocities and accelerations induced by link length changes whereas these terms disappear for the drogue link which is of constant length. Hence,

FOR ALL HOSE LINKS: $1 \leq k \leq n-1$

$$\dot{\boldsymbol{p}}_{\boldsymbol{k}}^{\boldsymbol{t}} = \boldsymbol{v_k^t} - \boldsymbol{v_j^t} = \frac{\partial \boldsymbol{p_k^t}}{\partial \theta_{k_y}} \dot{\theta}_{k_y} + \frac{\partial \boldsymbol{p_k^t}}{\partial \theta_{k_z}} \dot{\theta}_{k_z} + \frac{\partial \boldsymbol{p_k^t}}{\partial l_k} \dot{l}_k \tag{3.12}$$

$$\begin{aligned} \ddot{\boldsymbol{p}}_{\boldsymbol{k}}^{\boldsymbol{t}} &= \boldsymbol{a_k^t} - \boldsymbol{a_j^t} \\ &= \frac{d}{dt}\left[\frac{\partial \boldsymbol{p_k^t}}{\partial \theta_{k_y}} \dot{\theta}_{k_y} + \frac{\partial \boldsymbol{p_k^t}}{\partial \theta_{k_z}} \dot{\theta}_{k_z} + \frac{\partial \boldsymbol{p_k^t}}{\partial l_k} \dot{l}_k\right] \\ &= \frac{d}{dt}\left[\frac{\partial \boldsymbol{p_k^t}}{\partial \theta_{k_y}}\right] \dot{\theta}_{k_y} + \left(\frac{\partial \boldsymbol{p_k^t}}{\partial \theta_{k_y}}\right) \ddot{\theta}_{k_y} + \frac{d}{dt}\left[\frac{\partial \boldsymbol{p_k^t}}{\partial \theta_{k_z}}\right] \dot{\theta}_{k_z} + \left(\frac{\partial \boldsymbol{p_k^t}}{\partial \theta_{k_z}}\right) \ddot{\theta}_{k_z} + \frac{d}{dt}\left[\frac{\partial \boldsymbol{p_k^t}}{\partial l_k}\right] \dot{l}_k + \left(\frac{\partial \boldsymbol{p_k^t}}{\partial l_k}\right) \ddot{l}_k \end{aligned} \tag{3.13}$$

Multiplying both sides of Equation 3.13 with $\frac{\partial \boldsymbol{p_k^t}}{\partial \theta_{k_y}}$ and $\frac{\partial \boldsymbol{p_k^t}}{\partial \theta_{k_z}}$ respectively, yields Equa-

tion 3.14 and Equation 3.15:

$$\left(\boldsymbol{a_k^t} - \boldsymbol{a_j^t}\right)\left(\frac{\partial \boldsymbol{p_k^t}}{\partial \theta_{k_y}}\right) = \frac{d}{dt}\left[\frac{\partial \boldsymbol{p_k^t}}{\partial \theta_{k_y}}\right]\left(\frac{\partial \boldsymbol{p_k^t}}{\partial \theta_{k_y}}\right)\dot{\theta}_{k_y} + \left(\frac{\partial \boldsymbol{p_k^t}}{\partial \theta_{k_y}}\right)\left(\frac{\partial \boldsymbol{p_k^t}}{\partial \theta_{k_y}}\right)\ddot{\theta}_{k_y} + \frac{d}{dt}\left[\frac{\partial \boldsymbol{p_k^t}}{\partial \theta_{k_z}}\right]\left(\frac{\partial \boldsymbol{p_k^t}}{\partial \theta_{k_y}}\right)\dot{\theta}_{k_z} + \left(\frac{\partial \boldsymbol{p_k^t}}{\partial \theta_{k_z}}\right)\left(\frac{\partial \boldsymbol{p_k^t}}{\partial \theta_{k_y}}\right)\ddot{\theta}_{k_z} + \frac{d}{dt}\left[\frac{\partial \boldsymbol{p_k^t}}{\partial l_k}\right]\left(\frac{\partial \boldsymbol{p_k^t}}{\partial \theta_{k_y}}\right)\dot{l}_k + \left(\frac{\partial \boldsymbol{p_k^t}}{\partial l_k}\right)\left(\frac{\partial \boldsymbol{p_k^t}}{\partial \theta_{k_y}}\right)\ddot{l}_k \tag{3.14}$$

$$\left(\boldsymbol{a_k^t} - \boldsymbol{a_j^t}\right)\left(\frac{\partial \boldsymbol{p_k^t}}{\partial \theta_{k_z}}\right) = \frac{d}{dt}\left[\frac{\partial \boldsymbol{p_k^t}}{\partial \theta_{k_y}}\right]\left(\frac{\partial \boldsymbol{p_k^t}}{\partial \theta_{k_z}}\right)\dot{\theta}_{k_y} + \left(\frac{\partial \boldsymbol{p_k^t}}{\partial \theta_{k_y}}\right)\left(\frac{\partial \boldsymbol{p_k^t}}{\partial \theta_{k_z}}\right)\ddot{\theta}_{k_y} + \frac{d}{dt}\left[\frac{\partial \boldsymbol{p_k^t}}{\partial \theta_{k_z}}\right]\left(\frac{\partial \boldsymbol{p_k^t}}{\partial \theta_{k_z}}\right)\dot{\theta}_{k_z} + \left(\frac{\partial \boldsymbol{p_k^t}}{\partial \theta_{k_z}}\right)\left(\frac{\partial \boldsymbol{p_k^t}}{\partial \theta_{k_z}}\right)\ddot{\theta}_{k_z} + \frac{d}{dt}\left[\frac{\partial \boldsymbol{p_k^t}}{\partial l_k}\right]\left(\frac{\partial \boldsymbol{p_k^t}}{\partial \theta_{k_z}}\right)\dot{l}_k + \left(\frac{\partial \boldsymbol{p_k^t}}{\partial l_k}\right)\left(\frac{\partial \boldsymbol{p_k^t}}{\partial \theta_{k_z}}\right)\ddot{l}_k \tag{3.15}$$

Noting that $\frac{\partial \boldsymbol{p_k^t}}{\partial \theta_{k_y}}$ and $\frac{\partial \boldsymbol{p_k^t}}{\partial \theta_{k_z}}$ are mutually perpendicular, the scalar products $\left(\frac{\partial \boldsymbol{p_k^t}}{\partial \theta_{k_y}}\right)\left(\frac{\partial \boldsymbol{p_k^t}}{\partial \theta_{k_z}}\right)$ vanish and individual equations for $\ddot{\theta}_{k_y}$ and $\ddot{\theta}_{k_z}$ can be obtained as follows:

$$\ddot{\theta}_{k_y} = \frac{\left(\boldsymbol{a_k^t} - \boldsymbol{a_j^t}\right)\left(\frac{\partial \boldsymbol{p_k^t}}{\partial \theta_{k_y}}\right) - \frac{d}{dt}\left[\frac{\partial \boldsymbol{p_k^t}}{\partial \theta_{k_y}}\right]\left(\frac{\partial \boldsymbol{p_k^t}}{\partial \theta_{k_y}}\right)\dot{\theta}_{k_y} - \frac{d}{dt}\left[\frac{\partial \boldsymbol{p_k^t}}{\partial \theta_{k_z}}\right]\left(\frac{\partial \boldsymbol{p_k^t}}{\partial \theta_{k_z}}\right)\dot{\theta}_{k_z} - \frac{d}{dt}\left[\frac{\partial \boldsymbol{p_k^t}}{\partial l_k}\right]\left(\frac{\partial \boldsymbol{p_k^t}}{\partial \theta_{k_y}}\right)\dot{l}_k - \left(\frac{\partial \boldsymbol{p_k^t}}{\partial l_k}\right)\left(\frac{\partial \boldsymbol{p_k^t}}{\partial \theta_{k_y}}\right)\ddot{l}_k}{\left(\frac{\partial \boldsymbol{p_k^t}}{\partial \theta_{k_y}}\right)\left(\frac{\partial \boldsymbol{p_k^t}}{\partial \theta_{k_y}}\right)} \tag{3.16}$$

$$\ddot{\theta}_{k_z} = \frac{\left(\boldsymbol{a_k^t} - \boldsymbol{a_j^t}\right)\left(\frac{\partial \boldsymbol{p_k^t}}{\partial \theta_{k_z}}\right) - \frac{d}{dt}\left[\frac{\partial \boldsymbol{p_k^t}}{\partial \theta_{k_y}}\right]\left(\frac{\partial \boldsymbol{p_k^t}}{\partial \theta_{k_z}}\right)\dot{\theta}_{k_y} - \frac{d}{dt}\left[\frac{\partial \boldsymbol{p_k^t}}{\partial \theta_{k_z}}\right]\left(\frac{\partial \boldsymbol{p_k^t}}{\partial \theta_{k_z}}\right)\dot{\theta}_{k_z} - \frac{d}{dt}\left[\frac{\partial \boldsymbol{p_k^t}}{\partial l_k}\right]\left(\frac{\partial \boldsymbol{p_k^t}}{\partial \theta_{k_z}}\right)\dot{l}_k - \left(\frac{\partial \boldsymbol{p_k^t}}{\partial l_k}\right)\left(\frac{\partial \boldsymbol{p_k^t}}{\partial \theta_{k_z}}\right)\ddot{l}_k}{\left(\frac{\partial \boldsymbol{p_k^t}}{\partial \theta_{k_z}}\right)\left(\frac{\partial \boldsymbol{p_k^t}}{\partial \theta_{k_z}}\right)} \tag{3.17}$$

where explicit forms for all partial derivatives and their respective time derivatives are given by:

$$\frac{\partial \boldsymbol{p_k^t}}{\partial \theta_{k_y}} = l_k \begin{pmatrix} s\theta_{k_y} c\theta_{k_z} \\ 0 \\ c\theta_{k_y} c\theta_{k_z} \end{pmatrix} \tag{3.18}$$

$$\frac{\partial \boldsymbol{p_k^t}}{\partial \theta_{k_z}} = l_k \begin{pmatrix} c\theta_{k_y} s\theta_{k_z} \\ -c\theta_{k_z} \\ -s\theta_{k_y} s\theta_{k_z} \end{pmatrix} \tag{3.19}$$

$$\frac{\partial \boldsymbol{p_k^t}}{\partial l_k} = \begin{pmatrix} -c\theta_{k_y} c\theta_{k_z} \\ -s\theta_{k_z} \\ s\theta_{k_y} c\theta_{k_z} \end{pmatrix} \tag{3.20}$$

$$\frac{d}{dt}\left[\frac{\partial \boldsymbol{p_k^t}}{\partial \theta_{k_y}}\right] = \begin{pmatrix} s\theta_{k_y} c\theta_{k_z} \dot{l}_k + l_k c\theta_{k_y} c\theta_{k_z} \dot{\theta}_{k_y} - l_k s\theta_{k_y} s\theta_{k_z} \dot{\theta}_{k_z} \\ 0 \\ c\theta_{k_y} c\theta_{k_z} \dot{l}_k - l_k s\theta_{k_y} c\theta_{k_z} \dot{\theta}_{k_y} - l_k c\theta_{k_y} s\theta_{k_z} \dot{\theta}_{k_z} \end{pmatrix} \tag{3.21}$$

$$\frac{d}{dt}\left[\frac{\partial \boldsymbol{p_k^t}}{\partial \theta_{k_z}}\right] = \begin{pmatrix} c\theta_{k_y} s\theta_{k_z} \dot{l}_k - l_k s\theta_{k_y} s\theta_{k_z} \dot{\theta}_{k_y} + l_k c\theta_{k_y} c\theta_{k_z} \dot{\theta}_{k_z} \\ -c\theta_{k_z} \dot{l}_k + l_k s\theta_{k_z} \dot{\theta}_{k_z} \\ -s\theta_{k_y} s\theta_{k_z} \dot{l}_k - l_k c\theta_{k_y} s\theta_{k_z} \dot{\theta}_{k_y} - l_k s\theta_{k_y} c\theta_{k_z} \dot{\theta}_{k_z} \end{pmatrix} \tag{3.22}$$

$$\frac{d}{dt}\left[\frac{\partial \boldsymbol{p_k^t}}{\partial l_k}\right] = \begin{pmatrix} s\theta_{k_y} c\theta_{k_z} \dot{\theta}_{k_y} + c\theta_{k_y} s\theta_{k_z} \dot{\theta}_{k_z} \\ -c\theta_{k_z} \dot{\theta}_{k_z} \\ c\theta_{k_y} c\theta_{k_z} \dot{\theta}_{k_y} - s\theta_{k_y} s\theta_{k_z} \dot{\theta}_{k_z} \end{pmatrix} \tag{3.23}$$

SIMILARLY FOR DROGUE LINK: $k = n$

$$\dot{l}_k = \ddot{l}_k = 0$$

$$\dot{\boldsymbol{p}}_{\boldsymbol{k}}^{\boldsymbol{t}} = \frac{\partial \boldsymbol{p_k^t}}{\partial \theta_{k_y}} \dot{\theta}_{k_y} + \frac{\partial \boldsymbol{p_k^t}}{\partial \theta_{k_z}} \dot{\theta}_{k_z} \tag{3.24}$$

$$\begin{aligned} \ddot{\boldsymbol{p}}_{\boldsymbol{k}}^{\boldsymbol{t}} &= \frac{d}{dt}\left[\frac{\partial \boldsymbol{p_k^t}}{\partial \theta_{k_y}} \dot{\theta}_{k_y} + \frac{\partial \boldsymbol{p_k^t}}{\partial \theta_{k_z}} \dot{\theta}_{k_z} + \frac{\partial \boldsymbol{p_k^t}}{\partial l_k} \dot{l}_k\right] \\ &= \frac{d}{dt}\left[\frac{\partial \boldsymbol{p_k^t}}{\partial \theta_{k_y}}\right] \dot{\theta}_{k_y} + \left(\frac{\partial \boldsymbol{p_k^t}}{\partial \theta_{k_y}}\right) \ddot{\theta}_{k_y} + \frac{d}{dt}\left[\frac{\partial \boldsymbol{p_k^t}}{\partial \theta_{k_z}}\right] \dot{\theta}_{k_z} + \left(\frac{\partial \boldsymbol{p_k^t}}{\partial \theta_{k_z}}\right) \ddot{\theta}_{k_z} \end{aligned} \tag{3.25}$$

Following the same procedure as above *i.e.* taking scalar products with $\left(\frac{\partial \boldsymbol{p_k^t}}{\partial \theta_{k_y}}\right)$ and $\left(\frac{\partial \boldsymbol{p_k^t}}{\partial \theta_{k_z}}\right)$ respectively and accounting for the fact that $\left(\frac{\partial \boldsymbol{p_k^t}}{\partial \theta_{k_y}}\right)\left(\frac{\partial \boldsymbol{p_k^t}}{\partial \theta_{k_z}}\right) = 0$, yields:

$$\ddot{\theta}_{k_y} = \frac{\left(\boldsymbol{a_k^t} - \boldsymbol{a_j^t}\right)\left(\frac{\partial \boldsymbol{p_k^t}}{\partial \theta_{k_y}}\right) - \frac{d}{dt}\left[\frac{\partial \boldsymbol{p_k^t}}{\partial \theta_{k_y}}\right]\left(\frac{\partial \boldsymbol{p_k^t}}{\partial \theta_{k_y}}\right)\dot{\theta}_{k_y} - \frac{d}{dt}\left[\frac{\partial \boldsymbol{p_k^t}}{\partial \theta_{k_z}}\right]\left(\frac{\partial \boldsymbol{p_k^t}}{\partial \theta_{k_z}}\right)\dot{\theta}_{k_z}}{\left(\frac{\partial \boldsymbol{p_k^t}}{\partial \theta_{k_y}}\right)\left(\frac{\partial \boldsymbol{p_k^t}}{\partial \theta_{k_y}}\right)} \tag{3.26}$$

$$\ddot{\theta}_{k_z} = \frac{\left(\boldsymbol{a_k^t} - \boldsymbol{a_j^t}\right)\left(\frac{\partial \boldsymbol{p_k^t}}{\partial \theta_{k_z}}\right) - \frac{d}{dt}\left[\frac{\partial \boldsymbol{p_k^t}}{\partial \theta_{k_y}}\right]\left(\frac{\partial \boldsymbol{p_k^t}}{\partial \theta_{k_z}}\right)\dot{\theta}_{k_y} - \frac{d}{dt}\left[\frac{\partial \boldsymbol{p_k^t}}{\partial \theta_{k_z}}\right]\left(\frac{\partial \boldsymbol{p_k^t}}{\partial \theta_{k_z}}\right)\dot{\theta}_{k_z}}{\left(\frac{\partial \boldsymbol{p_k^t}}{\partial \theta_{k_z}}\right)\left(\frac{\partial \boldsymbol{p_k^t}}{\partial \theta_{k_z}}\right)} \tag{3.27}$$

Where explicit forms for all partial derivatives and their respective time derivatives are given by:

$$\frac{\partial \boldsymbol{p_k^t}}{\partial \theta_{k_y}} = l_k \begin{pmatrix} s\theta_{k_y} c\theta_{k_z} \\ 0 \\ c\theta_{k_y} c\theta_{k_z} \end{pmatrix} \tag{3.28}$$

$$\frac{\partial \boldsymbol{p_k^t}}{\partial \theta_{k_z}} = l_k \begin{pmatrix} c\theta_{k_y} s\theta_{k_z} \\ -c\theta_{k_z} \\ -s\theta_{k_y} s\theta k_z \end{pmatrix} \tag{3.29}$$

$$\frac{d}{dt}\left[\frac{\partial \boldsymbol{p_k^t}}{\partial \theta_{k_y}}\right] = \begin{pmatrix} l_k c\theta_{k_y} c\theta_{k_z} \dot{\theta}_{k_y} - l_k s\theta_{k_y} s\theta_{k_z} \dot{\theta}_{k_z} \\ 0 \\ -l_k s\theta_{k_y} c\theta_{k_z} \dot{\theta}_{k_y} - l_k c\theta_{k_y} s\theta_{k_z} \dot{\theta}_{k_z} \end{pmatrix} \tag{3.30}$$

$$\frac{d}{dt}\left[\frac{\partial \boldsymbol{p_k^t}}{\partial \theta_{k_z}}\right] = \begin{pmatrix} -l_k s\theta_{k_y} s\theta_{k_z}\dot{\theta}_{k_y} + l_k c\theta_{k_y} c\theta_{k_z}\dot{\theta}_{k_z} \\ l_k s\theta_{k_z}\dot{\theta}_{k_z} \\ -l_k c\theta_{k_y} s\theta_{k_z}\dot{\theta}_{k_y} - l_k s\theta_{k_y} c\theta_{k_z}\dot{\theta}_{k_z} \end{pmatrix} \tag{3.31}$$

Preliminary Recapitulation

The above derivation, in particular expressions in Equation 3.16 and Equation 3.17 (for the hose links) and Equation 3.26 and Equation 3.27 (for the drogue link), show that the angular link accelerations are a function of the linear lumped mass accelerations, the link angles and angular velocities, the link lengths as well as their first and second derivatives and, of course, time:

$$\ddot{\theta}_{k_{y,z}} = f\left(\boldsymbol{a_k^t}, \boldsymbol{a_j^t}, \theta_{k_{y,z}}, \dot{\theta}_{k_{y,z}}, l_k, \dot{l}_k, \ddot{l}_k, t\right) \tag{3.32}$$

Given that these parameters are known at each simulation step, either by initial conditions or as the result of numerical integration of $\ddot{\theta}_{k_y}$ and $\ddot{\theta}_{k_z}$ in previous time steps, the second derivatives of the link orientations can be calculated explicitly throughout the simulation. In turn, numerical integration will yield estimates for the link angles and their angular velocities in the next time step. The computation of the linear lumped mass accelerations is discussed next.

3.5.2 Dynamics

As stated in Section 1.2 and outlined by Figure 3.1 in particular, the in-flight dynamics of the hose-drogue assembly are directly influenced by a variety of external forces associated with the contact scenario and flight regime as well as internal restoring forces that develop in response to hose bending. In addition to these factors, the reel-in and pay-out action by the HDU may have a further significant effect on the system dynamics. In practice, adequate hose take-up upon contact is of utmost importance to avoid the formation of excessive hose slack and the onset of large amplitude oscillations that may turn into hose whip if left uncompensated for. Thus, the integration of an accurate model for the HDU action is a necessity. While the topology of the chosen lumped parameter modelling approach lends itself to the application of the environmental and structural forces by nodal excitation, a model of the hose reel-in process onto a drum would typically require the definition of additional constraint equations to accurately account for hose take-up. However, this would inevitably lead to an increased model complexity and add to the computational expense and implementation difficulty. Con-

sequently an alternative mechanism based on adaptive finite segment sizes is proposed and evaluated in this section. To this end, the lengths of the hose links are uniformly reduced throughout the reel-in process while impulsive forces are applied to individual lumped masses to account for the corresponding changes in linear momentum that is associated with the mass transfer from hose to HDU. A uniform increase in the models spatial resolution throughout the reel-in process at little computational cost is a favourable by-product of this approach. The implementation of this model is described over the following sections.

Recall that hose and HDU are treated as separated but dynamically coupled entities. During reel-in, the reel-in force produced by the HDU is directly applied to m_1 and assumed to act along n_{x_1}, *i.e.* the unit vector pointing in the X-direction of the first link, at all times. Note that this has the same effect as modelling the tow point as a frictionless roller that does not change the nominal cable forces. The reel-in force accelerates the hose leading to the uniform length reductions of the individual links as described above. Evidently, length reductions must go along with reductions in link masses. Consequently, mass transfer effects have to be considered in order to formulate a complete model. To this end, a mechanism is proposed whereby individual lumped masses along the hose can gain and expel small masses while corresponding changes in linear momentum are accounted for.

Consider the schematic shown in Figure 3.7a) which illustrates the mass transfer during reel-in. Starting at the hose end and given that the last mass m_n stays constant, mass $m_{(n-1)}$ is the first lump mass to expel a small mass δ_m to m_{n-2}, *i.e* the next mass hose-upwards. In turn, mass $m_{(n-2)}$ gains this small mass δ_m and instantaneously expels the equivalent of $2\delta_m$ to lump mass $m_{(n-3)}$. This procedure continues until the first lumped mass down the hose m_1 gains $(n-2)\delta_m$ and expels $(n-1)\delta_m$ (which is equivalent to the total loss of hose mass in one simulation step) to the HDU. For the final mass transfer off the hose, a virtual tow point velocity is assumed such the small mass $(n-1)\delta_m$ undergoes a change in velocity from $\boldsymbol{v_1^t}$ to $\boldsymbol{v_{hdu}^t} = w_d r_d \boldsymbol{R^t_{Y,\theta_{duct}}} \boldsymbol{n_{t_x}}$, where θ_{duct} is the duct angle of the refuelling pod, $w_d$is the drum speed and the drum radius is given by r_d as shown in Figure 3.7. The process of gaining and expelling masses is assumed to occur over the small time period δt, and average impulsive forces f act on both the incremental masses and the lumped masses as part of the mass capture and mass loss process.

Considering the more generic hose segment shown in (Figure 3.8), it follows that mass m_k gains $(n-l)\delta_m$ from m_l and expels $(n-k)\delta_m$ to m_j. Further note that m_k is acted upon by $\boldsymbol{f_k^l}$ and $\boldsymbol{f_k^j}$, the tension forces $\boldsymbol{t_k}$ and $\boldsymbol{t_l}$ as well as $\boldsymbol{Q_k}$, *i.e* the sum of aerodynamic, gravitational and hose bending forces. Here, $\boldsymbol{f_k^l}$ and $\boldsymbol{f_k^j}$ are the average impulsive forces

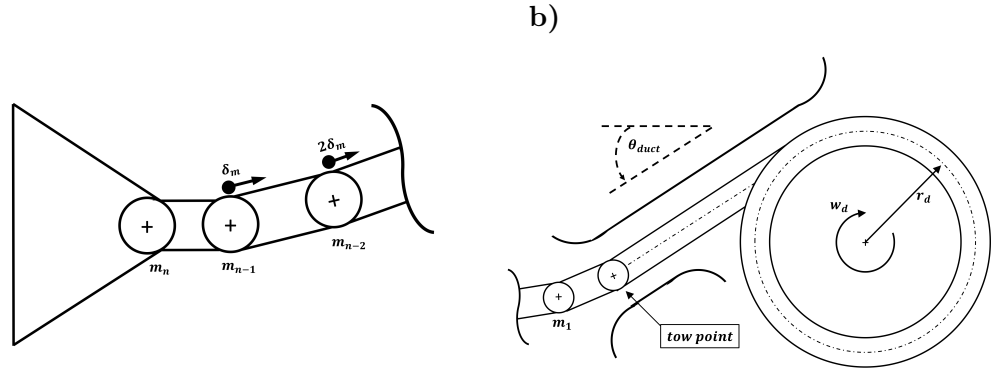

Figure 3.7: a) Mass transfer mechanism during reel in at hose end. b) Schematic of HDU and refuelling pod.

.

over δt due to the mass transfer of $(n-l)\delta_m$ from m_l to m_k and $(n-k)\delta_m$ from m_k to m_j respectively. From the free body diagram in Figure 3.8b), impulse and changes in linear momentum can be equated as follows:

Perspective of gained mass $(n-l)\delta_m$:

$$-\boldsymbol{f_k^l}\delta t = (n-l)\delta_m \left[(\boldsymbol{v_k^t} + \delta \boldsymbol{v_k^t}) - \boldsymbol{v_l^t}\right] \tag{3.33}$$

Perspective of expelled mass $(n-k)\delta_m$:

$$-\boldsymbol{f_k^j}\delta t = (n-k)\delta_m \left[(\boldsymbol{v_j^t} + \delta \boldsymbol{v_j^t}) - \boldsymbol{v_k^t}\right] \tag{3.34}$$

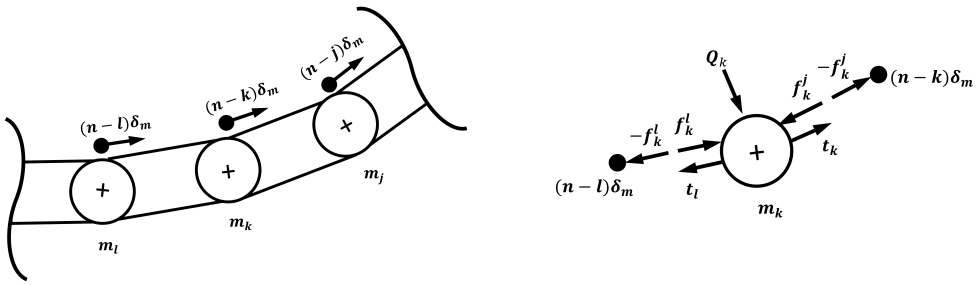

Figure 3.8: a) Mass transfer mechanism illustrated for generic mass m_k. b) Free body diagram for generic mass m_k

.

Perspective of m_k:

$$\left[\boldsymbol{Q_k^t} + \boldsymbol{t_k^t} + \boldsymbol{t_l^t}\right]\delta t + \boldsymbol{f_k^l}\delta t + \boldsymbol{f_k^j}\delta t = m_k\left[(\boldsymbol{v_k^t} + \delta\boldsymbol{v_k^t}) - \boldsymbol{v_k^t}\right] \tag{3.35}$$

Substituting Equation 3.33 and Equation 3.34 into Equation 3.35 yields:

$$\left[\boldsymbol{Q_k^t} + \boldsymbol{t_k^t} + \boldsymbol{t_l^t}\right]\delta t - (n-l)\delta_m\left[(\boldsymbol{v_k^t} + \delta\boldsymbol{v_k^t}) - \boldsymbol{v_l^t}\right] - (n-k)\delta_m\left[(\boldsymbol{v_j^t} + \delta\boldsymbol{v_j^t}) - \boldsymbol{v_k^t}\right] = m_k\left[\boldsymbol{v_k^t} + \delta\boldsymbol{v_k^t} - \boldsymbol{v_k^t}\right] \tag{3.36}$$

and dividing by δt yields:

$$\boldsymbol{Q_k^t} + \boldsymbol{t_k^t} + \boldsymbol{t_l^t} - (n-l)\left[(\boldsymbol{v_k^t} + \delta\boldsymbol{v_k^t}) - \boldsymbol{v_l^t}\right]\frac{\delta_m}{\delta t} - (n-k)\left[(\boldsymbol{v_j^t} + \delta\boldsymbol{v_j^t}) - \boldsymbol{v_k^t}\right]\frac{\delta_m}{\delta t} = m_k\frac{\delta\boldsymbol{v_k^t}}{\delta t} \tag{3.37}$$

Taking the limits $\delta_m \to 0$, $\delta t \to 0$, $\delta\boldsymbol{v_k^t} \to 0$ and $\delta\boldsymbol{v_j^t} \to 0$ gives $\frac{\delta_m}{\delta t} \to \frac{dm}{dt}$, $\frac{\boldsymbol{v_k^t}}{\delta t} \to \frac{d\boldsymbol{v_k^t}}{dt} = \boldsymbol{a_k^t}$, $\frac{\delta_m\delta\boldsymbol{v_k^t}}{\delta t} = \frac{\delta_m\delta\boldsymbol{v_j^t}}{\delta t} = 0$ Equation 3.37 can be restated as:

$$\boldsymbol{Q_k^t} + \boldsymbol{t_k^t} + \boldsymbol{t_l^t} - (n-l)\left[\boldsymbol{v_k^t} - \boldsymbol{v_l^t}\right]\frac{dm}{dt} - (n-k)\left[\boldsymbol{v_j^t} - \boldsymbol{v_k^t}\right]\frac{dm}{dt} = m_k\boldsymbol{a_k^t} \tag{3.38}$$

and recalling the definition of the relative lumped mass velocities as per Equation 3.12, the expressions in Equation 3.38 can be further reduced to:

$$\boldsymbol{Q_k^t} + \boldsymbol{t_k^t} + \boldsymbol{t_l^t} + (n-l)\dot{\boldsymbol{p}}_{\boldsymbol{l}}^{\boldsymbol{t}}\frac{dm}{dt} + (n-k)\dot{\boldsymbol{p}}_{\boldsymbol{k}}^{\boldsymbol{t}}\frac{dm}{dt} = m_k\boldsymbol{a_k^t} \tag{3.39}$$

Equivalently, the motion equation for the *j-th* lump mass can be written as:

$$\boldsymbol{Q_j^t} + \boldsymbol{t_j^t} + \boldsymbol{t_k^t} + (n-k)\dot{\boldsymbol{p}}_{\boldsymbol{k}}^{\boldsymbol{t}}\frac{dm}{dt} + (n-j)\dot{\boldsymbol{p}}_{\boldsymbol{j}}^{\boldsymbol{t}}\frac{dm}{dt} = m_j\boldsymbol{a_j^t} \tag{3.40}$$

Note that the expressions $(n-k)\dot{\boldsymbol{p}}_{\boldsymbol{k}}^{\boldsymbol{t}}\frac{dm}{dt} + (n-j)\dot{\boldsymbol{p}}_{\boldsymbol{j}}^{\boldsymbol{t}}\frac{dm}{dt}$ and $(n-l)\dot{\boldsymbol{p}}_{\boldsymbol{l}}^{\boldsymbol{t}}\frac{dm}{dt} + (n-k)\dot{\boldsymbol{p}}_{\boldsymbol{k}}^{\boldsymbol{t}}\frac{dm}{dt}$ are forces acting on the lumped mass to account for the change in linear momentum due to the link mass change and if ignored the expressions reduce to those stated in [19]. Further note that Equation 3.39 and Equation 3.40 cannot be solved on their own, but tension forces need to be computed such that link length constraints are satisfied. This is done by combining the individual motion equations with algebraic constraint equations to form a system of differential-algebraic equations. Tension forces that satisfy the constraints can then be computed and subsequently applied to the motion equations in order to solve for the lumped mass accelerations. To this end, it is convenient to restate the motion equations as shown in Equation 3.41 and Equation 3.42 respectively, where the individual tension forces have been separated into their norm and the unit vector of the link they are acting along. In addition, the terms $\boldsymbol{P_j^t} = \boldsymbol{Q_j^t} + (n-k)\dot{\boldsymbol{p}}_{\boldsymbol{k}}^{\boldsymbol{t}}\frac{dm}{dt} + (n-j)\dot{\boldsymbol{p}}_{\boldsymbol{j}}^{\boldsymbol{t}}\frac{dm}{dt}$

and $\boldsymbol{P_k^t} = \boldsymbol{Q_k^t} + (n-l)\dot{\boldsymbol{p}}_{\boldsymbol{l}}^{\boldsymbol{t}}\frac{dm}{dt} + (n-k)\dot{\boldsymbol{p}}_{\boldsymbol{k}}^{\boldsymbol{t}}\frac{dm}{dt}$ have been defined to account for the sum of all forces (except tension forces) and μ_j and μ_k are the inverse masses respectively.

$$\boldsymbol{a_j^t} = \mu_j \left(\boldsymbol{P_j^t} + |\boldsymbol{t_j^t}|\boldsymbol{n_{j_x}^t} - |\boldsymbol{t_k^t}|\boldsymbol{n_{k_x}^t} \right) \tag{3.41}$$

$$\boldsymbol{a_k^t} = \mu_k \left(\boldsymbol{P_k^t} + |\boldsymbol{t_k^t}|\boldsymbol{n_{k_x}^t} - |\boldsymbol{t_l^t}|\boldsymbol{n_{l_x}^t} \right) \tag{3.42}$$

Definition of Constraint Equations

Starting from Equation 3.43, where all parameters are functions of time, it can be shown (Appendix B) that a constraint equation to solve the system is given by Equation 3.44. Note from Figure 3.7b) that a positive drum speed $+ve\ w_d$ acts to shorten the hose and that the term $n-1$ represents the number of links with variable length. Also note, that from this point onwards the superscript ^{t} is discontinued but all vectors are expressed in the tanker frame unless otherwise stated.

$$\boldsymbol{p_k p_k} = l_k^2 \tag{3.43}$$

$$\left(\boldsymbol{a_k} - \boldsymbol{a_j} \right) \boldsymbol{n_{k_x}} = l_k \dot{\boldsymbol{n}}_{\boldsymbol{k_x}}^2 - \ddot{l}_k = l_k \dot{\boldsymbol{n}}_{\boldsymbol{k_x}}^2 + \frac{\dot{w}_d r_d}{n-1} \tag{3.44}$$

Similarly, Equation 3.45 is obtained for the drogue link $(k = n)$ where link length l_n is not a function of time:

$$\left(\boldsymbol{a_n} - \boldsymbol{a_{(n-1)}} \right) \boldsymbol{n_{n_x}} = l_n \dot{\boldsymbol{n}}_{\boldsymbol{n_x}}^2 \tag{3.45}$$

Assembling the Differential-Algebraic Equations

Substituting Equation 3.41 and Equation 3.42 into Equation 3.44 for all hose-links and into Equation 3.45 for the drogue link, yields a set of linear-algebraic equations which can be re-written in matrix form to produce a tri-diagonal matrix of tension coefficients. This is detailed on a case by case basis in the following:

FOR LUMPED MASS $k = 1$ (first row)

Constraint equation is given by:

$$(\boldsymbol{a_1} - \boldsymbol{a_0})\, \boldsymbol{n_{1_x}} = l_1 \dot{\boldsymbol{n}}_{\boldsymbol{1_x}}^2 + \frac{\dot{w}_d r_d}{n-1} \tag{3.46}$$

Here, the acceleration of the first lumped mass $\boldsymbol{a_1}$ follows from the motion equation

below while the tow point remains static and hence $\boldsymbol{a_0} = [0]$.

$$\boldsymbol{a_1} = \mu_1 \left(\boldsymbol{P_1} + \boldsymbol{t_1} + \boldsymbol{t_2} \right) \tag{3.47}$$

Substitution yields:

$$\begin{aligned}
\left[\mu_1 \boldsymbol{P_1} + \mu_1 |\boldsymbol{t_1}| \boldsymbol{n_{1_x}} - \mu_2 |\boldsymbol{t_2}| \boldsymbol{n_{2_x}} - \boldsymbol{a_0} \right] \boldsymbol{n_{1_x}} &= l_1 \dot{\boldsymbol{n}}_{\boldsymbol{1_x}}^2 + \frac{\dot{w}_d r_d}{n-1} \\
\mu_1 \left(\boldsymbol{n_{1_x}} \boldsymbol{n_{1_x}} \right) |\boldsymbol{t_1}| - \mu_1 \left(\boldsymbol{n_{2_x}} \boldsymbol{n_{1_x}} \right) |\boldsymbol{t_2}| &= l_1 \dot{\boldsymbol{n}}_{\boldsymbol{1_x}}^2 + \frac{\dot{w}_d r_d}{n-1} - \mu_1 \left[\boldsymbol{P_1} \boldsymbol{n_{1_x}} \right] + \left(\boldsymbol{a_0} \boldsymbol{n_{1_x}} \right) \\
\mu_1 |\boldsymbol{t_1}| - \mu_1 \left(\boldsymbol{n_{2_x}} \boldsymbol{n_{1_x}} \right) |\boldsymbol{t_2}| &= l_1 \dot{\boldsymbol{n}}_{\boldsymbol{1_x}}^2 + \frac{\dot{w}_d r_d}{n-1} - \mu_1 \left[\boldsymbol{P_1} \boldsymbol{n_{1_x}} \right]
\end{aligned} \tag{3.48}$$

FOR LUMPED MASS $k = 2$ **TO** $k = n - 2$ (second row to third last row)

Constraint equation is given by Equation 3.44 and motion equations are given by Equation 3.41 and Equation 3.42 respectively. Substitution yields:

$$\begin{aligned}
\left[\mu_k \boldsymbol{P_k} + \mu_k |\boldsymbol{t_k}| \boldsymbol{n_{k_x}} - \mu_k |\boldsymbol{t_l}| \boldsymbol{n_{l_x}} - \mu_j \boldsymbol{P_j} - \mu_j |\boldsymbol{t_j}| \boldsymbol{n_{j_x}} + \mu_j |\boldsymbol{t_k}| \boldsymbol{n_{k_x}} \right] \boldsymbol{n_{k_x}} &= l_k \dot{\boldsymbol{n}}_{\boldsymbol{k_x}}^2 + \frac{\dot{w}_d r_d}{n-1} \\
-\mu_j \left(\boldsymbol{n_{j_x}} \boldsymbol{n_{k_x}} \right) |\boldsymbol{t_j}| + \left(\mu_j + \mu_k \right) |\boldsymbol{t_k}| - \mu_k \left(\boldsymbol{n_{k_x}} \boldsymbol{n_{l_x}} \right) |\boldsymbol{t_l}| &= l_k \dot{\boldsymbol{n}}_{\boldsymbol{k_x}}^2 + \frac{\dot{w}_d r_d}{n-1} - \mu_k \left(\boldsymbol{P_k} \boldsymbol{n_{k_x}} \right) + \mu_j \left(\boldsymbol{P_j} \boldsymbol{n_{k_x}} \right) \\
-\mu_j \left(\boldsymbol{n_{j_x}} \boldsymbol{n_{k_x}} \right) |\boldsymbol{t_j}| + \left(\mu_j + \mu_k \right) |\boldsymbol{t_k}| - \mu_k \left(\boldsymbol{n_{k_x}} \boldsymbol{n_{l_x}} \right) |\boldsymbol{t_l}| &= l_k \dot{\boldsymbol{n}}_{\boldsymbol{k_x}}^2 + \frac{\dot{w}_d r_d}{n-1} + \left(\mu_j \boldsymbol{P_j} - \mu_k \boldsymbol{P_k} \right) \boldsymbol{n_{k_x}}
\end{aligned} \tag{3.49}$$

FOR LUMPED MASS $k = n - 1$ (second-last row)

The second-last lumped mass is representative of the ball-joint & reception coupling. It is this mass that is constrained to follow the acceleration profile of the receiver aircraft when probe and drogue are successfully coupled. The last mass represents the drogue's COG and the subscripts $_{bj}$ and $_n$ are introduced to denote the last and second-last lumped masses respectively. Two different cases need to be considered:

(CASE A) BALL-JOINT IS NOT COUPLED TO NOZZLE:

In this case the equations for k = 2 to k = n-2 apply, *i.e.*:

$$-\mu_{(n-2)}\left(\boldsymbol{n_{(n-2)_x}}\boldsymbol{n_{bj_x}}\right)|\boldsymbol{t_{(n-2)}}|+\left(\mu_{(n-2)}+\mu_{bj}\right)|\boldsymbol{t_{bj}}|-\mu_{bj}\left(\boldsymbol{n_{bj_x}}\boldsymbol{n_{n_x}}\right)|\boldsymbol{t_n}|= l_{bj}\dot{\boldsymbol{n}}^2_{\boldsymbol{k_x}}+\frac{\dot{w}_d r_d}{n-1}+\left(\mu_{(n-2)}\boldsymbol{P_{(n-2)}}-\mu_{bj}\boldsymbol{P_{bj}}\right)\boldsymbol{n_{bj_x}} \tag{3.50}$$

(CASE B) BALL-JOINT IS COUPLED TO NOZZLE:

Upon coupling the ball-joint follows the externally imposed acceleration pattern of the receiver aircraft, *i.e.*:

$$\boldsymbol{a_k}=\boldsymbol{a_{bj}}=\boldsymbol{a_{noz}} \tag{3.51}$$

As before, $\boldsymbol{a_j}$ is given by:

$$\boldsymbol{a_j}=\boldsymbol{a_{(n-2)}}=\mu_{(n-2)}\left(\boldsymbol{P_{(n-2)}}+|\boldsymbol{t_{(n-2)}}|\boldsymbol{n_{(n-2)_x}}-|\boldsymbol{t_{bj}}|\boldsymbol{n_{bj_x}}\right) \tag{3.52}$$

and the constraint equation is given by:

$$\left(\boldsymbol{a_{bj}}-\boldsymbol{a_{(n-2)}}\right)\boldsymbol{n_{bj_x}}=l_{bj}\dot{\boldsymbol{n}}^2_{\boldsymbol{bj_x}}+\frac{\dot{w}_d r_d}{n-1} \tag{3.53}$$

Substitution yields:

$$\begin{aligned}\boldsymbol{a_{noz}}\boldsymbol{n_{bj_x}}-\mu_{(n-2)}\left(\boldsymbol{P_{(n-2)}}\boldsymbol{n_{bj_x}}\right)-\mu_{(n-2)}\left(\boldsymbol{n_{bj_x}}\boldsymbol{n_{(n-2)_x}}\right)|\boldsymbol{t_{(n-2)}}|+\mu_{(n-2)}|\boldsymbol{t_{bj}}|&=l_{bj}\dot{\boldsymbol{n}}^2_{\boldsymbol{bj_x}}+\frac{\dot{w}_d r_d}{n-1}\\ -\mu_{(n-2)}\left(\boldsymbol{n_{bj_x}}\boldsymbol{n_{(n-2)_x}}\right)|\boldsymbol{t_{(n-2)}}|+\mu_{(n-2)}|\boldsymbol{t_{bj}}|&=l_{bj}\dot{\boldsymbol{n}}^2_{\boldsymbol{bj_x}}+\frac{\dot{w}_d r_d}{n-1}-\boldsymbol{a_{noz}}\boldsymbol{n_{bj_x}}+\mu_{(n-2)}\left(\boldsymbol{P_{(n-2)}}\boldsymbol{n_{bj_x}}\right)\end{aligned} \tag{3.54}$$

FOR LAST LINK $k=n$ (last row)

(CASE A) BALL-JOINT IS NOT COUPLED TO NOZZLE:

There is no *l-th* link further down the chain.

$$\boldsymbol{a_k}=\boldsymbol{a_n}=\mu_n\left(\boldsymbol{P_n}+\boldsymbol{t_n}\right) \tag{3.55}$$

$$\boldsymbol{a_j}=\boldsymbol{a_{bj}}=\mu_{bj}\left(\boldsymbol{P_{bj}}+\boldsymbol{t_{bj}}+\boldsymbol{t_n}\right) \tag{3.56}$$

Both of the above expressions must be used with the constant length constrained below:

$$\left(\boldsymbol{a_n} - \boldsymbol{a_{bj}}\right) \boldsymbol{n_{n_x}} = l_n \dot{\boldsymbol{n}}^2_{\boldsymbol{n_x}} \tag{3.57}$$

This gives:

$$\begin{aligned} \mu_n \boldsymbol{P_n} \boldsymbol{n_{n_x}} + \mu_n |\boldsymbol{t_n}| \boldsymbol{n_{n_x}} \boldsymbol{n_{n_x}} - \mu_{bj} \boldsymbol{P_{bj}} \boldsymbol{n_{n_x}} - \mu_{bj} |\boldsymbol{t_{bj}}| \boldsymbol{n_{bj_x}} \boldsymbol{n_{n_x}} + \mu_{bj} |\boldsymbol{t_n}| \boldsymbol{n_{n_x}} \boldsymbol{n_{n_x}} = l_n \dot{\boldsymbol{n}}^2_{\boldsymbol{n_x}} \\ -\mu_{bj} \left(\boldsymbol{n_{bj_x}} \boldsymbol{n_{n_x}}\right) |\boldsymbol{t_{bj}}| + \left(\mu_n + \mu_{bj}\right) |\boldsymbol{t_n}| = l_n \dot{\boldsymbol{n}}^2_{\boldsymbol{n_x}} + \left(\mu_{bj} \boldsymbol{P_{bj}} - \mu_n \boldsymbol{P_n}\right) \boldsymbol{n_{n_x}} \end{aligned} \tag{3.58}$$

(CASE B) BALL-JOINT IS COUPLED TO NOZZLE:

The ball joint is treated as the effective hose end and follows the receiver motion while the drogue link is artificially aligned with the refuelling probe. No further equation needs to be established.

Matrix Form

From the descriptions above, the algebraic differential equations can be directly assembled in matrix form. For the uncoupled case 'CASE A' and a generic system of N links and $2N$ DOF, the result is a system of simultaneous equations of the form $[A_A][|t_A|] = [F_A]$, where $[A_A]$ is a tridiagonal matrix of tension coefficients of size NxN, $[|t_A|]$ is an $Nx1$ vector formed of the absolute values of the link tensions and $[F_B]$ is an $Nx1$ vector of excitation forces applied to the individual lumped masses.
In analogy to this, a system of the form $[A_B][|t_B|] = [F_B]]$ can be formed for 'CASE B' where probe and drogue are successfully coupled. Since the ball joint is constraint to the receiver aircraft motion in this case, the last row becomes superfluous and $[A_B]$ reduces to size $(N-1)x(N-1)$ while the length of vectors $[|t_B|]$ and $[F_B]$ is equivalently reduced to $(N-1)$. The complete matrix systems for the uncoupled and coupled cases are shown in Equation 3.59 and Equation 3.60 respectively.

$$
\begin{bmatrix}
\mu_1 & -\mu_1\left(\boldsymbol{n_{2_x}} \boldsymbol{n_{1_x}}\right) & 0 & 0 & 0 & 0 & 0 & 0 & 0 \\
-\mu_1\left(\boldsymbol{n_{1_x}} \boldsymbol{n_{2_x}}\right) & \left(\mu_1+\mu_2\right) & -\mu_2\left(\boldsymbol{n_{2_x}} \boldsymbol{n_{3_x}}\right) & 0 & \ldots & \ldots & \ldots & \ldots & 0 \\
0 & -\mu_2\left(\boldsymbol{n_{2_x}} \boldsymbol{n_{3_x}}\right) & \left(\mu_2+\mu_3\right) & -\mu_3\left(\boldsymbol{n_{3_x}} \boldsymbol{n_{4_x}}\right) & 0 & \ldots & \ldots & \ldots & 0 \\
0 & 0 & \ddots & \ddots & \ddots & 0 & \ldots & \ldots & 0 \\
0 & \ldots & \ldots & \ldots & 0 & -\mu_{(n-3)}\left(\boldsymbol{n_{(n-3)_x}} \boldsymbol{n_{(n-2)_x}}\right) & \left(\mu_{(n-3)}+\mu_{(n-2)}\right) & -\mu_{(n-2)}\left(\boldsymbol{n_{(n-2)_x}} \boldsymbol{n_{bj_x}}\right) & 0 \\
0 & \ldots & \ldots & \ldots & \ldots & 0 & -\mu_{(n-2)}\left(\boldsymbol{n_{(n-2)_x}} \boldsymbol{n_{bj_x}}\right) & \left(\mu_{(n-2)}+\mu_{bj}\right) & -\mu_{bj}\left(\boldsymbol{n_{bj_x}} \boldsymbol{n_{n_x}}\right) \\
0 & 0 & 0 & 0 & 0 & 0 & 0 & -\mu_{bj}\left(\boldsymbol{n_{bj_x}} \boldsymbol{n_{n_x}}\right) & \left(\mu_{bj}+\mu_n\right)
\end{bmatrix}
\begin{bmatrix}
\left|\boldsymbol{t_1}\right| \\
\left|\boldsymbol{t_2}\right| \\
\left|\boldsymbol{t_3}\right| \\
\left|\boldsymbol{t_4}\right| \\
\vdots \\
\left|\boldsymbol{t_{(n-3)}}\right| \\
\left|\boldsymbol{t_{(n-3)}}\right| \\
\left|\boldsymbol{t_{bj}}\right| \\
\left|\boldsymbol{t_n}\right|
\end{bmatrix} =
$$

$$
\begin{bmatrix}
l_1 \dot{\boldsymbol{n}}_{\boldsymbol{1_x}}^2+\frac{\dot{w}_d r_d}{n-1}-\mu_1\left[\boldsymbol{P_1} \boldsymbol{n_{1_x}}\right] \\
l_2 \dot{\boldsymbol{n}}_{\boldsymbol{2_x}}^2+\frac{\dot{w}_d r_d}{n-1}+\left(\mu_1 \boldsymbol{P_1}-\mu_2 \boldsymbol{P_2}\right) \boldsymbol{n_{2_x}} \\
l_3 \dot{\boldsymbol{n}}_{\boldsymbol{3_x}}^2+\frac{\dot{w}_d r_d}{n-1}+\left(\mu_2 \boldsymbol{P_2}-\mu_3 \boldsymbol{P_3}\right) \boldsymbol{n_{3_x}} \\
\vdots \\
l_{(n-2)} \dot{\boldsymbol{n}}_{\boldsymbol{(n-2)_x}}^2+\frac{\dot{w}_d r_d}{n-1}+\left(\mu_{(n-3)} \boldsymbol{P_{(n-3)}}-\mu_{(n-2)} \boldsymbol{P_{(n-2)}}\right) \boldsymbol{n_{(n-2)_x}} \\
l_{bj} \dot{\boldsymbol{n}}_{\boldsymbol{bj_x}}^2+\frac{\dot{w}_d r_d}{n-1}+\left(\mu_{(n-2)} \boldsymbol{P_{(n-2)}}-\mu_3 \boldsymbol{P_{bj}}\right) \boldsymbol{n_{bj_x}} \\
l_n \dot{\boldsymbol{n}}_{\boldsymbol{n_x}}^2+\frac{\dot{w}_d r_d}{n-1}+\left(\mu_{bj} \boldsymbol{P_{bj}}-\mu_n \boldsymbol{P_n}\right) \boldsymbol{n_{n_x}}
\end{bmatrix}
\tag{3.59}
$$

$$\begin{bmatrix} \mu_1 & -\mu_1\left(\boldsymbol{n_{2_x}} \boldsymbol{n_{1_x}}\right) & 0 & 0 & 0 & 0 & 0 & 0 \\ -\mu_1\left(\boldsymbol{n_{1_x}} \boldsymbol{n_{2_x}}\right) & (\mu_1+\mu_2) & -\mu_2\left(\boldsymbol{n_{2_x}} \boldsymbol{n_{3_x}}\right) & 0 & \dots & \dots & \dots & 0 \\ 0 & -\mu_2\left(\boldsymbol{n_{2_x}} \boldsymbol{n_{3_x}}\right) & (\mu_2+\mu_3) & -\mu_3\left(\boldsymbol{n_{3_x}} \boldsymbol{n_{4_x}}\right) & 0 & \dots & \dots & 0 \\ & & \ddots & \ddots & \ddots & & & \\ 0 & 0 & \ddots & \ddots & \ddots & 0 & \dots & 0 \\ 0 & \dots & \dots & \dots & 0 & -\mu_{(n-3)}\left(\boldsymbol{n_{(n-3)_x}} \boldsymbol{n_{(n-2)_x}}\right) & \left(\mu_{(n-3)}+\mu_{(n-2)}\right) & -\mu_{(n-2)}\left(\boldsymbol{n_{(n-2)_x}} \boldsymbol{n_{bj_x}}\right) \\ 0 & \dots & \dots & \dots & \dots & 0 & -\mu_{(n-2)}\left(\boldsymbol{n_{(n-2)_x}} \boldsymbol{n_{bj_x}}\right) & \mu_{(n-2)} \end{bmatrix} \begin{bmatrix} |\boldsymbol{t_1}| \\ |\boldsymbol{t_2}| \\ |\boldsymbol{t_3}| \\ \vdots \\ |\boldsymbol{t_{(n-3)}}| \\ |\boldsymbol{t_{(n-2)}}| \\ |\boldsymbol{t_{bj}}| \end{bmatrix} =$$

$$\begin{bmatrix} l_1 \dot{\boldsymbol{n}}^2_{\boldsymbol{1_x}} + \frac{\dot{w}_d r_d}{n-1} - \mu_1 \left[\boldsymbol{P_1} \boldsymbol{n_{1_x}}\right] \\ l_2 \dot{\boldsymbol{n}}^2_{\boldsymbol{2_x}} + \frac{\dot{w}_d r_d}{n-1} + \left(\mu_1 \boldsymbol{P_1} - \mu_2 \boldsymbol{P_2}\right) \boldsymbol{n_{2_x}} \\ l_3 \dot{\boldsymbol{n}}^2_{\boldsymbol{3_x}} + \frac{\dot{w}_d r_d}{n-1} + \left(\mu_2 \boldsymbol{P_2} - \mu_3 \boldsymbol{P_3}\right) \boldsymbol{n_{3_x}} \\ \vdots \\ l_{(n-2)} \dot{\boldsymbol{n}}^2_{\boldsymbol{(n-2)_x}} - \frac{\dot{w}_d r_d}{n-1} + \left(\mu_{(n-3)} \boldsymbol{P_{(n-3)}} - \mu_{(n-2)} \boldsymbol{P_{(n-2)}}\right) \boldsymbol{n_{(n-2)_x}} \\ l_{bj} \dot{\boldsymbol{n}}^2_{\boldsymbol{bj_x}} + \frac{\dot{w}_d r_d}{n-1} - \boldsymbol{a_{noz}} \boldsymbol{n_{bj_x}} + \mu_{(n-2)} \boldsymbol{P_{(n-2)}} \boldsymbol{n_{bj_x}} \end{bmatrix} \tag{3.60}$$

3.5.3 Model Evaluation

For evaluation purposes, the model developed over the previous sections is compared to two reference models, both of which have also been created by the author. For convenience, the model that was developed over the previous sections shall be referred to as 'Model A' while the reference models created by the author are designated as 'Model B' and 'Model C' respectively. While 'Model A' was implemented from first principles as per the equations outlined above, 'Model B' and 'Model C' have been created in Simscape as rigid body systems with fixed link lengths and incorporate constraints to reproduce the reel-in behaviour. Note that the Simscape modelling tool was chosen (as opposed to a further implementation from first principles), since it reduces the modelling effort to the concatenation and parametrisation of interconnected lumped masses, revolute joints and appropriate rigid body transformations (see Figure 3.9). By the author's judgement, this provides a quicker and less error prone way for the modelling of simple systems.

For simplicity, the reel-in constraints in 'Model B' and 'Model C' do not cause the hose to be wound onto a drum but instead the hose is drawn in linearly in the direction of the duct by a prismatic actuator while torsional spring-damper systems are activated as the links move past the tow point and enter the duct on the refuelling pod. These spring-damper systems produce constraint torques on the spherical joints that force the relative angles between consecutive hose links to zero, thereby aligning the links in the direction of the hose duct. An extract of the underlying Simscape model topology for 'Model B' and 'Model C' is shown in Figure 3.9.

A comparative study of the reel-in behaviour of the three models is outlined over the following pages.

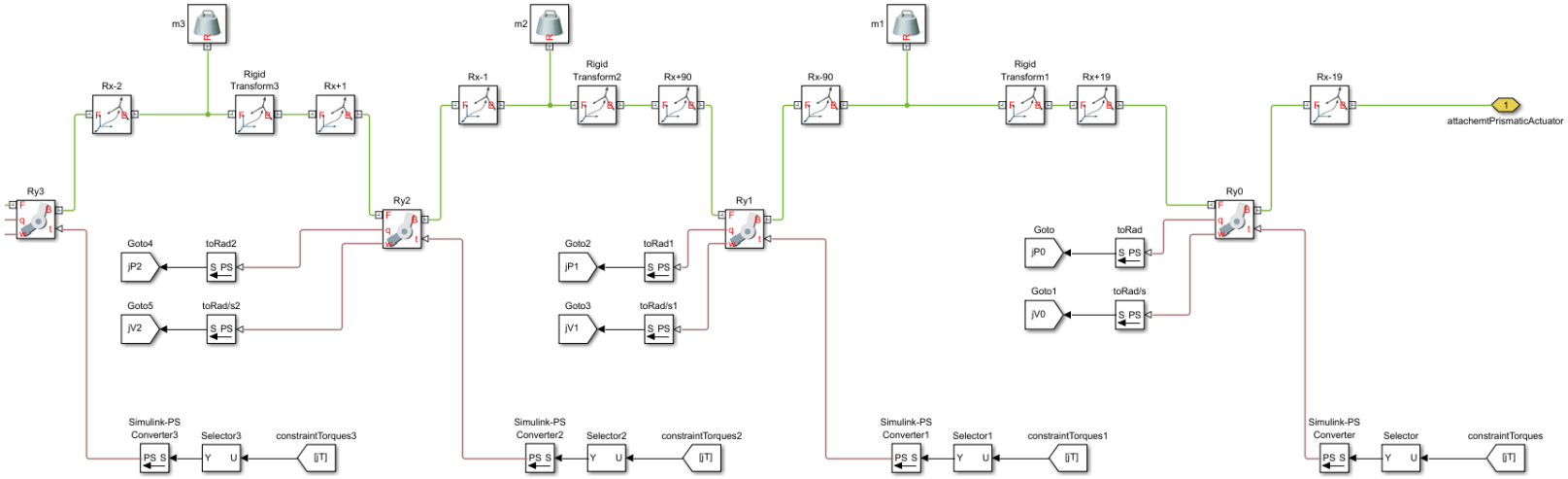

Figure 3.9: Model topology of two dimensional (X-Z plane) reference systems. The figure shows the connection port for the prismatic actuator that imposes the HDU action onto the hose and the first section of the hose chain which is composed of three lumped masses. The reel-in constraints are imposed by constraint torques that are externally computed based on the relative link angle and angular velocity (torsional spring-damper systems) and applied to individual revolute joints as the respective links move past the tow point to enter the HDU duct.

The reel-in behaviour of the three models is evaluated in simulation. At the start of the simulation the hose is extended to its full pay-out length of $27m$ and trailed from a centrally mounted fuselage refuelling pod. The hose exit point on the refuelling pod is defined as the tow point and located at $r_{tp}^{t} = [-21.14, 0, 0.5]$ with respect to the tanker's centre of gravity. For 'Model A' and 'Model B' the hose is discretised into 19 segments followed by a final $0.3m$ drogue segment. For comparison, 'Model C' has twice the spatial resolution along the hose (*i.e.* 38 hose links plus 1 drogue link). As such, 'Model C' serves as a reference model that provides improved accuracy and shows how closely a solution is converged to a continuous model.
In order to emphasise the effects of the reel-in dynamics, all external forces (including gravity, aerodynamics, hose bending and ball-joint friction) are deactivated and the hose configuration is initialised to an S-shape in the X-Z plane. The latter configuration is regarded as a particularly convenient means of tracking and highlighting shape changes over the course of the reel-in process. Intuitively, it can be expected that the hose slack provided by the two 'humps' along the S-shape will be successively reduced before the drogue begins to accelerate significantly. In addition, to the quantitative comparisons between all three models, such observations enable qualitative judgements to be made about the soundness of the modelling approaches.

For the tests at hand, the HDU is commanded to reel-in the hose by a length of $5(\frac{27}{19})m = 7.11m$ in $5s$ which is equivalent to the nominal length of the first 5 links for 'Model A' and 'Model B' (or first 10 links for 'Model C'). The time variation of the reel-in commands is given by a 5-th order polynomial subject to zero velocity and zero acceleration boundary conditions. Identical controllers are defined for all models

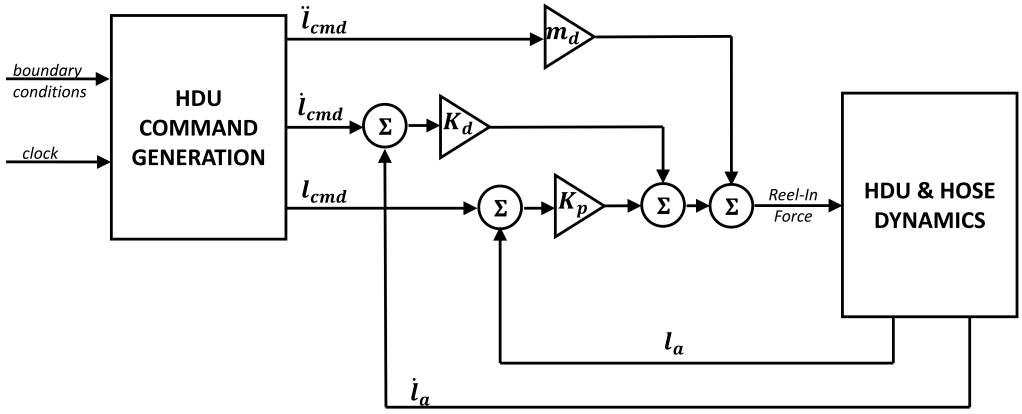

Figure 3.10: HDU controller.

(Figure 3.10). These include an acceleration based feed forward controller to overcome the equivalent linear inertia $m_d = 100kg$ of the HDU as well as position and velocity feedback loops with (gains $K_p = 1000\frac{N}{m}$ and $K_v = 100\frac{N}{(m/s)}$) respectively for residual error compensation.

The commanded HDU trajectories and the efficacy of the controller are shown in Figure 3.11. Despite a crude tuning of the controller gains and the absence of an integral error loop, the tracking performance is adequate, not least due to the smoothness of the command trajectories. Furthermore, the reel-in profiles of the individual models are sufficiently similar to make a 'fair' comparison of the resulting hose dynamics. Discrepancies in the reel-in behaviour between 'Model A' and 'Model B' / 'Model C' arise primarily from constraint torques in 'Model B' / 'Model C' provided by the activation of the torsional spring damper systems. These manifest themselves as disturbances to

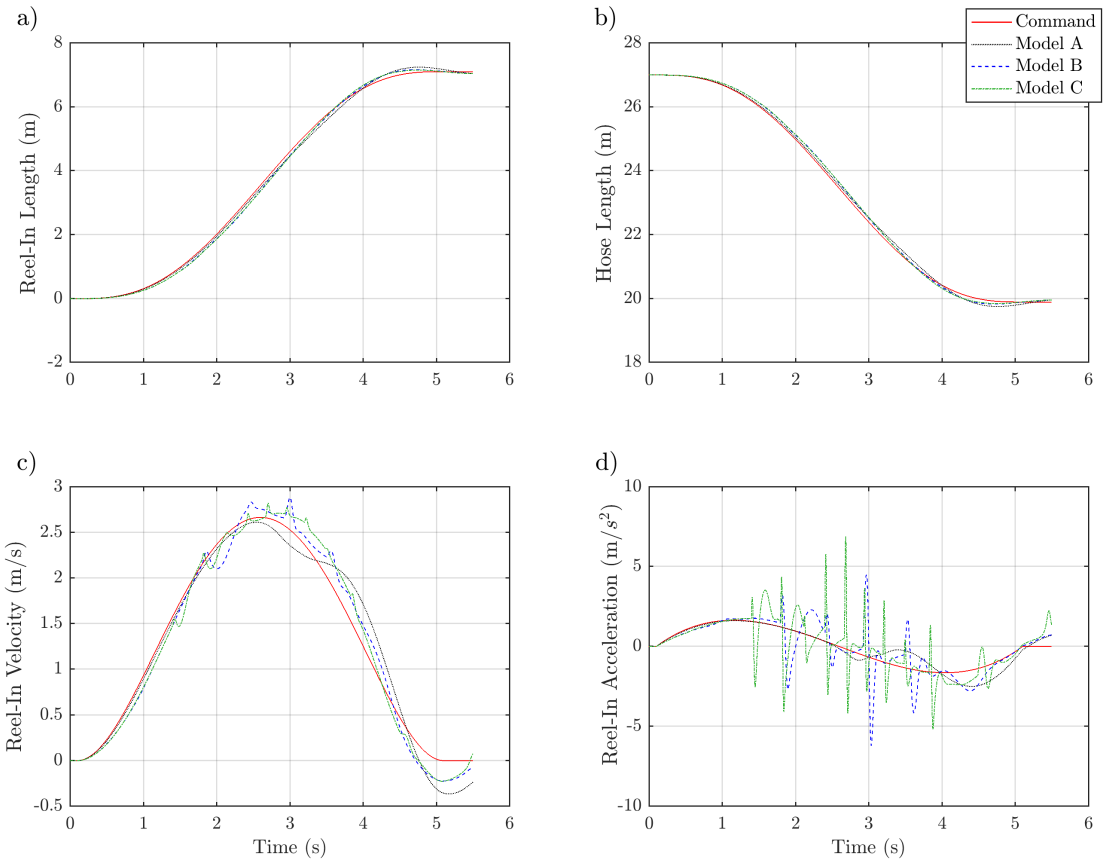

Figure 3.11: HDU command tracking during reel-in action. Reel-in action starts at $0.5s$ and ends at $5.5s$.

the reel-in process which is well pronounced in the velocity and acceleration profiles in Figure 3.11c)/d). The extend to which the hose dynamics are affected by these artificial constraints throughout the reel-in process are further examined below.

A direct comparison of the drogue trajectories from all models (Figure 3.12) reveals an expectedly close match between 'Model B' and 'Model C' which only differ based on the number of hose links. By contrast, the X-motion of 'Model A' lags significantly behind the response of 'Model B' and 'Model C', *i.e* the hose-drogue assembly in 'Model A' experiences a less drastic horizontal acceleration than 'Model B' and 'Model C' respectively. Although discrepancies exist also on the vertical Z-axis and for the drogue link orientation θ_Y, these are less pronounced meaning that a similar shape is developed by all models as the hose is drawn in. This is also confirmed by the time history of the hose configurations in Figure 3.13. Here, a great level of similarity in the qualitative behaviour of the hose models is revealed and the effects of the constraint springs in 'Model B' and 'Model C' are clearly visible, for instance at time $2.0s$.

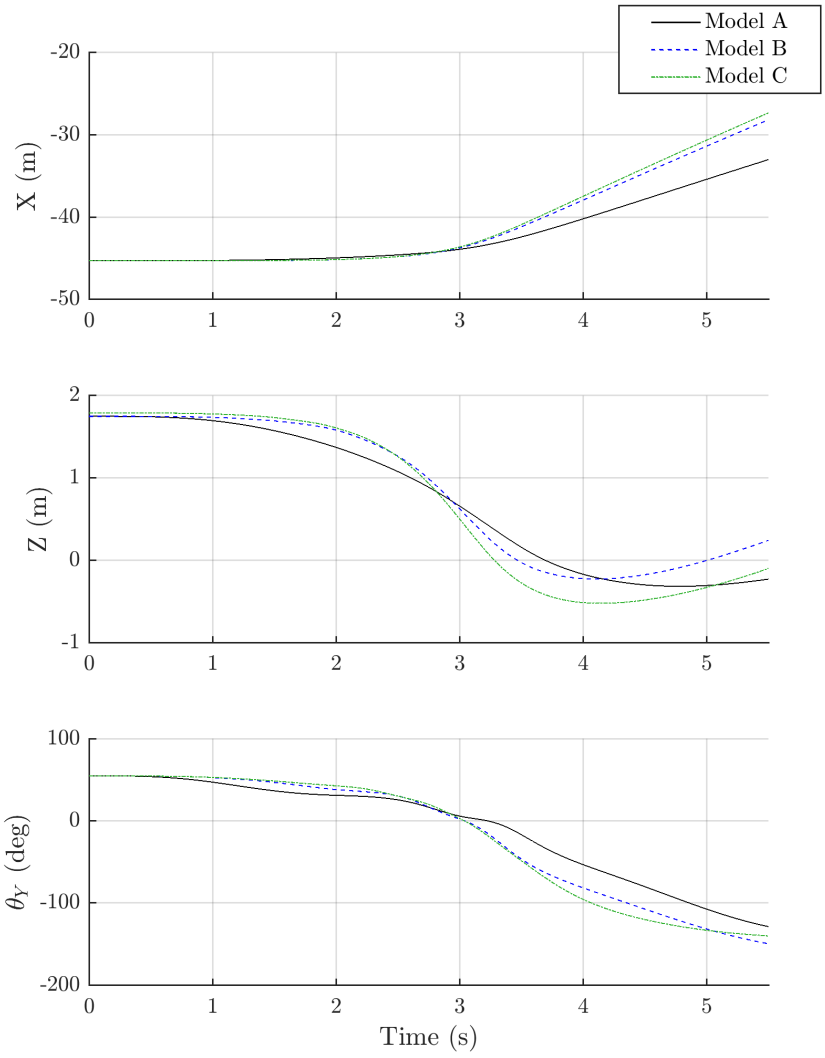

Figure 3.12: Drogue trajectories during reel-in.

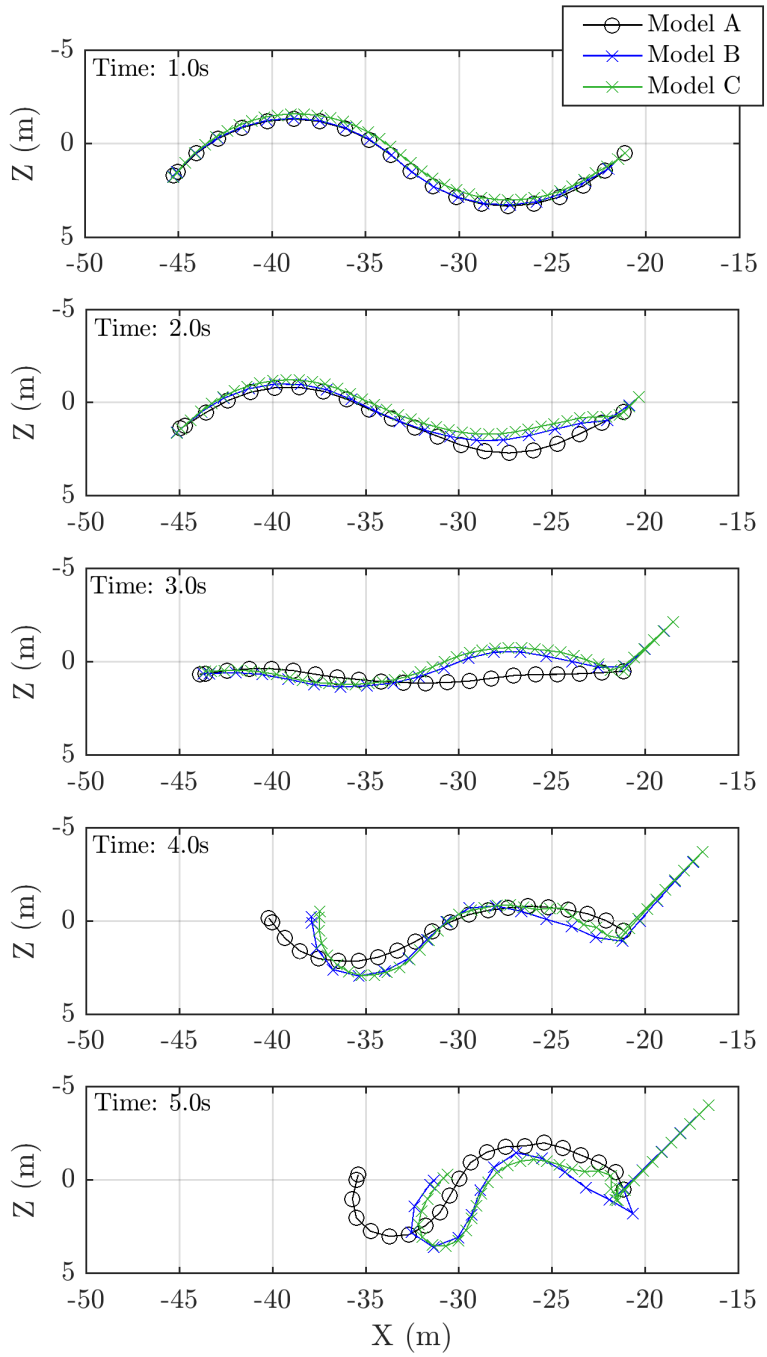

Figure 3.13: Time history of hose configurations during reel-in process.

The observed discrepancies, in particular the differences in the horizontal acceleration between 'Model A' and 'Model B' and 'Model C' may result from the energy gain associated with the constraint activation in 'Model B' and 'Model C' that forces the lumped masses to align with the hose duct. Fundamentally, such constraints would be similar to suddenly activated torsional springs at the tow point of 'Model A' as new hose segment enter the duct on the refuelling pod. However, given that the tow point in 'Model A' is represented as a frictionless roller, no equivalent energy gain is introduced, meaning that the hose responds slower and eventually forms a wider arch as it is drawn into the duct.

3.6 Recapitulation

This chapter has outlined the proposed methodology for conducting hybrid tests of the contact and coupling phase in AAR maneuvers. A framework was introduced by which industrial robots physically reproduce the relative motion of the refuelling hardware in a step-wise pseudo-dynamic fashion to acquire experimental contact force measurements that are subsequently fed back to a numerical simulation. The latter includes models for a tanker and receiver aircraft, the hose-drogue assembly and a flight regime. The test method and procedure have been discussed and architectural as well as implementation considerations, including a dedicated trajectory planning and execution mechanism, have been proposed for test integration with ABB IRC5 controllers.

A popular finite segment/lumped parameter modelling approach for towed and tethered cable systems was extended to provide a more elaborate and computationally efficient model for the reel-in dynamics. While the underlying finite segment/lumped parameter modelling approach was found to be widely accepted for the modelling of the hose-drogue assembly, prominent implementations such as [19] either did not provide a mechanism for hose take-up or incorporated a questionable implementation whereby a first link of excessive length was employed and artificially shrunk to account for the reel-in effect [20]. To improve upon this, an enhanced model was developed which accounts for the reel-in process using adaptive finite segment sizes. This enables the hose links to shrink uniformly throughout the reel-in process while the dynamics associated with the mass transfer from hose to HDU are accurately accounted for. The computational efficiency and inherent increase in spatial resolution of the finite segment model throughout the reel-in process are factors that distinguish the author's model from other models currently available in the literature.

For evaluation purposes, the hose take-up mechanism presented in [20] was deemed unsuitable and instead two separate reference models, *i.e* 'Model B' and 'Model C', incorporating reel-in constraints were created to contrast the hose take-up dynamics. By direct comparison, a close qualitative match of the hose dynamics during the reel-in process could be revealed, however quantitative discrepancies arising from an apparent energy gain associated with the constraint activation in the reference models were also highlighted. This energy gain was primarily manifested as an increase in the hose acceleration and led the author to the conclusion that his proposed model, *i.e.* 'Model A' provides a physically more accurate representation of the reel-in dynamics. Nevertheless, at this stage the model evaluation has to be considered inconclusive with regard to the validity and level of sophistication of the proposed modelling approach and future work is needed to further substantiate this claim. To this end, 'Model A' may be adapted to include an equivalent constraint torque at the tow point in order to align the dynamic behaviour of the developed and reference models quantitatively.

In the following chapters, the proposed methodical developments are first implemented and evaluated at scale in preliminary tests before being ported to the RMR for full-scale testing. Since the development and evaluation of the hose model was not completed at the time the experimental work was conducted, the author resorted to the model described in [20] for the tests in Chapter 4 and Chapter 5 respectively, meaning that the hose segments are shrunk sequentially without any dynamic compensation.

Chapter 4

Preliminary Tests

This chapter is publication-based and comprises a conference paper in Section 4.1 as well as a more comprehensive journal article in Section 4.2. Both publications outline early tests that were conducted by the author to assess the capabilities of the RPsDT method for the application to AAR scenarios and evaluated architectural implementations as well as proposed motion control schemes. The presented experimental work was carried out at the Bath robotics laboratory in an attempt to ready the development of the RPsDT method for the full scale tests at the RMR presented in Chapter 5.

The conference paper in Section 4.1 focuses on a comparative study of a simple and easily reproducible experimental contact scenario between a rigid mass and a compliant object and the corresponding emulation of this scenario based on the RPsDT method. The ability of the RPsDT method to capture the non-linear stiffness properties of the experimental specimen including structural damping due to hysteresis is demonstrated. Clear limitations of the method resulting from the neglect of rate and time dependent effects including viscous damping and creep are discussed. It is concluded that RPsDT offers useful potential for the study of probe-drogue contact scenarios in AAR but a need for careful validation is highlighted.

The journal article in Section 4.2 elaborates on the simple contact experiment and extends the work to an investigation of an AAR scenario. A first hybrid simulation of the docking phase is presented using a scaled setup and a qualitative assessment revealed refuelling hardware behaviour that is in-line with AAR observations. This includes the discontinuous nature of the contact event which causes significant drops in the hose tension, a clear indication of drogue tipping behaviour as well as characteristic post-contact hose dynamics in response to the probe strike. Importantly, the methodology

and system architecture are validated in preparation for the full scale testing at the RMR detailed in Chapter 5.

4.1 Robotic Pseudo-Dynamic Testing (RPsDT) of Contact-Impact Scenarios

Conference paper presented at *Towards Autonomous Robotic System (TAROS) 2015*, Liverpool, United Kingdom and published in the associated conference proceedings [98]:

Bolien M., Iravani P., du Bois J.L. (2015) Robotic Pseudo-Dynamic Testing (RPsDT) of Contact-Impact Scenarios. In: Dixon C., Tuyls K. (eds) Towards Autonomous Robotic Systems. TAROS 2015. Lecture Notes in Computer Science, vol 9287. Springer, Cham.

Statement of Contribution for Joint Authorship

M. Bolien (candidate): development and implementation of methodology, experimental work, data analysis, preparation of tables and figures, writing and compilation of manuscript.

P. Iravani (second supervisor): supervision of experimental work, review and editing of manuscript.

J.L. du Bois (lead supervisor): supervision of experimental work, review and editing of manuscript.

Copyright

Robotic Pseudo-Dynamic Testing (RPsDT) of Contact-Impact Scenarios

Mario Bolien(✉), Pejman Iravani, and Jonathan Luke du Bois

Robotics and Autonomous Systems Group, Department of Mechanical Engineering, University of Bath, Bath BA2 7AY, UK
{M.Bolien,P.Iravani,J.L.du.Bois}@bath.ac.uk

Abstract. This paper presents a hybrid test method that enables the investigation of contact-impact scenarios in complex systems using kinematically versatile, off-the-shelf industrial robots. Based on the pseudo-dynamic test method, the technique conducts tests on an enlarged time scale, thereby circumventing control rate and response time limitations of the transfer system. An initial exploratory study of a drop test demonstrates that non-rate dependant effects including non-linear stiffness and structural hysteresis can be captured accurately while limitations result from the neglect of rate- and time-dependant effects such as viscous damping and creep. Future work will apply the new method to contact scenarios in air-to-air refuelling.

Keywords: Industrial robot · Robotic pseudo dynamic testing · RPsDT · Hardware in the loop · Hybrid testing · Contact dynamics · Impact testing · Pseudo-dynamic testing · Drop test

1 Introduction

The work in this paper builds upon the use of industrial robots for hybrid tests of pre-contact docking manoevres for satellites and air-to-air refuelling [1,2], and serves as a feasibility study into the extension of these tests into the contact phase of the manoeuvre. Challenges in the realisation of hybrid tests of contact dynamics predominately arise due to the non-linear and discontinuous nature of contact events. Crucial factors for successful hybrid testing are *(i)* precise manipulation of the position and orientation of the colliding structure(s) in 3D space, *(ii)* sufficiently fast response times for the contact event and *(iii)* compensation of the induced transfer dynamics. While current industrial robots satisfy the first factor, they fall short of the latter two, especially for high velocity impacts and particularly stiff collisions. The main limitations for satisfactory response-speeds and real-time (RT) performance result from the large link inertia as well as proprietary control architectures. The latter typically preclude low level access to the axis controller such that favourable RT control schemes like impedance control [3], passivity based control [4] or model inversion schemes [5] cannot be easily realised.

C. Dixon and K. Tuyls (Eds.): TAROS 2015, LNAI 9287, pp. 50–55, 2015.
DOI: 10.1007/978-3-319-22416-9_7

This paper contributes to preceding efforts of realising hybrid tests of contact scenarios with robots by grounding the hybrid test on the pseudo-dynamic (PsD) testing method. The PsD testing technique enables dynamic hybrid testing on an expanded time scale with actuators of suitable load ratings but inadequate response speeds and power ratings [6]. The application of this technique to contact testing circumvents the response-time and transfer-dynamics issues of industrial robots from the outset at the expense of neglecting time-dependent test characteristics. To the best of the authors' knowledge, neither the applicability of the PsD test method to contact-impact problems has been extensively discussed nor is the realisation of robot assisted pseudo-dynamic testing reported in literature and from this point onwards the test method will be referred to as Robotic Pseudo-Dynamic Testing (RPsDT).

2 Application of the Pseudo Dynamic Test Method to Robots and Contact Scenarios

System hybridisation for RPsDT is performed according to the same principle as for PsD testing: The system under investigation is broken up into an experimental and a numerically simulated substructure. For RPsDT of contact scenarios, the experimental substructure would typically consist of exactly those components that make physical contact in the real system or a representative mock-up. The numeric simulation computes the positional response of the full system to the combination of measured interface forces and numerically simulated forces. The transfer system consists of an industrial robot equipped with a 6DOF force/torque sensor at its end effector. As in standard hybrid tests, additional sensors may be fitted directly to the mock-up for the purpose of further data acquisition throughout the study. The fundamental RPsDT architecture then complies with the schematic in Figure 1.

As opposed to standard PsD tests, data from the experimental specimen is not acquired in every time-step but only throughout the contact phase which can be identified based on kinematic constraints in simulation. If in contact, the

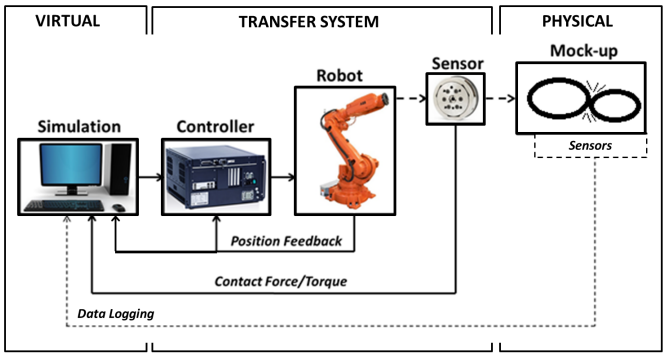

Fig. 1. RPsDT hardware architecture

robot is quasi-statically moved to reproduce the relative position and orientation of the colliding structures. This strains the specimen and allows measurement of the restoring forces and moments which are then fed back into the simulation. In a non-contact phase, the robot is kept stationary and the simulation can advance immediately without prior contact force acquisition.

Upon acquisition of the restoring force, the simulation proceeds by treating the model as an initial value problem: Based on the current states of the contacting structures and physically acquired force measurements from the experimental substructure, the new accelerations are computed and the new system states are obtained with a suitable integration algorithm. The cycle then repeats with the next time-step.

3 RPsDT Drop Test Investigation and Validation

Validation of RPsDT results is difficult because the motivation for RPsDT is the predictive deficit of purely simulated or purely experimental methods. For complex tests, validation approaches must be carefully considered. Here, a simple, reproducible test of a high-speed contact-impact scenario is devised to examine the validity and accuracy of the RPsDT method as a precursor to more complex testing. To this end, the vertical drop of a mass (steel plate) onto a compliant object (tennis ball) is emulated.

3.1 Experimental Setup and Procedure

The basic experimental set-up and test reference frame for RPsDT are illustrated in Figure 2(a). The drop-test rig in Figure 2(b) served the purely experimental reproduction of the contact scenario for validation purposes. Using high speed video capture (1500 frames/sec), plate drops on the experimental rig from an initial height $z_0 = 0.205m$ ($\dot{z}_0 = 0\frac{m}{s}$) were recorded with and without a tennis ball located on the bottom plate. Based on manual frame-by-frame tracking of the dropping plate's lower edge, the true experimental trajectories could be extracted from the video footage. The data from a first drop (without tennis ball) was used to identify the combined effects of rail friction and air resistance and allowed to tune the damping coefficient of a linear viscous damper element

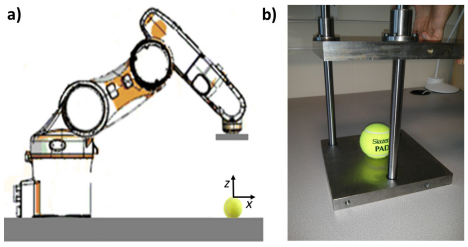

Fig. 2. (a) RPsDT setup and test reference frame. (b) Validation rig.

($c = 5.18\frac{N}{m/s}$) to give good agreement between the plate trajectories of the experimental drop and a simulated drop prior to contact. The trajectory data from the second drop (with tennis ball located centrally on lower plate) were used to validate the results from a subsequent RPsDT reproduction of the same contact scenario.

The simulated substructure of the RPsDT reproduction featured a point-mass model of the plate ($m = 6.50kg$) which, released from rest in a $1g$ environment and constrained to 1 DOF, drops under the combined influence of rail friction and air resistance as per the previously experimentally identified viscous damping element. The tennis ball and plates from the validation rig (rails removed) were used as specimen in the experimental substructure and the contact force was experimentally measured by the force sensor installed in between robot end effector and 'dropping' plate. As such, the plate's motion was governed by Equation (1).

$$m\ddot{z} = F_c - c\dot{z} - mg \tag{1}$$

RPsDT was conducted in its simplest from: Based on the newly acquired force measurement F_i at the start of each pseudo-step, the current plate acceleration $\ddot{z}_i$ was computed from Equation (1). The new position z_{i+1} and velocity $\dot{z}_{i+1}$ of the next time-step were found by integration based on the explicit 1^{st}-order Euler method using fixed step sizes of $h_s = 0.01ms$ and $h_c = 0.2ms$ throughout simulation and contact phases respectively.

3.2 Results and Discussion

While the true experimental time for the drop test reproduction using RPsDT amounted to about 90 minutes, RPsDT data presented in this section is plotted against the equivalent 'pseudo-time'. Plate trajectories from both the RPsDT study and drop test on the validation rig are shown in Figure 3(a). Prior to initial impact, both trajectories are in good agreement which emphasis the validity of the model in the virtual substructure throughout non-contact phases. Upon contact, RPsDT and experimental trajectory diverge. In the experimental drop test, the plate loses energy at a much higher rate and settles to rest within 1.5 seconds. The onset of trajectory divergence becomes evident in the initial impact phase. More pronounced asymmetry is apparent for the experimental trajectory, *i.e.* the experimental trajectory shows a greater difference between rates of compression (faster) and restitution (slower) than the RPsDT trajectory. This is also visible on the corresponding contact force graph in Figure 3(b). Here, force measurements were not available and the experimental contact force was computed as the product of plate mass and plate acceleration (obtained as 2^{nd} derivative of the position trajectory). Despite application of a running-mean filter, noise introduction by double differentiation causes apparent abnormalities in the data, however, general trends remain obvious: *(i)* compared with RPsDT data the experimental force shows a sharper rise to a higher peak and *(ii)* the difference in 'sharpness' of contact force increase and contact force decrease is greater in the experimental data, giving a more asymmetric contact force profile.

Both phenomena are attributed to rate dependent damping forces captured as part of the experimental study which during compression act in addition to the restoring forces to decelerate the plate but inhibit plate acceleration in restitution. Due to quasi-static loading, such effects are not observable in RPsDT data and both RPsDT trajectory and contact force graph are consequently more symmetric. Asymmetry that is nonetheless observable in the RPsDT data is attributed to non rate-dependent structural damping which originates from a hysteretic, *i.e.* path dependent stiffness variation that is an inherent property of the tennis ball. This is well-pronounced in Figure 3(c) where contact forces are plotted against tennis ball deformation for all four contact phases of the recorded RPsDT data. The transition from a nominally linear elastic response to a nonlinear response is apparent at around 0.035m deformation, with the deformation from the first impact extending far into the nonlinear region and peaking at about 90% of the ball's original diameter. In addition, it can be noted that RPsDT data shows greater stiffness in the initial compression phase than it does throughout successive contact phases. This stiffness change does not correspond to a true contact phenomenon but is attributed to a time dependent

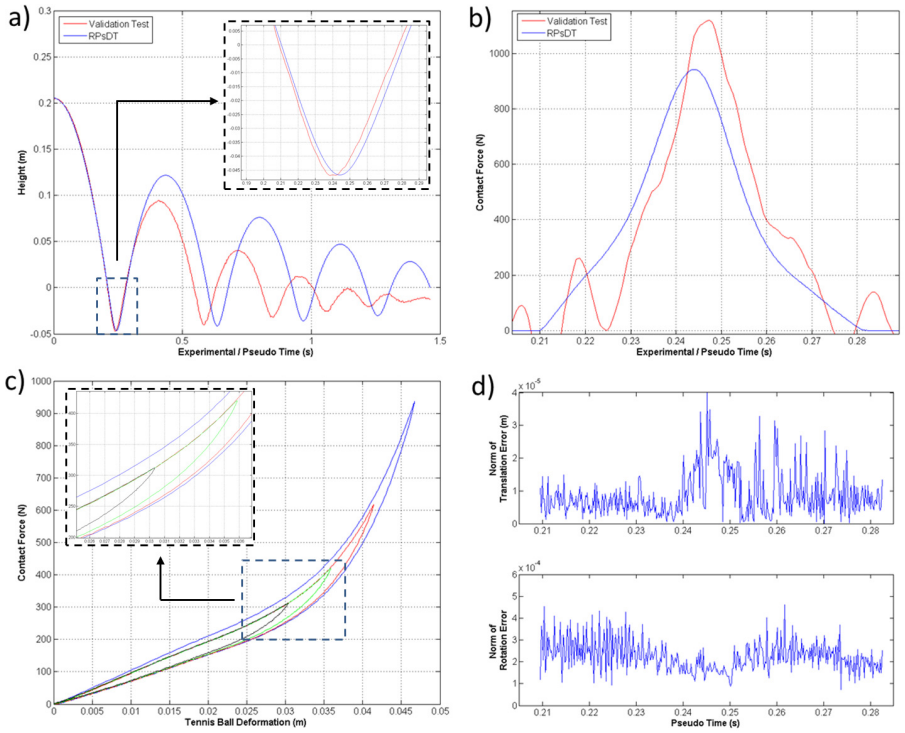

Fig. 3. (a) Experimental and RPsDT plate trajectories. (b) Contact forces on first impact. (c) Contact force vs. tennis ball deformation for RPsDT data. (d) Translation and rotation errors throughout first contact phase expressed as Euclidean and Frobenius norm respectively.

creep caused by sustained stress application over a prolonged period of time in RPsDT.

The extent to which the presented data is afflicted with errors resulting from the robot's positioning accuracy is shown in Figure 3(d). Good position and orientation tracking is suggested with the net translational and fixed frame rotational errors being consistently controlled to within $50\mu m$ and $0.015°$ respectively. It must be noted that this apparent accuracy neglects effects of joint flexure, backlash and deviation from catalogue DH-parameters.

4 Conclusions

This paper has demonstrated the feasibility of studying contact-impact problems in a hybrid test using an off-the-shelf industrial robot in a technique based on the well-established pseudo-dynamic method. This *RPsDT* circumvents robot response time issues for dynamic testing at the expense of disregarding rate dependent effects in the specimen's response. An RPsDT-based investigation of a drop test clearly indicated the ability of the method to account for non-rate dependent effects throughout contact events including the capture of non-linear damping characteristics due to hysteresis. Limitations were identified arising from the neglect of rate- and time-dependent effects, in particular those of viscous damping and creep. Inertial effects are a further concern but had little effect on the observations herein. It is suggested that *a priori* estimates of the time- and rate-dependent effects could be incorporated into the simulation to further improve test fidelity. In conclusion, RPsDT has shown useful potential but a need for careful test design and/or validation has been highlighted. Future work will employ the technique to evaluate contact dynamics in air-to-air refuelling scenarios.This research is sponsored by Cobham Mission Systems.

References

1. du Bois, J.L., Thomas, P.R., Richardson, T.S.: Development of a relative motion facility for simulations of autonomous air to air refuelling. In: 2012 IEEE Aerospace Conference, pp. 1–12. IEEE (2012)
2. Du Bois, J.L., Newell, P., Bullock, S., Thomas, P., Richardson, T.: Vision based closed-loop control systems for satellite rendezvous with model-in-the-loop validation and testing. In: 23rd International Symposium on Space Flight Dynamics. University of Bath (2012)
3. Hogan, N.: Impedance control: an approach to manipulation. In: American Control Conference, pp. 304–313. IEEE (1984)
4. Ortega, R., Van Der Schaft, A.J., Mareels, I., Maschke, B.: Putting energy back in control. IEEE Control Systems **21**(2), 18–33 (2001)
5. De Luca, A.: Feedforward/feedback laws for the control of flexible robots. In: Proceedings of the IEEE International Conference on Robotics and Automation, ICRA 2000, vol. 1, pp. 233–240. IEEE (2000)
6. Williams, M.S., Blakeborough, A.: Laboratory testing of structures under dynamic loads: an introductory review. Philosophical Transactions of the Royal Society of London. Series A: Mathematical, Physical and Engineering Sciences **359**(1786), 1651–1669 (2001)

4.2 Towards Robotic Pseudo-Dynamic Testing for Hybrid Simulations of Air-to-Air Refuelling

Article published in *IEEE/ASME Transactions on Mechatronics*, [90]:

Bolien, M., Iravani, P. and du Bois, J.L., 2017. Toward Robotic Pseudodynamic Testing for Hybrid Simulations of Air-to-Air Refueling. IEEE/ASME Transactions on Mechatronics*, 22(2), pp.1004-1013.*

Statement of Contribution for Joint Authorship

M. Bolien (candidate): development and implementation of methodology, experimental work, data analysis, preparation of tables and figures, writing and compilation of manuscript.

P. Iravani (second supervisor): supervision of experimental work, review and editing of manuscript.

J.L. du Bois (lead supervisor): supervision of experimental work, review and editing of manuscript.

Copyright

Toward Robotic Pseudodynamic Testing for Hybrid Simulations of Air-to-Air Refueling

Mario Bolien, Pejman Iravani, and Jonathan Luke du Bois

***Abstract*—Hybrid simulation couples experimental tests of novel components to validated numerical models of the remainder of a system and provides high-confidence predictions of their coupled dynamic behavior. Air-to-air refueling (AAR) is an example of the type of system that can benefit from this development approach. The work in this paper concerns the on-ground validation and preflight verification of probe–drogue contact–impact scenarios in AAR maneuvers using off-the-shelf multiaxis industrial robots as part of a hybrid test to interface the refueling hardware with numerical models of the flight environment. While industrial manipulators present a cost-effective solution, bandwidth and power limitations inevitably cause practical problems for real-time hybrid testing. These deficiencies typically manifest themselves as significant tracking inaccuracies or instabilities when sharp nonlinearities or discontinuities are encountered as part of a contact phase. Here, the novel robotic pseudodynamic testing (RPsDT) method is employed to circumvent the contact-response speed limitations of industrial robots. This paper presents and discusses the application of RPsDT to contact–impact problems, outlines the challenges and limitations of the technique in an easily reproducible validation experiment, and details the first RPsDT hybrid simulation of an AAR maneuver using scaled refueling hardware. It is concluded that RPsDT provides a useful tool for the investigation of a particular subclass of multibody contact–impact problems including AAR, where the response of the contacting structures does not possess significant rate-of-loading effects. Future work will comprise tests with full-scale AAR hardware.**

***Index Terms*—Air-to-air refueling, contact dynamics, hybrid testing, robotic pseudodynamic testing (RPsDT).**

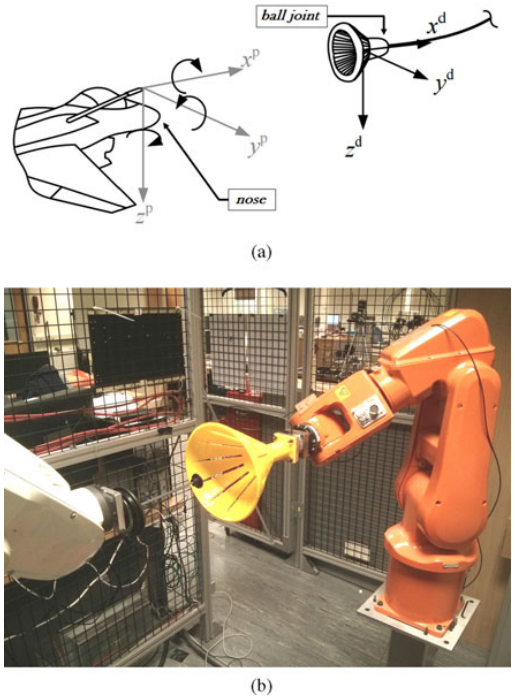

Fig. 1. (a) Schematic of a probe–drogue AAR system including frame assignment for receiver and drogue. Tanker and tow-point frame (not shown) comply with steady-state orientation of the drogue frame. (b) Setup for reduced-scale testing of probe–drogue contact–impact scenarios in AAR.

I. Introduction

AIR-TO-AIR refueling (AAR) provides a means for extending the range, payload, and endurance of aircraft and increases efficiency through the elimination of the large fuel consumption in repeated takeoff and landing operations [1]. The work documented here is concerned with probe and drogue refueling, where the tanker trails a flexible hose equipped with a coupling and drogue assembly [see Fig. 1(a)]. The receiver aircraft is equipped with a probe, rigidly mounted to the aircraft, which is maneuvered by the pilot to engage the drogue.

The emergence of unmanned aerial vehicles brings the prospect of aircraft staying airborne indefinitely, supported by autonomous AAR so that landing becomes necessary for maintenance only. Consequently, reliable tools for the on-ground validation and preflight verification of docking maneuvers are widely regarded as an important enabling technology. The complexity of an AAR environment demands the development of special techniques to satisfy this need, and hybrid testing is one such tool.

Hybrid testing allows for representative conditions in a repeatable laboratory-based setup and provides a valuable intermediate derisking step between component testing and full system

Manuscript received July 25, 2016; revised October 25, 2016; accepted November 30, 2016. Date of publication January 23, 2017; date of current version April 14, 2017. Recommended by Technical Editor Z. Xiong. This work was supported by Cobham Mission Systems, and by the U.K. Engineering and Physical Sciences Research Council under Grant EP/L504890/1.

The authors are with the Department of Mechanical Engineering, University of Bath, Bath BA2 7AY, U.K. (e-mail: M.Bolien@bath.ac.uk; P.Iravani@bath.ac.uk; J.L.du.Bois@bath.ac.uk).

Color versions of one or more of the figures in this paper are available online at http://ieeexplore.ieee.org.

Digital Object Identifier 10.1109/TMECH.2016.2644200

flight testing. Hybrid tests are comprised of two domains: 1) the physical domain where real components are evaluated experimentally; and 2) the numerical domain where computer models simulate the response of the remainder of the system. The two domains are coupled together to reproduce the transient and/or nonlinear behavior of the complete emulated system.

The use of industrial robots as a cost-effective means for relative motion reproduction has been a popular choice for hybrid tests of both AAR scenarios [2] and the related application of satellite docking [3].

Actuators for real-time (RT) hybrid testing must be accurate and fast so as to minimize the influence of the actuator transfer dynamics. While contemporary industrial robots satisfy the first criterion, they fall short of the latter, especially for high-velocity impacts and stiff collisions such as those experienced in AAR contact scenarios. The main limitations for satisfactory response speeds and RT performance result from the large link inertias as well as proprietary control architectures that are optimized for precision in repetitive positioning tasks. The latter typically preclude low-level access to the axis controller such that favorable RT control schemes such as impedance control [4], passivity-based control [5], or model inversion schemes [6] cannot be easily realized. High-level proprietary interfaces provide low controller sample rates and considerable dead times in command execution: typically 10–120 ms, and upwards. These dead times have detrimental effects on the fidelity and, critically, the stability of a hybrid test [7]. Typical approaches for mitigation of these effects include forward predictive methods [8], as well as delay and lag compensation [9]. The latter often suffer from demand saturation, and efforts have been made to compensate for this with model-predictive control [10]. All of these approaches work best for a linear plant response and cannot compensate for significant nonlinearities or discontinuous behavior without *a priori* knowledge of the physical system being tested. The existence of reliable models for the physical system would, however, render the hybrid test largely obsolete.

These problems have been approached in a variety of ways. Ma *et al.* [3] realized an admittance control scheme around the proprietary architecture of a KUKA industrial controller for the hardware-in-the-loop (HIL) simulation of satellite docking maneuvers. These maneuvers occur at speeds of the order of centimeters per second so delay and sample rates in the robot control interface did not present a limiting factor. Blomdell *et al.* [11] created an application for motion control of ABB robots, which intercepts and overwrites the messages exchanged between the high-level computer and the low-level axis controller. This grants access to position and velocity reference and feedback signals with low latency and high rates ($\sim$250 Hz), sufficient to perform HIL tests of tracking sensors and control systems for automated AAR procedures [12], [13]. The aircraft, hose/drogue, sensor, and flight controller dynamics are faithfully simulated using this system, but the performance still falls short of that required for the stiff fast contact dynamics as the probe engages the drogue assembly [14].

The work in this paper investigates methods at reduced scale [see Fig. 1(b)] for simulating probe–drogue contact–impact events with hybrid tests. This is done with a view to extending the simulation capabilities of the systems described by du Bois *et al.* [12]. The approach taken is to employ pseudodynamic (PsD) testing in place of RT methods for the duration of the contact event. The PsD method enables dynamic testing on an expanded time scale, thus mitigating instabilities arising through actuator delays. This paper expands upon the robotic pseudodynamic testing (RPsDT) method first outlined in [15] by the present authors and, then, goes on to demonstrate its application in reduced-scale AAR experiments as a precursor to future full-scale tests. This paper provides the first comprehensive work that outlines the motivation, application, and validation of RPsDT, and demonstrates the application of RPsDT to hybrid testing of probe–drogue contact–impact scenarios in an AAR environment. The work seeks to provide valuable contributions to the study of multibody contact–impact problems taking place in complex environmental settings.

This paper is divided into the following parts. Section II describes the RPsDT method including system architecture considerations and implementations from a control perspective. Section III validates RPsDT in an easily reproducible drop-test experiment that was specifically designed to emphasize the remaining challenges and methodical limitations of the technique. This section also builds an argument for the applicability of RPsDT to probe–drogue contact–impact scenarios in AAR, which are then demonstrated and investigated in Section IV. Conclusions are drawn and future work is outlined in Section V.

II. RPsDT of Contact Scenarios

PsD testing was originally developed for the assessment of structural responses to earthquakes in civil engineering [16]. Throughout a PsD test, the specimen is subjected to a displacement history as specified by the simulated environment. In each time step, the displacement is imposed onto the structure in a quasi-static fashion, i.e., non-RT. Physical measurements of the specimen's restoring force are acquired at static equilibrium points and fed back into the simulation. The technique predates current state-of-the-art RT dynamic substructuring methods, but circumvents some of their shortcomings to enable dynamic hybrid testing on an expanded time scale. The actuators require suitable load ratings, but the constraints on bandwidth, response speeds, and power ratings are relaxed [17]. The drawback is the loss of rate-dependent load effects from the physical domain.

PsD testing has been shown to be an effective technique for the investigation of component behavior, for which rate-dependent effects are either easily modeled or negligible compared to dominant elastic/plastic forces [17]. The application of this technique to contact testing circumvents the response time and transfer dynamics issues of industrial robots from the outset at the expense of neglecting time-dependent test characteristics. To the best of the authors' knowledge, neither the application of the PsD test method to contact–impact problems nor the realization of robot-assisted PsD testing has been explored in the academic literature prior to the preliminary results arising from the present work [15].

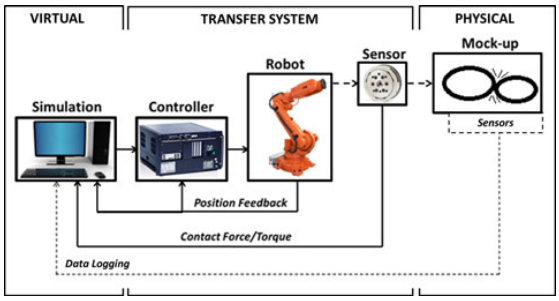

Fig. 2. RPsDT hardware architecture.

A. RPsDT Method

System hybridization for RPsDT is performed according to the same principle as for PsD testing: The system under investigation is broken up into an experimental and a numerically simulated substructure. For RPsDT of contact scenarios, the experimental substructure would typically consist of exactly those components that make physical contact in the real system. The numerical simulation computes the positional response to the combination of measured interface forces and numerically simulated forces. The transfer system consists of an industrial robot equipped with a 6-degree-of-freedom (DOF) force/torque sensor at its end effector. As in standard hybrid tests, additional sensors may be fitted directly to the physical hardware for the purpose of further data acquisition throughout the study. The fundamental RPsDT architecture then complies with the schematic in Fig. 2.

RPsDT of contact scenarios follows the algorithm depicted in Fig. 3. As opposed to standard PsD tests, data from the experimental specimen is not acquired in every time step but only throughout the contact- and near-contact phase, which can be identified based on kinematic constraints in simulation. If in contact, the robot is quasi-statically moved to reproduce the relative position and orientation of the colliding structures. This strains the specimen and allows measurement of the restoring forces and moments, which are then fed back into the simulation. In a noncontact phase, the robot is kept stationary and the simulation can advance immediately without prior contact force acquisition. Upon acquisition of the restoring force, the simulation is treated as an initial value problem: Based on the current states of the contacting structures and physically acquired force measurements from the experimental substructure, the new accelerations are computed and the new system states are obtained with a suitable integration algorithm. The cycle then repeats with the next time step.

B. RPsDT Architecture

The RPsDT method is implemented on a KUKA KR 5 sixx R650 industrial robot controlled via the KUKA robot sensor interface (RSI). Among other control modes, RSI enables the exchange of joint velocity reference commands and joint position feedback between an external PC and the proprietary industrial controller at a sample rate of 12 ms with soft-RT determinism. Our experiments show that the low-level implementation of motor and motion controller execute the reference commands with a considerable delay of 120 ms but achieve accurate demand tracking so long as any form of limit saturation is avoided. This is in agreement with the findings in [18].

The high-level RPsDT architecture is shown in Fig. 4(a). The architecture comprises an offline environment for the numerical simulation and Cartesian-space motion planning as well as an online state -machine-based safety and supervisory logic controller (SSLC) and a joint-space command generator. Both the SSLC and the command generator are embedded in a soft-RT task, and the underlying state machine is directly invokable from the offline simulation environment. To this end, the data exchange between simulation environment and online robot motion controller is kept entirely event based using a fixed transmission control protocol connection that guards the application from unreliability associated with the network protocol. This effectively implements a master–slave hierarchy that completely decouples the simulation from robot motion execution, which has the advantage that robot controller update rates can be met regardless of the computational time required by the simulation, and hence, numerical models can be of almost arbitrarily high fidelity. By contrast, force/torque measurements acquired with the open-source ICub IIT 6DOF FT sensor are fed into the soft-RT task as a continuous stream of datagrams using nonblocking UDP-based interprocess communication so that the SSLC can quickly detect force limit violations and respond with minimal delay. This architecture effectively enslaves the transfer system (robot and controller) and thereby embeds an experimental contact test into the loop of a master simulation. That is, at each simulation time step, the robot can be ordered to pseudodynamically reproduce the relative motion of the contacting structures to acquire and feed back the current contact force such that the following simulation steps become a function of numerically modeled and experimentally measured data.

C. Motion Control

Relative motion reproduction of the physical hardware specimens throughout contact requires manipulation along the shortest path in Cartesian space, i.e., the "tool" must translate along a straight line between demand and target position, while "tool orientation" must simultaneously change from initial to target orientation along the shortest arc (on the surface of a unit sphere). This demand is satisfied by independently planned Cartesian space trajectories for tool translation and orientation. Hence, translation trajectories are specified as cubic polynomials, which accommodate position and zero-velocity boundary conditions for the point-to-point (P2P) motions [see (1)], while intermediate orientations q_{int} follow from the standard textbook definition of spherical linear interpolation (SLERP) [19] between start and target quaternions q_{start} and q_{target}, as per (2). Here, $\Omega = \arccos(q_{\text{start}} \cdot q_{\text{target}})$ describes the angle subtended by the arc of rotation, and the scale factor $s(t)$ is computed as the linear time function $s(t) = \frac{t}{t_{\text{exc}}}$, where t_{exc} represents the total trajectory execution time, as shown in Fig. 5, and t is the time

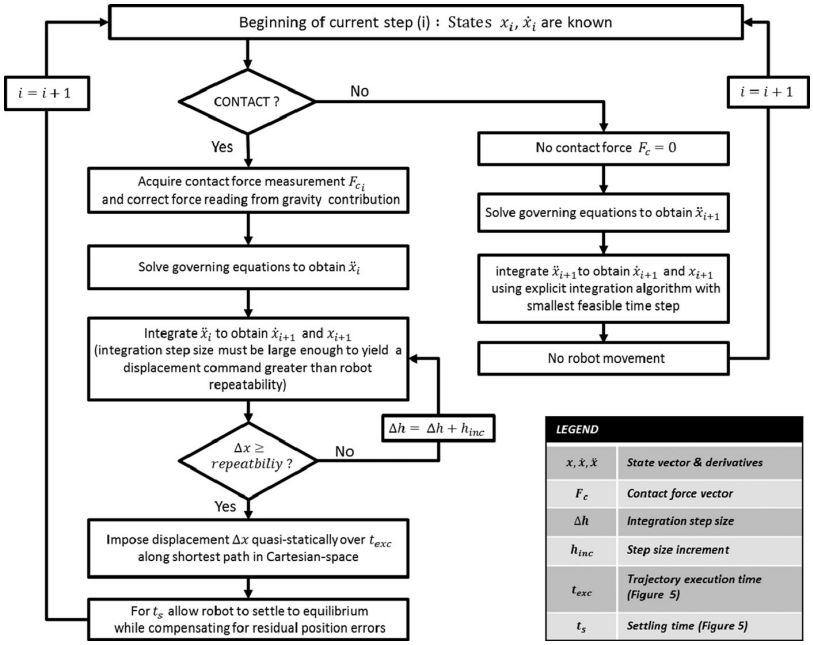

Fig. 3. Algorithmic procedure for RPsDT of contact scenarios.

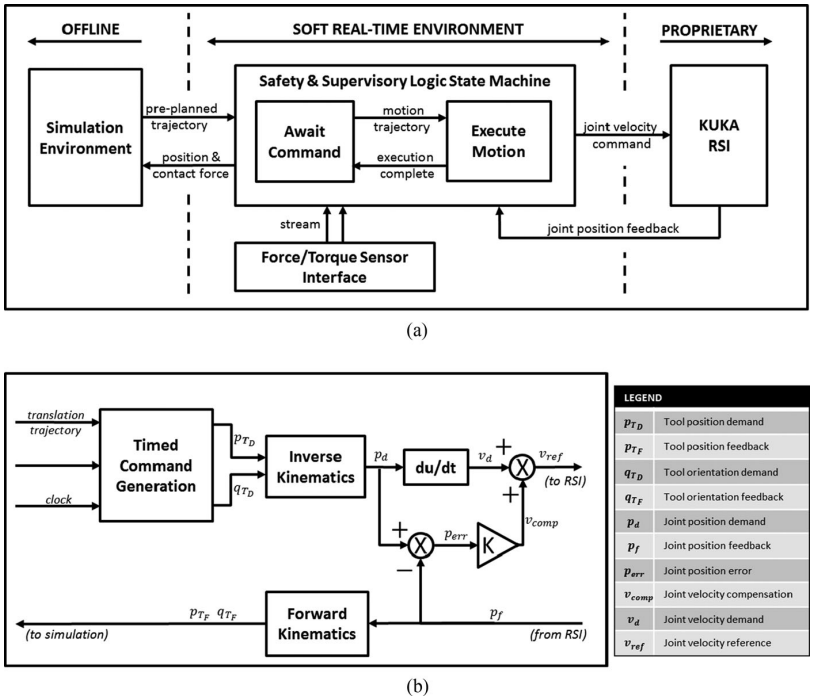

Fig. 4. (a) High-level RPsDT software architecture. (b) RPsDT motion command generator.

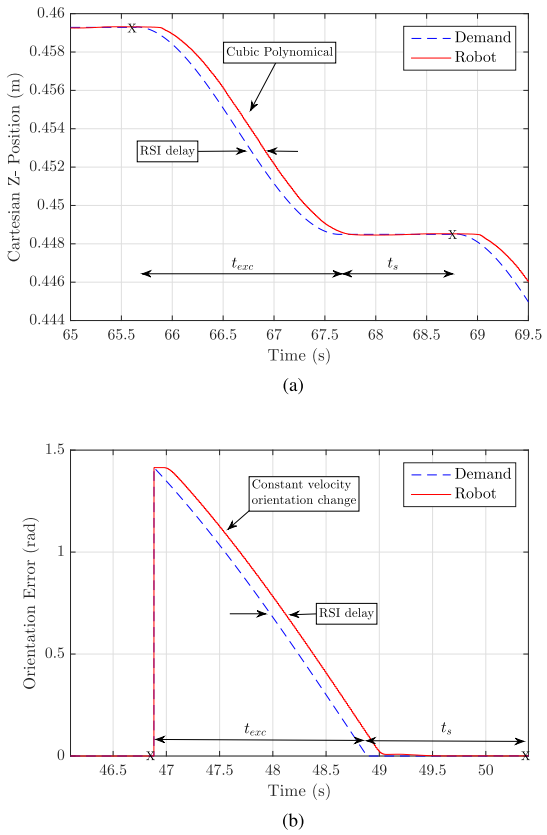

Fig. 5. Examples of quasi-static trajectories showing (a) end effector translation and (b) SLERP-based end effector orientation change. Trajectory execution time, settling time, and points of contact force measurement are identified by "t_{exc}," "t_s," and "X," respectively.

from start of the motion

$$\begin{bmatrix} x_{\mathrm{tool}}(t) \\ y_{\mathrm{tool}}(t) \\ z_{\mathrm{tool}}(t) \end{bmatrix} = \begin{bmatrix} a_{x0} \\ a_{y0} \\ a_{z0} \end{bmatrix} + \begin{bmatrix} a_{x1} \\ a_{y1} \\ a_{z1} \end{bmatrix} t + \begin{bmatrix} a_{x2} \\ a_{y2} \\ a_{z2} \end{bmatrix} t^2 + \begin{bmatrix} a_{x3} \\ a_{y3} \\ a_{z3} \end{bmatrix} t^3 \tag{1}$$

$$q_{\mathrm{int}}(t) = \left[\frac{\sin(1-s(t))\Omega}{\sin(\Omega)}\right] q_{\mathrm{start}} + \left[\frac{\sin(s(t)\Omega)}{\sin(\Omega)}\right] q_{\mathrm{target}}. \tag{2}$$

Corresponding joint space trajectories are then computed by kinematic inversion in each time step [see Fig. 4(b)]. Due to the unavailability of a position reference input for RSI, a simple joint position error compensation loop with an adaptive gain has been integrated to minimize the effects of drift resulting from potentially erratic joint space commands. The compensation gain K is only active ($K = 1$) for the duration of the settling time (t_s) at the end of a P2P motion to avoid systematic error accumulation due to interference with the integral action of the proprietary industrial controller. The efficacy of this control approach is illustrated in Fig. 5. Simpler trajectory planning schemes (e.g., joint space schemes) bear the risk of incurring hardware damage and/or invalidating measurements of path-dependent effects since the corresponding Cartesian-space trajectories can cause specimen penetration beyond what is demanded throughout trajectory execution.

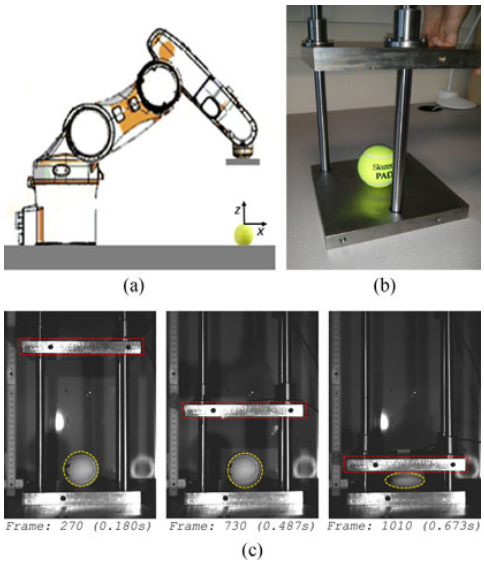

Fig. 6. (a) RPsDT setup and test reference frame. (b) Validation rig. (c) High-speed video footage of plate drop on validation rig.

III. Validation Experiments

Validation of RPsDT results is difficult, since the motivation for a hybrid test is usually based around the challenge of reproducing the full system behavior in purely experimental or purely numerical form. Without validation, however, the results of a hybrid test are unreliable. For complex tests, validation approaches must, therefore, be carefully considered on an individual basis. Here, a simple reproducible test is designed to validate the methods as a precursor to applying the technique to more complex scenarios. A specimen with significant viscous properties is included in the experimental substructure of the test to clearly outline challenges and limitations of the technique while simultaneously highlighting its strengths, and defining a subclass of contact–impact problems, to which the technique is readily applicable. To this end, a steel mass is dropped onto a spherical viscoelastic shell to validate the methodology.

A. Setup and Procedure

The basic experimental setup and test reference frame for RPsDT are illustrated in Fig. 6(a). The drop-test rig in Fig. 6(b) served the purely experimental reproduction of the contact scenario for validation purposes. Using high-speed video capture (1500 frames/s), a drop of the plate ($m = 6.50$ kg) from an initial height $z_0 = 0.205$ m ($\dot{z}_0 = 0$ m/s) was recorded. Based on manual frame-by-frame tracking of the plate's lower edge [see Fig. 6(c)], the true experimental trajectories could be extracted

from the video footage and a viscous damper model for air and rail resistance ($c = 5.18$ N/m/s) could be identified.

The RPsDT reproduction featured a point-mass model of the plate which, released from rest in a $1g$ environment and constrained to 1 DOF, drops under the combined influence of rail friction and air resistance. The viscoelastic shell (tennis ball) and plates from the validation rig (rails removed) were used as specimens in the experimental substructure and the contact force was experimentally measured by the force sensor installed between the robot end-effector and the "dropping" plate. As such, the plate's motion was governed by

$$m\ddot{z}_i = F_{c_i} - c\dot{z}_i - mg \tag{3}$$

Using a trajectory execution- and settling time of $t_{\text{exc}} = 2$ s and $t_s = 1$ s, respectively, the test procedure followed the RPsDT algorithm in Fig. 3 in its simplest from: Based on the newly acquired force measurement F_{c_i} at the start of each pseudostep, the current plate acceleration $\ddot{z}_i$ was computed from (3). The new position z_{i+1} and velocity $\dot{z}_{i+1}$ of the next time step were found by integration based on the explicit first-order Euler method using fixed step sizes of $h_s = 0.01$ ms and $h_c = 0.2$ ms throughout simulation and contact phases, respectively.

B. Results and Validation

The main drop-test results are shown in Fig. 7(a)–(c), comprising plate trajectories, force profiles for the first contact phase, as well as RPsDT-derived contact stiffness profiles of the tennis ball, respectively. All RPsDT data presented in this section are plotted against the "pseudotime," or "simulation time," rather than the true experimental time scale.

The RPsDT and experimental trajectories are shown to be in good agreement prior to the initial impact [see Fig. 7(a)], which emphasizes the validity of the friction and air resistance model in the numerical substructure throughout noncontact phases. Despite a divergence of plate trajectories thereafter and apparent differences in the contact force profiles [see Fig. 7(b)], the decisive test features in the RPsDT emulation correlate qualitatively well with those of the experimental validation test. That is, without any underlying contact model, the RPsDT method predicts:

1) successive contact scenarios with significantly damped dynamics;
2) contact force profiles that are similar to those in the experimental test with regard to shape, contact-time, as well as peak amplitude;
3) periodicity and overall frequency content comparable to experimental test data.

While such information may appear trivial for the study at hand, it can prove immediately valuable to tests of more complex systems, for which even the fundamental contact and postcontact behavior would be highly uncertain otherwise; and may provide sufficient detail to derive or enforce practically useful design changes for the tested equipment.

The increasing trajectory divergence noted above is the result of contact force discrepancies, where even minor inaccuracies can cause substantial error accumulation in the position

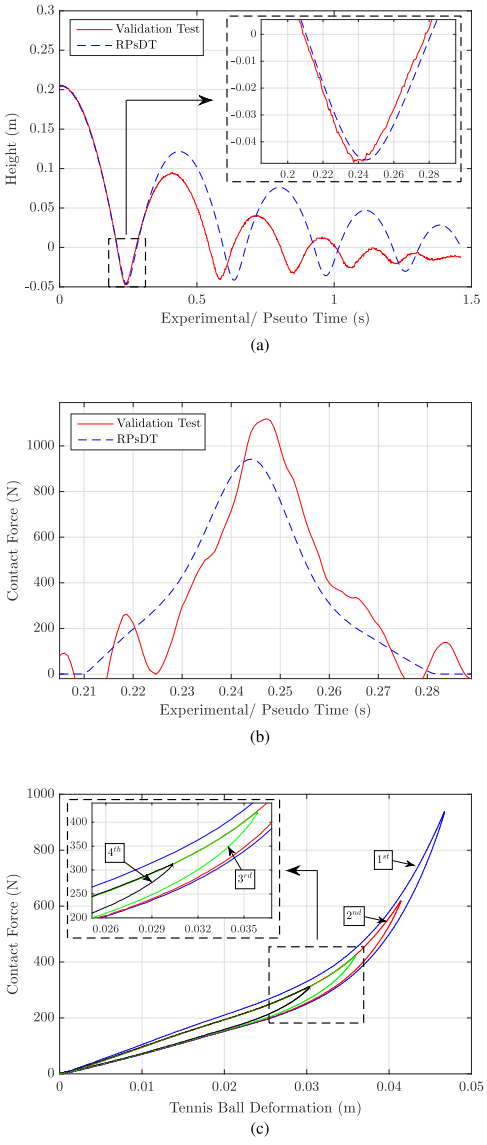

Fig. 7. (a) Experimental and RPsDT plate trajectories. (b) Contact forces on first impact. RPsDT uses direct force measurement, while experimental force is computed as a product of plate mass and acceleration (obtained by double differentiation of trajectory data) subject to application of running mean filter. (c) RPsDT contact force versus tennis ball deformation for first four contact phases.

response over time. In Fig. 7(b), the experimental contact force shows a sharper rise to a higher peak than the RPsDT force and a more asymmetric force profile, which results in a greater difference between rates of compression (faster) and restitution (slower) of the experimental data on the corresponding trajectory plot in Fig. 7(a). Both phenomena are attributed to rate-dependent damping forces captured as part of the experimental study, which contribute more significantly to the plate deceleration in compression than to a reacceleration in the restitution phase. A significant contribution to the rate-dependent

effects arises from the fluid and thermodynamic processes of the gas inside the ball: a complexity that can be avoided for a large class of systems. Due to quasi-static loading, such effects are not observable in RPsDT data, and both the RPsDT trajectory and contact force graph are consequently more symmetric. Asymmetry that is nonetheless observable in the RPsDT data is attributed to nonrate-dependent structural damping, which originates from a hysteretic, i.e., path-dependent stiffness variation that is an inherent property of the viscoelastic material. This is well pronounced in Fig. 7(c), where contact forces are plotted against deformation for all four contact phases of the recorded RPsDT data. The transition from a nominally linear elastic response to a nonlinear response is apparent at around 0.035-m deformation, with the deformation from the first impact extending far into the nonlinear region and peaking at about 90% of the ball's original diameter. In addition, it can be noted that RPsDT data show greater stiffness in the initial compression phase than throughout successive contact phases. This stiffness change does not correspond to a true RT contact phenomenon but is attributed to a time-dependent creep caused by sustained stress application over a prolonged period of time in RPsDT.

These results have promising implications with respect to hybrid simulations for AAR: The structure of the refueling drogue is predominantly elastic, and it is expected that Coulomb friction in articulated parts and hysteric damping in woven components will dominate the damping effects; these forces have correlated well in these exploratory tests. The creep effect is a minor concern, and this is mitigated as far as possible by reducing loiter times at the static equilibrium points and by screening results for such artefacts. Loiter time reductions can be achieved by replacing the constant rate orientation variation in (2) with a cubic time function subject to $s(0) = \dot{s}(0) = \dot{s}(t_{\mathrm{exc}}) = 0$ and $s(t_{\mathrm{exc}}) = 1$ to eliminate the infinite acceleration demands at the start and end of the motion and reduce settling time. This was implemented for the study in Section IV. Finally, good tracking accuracy can be reported for the test above, with translational and rotational errors being consistently controlled to within an apparent accuracy of 50 μm and 0.015°, respectively, subject to errors in link flexure, backlash, and forward kinematics calibration.

IV. RPsDT of Probe–Drogue Contact–Impact Scenarios in AAR

This section demonstrates the application of RPsDT to AAR maneuvers at reduced scale. While this scaling implies that none of the presented data can be regarded as representative of an actual refueling scenario, the primary focus lies on the demonstration of the capability of the underlying test method as well as the potential value for future predictions of the probe–drogue contact and coupling behavior in full-scale reproductions.

A. Physical Substructure

Resembling receiver and tanker aircraft, respectively, a KUKA KR5 sixx R650 and an ABB IRB 120 robot, are equipped with scaled probe and drogue specimens, as depicted in Fig. 1(b). Probe–drogue contact–impact scenarios are physically reproduced with both robots and coupled to numerical simulations of full-scale AAR maneuvers. To this end, interface forces measured by the FT sensor installed in-between drogue and end-effector of the ABB robot are amplified by a factor of 300 to yield a realistic effect on the simulated full-scale hose–drogue assembly upon contact, while a geometric scaling factor of 5 reduces the relative contact penetration of probe and drogue in the physical domain to avoid violation of robot workspace limits.

B. Numerical Simulation

The numerical substructure of the presented hybrid test features an AAR simulation based on previous developments detailed in [12], [20], and [21] to enable the simulation of contact-induced responses of the hose–drogue assembly in a realistic flight regime. As such, the simulation computes the relative motion of tanker, hose, drogue, and receiver aircraft as per the frame assignment in Fig. 1(a) as well as the dynamic response of the hose–drogue assembly to induced contact forces. At the start of a simulation, the hose is extended to its full pay-out length of 27 m and trailed centrally behind the tanker from a fuselage-mounted refueling pod. The hose exit point on the refueling pod is defined as the tow point and located at $p = [-21.14, 0, 0.5]$ with respect to the tanker's center of gravity that also serves as the inertial reference frame in the simulation. While the receiver aircraft follows a predefined path leading to a head-on probe–drogue collision, the flight path of the tanker is assumed undisturbed and neglects any inherent tanker dynamics. This is, over the course of the maneuver, the tanker is in straight level flight at constant altitude of 8000 m with an airspeed of 200 m/s representing an ideal docking environment. Atmospheric variations, gusts, wake, and bow wave effects are not introduced to solely highlight hose–drogue perturbations arising from contact–impact phenomena.

C. RPsDT-Based Hybrid Simulation

Off-center drogue hits are among the most critical and difficult-to-predict scenarios in AAR maneuvers. While the simulations in [20] and [21] assume that coupling attempts are instantly successful, by imposing the receiver's acceleration pattern onto the drogue immediately upon contact, the RPsDT method allows the study of the entire contact phase as well as the transition to coupling if the hit results in successful docking. This will be exemplified in the following examination of a head-on probe–drogue hit just beneath the canopy at the "12 o'clock" location. The receiver aircraft contacts the drogue at a relative speed of 1.5 m/s and decelerates to zero relative speed over 0.5 s.

The induced perturbations at the drogue's center of gravity and at the ball joint are shown in Fig. 8. Due to the specimen's large structural stiffness, the drogue does not provide for much elastic behavior but predominately reacts to the initial contact event by pivoting, i.e., tipping, about the ball joint on the Y-axis. Initially, this acts to align the relative pitch of drogue and tanker, which explains the drogue movement in the negative X-direction, i.e., away from the tanker right upon contact. As this pivoting is counteracted by both the gravitational force

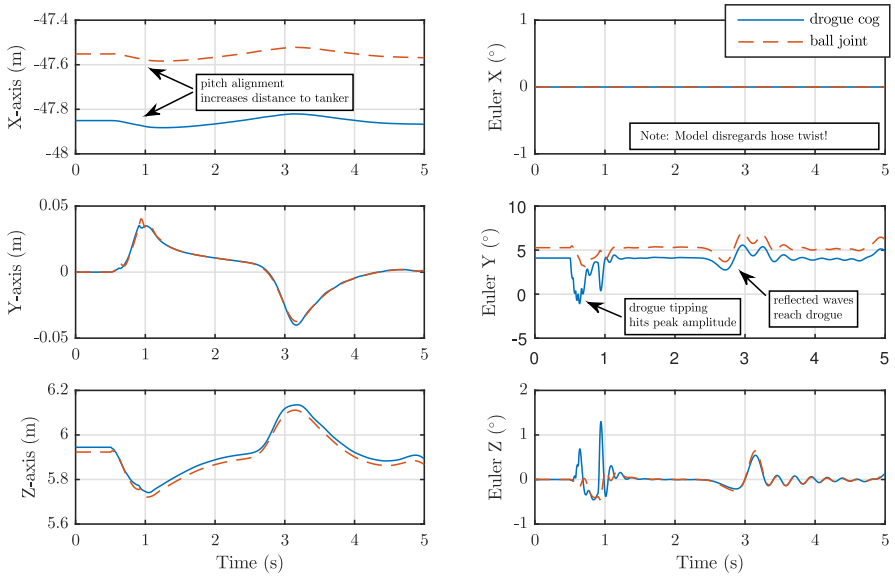

Fig. 8. Trajectory of drogue center of gravity and ball joint in a tanker reference frame.

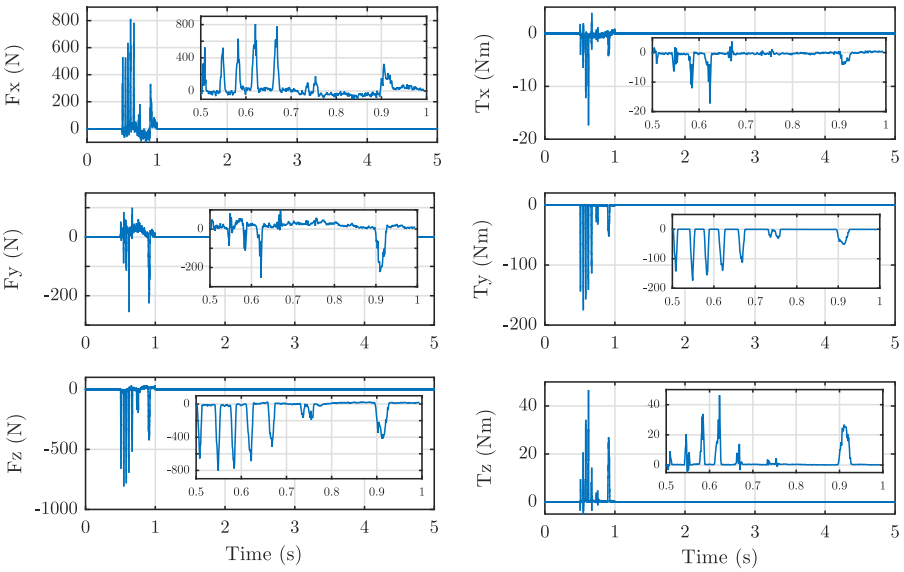

Fig. 9. Contact forces and moments in a drogue reference frame.

on the drogue and increasing aerodynamic moments, the Y-rotation reverses at a peak perturbation of about 7° to result in a rotational oscillation about the ball joint. With a minor time delay and attenuated amplitude, the ball joint follows the drogue's behavior. This is, the oscillations are also transferred onto the ball joint and further hose-upwards in the form of mechanical waves. Upon reaching the tow point, i.e., the fixed end of the hose–drogue assembly, the waves get reflected, travel down the hose, and cause a whip effect back at the drogue. Due to a viscous damping element at the ball joint, intermittent oscillations die-down quickly and make the effects of these traversing waves stand out.

The vastly discontinuous nature of the contact events becomes evident on the contact profiles in Fig. 9. Multiple losses of contact occur as the nozzle drifts increasingly toward the center of the drogue. The tipping behavior and the drogue's conical geometry contribute significantly to this. In addition, it can be noted that peak force and moments do not occur on the first impact when the relative speed is largest but on subsequent contact events instead. This is a result of the contact angle

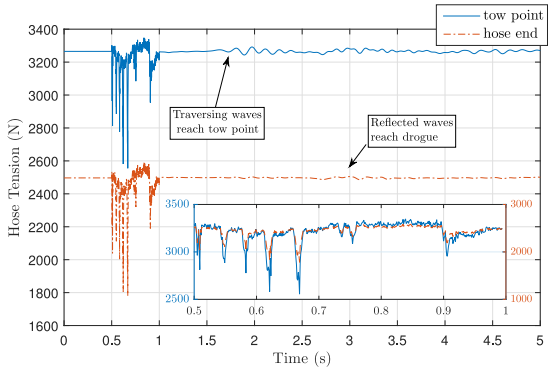

Fig. 10. Time variation of hose tension at drum exit point and hose end.

between the nozzle and the drogue that is initially steep, allowing easy slipping, but becomes increasingly more shallow as the drogue pivots. Thus, larger contact forces and moments develop at reduced relative speeds.

The induced contact forces lead to an immediate tension drop throughout the hose with following contacts resulting in further drops as the simulation progresses (see Fig. 10). At the same time, the initiation of low-frequency oscillation is recorded in the tension profiles. This is a consequence of the initial drogue rotation about the ball joint that triggers the traversing waves. While the ball-joint dampens the tension fluctuations and the aerodynamic forces and moments act to restraighten the hose–drogue assembly, the initiated waves cause persistent fluctuations as the they travel up and down the hose. In particular, prominent oscillations occur in between 2.1 and 2.6 s when the waves reach the fixed end of the hose and in between 3.2 and 3.9 s when the reflected waves cause hose whip back at the drogue.

V. Conclusion

This paper has demonstrated the feasibility of studying contact–impact problems in hybrid tests using off-the-shelf industrial robots with the robotic pseudodynamic method (RPsDT), validated both the methodology and the system architecture, and demonstrated the first hybrid simulation of docking maneuvers in AAR. The RPsDT method circumvents shortcomings in the robot response time for dynamic testing and has laid the foundation for integration of contact events into full-scale AAR simulations.

An easily reproducible validation test has shown the ability of the method to account for important nonrate-dependent effects throughout contact events including the capture of nonlinear hysteric damping characteristics. Limitations were identified to arise from the neglect of rate- and time-dependent effects, in particular those of viscous damping and creep. Shortcomings that can be addressed through improved test design have been highlighted, including the mitigation of creep effects for which careful scrutiny of results must be applied.

The RPsDT study of probe–drogue contact–impact scenarios yielded results that compared qualitatively well to phenomena known to occur in AAR maneuvers. Especially, the capture of the discontinuous contact-force profiles and drogue tipping effects that trigger much of the prominent postcontact dynamics of the hose–drogue assembly have promising implications for further investigations using the RPsDT method. Full-scale tests of more complex AAR scenarios are anticipated as future work and expected to provide further insight into the contact and postcontact behavior of the hose–drogue assembly.

References

[1] P. R. Thomas, U. Bhandari, S. Bullock, T. S. Richardson, and J. L. du Bois, "Advances in air to air refuelling," *Prog. Aerosp. Sci.*, vol. 71, pp. 14–35, Jul. 2014.

[2] J. L. duBois, P. R. Thomas, and T. S. Richardson, "Development of a relative motion facility for simulations of autonomous air to air refuelling," in *Proc. IEEE Aerosp. Conf.*, Big Sky, MT, USA, Mar. 2012, pp. 1–12.

[3] O. Ma, A. Flores-Abad, and T. Boge, "Use of industrial robots for hardware-in-the-loop simulation of satellite rendezvous and docking," *Acta Astronaut.*, vol. 81, no. 1, pp. 335–347, 2012.

[4] N. Hogan, "Impedance control: An approach to manipulation," in *Proc. IEEE Amer. Control Conf.*, 1984, pp. 304–313.

[5] R. Ortega, A. J. Van Der Schaft, I. Mareels, and B. Maschke, "Putting energy back in control," *IEEE Control Syst.*, vol. 21, no. 2, pp. 18–33, Apr. 2001.

[6] A. De Luca, "Feedforward/feedback laws for the control of flexible robots," in *Proc. IEEE Int. Conf. Robot. Autom.*, 2000, vol. 1, pp. 233–240.

[7] R. Krenn and B. Schaefer, "Limitations of hardware-in-the-loop simulations of space robotics dynamics using industrial robots," *Eur. Space Agency Publ.*, vol. 440, pp. 681–686, 1999.

[8] M. I. Wallace, D. J. Wagg, and S. A. Neild, "An adaptive polynomial based forward prediction algorithm for multi-actuator real-time dynamic substructuring," in *Proc. Roy. Soc. A, Math., Phys. Eng. Sci.*, vol. 461, no. 2064, 2005, p. 3807.

[9] T. Horiuchi, M. Inoue, T. Konno, and Y. Namita, "Real-time hybrid experimental system with actuator delay compensation and its application to a piping system with energy absorber," *Earthquake Eng. Struct. Dyn.*, vol. 28, no. 10, pp. 1121–1141, 1999.

[10] D. P. Stoten, G. Li, and J.-Y. Tu, "Model predictive control of dynamically substructured systems with application to a servohydraulically actuated mechanical plant," *IET Control Theory Appl.*, vol. 4, no. 2, pp. 253–264, Feb. 2010.

[11] A. Blomdell, I. Dressler, K. Nilsson, and A. Robertsson, "Flexible application development and high-performance motion control based on external sensing and reconfiguration of ABB industrial robot controllers," in *Proc. IEEE Int. Conf. Robot. Autom.*, 2010, pp. 62–66.

[12] J. L. du Bois, P. Thomas, S. Bullock, U. Bhandari, and T. Richardson, "Control methodologies for relative motion reproduction in a robotic hybrid test simulation of aerial refuelling," in *Proc. AIAA Guid., Navigat., Control Conf.*, Minneapolis, MN, USA, 2012, pp. 4676–4696.

[13] C. Martínez, T. Richardson, P. Thomas, J. L. duBois, and P. Campoy, "A vision-based strategy for autonomous aerial refueling tasks," *Robot. Auton. Syst.*, vol. 61, no. 8, pp. 876–895, Aug. 2013.

[14] J. L. du Bois, "A strategy for improving performance in real time hybrid testing," in *Dynamics of Civil Structures*, vol. 4. New York, NY, USA: Springer, 2014, pp. 219–225.

[15] M. Bolien, P. Iravani, and J. L. du Bois, "Robotic pseudo-dynamic testing (RPsDT) of contact-impact scenarios," in *Towards Autonomous Robotic Systems*. New York, NY, USA: Springer, 2015, pp. 50–55.

[16] S. A. Mahin and P.-S. B. Shing, "Pseudodynamic method for seismic testing," *J. Struct. Eng.*, vol. 111, no. 7, pp. 1482–1503, 1985.

[17] M. S. Williams and A. Blakeborough, "Laboratory testing of structures under dynamic loads: An introductory review," *Philosoph. Trans., Math., Phys. Eng. Sci.*, vol. 359, no. 1786, pp. 1651–1669, 2001.

[18] M. Geravand, F. Flacco, and A. De Luca, "Human-robot physical interaction and collaboration using an industrial robot with a closed control architecture," in *Proc. IEEE Int. Conf. Robot. Autom.*, 2013, pp. 4000–4007.

[19] K. Shoemake, "Animating rotation with quaternion curves," *ACM SIGGRAPH Comput. Graph.*, vol. 19, pp. 245–254, 1985.
[20] K. Ro, T. Kuk, and J. W. Kamman, "Dynamics and control of hose-drogue refueling systems during coupling," *J. Guid., Control, Dyn.*, vol. 34, no. 6, pp. 1694–1708, 2011.
[21] J. C. Vassberg, D. T. Yeh, A. J. Blair, and J. M. Evert, "Numerical simulations of KC-10 wing-mount aerial refueling hose-drogue dynamics with a reel take-up system," in *Proc. 21st Appl. Aerodyn. Conf.*, Orlando, FL, USA, 2003, vol. 26, pp. 3508–3529.

Mario Bolien received the M.Eng. degree in mechanical engineering from the University of Bath, Bath, U.K., in 2013, where he is working toward the doctoral degree.

He is an Honorary Research Associate with the University of Bristol, Bristol, U.K. He has a vast interest in the design, simulation, analysis, and control of multidomain dynamic systems. His research focuses on the development of methods and techniques for the mechanical hybrid testing of highly nonlinear and discontinuous systems, and has direct industrial relevance for the on-ground assessment of aerial refuelling hardware.

Pejman Iravani received the undergraduate degree in electrical engineering from the Universitat de Girona, Girona, Spain, in 2001, and the Ph.D. degree in distributed robot control from Open University, Milton Keynes, U.K., in 2005.

He is a Lecturer (Assistant Professor) with the Department of Mechanical Engineering, University of Bath, Bath, U.K. His research interests include robotics and autonomous systems.

Jonathan Luke du Bois received the undergraduate degree in aeronautical engineering from the University of Bristol, Bristol, U.K., in 2002, and the doctoral degree in adaptive fuselage response suppression from the Deptartment of Aerospace Engineering, University of Bristol, Bristol, U.K., in 2009.

He is a Lecturer (Assistant Professor) specializing in dynamics and control for aerospace systems with the University of Bath, Bath, U.K. He worked at the University of California, San Diego, CA, USA, before joining the University of Bath.

Chapter 5

Full-Scale Tests

This chapter outlines comprehensive experimental studies of the probe-drogue contact and coupling phase conducted at the RMR and features the major contributions of the candidate's experimental work. Once more, this chapter is publication-based, comprising a journal paper published with the *AIAA Journal of Aircraft*.

The first part of the manuscript details independent contact tests that are performed with full-scale industrial refuelling hardware and compared with an RPsDT reproduction to provide a further validation basis for the technique in addition to that established in Chapter 4. The results of the validation tests show a good agreement between the pseudo-dynamic and full speed data and reveal that dominant contact response characteristics can be reproduced with high repeatability as well as low sensitivity to parameter perturbations using the RPsDT method. Moreover, it is found that strain measurements taken at the drogue ribs throughout the tests are a useful tool to record characteristic contact loading patterns for off-centre hits which can serve as guidelines in the structural hardware design. Supplementary information about the validation tests, including the test setup, instrumentation, RPsDT model generation and parameter tuning are found in Appendix C.

Building upon the successful validation, the paper extends the study to the investigation of a complete AAR scenario under simulation based emulation of a flight environment. Predictions for the operational contact and coupling behaviour in response to off-centre drogue hits are made and estimates for the contact forces provided. As in the preliminary tests presented in Chapter 4, the predicted refuelling hardware behaviour shows a great level of qualitative agreement with hardware behaviour reported in flight tests and operation.

5.1 Hybrid Tests of Contact Events in Air-to-Air Refuelling

Article in Advance. Published by *AIAA Journal of Aircraft* on April 30, 2018.

Mario Bolien, Pejman Iravani, Jonathan L. du Bois, Tom Richardson, and Anders Robertsson. "Hybrid Tests of Contact Events in Air-to-Air Refueling", AIAA Journal of Aircraft, 2018. DOI: https://doi.org/10.2514/1.C034830

Statement of Contribution for Joint Authorship

M. Bolien (candidate): development and implementation of methodology; experimental work; data analysis; preparation of tables and figures; writing and compilation of manuscript.

P. Iravani (second supervisor): supervision of method development, implementation and experimental work; review of manuscript.

T. Richardson (co-author): provision of test facility; review of manuscript.

A. Robertsson (co-author): provision of low level software components for IRC5 controller augmentation; review of manuscript.

J.L. du Bois (lead supervisor): supervision of method development, implementation and experimental work; review and editing of manuscript.

Copyright

Hybrid Tests of Contact Events in Air-to-Air Refueling

Mario Bolien,* Pejman Iravani,† and Jonathan L. du Bois‡
University of Bath, Bath, England BA2 7AY, United Kingdom
Tom Richardson§
University of Bristol, Bristol, England BS8 1TR, United Kingdom
and
Anders Robertsson¶
Lund University, SE-221 00 Lund, Sweden

DOI: 10.2514/1.C034830

Air-to-air refueling is a vital technique for extending the range and endurance of manned or unmanned aircraft, with over 1000 refueling procedures flown per day in military operations. The hardware used for air-to-air refueling needs to be tailored to the specific aircraft and airspeeds involved, performing markedly different for permutations of tanker and receiver craft. Extensive flight testing is costly and risky to equipment and personnel, but laboratory testing is marred by unrepresentative test conditions. This Paper presents the first full-scale hybrid test of an air-to-air refueling probe and drogue contact, where physical refueling hardware in the laboratory is coupled to a numerical simulation of the remainder of the system using sensors and actuators. It is found that the forces and motion trajectories faithfully capture the characteristic drogue response dynamics in full refueling scenarios. Rigorous validation shows that the method can emulate the dominant contact–impact phenomena observed in air-to-air refueling scenarios with high repeatability, including problematic design-critical responses such as drogue tipping and hose whip. With the costs of equipping a tanker fleet standing around 500 million, the technique offers an important means of laboratory testing to inform design iterations, reducing development timescales and costs, as well as improving safety and reliability before flight testing.

I. Introduction

AIR-TO-AIR refueling (AAR) is the process of in-flight fuel transfer between aircraft with the primary aim of increasing the receiver aircraft's range and endurance. It forms a vital part of defense infrastructure and can offer substantial fuel efficiency gains in the civil sector. During Operation Desert Storm, an average of 1061 U.S. Air Force aircraft were refueled with AAR per day [1]. Fuel consumption reductions of 30–40% in civil transportation are thought to be achievable using AAR [2]. The technique is increasingly important for unmanned aircraft systems (UASs), which are likely to be tasked with more long-endurance operations and risky refueling operations than manned aircraft, with projections of a total commercial UAS fleet size of around 422,000 by 2021 [3]. Recent cost estimates for equipping 100 KC-135 aircraft with existing multipoint refueling systems stood at 510 million U.S. dollars (USD) [4]. Despite AAR being a mature technology, new hardware designs are regularly needed for different aircraft configurations, and techniques for the on-ground validation and preflight verification of AAR docking maneuvers are subject to continuous improvements. Flight testing is costly, with a single flight test in the region of 65,000 USD, and risky for test pilots and equipment. Thorough preoperational testing can mitigate risks at early design stages, expedite development cycles, and ensure hardware and systems safety before initial flight testing. In addition, with the focus rapidly shifting from manned to unmanned aviation, well-designed preflight tests can aid in demonstrating UAS technology readiness, thereby providing a certification pathway for the opening of nonsegregated airspace to unmanned aerial vehicles (UAVs).

Among the most critical parts of an AAR maneuver is the contact phase: In close-proximity flight, the pilot of the receiver aircraft attempts to engage the nozzle located at the end of the receiver's probe with a drogue that is trailed behind the tanker aircraft on a hose. Successful docking requires a central drogue hit at a relative speed of about 1.5 m/s [5]. This triggers a mechanical latch in the reception coupling that retains the nozzle, opens fuel valves on either side, and allows the offloading of fuel to commence. However, the entire maneuver is complicated by the dynamics in the hookup space, where the combined effects of tanker wake, receiver bow wave, wind gusts, and atmospheric disturbances constantly act to perturb the drogue's position behind the tanker. This frequently results in missed attempts or offcenter hits, which can expose equipment and personnel to large risks. At the same time, the complexity of both the flight regime and the contact–impact mechanics makes the design of reliable preflight testing methods a particularly difficult job.

Substantial advances have been made in the numerical analysis and simulation of probe–hose–drogue systems. Widely cited studies such as [6–9] represented the hose as a towed and tethered cable system in finite element/lumped parameter form where nodal excitement accounted for structural and aerodynamic forces and was calculated according to the particular hose configuration and flight regime. To this end, effects could be individually examined, identified, and described [for example, based on lookup tables from wind-tunnel tests for drag coefficients and aeromoments or (simplified) structural analysis for hose bending], providing a highly modular simulation environment. Although such approaches enable the investigation of the free- and postcoupling dynamics of the hose–drogue assembly, by assuming instantly successful drogue capture (i.e., immediately constraining the hose end to the motion profile of the receiver aircraft upon contact), the critical contact and coupling phase is inherently disregarded.

A major reason for the absence of reliable models of the contact and coupling phase is the sheer complexity, which can render numerical modeling inaccurate or infeasible. Contact–impact dynamics are heavily influenced by a variety of factors including surface shapes and geometries, incidence strike angles, material properties, and impact velocity [10], which determine if the contact scenario following an offcenter hit is governed by slip of the probe toward the drogue's center, contact losses and discontinuous impacts, drogue tipping, penetration of the nozzle beyond the drogue ribs, or combinations of these. To date, numerical contact models rely on extensive simplifications and suffer

Received 14 November 2017; revision received 2 March 2018; accepted for publication 8 March 2018; published online 30 April 2018.

*Doctoral Candidate, Mechanical Engineering.
†Senior Lecturer, Mechanical Engineering.
‡Lecturer, Mechanical Engineering.
§Senior Lecturer, Aerospace Engineering.
¶Professor, Department of Automatic Control, Box 118.

from parameter uncertainties that make experimental validation imperative. In contrast, complete experimental studies including a realistic laboratory reproduction of a full flight environment have been logistically infeasible for technical and financial reasons.

From these observations follows the motivation to study the contact and coupling phase in AAR maneuvers as part of a mechanical hybrid test that can benefit from the respective advantages of both numerical modeling and experimental testing. Full-scale physical probe and drogue refueling hardware is manipulated by robotic actuators, which are coupled to a numerical simulation of the full flight environment. Forces and displacements at the interface between the numerical and physical substructures are continuously interchanged at each time step using sensors and actuators.

The aim of this work is to determine the efficacy of hybrid tests in providing reliable simulation of the coupling phase of an AAR operation, thereby informing design iterations and reducing cost and risk before flight testing. The Paper proceeds first with an overview of the newly created robotic hybrid testing framework in Sec. II. Section III presents the method and results for a validation study, which are used to quantify the extent to which hybrid tests can reproduce the results of a complete experiment. Information on repeatability and parameter sensitivity is also presented here. Section IV describes the hybrid testing of AAR docking maneuvers in a fully representative refueling environment, and it evaluates the ability of the method to discern thresholds for critical dynamic phenomena observed in AAR maneuvers. Conclusions are drawn in Sec. V.

II. Hybrid Testing Framework for AAR Operations

(Robot-assisted) hybrid tests have received much recent attention for the preoperational testing of complex systems. Examples range from verification tests of sensor and flight controllers in the precontact phase of refueling operations for UAVs [11–13] to (on-ground) tests of satellite docking maneuvers in zero-gravity conditions [14]. Similar to hardware-in-the-Loop tests for electronic components, hybrid tests physically embed a critical mechanical substructure of a system into a simulation loop to provide high-confidence predictions of the combined dynamic behavior. To this end, the numerical simulation and physical substructure are coupled by a transfer system composed of actuators and sensors, allowing the division of individual system parts into a physical and a numerical domain to be performed according to the 1) component criticality, 2) ease of modeling, as well as 3) logistics and financial constraints for a laboratory reproduction [15].

Here, hybrid tests of the contact and coupling phase in AAR maneuvers are presented on the basis of the framework depicted in Fig. 1. Industrial robots equipped with six-degree-of-freedom force/torque sensors and full-scale refueling hardware are used as a transfer system to couple a numerical simulation of a complete flight regime with experimental tests of probe–drogue contact scenarios. This permits the prediction of the dynamics of the complete system in realistic operating conditions. To this end, the numerical side contains simulations of the hose–drogue assembly and aerodynamics based on work presented in [8,11], whereas the robots reproduce the relative motion of the probe and drogue in each simulation step and feedback contact force measurements to close the loop. From a system design and operation perspective, the test setup exhibits a strict hierarchical order where the robots function as slave devices to a superior master simulation. This type of architecture enables the simulation side to take full control over the robot motion execution, helping to seamlessly embed the experimental contact test into the simulation loop of an AAR maneuver. As the simulation proceeds, this ensures that its states become a function of both numerically modeled and experimentally measured data.

The chosen division of system parts and components into numerical and experimental substructures (shown in Fig. 1) reflects our argument from Sec. I that the most severe deficiencies lie in the modeling and simulation of the contact dynamics. Consequently, these have to be studied experimentally, whereas reliable models have been developed and validated for the continuum dynamics of the remainder of the system in previous work and can be included in simulation. The advantages of this hybrid approach over alternative methods for preoperational testing are substantial: 1) Forces and moments that develop throughout the contact and coupling phases are based on direct measurements, obviating the need for simplified assumptions in numeric simulations while 2) eliminating the need for the implementation of contact models with uncertain parameters and 3) enabling the investigation of realistic hits and drogue reactions. Hence, diverse scenarios including offcenter hits and missed attempts can be studied quickly and inexpensively in a controlled laboratory environment without putting equipment or personnel at significant risk.

A common problem with hybrid testing approaches is that the transfer system itself inevitably introduces its own inherent dynamics into the simulation loop, which is typically manifested as lags, delays, and noise [16,17]. Given that the robots can never react satisfactorily within the bandwidth required for stiff and fast contact–impact scenarios that are common in AAR, here, the hybrid tests are realized based on the robotic pseudodynamic testing (RPSDT) method [18]. To this end, the robots impose the relative motion of the probe and drogue pseudodynamically, i.e., on an enlarged timescale that circumvents any problems due to actuator response times.

By design, the RPSDT method sets stringent requirements for the execution of the relative motion of the probe and drogue throughout the

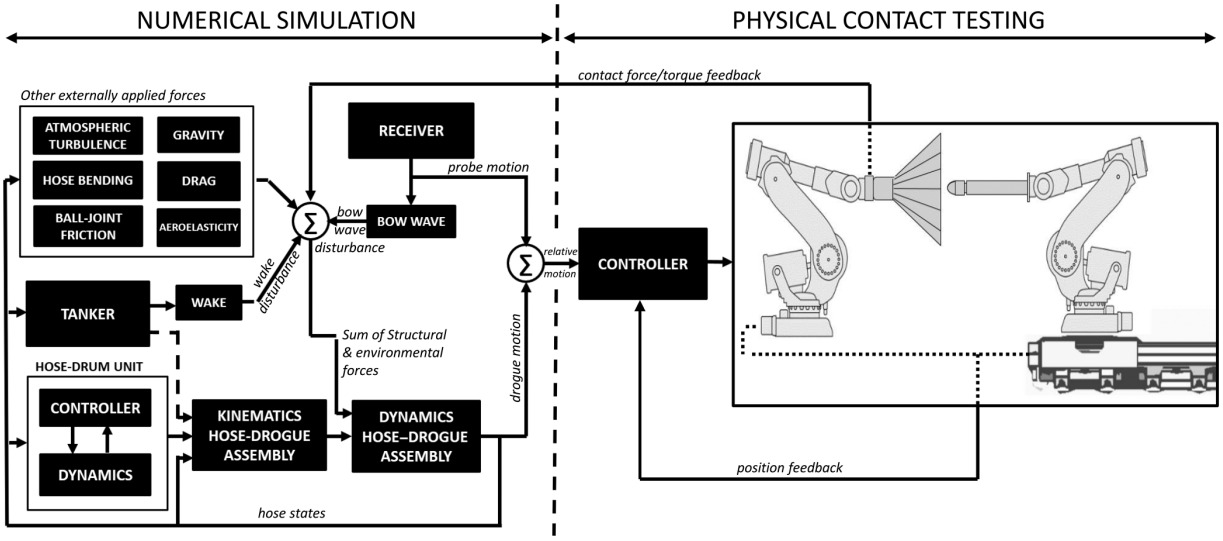

Fig. 1 Hybrid testing framework for AAR contact scenarios and proposed system division.

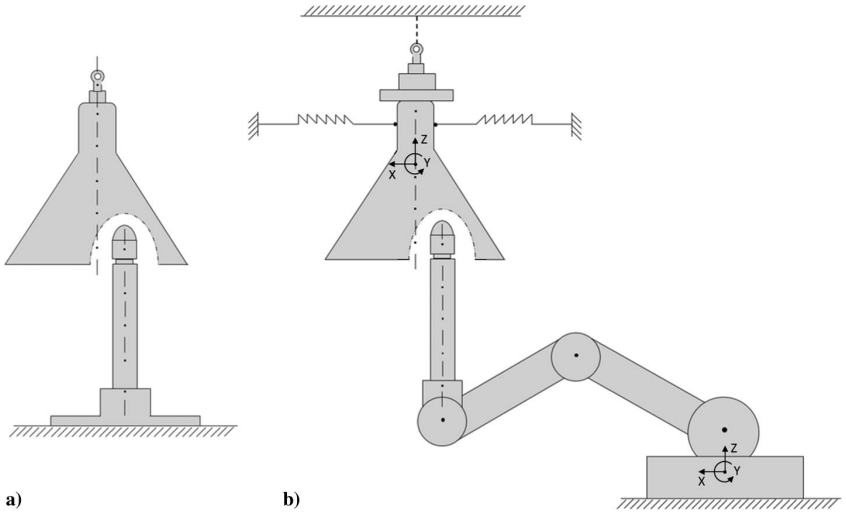

a) b)

Fig. 2 Validation test setup: a) configuration as per MIL-PRF-81975C [25], and b) modified configuration.

contact and coupling phase. These include 1) the precisely timed execution of bespoke trajectories with spherical linear-interpolation-based [19] orientation interpolation to guarantee that the Cartesian space manipulation occurs along the shortest path between original and target poses [18], 2) external force sensing, and 3) integration with a simulation environment: all of which are nontrivial to achieve with modern industrial robots that rely on closed systems with proprietary architectures. Here, the necessary level of control and freedom in application development are attained through augmentation of a conventional ABB IRC5 system to provide an external real-time extension for low-level application deployment with direct access to the IRC5 axis controller [20]. To this end, an additional task is spawned on the VXworks system of the IRC5 main computer with callbacks installed to 1) retrieve and forward current arm states (i.e., motor angles, velocities, torques, etc.) for processing to an external real-time target via a real-time Ethernet connection, 2) receive a reply with modified states from the real-time target within a 1 ms window, and 3) set the modified states as new reference commands for the axis controller. Purposely, the external real-time target takes the form of a Linux machine that gains the relevant real-time capabilities on the basis of the Xenomai[**]/I-pipe patch [21,22] and RTnet driver framework [23]. The external control application is then implemented and run as a kernel task for which a tool chain described in [20,24] aides with the cross compilation and dynamic linking in the deployment process directly from Simulink. Applying the RPSDT technique in this way provides inherent loop stability for the hybrid test at the expense of loosing rate-dependent effects in the feedback force measurements; the implications of this for probe–drogue contact scenarios are examined in the validation experiments in Sec. III.

III. Hybrid Test Validation Studies

Independent validation of the fundamental techniques involved in hybrid testing is crucial to demonstrate reliability of the results. Because the motivation for a hybrid test typically lies in the difficulty of reproducing a complete system with traditional experimental or modeling approaches, separate validation tests have to be devised on an individual basis that allow conclusions to be drawn about the trustworthiness and accuracy with which the hybrid tests can reproduce a particular scenario under a given set of conditions. This should be seen as a mandatory precursor to applying the technique to more complex scenarios. For such validation tests to be reliable, they have to make use of identical hardware specimens under representative conditions but in a way that allows full experimental test reproduction. The numerical part of the simulation must be reproduced in a physical embodiment in the laboratory to allow comparisons between the hybrid test results and those of the complete physical system.

A. Validation Method

Here, a validation test on the basis of the long-established drop test apparatus is proposed, which is used according to MIL-PRF-81975C [25] for impact and endurance testing of aerial refueling equipment in industry. The standard test (Fig. 2a) involves suspending a drogue above a nozzle, with both vertically aligned, and releasing the drogue such that it falls under gravity to make contact with the nozzle. By contrast, in the modified test (Fig. 2b), the drogue remains vertically suspended and is additionally weighed down by a reaction mass and elastically retained by horizontally spanned bungee cord. The refueling probe is rigidly mounted to the robot end effector and is accelerated toward the drogue to strike at a specified angle, speed, and radial position from the drogue's axis of symmetry. Using this setup, validation of the RPSDT-based hybrid testing method for offcenter drogue hits follows a four-step process:

1) Strikes at the same contact point located 150 mm radially outward from the drogue's line of symmetry are performed at full speed (i.e., non-pseudodynamic) for incidence angles in the range from 0 to 35 deg in increments of 5 deg and relative contact speeds in the range from 250 to 1000 mm/s in increments of 250 mm/s, repeated 12 times for each combination of angle and speed, resulting in a total of 384 experiments. Note that the highest contact speed of 1000 mm/s that corresponds to the lower end of the operational regime contact scenarios is AAR, which typically take place at a relative speed of 1000–3000 mm/s. Throughout the contact tests, a three-dimensional (3-D) tracking system records the position of the drogue and bungees, whereas the radial and lateral strains developing in the drogue ribs (representative of bending and flexure) are monitored with a bespoke data acquisition system.

2) The entire rig is modeled using a bond-graph approach. To this end, the inertias and center of gravity of the drogue and reaction mass assembly, as well as the bungee cord stiffness characteristics, are experimentally identified in separate tests. The rig geometry, including bungee attachment points, is measured with the 3-D tracking systems and related to a frame of reference that is common with the robot.

3) By releasing the drogue from different initial conditions and recording its swing phase both with and without bungee attachments, a constraint parameter optimization is used to fine tune the inertia and stiffness estimates from step 2 and introduce damping elements to account for structural hysteresis in the bungee cords as well as friction at the rope attachment point so as to minimize the Euclidean error norm between the experimental and modeled swing phase trajectories.

**Data available online at https://xenomai.org/ [retrieved 2018].

4) The contact scenarios of step 1 are then reproduced in a hybrid test based on the RPSDT method: In each simulation step, the robots replicate the relative motion of the probe and drogue quasi statically, as per the original robot trajectory of step 1 (same motion profiles, contact points, and strike angles). The measured restoring forces and torques are fed back to the simulation of the rig developed in steps 2 and 3 and are applied to the simulated drogue as an external force input. Subsequent stepwise integration of these experimental force inputs (every 0.5 ms in pseudotime) yields new drogue states that, in combination with the known nozzle trajectories, determine the next relative positions of the probe and drogue to be reproduced by the robots. The hybrid tests proceed in this way, thus covering a single contact reproduction on an expanded timescale of roughly 240 min.

Note that the test setup presented here has been designed for the purpose of validating the application of the RPSDT method to the study of contact scenarios with full-scale refueling hardware, keeping in mind the ease of model construction for use in the numerical substructure. This is to say, the presented validation tests are neither aimed at an accurate emulation of in-flight conditions nor intended to represent a direct improvement to the endurance test. As such, the setup has been kept simple, with only three bungee cords fitted approximately 120 deg apart; this adds to the nonlinearity and introduces sufficient damping to suppress slowly decaying pendulumlike oscillations upon contact.

B. Validation Results

Examples of drogue trajectories from full-speed tests (i.e., not pseudodynamic) for contact speeds of 1000 mm/s and shallow, moderate, and steep strike angles of 0, 15, and 35 deg (denoted V1000A0, V1000A15, and V1000A35, respectively) measured against the drogue's line of symmetry are shown in Fig. 3. Here, the drogue's mean position and orientation perturbations (based on 12 repetitions) are plotted with reference to the steady-state pose, including lower and upper bounds (dotted lines) corresponding to one standard deviation. With reference to the frame assignment in Fig. 2b, note that 1) the drogue's origin is coincident with the its center of gravity (COG), 2) its Z ordinate complies with the axis of symmetry (pointing vertically upward to the anchor point along the line of suspension), 3) the X ordinate has been defined to extend forward in the direction of the bungee cord that is farthest displaced from the robot base, and 4) the Y ordinate follows from the right-hand rule by convention. High levels of repeatability can be reported for the full-speed contact tests, with mean Euclidean and mean rotational standard deviations of 1.1 mm and 0.32 deg, respectively, for the cases shown.

One of the advantages of hybrid testing is the scope it offers for a large amount of instrumentation to be applied to test specimens. In the case of AAR, the rib strain measurements are of great interest in understanding the loading in the specimen during an AAR procedure. This instrumentation is difficult to apply in flight tests and is a key advantage of hybrid testing. It is important that this information is reliable and repeatable. This can be evaluated in Fig. 4. Salient profiles and features in the time variation of strains induced into individual drogue ribs (Figs. 4a/4b) and characteristic peak strain patterns formed by the spatial strain distribution across the basket (Figs. 4c/4d) can be observed. As before, the data reveal high levels of repeatability. Again, mean values have been computed from 12 repetitions and the standard deviation averages 13.3 μStrain across all data points for both the radial and lateral strains measured by the top and side gauges, respectively. Corresponding lower and upper bounds are given by the dotted lines in Figs. 4a/4b. Here, Fig. 4a shows the mean strain induced in one of the two drogue ribs that is directly hit by the nozzle at a speed of 1000 mm/s and a strike angle of 35 deg. As a result, the rib bends radially outward about the anchor point, thus distorting the originally circular shape of the basket into an oval shape. Figure 4b shows the lateral strains that are simultaneously induced into a rib approximately located at a 90 deg offset from the struck position on the drogue circumference (see 270 deg location in Fig. 4d). Evidently, the circumferential distortion of the basket causes

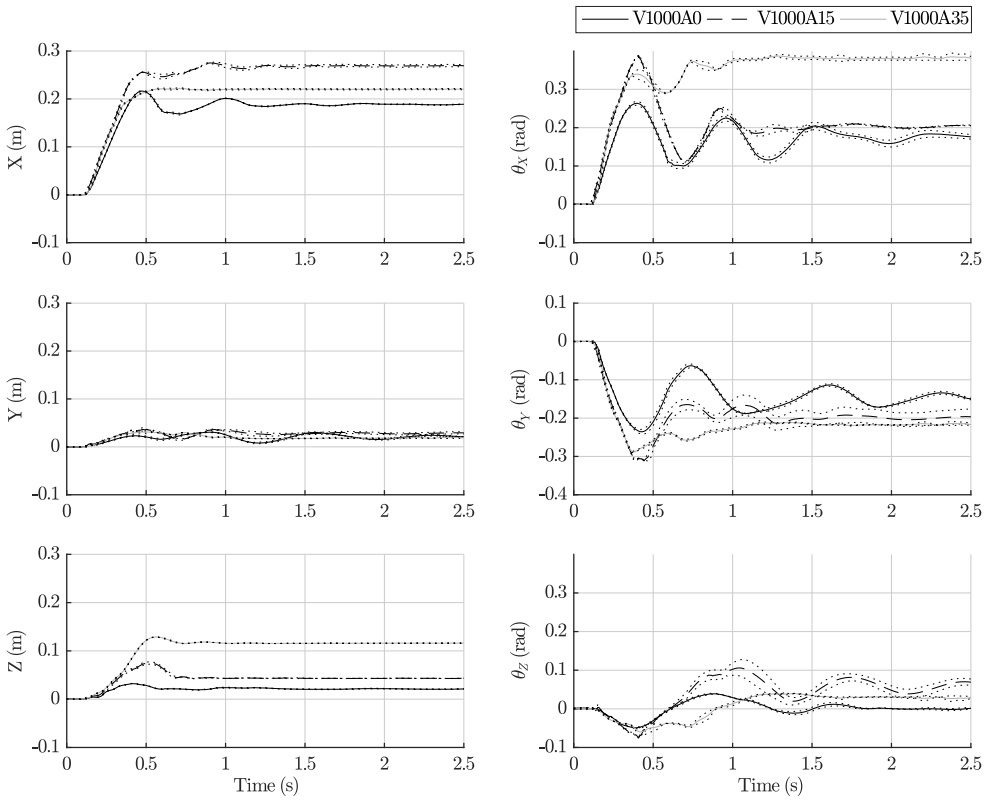

Fig. 3 Drogue position and rotation perturbations.

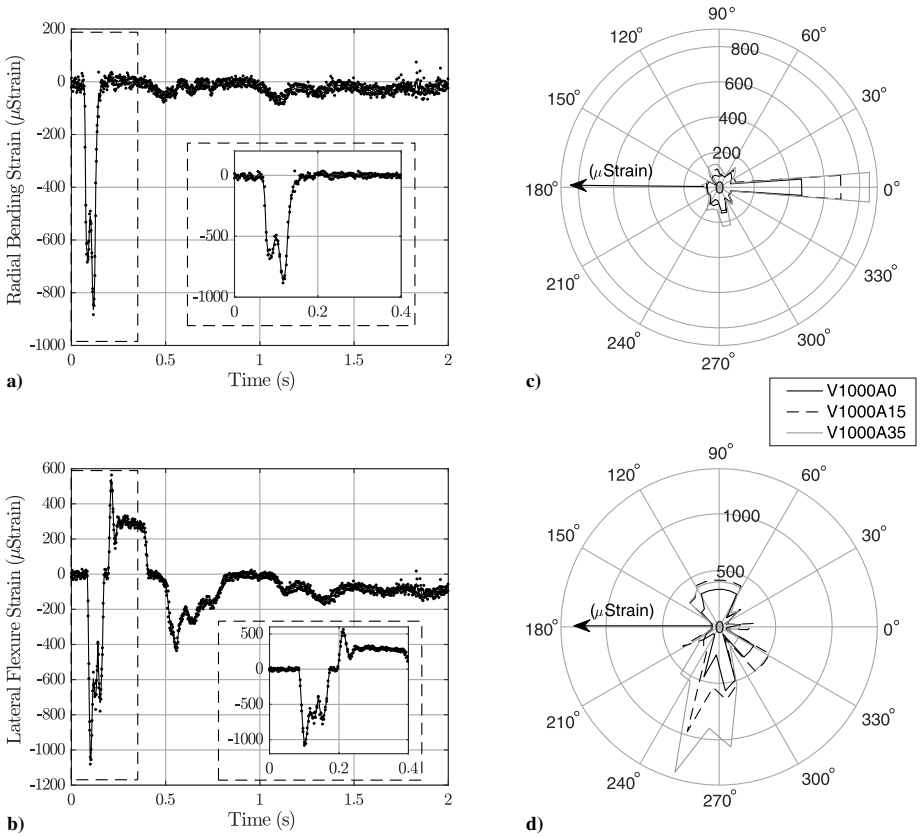

Fig. 4 Induced strain profiles and peak strain patterns.

large lateral strains to develop as the rib is forced to flex sideways (i.e., perpendicular to the hinge) and effectively remains cantilevered at the anchor point.

The average peak strains for all 32 ribs are shown in Figs. 4c and 4d for radial bending and lateral flexure, respectively. The struck rib position on the drogue circumference is shown as the 0 deg location where the radial strains have the most dominant components. By contrast, prevailing lateral strain components are clearly offset by 90 deg from the contact position for the reasons discussed previously. In addition, it is evident that both radial and lateral strains increase at larger incidence strike angles (0, 15, 35 deg). Together with the individual strain profiles exemplified in Figs. 4a and 4b, the data enable immediate deductions to be made about radial and circumferential contact load distributions across the basket and can inform structural considerations regarding the rib, anchor point, and canopy design.

The aforementioned full-speed contact scenarios have been replicated using RPSDT methods, and a comparison of contact perturbations and corresponding frequency spectra for the most extreme contact scenario of 1000 m/s and 35 deg is presented in Fig. 5. Note that 1) twist θ_Z about the drogue's axis of symmetry is not considered in the rig model in the numerical substructure; and 2) the RPSDT-based contact reproduction for the scenarios shown amounts to an experimental time in excess of 3 h, whereas here, all RPSDT data are plotted against the equivalent pseudotime. Due to the long experimental time for a single test, the RPSDT data are based on only four repetitions; however, high repeatability has been shown and mean standard deviations of 0.9 mm and 0.15 deg could be computed as indicative values for the positional and rotational axes, respectively. Furthermore, it is shown that the RPSDT method clearly reproduces the dominant contact–impact phenomena in the perturbation profiles, both in terms of position and Euler angle variations. This is true for all prevailing motion axes. Steady-state offsets in the settled positions of the drogue can be attributed to uncertainties in the underlying numeric model of the rig. Further discrepancies arise as expected from the neglect of rate-dependent effects in the RPSDT contact force feedback measurements due to the structural excitation being quasi static in nature. The latter effects are primarily manifested in a more oscillatory (i.e., less damped) response in the RPSDT data. This is reflected in the frequency spectra, where the RPSDT data have a lower attenuation level across the entire bandwidth, implying less energy dissipation as compared with the full-speed tests.

The discontinuous nature of the contact events becomes evident on the RPSDT force profiles in Fig. 6. Multiple losses of contact occur as the nozzle drifts increasingly toward the center of the drogue. The drogue's rotational response and conical geometry contribute significantly to this effect. Forces and moments reach nominal peak values of 1350 N on the Z axis and 340 N · m about the X axis, respectively. It can be noted that these peaks do not occur on first impact when the relative speed is largest but on subsequent contact events instead. This is a result of the contact angle between nozzle and drogue that is initially steep, allowing easy slipping, but becomes increasingly more shallow as the drogue tips. Thus, larger contact forces and moments develop at reduced relative speeds. Once more, high levels of repeatability can be confirmed with standard deviations on force and torque data averaging 20.52 N and 6.26 N · m, respectively.

The sensitivity to parameter variations for RPSDT has been assessed experimentally by perturbing both the contact position and the strike angle by 1 cm and 1 deg, respectively. As such, the nozzle contacts the ribs at a point radially further offset from the drogue's line of symmetry (160 mm instead of 150 mm) in the first run while making contact at the original location but following a steeper strike angle of 36 deg in the second run. As shown in Fig. 7, low sensitivity to changes in these parameters can be reported. Thus, it may be concluded that small inaccuracies and uncertainties introduced by the transfer system (robot positioning accuracy, repeatability, etc.) and

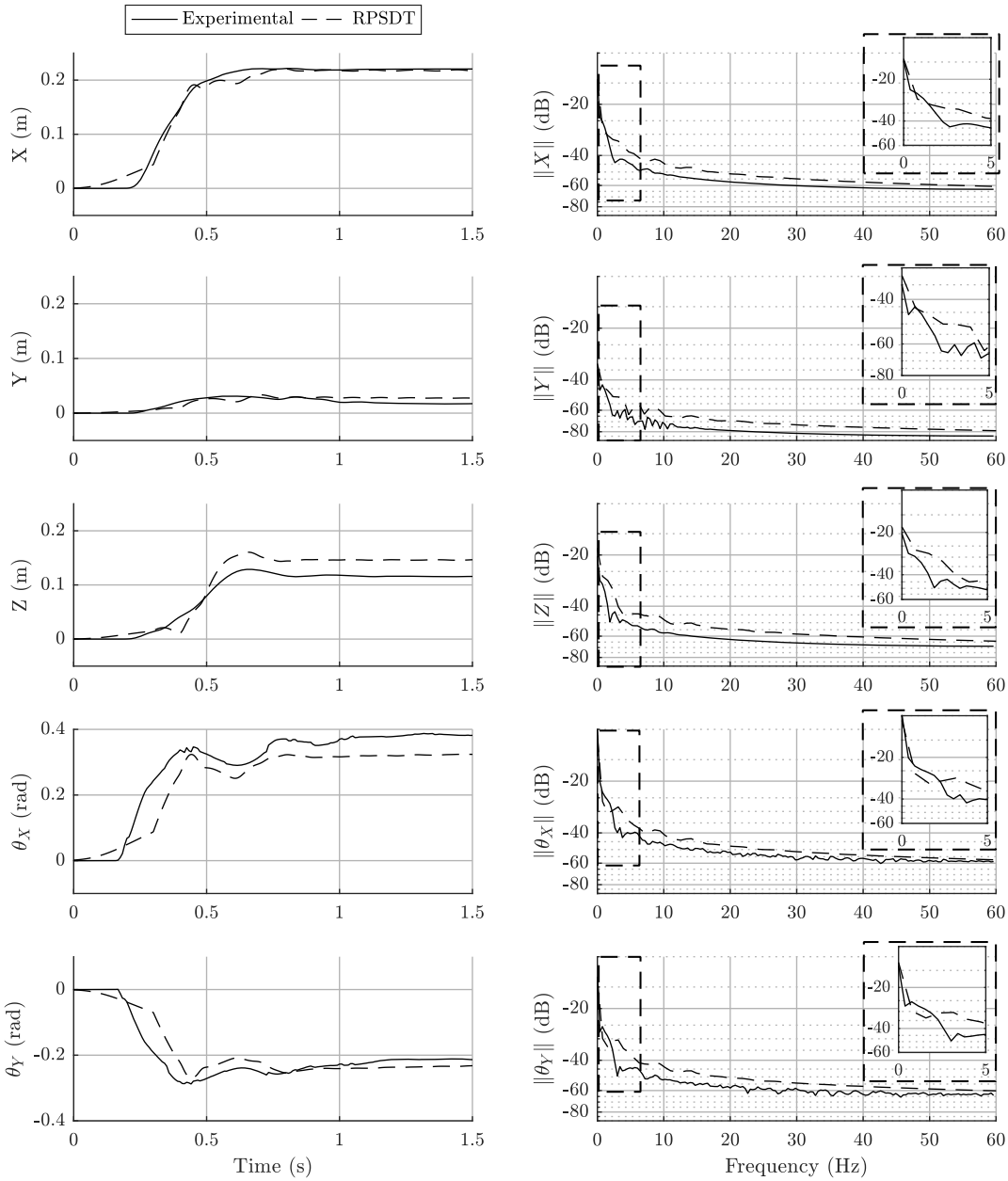

Fig. 5 RPSDT vs full-speed data in time and frequency domains.

any modeling inaccuracies are unlikely to significantly compromise or adversely affect the test validity. Hence, the argument for the suitability, applicability, and reliability of the RPSDT method for the study of the coupling phase and offcenter drogue hits is further emphasized.

IV. Hybrid Tests of AAR Maneuvers

This section presents the results from full-scale hybrid simulations of AAR operations conducted based on the framework outlined in Sec. II. The focus of the analysis lies on the refueling hardware behavior and contact forces that develop throughout the contact and coupling phases.

A. Hybrid Test Setup

The numerical domain features a model of the hose–drogue assembly that augments the developments in [8,9] to incorporate hose bending effects based on Timoshenko's beam theory as shown in [6] and includes ball-joint friction and separate aerodynamic restoring moments. A full list of parameters is given in Table 1. The adopted frame assignment for the nozzle and hose–drogue assembly complies with Figs. 8a and 8b, and the application of contact forces and moments from the physical substructure is detailed in Fig. 8c. Notably, here, the complete final hose link is regarded as the drogue and reception coupling assembly and the link length l_N corresponds to the distance from ball-joint connection to the drogue's center of gravity. This is in agreement with the configuration on the robot where the reception coupling is mounted to the force sensor flange at the end effector, thus creating the interface between the numerical and physical domains in place of the ball joint that would typically connect the hose to the drogue assembly. Hence, contact forces that are fed back to the simulation environment can be applied to the second-last lumped mass right after a transformation from drogue to tanker coordinates. As the modeling approach in [8,9] did not allow

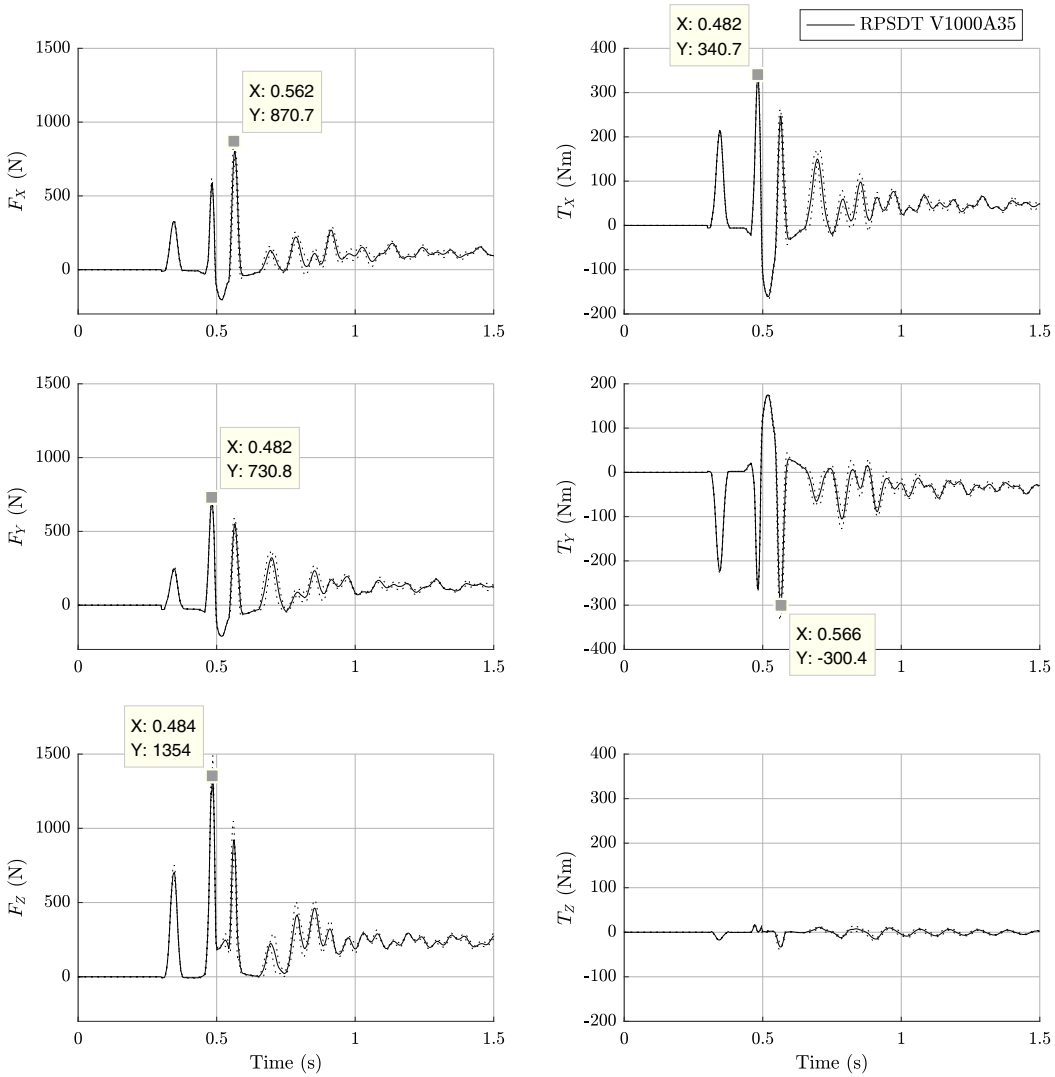

Fig. 6 Mean contact force profiles recorded in RPSDT tests shown in the drogue's frame of reference.

the direct application of moments, forces F_{cog} and F_{bj} are computed based on the moment arm l_N and applied to the final link as shown in Fig. 8c to account for feedback torques and generate an equivalent ball-joint moment on the hose model.

The simulation starts in steady-state conditions with the hose extended to its full payout length of 27 m and trailed centrally behind the tanker from a fuselage-mounted refueling pod. Any inherent tanker dynamics are neglected; i.e., over the course of the maneuver, the tanker remains undisturbed in straight level flight at a constant altitude of 8000 m, with an airspeed of 200 m/s representing an ideal docking environment. To isolate effects arising from probe–drogue contact–impact phenomena, atmospheric variations, gusts, and wake and bow wave effects are not included in the present study. The principle result of these effects is to produce a change in the relative position, velocity, and orientation of the probe and drogue, so this can instead be controlled directly through variation of these parameters. The receiver aircraft dynamics are not modeled, but the nozzle follows a predefined path leading to a head-on hit at the 12 o'clock location at various radial offsets from the drogue's axis of symmetry. A relative closure speed of 1.5 m/s is prescribed, and deceleration to zero relative speed takes place over a distance of 0.5 m once the nozzle passes the nominal unperturbed resting position of the latch mechanism. This is representative of a refueling scenario where pilots decelerate only after drogue capture occurs. Hose takeup is triggered with a 0.1 s delay from the initial contact point and covers a duration of three times the receiver aircraft's deceleration time, with the reel-in length ultimately amounting to the receiver's nominal deceleration length.

B. Results and Analysis

Three hybrid simulations are presented, for drogue hits at centerline offsets of 50, 100, and 200 mm, constituting initial contact with the outer coupling as well as low and high rib strikes, respectively. The full drogue trajectories in the tanker's frame of reference and the corresponding contact force/torque excitation profiles are shown in Fig. 9. The corresponding refueling hardware behavior is illustrated in Fig. 10, where sequential photographs taken throughout the tests are arranged columnwise by individual test cases. Due to the head-on centerline hits at the 12 o'clock location and the absence of wake and bow wave effects, both contact excitation forces (and, consequently, the drogue response) are dominant in the X–Z plane while out-of-plane dynamics remain negligible.

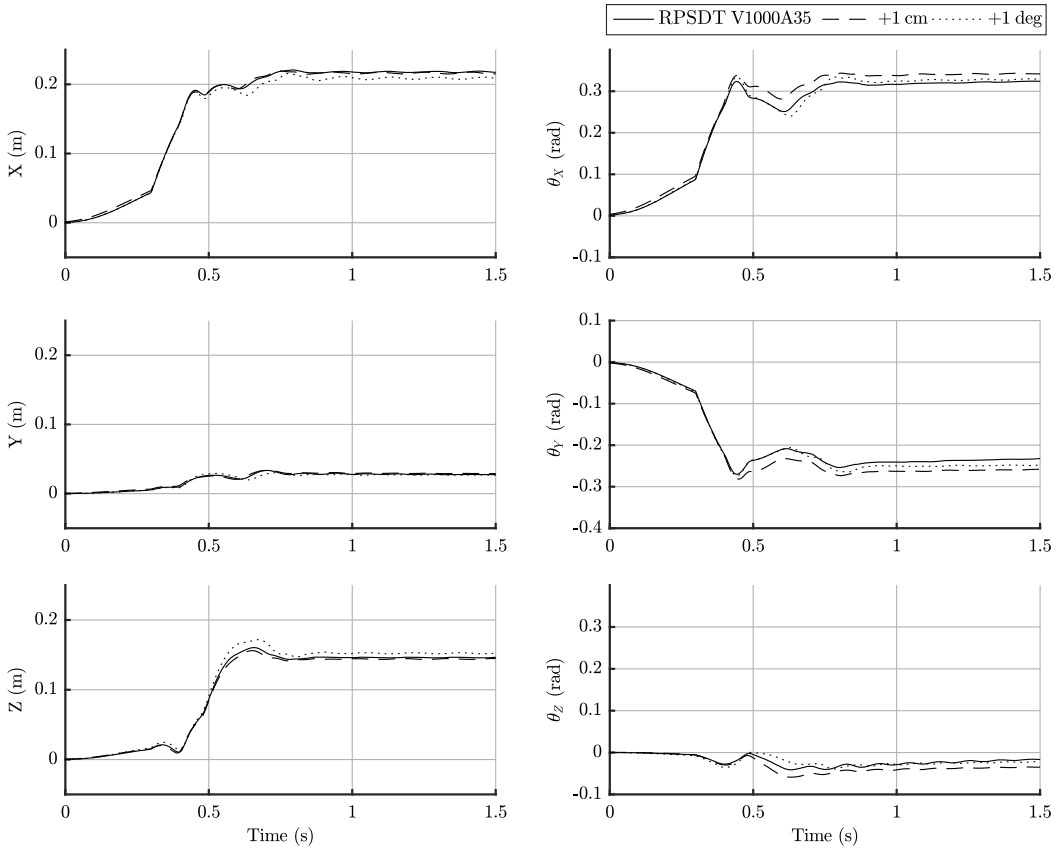

Fig. 7 Experimental sensitivity analysis for RPSDT-based contact tests.

It is shown that, upon contact, the drogue mainly reacts with a rotational tipping motion about its *Y* axis, whereas any response along the *X* axis toward the tanker remains insignificant due to the large drag forces involved. By contrast, the drogue, although temporarily pushed down as a result of the tipping motion, undergoes a distinct upward motion along the negative *Z* axis toward the tanker as the nozzle advances on a straight path along the *X* axis. This upward motion is a direct cause of the conical geometry of the ribs that produces the contact force components in the negative *Z* axis (Fig. 9), thus deflecting the drogue upward to align its line of symmetry with that of the probe. This is particularly well emphasized in the central photograph sequence in Fig. 10, corresponding to the 100 mm offset hit.

The tipping motion described is more pronounced for hits at increased centerline offsets, which produce larger rotational moments about the ball joint located at the point of hose attachment. Such behavior has been widely observed in AAR operations where particularly large rotational drogue responses are known to result from extreme offcenter hits at excessive speeds. Here, the tipping remains minimal for the 50 mm case, approaches 10 deg for hits at offsets of 100 mm, and is estimated to exceed 20 deg for the hit at a 200 mm offset.

The 50 and 100 mm test cases encompass the contact phase up to the point of successful engagement of the nozzle and coupling/latch mechanism, whereas a critical torque sensor limit of 400 N · m is exceeded for the 200 mm case, necessitating a premature test termination. As shown in Fig. 10, this occurs upon nozzle transition from rib to coupling contact and results primarily from the nature of the far offcenter hit in which the nozzle forces the ribs radially outward about the anchor point to such an extent that the conical geometry of the funnel is significantly distorted and the nozzle gets caught on the coupling edge. In combination with the large tipping described previously, it is concluded that this contact scenario, if it had run to completion, would not have resulted in successful coupling. By contrast, for hits at 50 and 100 mm offsets, the 400 N · m limit is only exceeded once the nozzle and drogue are successfully engaged. Note that, if the postcoupling dynamics were to be studied from this point onward, this could be done purely in simulation by constraining the drogue to follow the deceleration profile of the nozzle as was done in the works mentioned in Sec. II.

Finally, it is shown in Fig. 11a that the hose end tensions take an abrupt drop upon contact and gradually reduce as the drogue pivots about the ball joint. For the 50 and 100 mm offset hit, it is clearly shown

Table 1 Model parameters for hose–drogue assembly

Parameter	Value
Hose	
Specific mass	4.09 kg/m
Outer diameter	0.071 m
Inner diameter	0.0355 m
Elastic modulus	1.3×10^7 Pa
Drag coefficient (tangential)	0.01
Drag coefficient (normal)	0.6
Tow point with regard to tanker	$[-21.14, 0, 0.5]^T$
Drogue	
Mass	17.91 kg
Canopy diameter	0.6096 m
Drag coefficient	0.8
Ball-joint friction	10.0 N · m/(rad/s)
Aeromoment	5.0 N · m/ deg
Flight regime	
Airspeed	200 m/s
Altitude	8000 m
Air density	0.525 kg/m^3

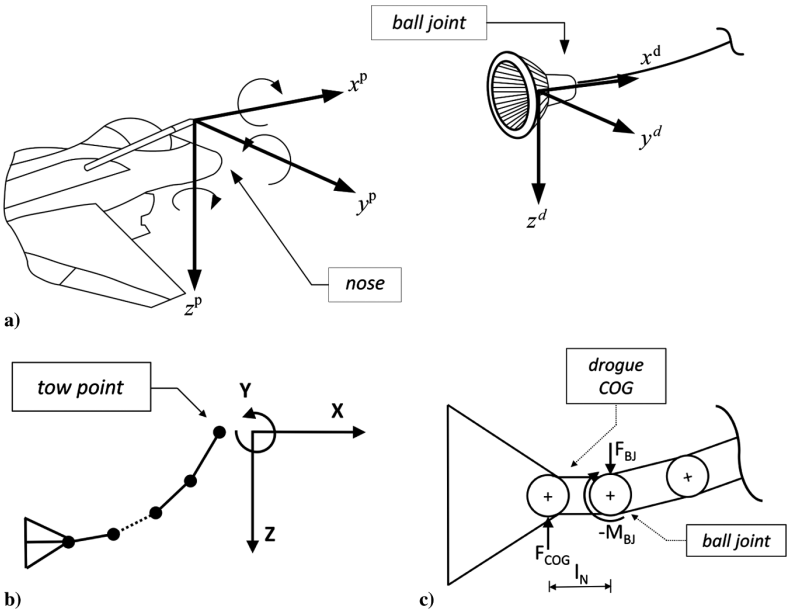

Fig. 8 Representations of a) frame assignment, b) model structure, and c) contact force application.

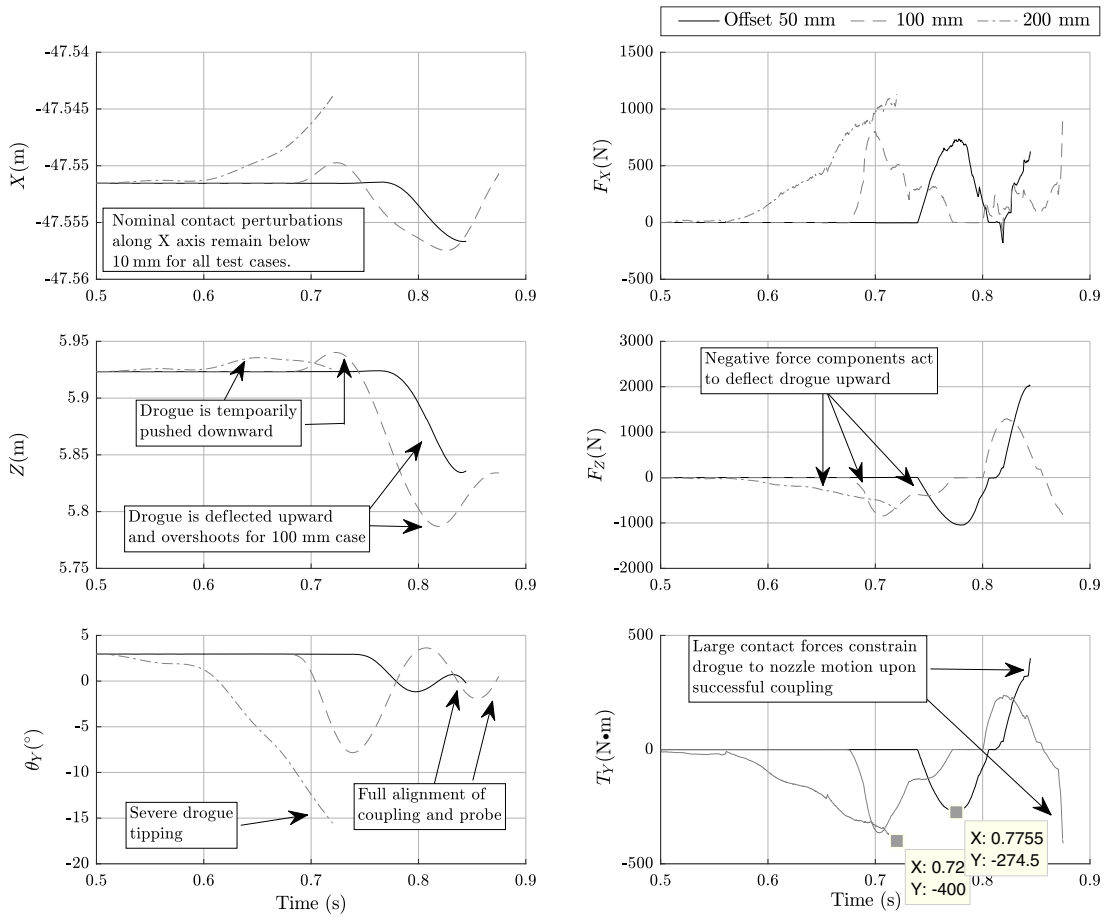

Fig. 9 Drogue response and contact force excitation in the *X–Z* plane.

how the tension drop reverses with an overshoot beyond the original value of 2500 N as the drogue is deflected upward to align the coupling and probe. It is this contact response that initiates the propagation of a mechanical wave up the hose, which can get reflected at the tow point on the refueling pod. While this occurs, intermittent fluctuations at the hose end die down and tensions begin to stabilize until they are

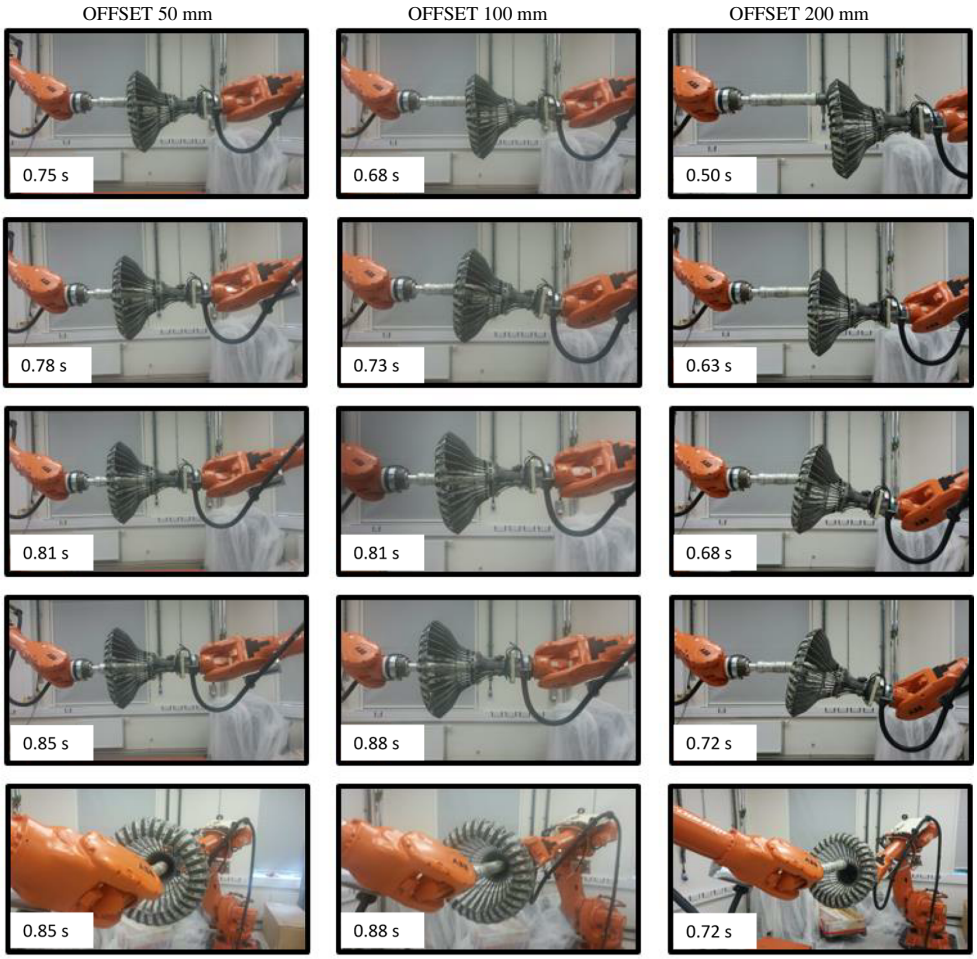

Fig. 10 Photographs from hybrid simulations in chronological order and grouped columnwise.

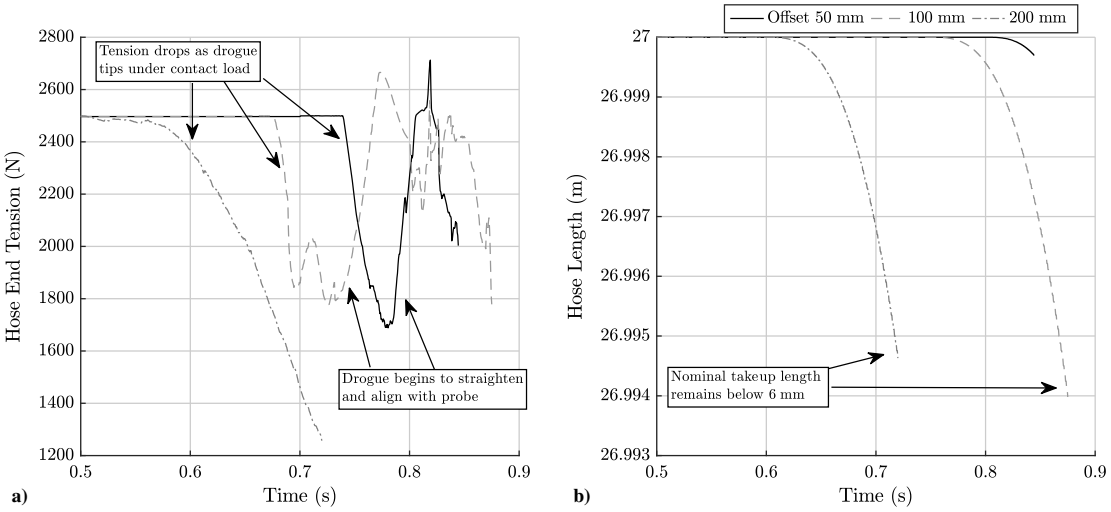

Fig. 11 Variations of a) hose tension and b) hose length throughout contact phase.

reexcited by the reflected wave. This can constitute a severe form of hose whip, especially if hose slack has not been taken up sufficiently by the hose-drum unit (HDU) and the waves are aerodynamically amplified. Here, a properly functioning HDU is simulated; however, as seen in Fig. 11b, its effects on the drogue response remain insignificant throughout the initial contact and coupling phase.

The results presented here show correlation with the phenomena observed in refueling operations and, in particular, with respect to two of the most problematic behaviors: namely, drogue tipping and hose whip. They demonstrate that the methods can be used to better understand the contact dynamics throughout the coupling phase, providing design insight and validation to improve not only the coupling success rates but also the robustness and mass optimization of the hardware. The use of validated hose models combines with rigorous validation of the RPSDT method to produce high confidence in the resulting datasets.

V. Conclusions

This Paper presents results from the first hybrid tests of air-to-air refueling contact dynamics. The findings show that the technique can provide greater insight than flight testing alone and at significantly lower cost and risk. This is an important contribution to the design and test practices for air-to-air refueling (AAR) equipment, and it comes at a time when AAR is seeing increasing interest as a means of improving civil fleet efficiencies as well as catering to a rapidly expanding unmanned aircraft fleet. The new robotic pseudodynamic testing technique for hybrid testing is outlined and used to produce results from two studies of contact tests for full-scale refueling hardware: 1) a validation of robotic pseudodynamic testing (RPSDT) fidelity with respect to a complete experimental laboratory setup, and 2) hybrid tests of complete AAR procedures using a simulated flight environment. The validation study finds that the RPSDT method is able to successfully reproduce the dominant dynamic characteristics between the probe and drogue in contact–impact events. Low parameter sensitivity and high levels of repeatability are identified, with mean standard deviations of 0.9 mm and 0.15 deg reported over motions of 220 mm and 18 deg, respectively. The full AAR scenario simulation demonstrates that RPSDT can reproduce important drogue response characteristics, including problematic behavior such as drogue tipping and the initiation of traveling waves in the hose, which can lead to hose whip. These behaviors will result, at best, in a failed engagement and, at worst, in the loss of the refueling equipment or the whole aircraft. The RPSDT observations are in line with flight-test observations and pilot reports. Laboratory-based hybrid testing is also shown to offer advantages over flight testing in the form of enhanced instrumentation, providing greater insight into trajectories, forces, and component strains to be used in design iterations. With the costs of equipping a tanker fleet standing around 500 million U.S. dollars, the technique offers an important means of laboratory testing to inform design iterations, reducing development timescales and costs, and improving safety and reliability before flight testing.

Acknowledgments

This work is sponsored and guided by Cobham Mission Systems (Wimborne, Dorset, U.K.). Additional financial support was received from the Engineering and Physical Sciences Research Council (United Kingdom) under grant EP/L504890/1. Thanks are due to Anders Blomdell and Klas Nilsson at Lund University for their part in creating the Open Robot Control Architecture (ORCA) robot control interface used in this work and for supporting its integration as described herein.

References

[1] Winnefeld, J. A., Niblack, P., and Johnson, D. J., "A League of Airmen: U.S. Air Power in the Gulf War," Tech. Rept. ADA282879, Rand Corp., Santa Monica, CA, 1994, p. 300, http://www.dtic.mil/dtic/tr/fulltext/u2/a282879.pdf [retrieved 01 Oct. 2017].

[2] Nangia, R. K., "Operations and Aircraft Design Towards Greener Civil Aviation Using Air-to-Air Refuelling," *Aeronautical Journal*, Vol. 110, No. 1113, 2006, pp. 705–721. doi:10.1017/S0001924000001585

[3] Schaufele, R., Ding, L., Miller, N., Barlett, H., Lukacs, M., and Bhadra, D., "FAA Aerospace Forecast: Fiscal Years 2017–2037," Tech. Rept., Federal Aviation Administration, 2017, http://www.dtic.mil/dtic/tr/fulltext/u2/a454450.pdf [retrieved 01 Oct. 2017].

[4] Bolkcom, C., "Air Force Aerial Refueling Methods: Flying Boom Versus Hose-and-Drogue," Tech. Rept. ADA454450, Library of Congress, Washington, D.C., 2006, http://www.dtic.mil/docs/citations/ADA454450 [retrieved 01 Oct. 2017].

[5] Thomas, P. R., Bhandari, U., Bullock, S., Richardson, T. S., and du Bois, J. L., "Advances in Air to Air Refuelling," *Progress in Aerospace Sciences*, Vol. 71, Nov. 2014, pp. 14–35. doi:10.1016/j.paerosci.2014.07.001

[6] Vassberg, J. C., Yeh, D. T., Blair, A. J., and Evert, J. M., "Numerical Simulations of KC-10 Wing-Mount Aerial Refueling Hose-Drogue Dynamics with a Reel Take-Up System," *21st AIAA Applied Aerodynamics Conference*, AIAA Paper 2003-3508, 2003. doi:10.2514/6.2003-3508

[7] Ribbens, W., Saggio, F., Wierenga, R., and Feldmann, M., "Dynamic Modeling of an Aerial Refueling Hose and Drogue System," *25th AIAA Applied Aerodynamics Conference*, AIAA Paper 2007-3802, 2007. doi:10.2514/6.2007-3802

[8] Ro, K., and Kamman, J. W., "Modeling and Simulation of Hose-Paradrogue Aerial Refueling Systems," *Journal of Guidance, Control, and Dynamics*, Vol. 33, No. 1, 2010, pp. 53–63. doi:10.2514/1.45482

[9] Ro, K., Kuk, T., and Kamman, J. W., "Dynamics and Control of Hose-Drogue Refueling Systems During Coupling," *Journal of Guidance, Control, and Dynamics*, Vol. 34, No. 6, 2011, pp. 1694–1708. doi:10.2514/1.53205

[10] Gilardi, G., and Sharf, I., "Literature Survey of Contact Dynamics Modelling," *Mechanism and Machine Theory*, Vol. 37, No. 10, 2002, pp. 1213–1239. doi:10.1016/S0094-114X(02)00045-9

[11] du Bois, J. L., Thomas, P. R., and Richardson, T. S., "Development of a Relative Motion Facility for Simulations of Autonomous Air to Air Refuelling," *2012 IEEE Aerospace Conference*, IEEE, New York, 2012, Paper 8.1306. doi:10.1109/AERO.2012.6187309

[12] du Bois, J. L., Thomas, P., Bullock, S., Bhandari, U., and Richardson, T., "Control Methodologies for Relative Motion Reproduction in a Robotic Hybrid Test Simulation of Aerial Refuelling," *AIAA Guidance, Navigation, and Control Conference*, AIAA Paper 2012-4676, 2012. doi:10.2514/6.2012-4676

[13] Martínez, C., Richardson, T., Thomas, P., du Bois, J. L., and Campoy, P., "A Vision-Based Strategy for Autonomous Aerial Refueling Tasks," *Robotics and Autonomous Systems*, Vol. 61, No. 8, 2013, pp. 876–895. doi:10.1016/j.robot.2013.02.006

[14] Ma, O., Flores-Abad, A., and Boge, T., "Use of Industrial Robots for Hardware-in-the-Loop Simulation of Satellite Rendezvous and Docking," *Acta Astronautica*, Vol. 81, No. 1, 2012, pp. 335–347. doi:10.1016/j.actaastro.2012.08.003

[15] du Bois, J. L., Titurus, B., and Lieven, N., "Transfer Dynamics Cancellation in Real-Time Dynamic Substructuring," *ISMA2010 International Conference on Noise and Vibration Engineering*, KU Leuven, Leuven, Belgium, 2010, pp. 1891–1914, http://past.isma-isaac.be/downloads/isma2010/papers/isma2010_0342.pdf [retrieved 2018].

[16] Plummer, A. R., "Model-in-the-Loop Testing," *Journal of Systems and Control Engineering*, Vol. 220, No. 3, 2006, pp. 183–199. doi:10.1243/09596518JSCE207

[17] Plummer, A. R., "Control Techniques for Structural Testing: A Review," *Journal of Systems and Control Engineering*, Vol. 221, No. 2, 2007, pp. 139–169. doi:10.1243/09596518JSCE295

[18] Bolien, M., Iravani, P., and du Bois, J. L., "Toward Robotic Pseudodynamic Testing for Hybrid Simulations of Air-to-Air Refueling," *IEEE/ASME Transactions on Mechatronics*, Vol. 22, No. 2, 2017, pp. 1004–1013. doi:10.1109/TMECH.2016.2644200

[19] Shoemake, K., "Animating Rotation with Quaternion Curves," *SIGGRAPH '85 Proceedings of the 12th Annual Conference on Computer Graphics and Interactive Techniques*, ACM Press, New York, 1985, pp. 245–254. doi:10.1145/325334.325242

[20] Blomdell, A., Dressler, I., Nilsson, K., and Robertsson, A., "Flexible Application Development and High-Performance Motion Control Based on External Sensing and Reconfiguration of ABB Industrial Robot Controllers," *IEEE International Conference on Robotics and Automation, 2010*, IEEE Publ., Piscataway, NJ, 2010, pp. 62–66, http://lup.lub.lu.se/record/1627720 [retrieved 2018].

[21] Gerum, P., "Xenomai: Implementing a RTOS Emulation Framework on GNU/Linux," Tech. Rept., 2004, http://www.xenomai.org/documentation/xenomai-2.0/pdf/xenomai.pdf [retrieved 23 April 2018].

[22] Gerum, P., "Life With Adeos, RevB," Tech. Rept., Oct. 2005, http://www.xenomai.org/documentation/branches/v2.0.x/pdf/Life-with-Adeos.pdf [retrieved 23 April 2018].

[23] Kiszka, J., and Wagner, B., "RTnet—A Flexible Hard Real-Time Networking Framework," *2005 IEEE Conference on Emerging Technologies and Factory Automation*, IEEE, New York, Sept. 2005, pp. 449–456. doi:10.1109/ETFA.2005.1612559

[24] Blomdell, A., Bolmsjo, G., Brogardh, T., Cederberg, P., Isaksson, M., Johansson, R., Haage, M., Nilsson, K., Olsson, M., Olsson, T., Robertsson, A., and Wang, J., "Extending an Industrial Robot Controller: Implementation and Applications of a Fast Open Sensor Interface," *IEEE Robotics and Automation Magazine*, Vol. 12, No. 3, 2005, pp. 85–94. doi:10.1109/MRA.2005.1511872

[25] "Couplings, Regulated, Aerial Pressure Refueling Type MA-2, Type MA-3 and Type MA-4," U.S. Dept. of Defense Performance Specification MIL-PRF-81975C, Jan. 2008, http://everyspec.com/MIL-PRF/MIL-PRF-080000-99999/download.php?spec=MIL-PRF-81975C.042388.pdf [retrieved 04 Sept. 2017].

Chapter 6

Discussion and Conclusions

This thesis has explored the feasibility of studying the probe-drogue contact and coupling dynamics in AAR systems using a hybrid testing method to synergistically combine and harness the individual benefits of simulative and experimental tests. To this end, the thesis has proposed, established and validated the technique of 'Robotic Pseudo-Dynamic Testing' (RPsDT), and shown that it can provide high-confidence predictions for the in-flight dynamics of aerial refuelling hardware. Conducted in close cooperation with Cobham Mission Systems, a leading AAR equipment manufacturer, the developments made in this thesis add rigorous methodical support to the on-ground validation and preflight verification processes used as part of the design and development cycles of AAR hardware, where the RPsDT technique can realise its full potential as an intermediate de-risking step between component-level testing and full system flight testing. The following sections conclude the thesis with an overarching discussion of the presented work, followed by a concise summary of the author's core contributions before providing closing remarks and suggestions for future work.

6.1 Discussion

The research presented in this thesis has primarily targeted the generation of reliable predictions for the hose-drogue dynamics throughout the critical contact and coupling phase of the AAR manoeuvre, where the complicated interaction of aerodynamic, atmospheric and contact factors decides whether a receiver craft approach results in the successful coupling of probe and drogue or in a missed attempt. Fundamentally, the research builds on the premise that the complicated dynamics due to the manifold

physical phenomena in the hook-up space render sole simulative and sole experimental studies inadequate to provide reliable predictions for the in-flight behaviour of the hose-drogue assembly. This is because experimental methods are hampered by evident logistical burdens in the laboratory reproduction of a flight environment, while simulative studies encounter severe uncertainties in the modelling of the contact and coupling phase. The latter result predominantely from the intrinsically difficult-to-model structure of the drogue which makes the contact and coupling forces between probe and drogue a complicated function of the equipment geometries, material properties, strike angles and contact speeds. The motivation to obtain reliable predictions with hybrid tests, where the contact phase is studied experimentally, has followed from these very drawbacks.
The incentive to use a robotic facility as the main part of the transfer system for the hybrid tests of AAR scenarios was based on a variety of reasons: From a technical perspective, the kinematic versatility of serial link industrial robots is vastly unmatched among COTS actuation systems. From an academic point of view, industrial robots present an interesting research platform, more so when used in an unconventional setting. Practically, Cobham's prior investment in the RMR as well as the research conducted on vision tracking and flight controller validation as part of the ASTRAEA programme [22, 23] have made the extension of the hybrid testing approach into the contact phase of the manoeuvre a native next step.

A comprehensive review of contemporary hybrid testing methods in Chapter 2 has provided a detailed discussion of known challenges for hybrid tests of mechanical substructures. Significantly, it was found that the dynamics induced into the test loop by the transfer system have an adverse effect on both test fidelity and stability. The most severe problems are known to arise from delays, latencies and bandwidth limitations in the actuation hardware and it was found that the standard mitigation schemes to counteract these effects are not applicable in the presence of the strong non-linearity and discontinuity found in AAR contact scenarios, especially since reliable contact models and preview information are not available throughout the tests. In order to circumvent these problems, the author proposed to perform the hybrid tests on the basis of the pseudo-dynamic method which vastly relaxes the response time demands for the industrial robots, accepting that the adoption of this technique comes at the expense of neglecting rate dependent effects in the contact force measurements. While the application of the pseudo-dynamic method to contact-impact problems is unconventional, the approach was underpinned by the hypothesis stating that

'*The contact response of the drogue is preponderantly structural and dominated by its non-linear stiffness properties, while the primary form of energy dissipation is expected to result from hysteresis inherent to the ribs and interlinked elastic cord.*'

which implies that high-confidence predictions of the contact and coupling phase are obtainable despite the neglect of rate dependent effects in the force feedback measurements (and likewise, that obtaining such high-confidence prediction in validation tests would in turn verify the hypothesis.) Hence, the hypothesis testing could be incorporated in the assessment of the test feasibility as per the aims and objectives set out in Section 1.6 and was performed according to a rigorous bottom-up approach. The latter spans the three core chapters of this thesis (Chapter 3 - Chapter 5) and covers the entire R&D process from the proposal of the framework through to the full scale testing at the RMR. In the following, a concise summary of this work including the author's main contributions is provided on a chapter-by-chapter basis before suggestions for future work and closing remarks are made.

The development of the RPsDT technique was outlined in Chapter 3. Beginning with a proposal for the framework of the hybrid tests and a justification for the underlying component division into the numerical and experimental substructures, the algorithmic procedure for RPsDT was established on the basis of a step-wise pseudo-dynamic test. Subsequently, architectural and implementation considerations were discussed from a systems and control perspective and the integration of a bespoke motion control unit, including a dedicated trajectory planning and execution mechanism, were presented for the test integration with ABB IRC5 controllers.
The second part of the chapter proposed and derived a novel modelling technique for the numerical simulation of the hose reel-in dynamics. Building upon a popular finite segment modelling approach for towed and tethered cable systems, the proposed model accommodates the reel-in process by means of a uniform variation of the finite segment size (*i.e.* the length of individual hose links). This provides the advantage of an automatically increasing spatial resolution throughout the reel-in process and eliminates the need to define additional constraints for the hose wind up process onto the HDU, thereby reducing the number of required computations. While the model evaluation revealed a very good qualitative agreement for the reel-in behaviour of the proposed and reference models, discrepancies were shown to arise from an energy gain associated with the activation of the reel-in constraints in the reference models themselves. Hence, it was proposed to perform an enhanced validation study as part of future work, where an equivalent constraint is included at the tow point of the developed model in order to align the dynamic behaviour of the models quantitatively and provide conclusive

evidence with regard to the validity of the proposed modelling approach.
As a matter of risk mitigation, the experimental work including the trial and testing of the RPsDT method was carried out in two separate stages. Preliminary scaled tests (Chapter 4) were conducted in parallel with the development process outlined in Chapter 3 and served as a validation basis for the subsequent application of the RPsDT method to full-scale test scenarios at the RMR (Chapter 5). The preliminary tests provided an initial evaluation of the RPsDT method in a comparative study of a simple and easily reproducible contact scenario between a rigid mass and a compliant object published in [98], as well as an extension of this work including a first hybrid simulation of the AAR docking phase based on a scaled setup published in [90]. Expectedly, limitations of the method resulting from the neglect of rate and time dependent effects including viscous damping and creep could be identified in both contributions, emphasising the need for careful validation testing on a case-by-case basis. At the same time the ability of the RPsDT method to capture the non-linear stiffness properties of the experimental specimen including structural damping due to hysteresis could be clearly demonstrated while an assessment of the qualitative refuelling hardware behaviour throughout the scaled tests highlighted the potential of the technique for full-scale tests at the RMR.

The need for careful validation testing of the full scale studies, as identified above, was addressed in Chapter 5 straight way. To this end, a redesign of the long established 'drop test' apparatus as per [21] was undertaken to enable robot controlled contact testing both at full speed and pseudo-dynamically. While the accurate reproduction of in-flight conditions was not a major concern at this stage, the tests served the independent validation of the RPsDT method for use with industrial refuelling hardware at the RMR ahead of performing hybrid simulations of complete AAR maneuvers. Probe-drogue contact scenarios were conducted for a variety of contact positions, impact speeds, and incidence strike angles and it was found that the RPsDT method was able to successfully reproduce the dominant dynamic characteristics between probe and drogue for such contact events. Low parameter sensitivity and high levels of repeatability were identified, with mean standard deviations of $0.9mm$ and $0.15°$ reported over motions of $220mm$ and $18°$ respectively. Moreover, the formation of characteristic strain patterns in response to the contact events could be recorded at ribs along the entire drogue circumference. Significant stress levels resulting from radial bending and lateral flexure were registered and it was concluded that accurate measurements obtained in this way could aid in the future definition of common design baselines, safety factors or be used as an additional data source in structural validation processes.
Building upon the successful validation with full scale refuelling hardware, the study

was extended to investigations of complete AAR scenarios under the simulation based emulation of a flight environment. Predictions for the operational contact and coupling behaviour in response to off-centre drogue hits were made and estimates for the contact forces provided. As in the preliminary tests presented in Chapter 4, the predicted refuelling hardware behaviour was inline with flight test observations and pilot reports, demonstrating that RPsDT can reproduce important drogue response characteristics including problematic behaviour such as drogue tipping and the initiation of hose oscillations. Thus, the hypothesis could be successfully verified and the argument for adopting the RPsDT method as a development tool in industrial processes was further substantiated.

6.2 Contributions

In summary, the author's core contributions made in this thesis include:

- The complete methodical development of *Robotic Pseudo-Dynamic Testing* (RPsDT) through adaptation of the pseudo-dynamic testing technique for the investigation of multi-body contact-impact problems using COTS robotic manipulators.
- The development of a simple drop test experiment and validation process to verify the feasibility of the RPsDT method for the study of contact-impact problems.
- The proposal of a framework for hybrid simulations of AAR manoeuvres with focus on the probe-drogue contact and coupling phase.
- The implementation of the proposed framework on the basis of the RPsDT method and the realisation of the first hybrid simulations of the probe-drogue contact and coupling phase in AAR manoeuvres (scaled & full scale)
- The validation of the RPsDT technique in independent contact tests based on an improved design of a standardised industrial endurance test rig for refuelling hardware.
- The generation and provision of high confidence predictions for the in-flight dynamics of the hose-drogue assembly in response to off-centre hits, in the form of contact trajectories, contact forces and stress distributions in the refuelling hardware.
- The publication of the RPsDT method and the dissemination of the performed studies and obtained data in peer reviewed conference and journal articles.

- The proposal and derivation of a novel modelling technique for the simulation of the reel-in dynamics of towed and tethered cable systems using adaptive finite segment sizes.

6.3 Future Work & Closing Remarks

Ideas must evolve, just like research, and one must come to accept that the generation of knowledge, by its very nature, is an iterative and incremental process leaving room for improvements at all stages. Unsurprisingly, this is also the case for the work at hand. One proposal for an enhanced validation study including the integration of an equivalent torsional constraint at the tow point of the developed hose model was already provided in Chapter 3.6. In addition to this, two more aspects have been identified by the author as meriting further attention by the academic community:

First, improvements in the agreement between full-speed and pseudo-dynamic data could be achieved by adapting the RPsDT technique to execute continuously at a reduced speed rather than in a step-wise fashion. To this end, the execution speed would be determined by a time scaling factor as is typical for the technique of Continuous Pseudo Dynamic Testing (see Chapter 2.3.1). Given that direction changes throughout the contact and coupling phase of AAR manoeuvres are uncommon (unlike in earthquake testing), the risk of encountering systematic force overshoots as stated in the literature review may be ignored. At the same time, the continuous nature of the actuation also reduces the risk of recording unwanted force relaxation effects. While a vast loss of rate dependent components from the feedback force measurements would still occur in such tests, a possibility exists that the capture of low frequency friction components is sufficient to manifest as a quality gain for the RPsDT technique. This needs to be examined with careful scrutiny.

Second, the conducted RPsDT tests have provided high confidence estimates of the coupling dynamics including the related contact forces and stiffness information. This data could form the basis for a thorough analysis of the bandwidth and actuation requirements for real-time tests, *e.g.* based on a stability analysis or similar. In this manner, it would be possible to *(i)* formally assess the feasibility of performing real-time tests of the contact and coupling phase with current hardware, *(ii)* identify bottlenecks in the hybrid testing loop and *(iii)* define requirements for necessary improvements in the control and actuation technology.

Finally, it is worth mentioning that the above suggestions should at no point overshadow

the contributions of this work. Establishing reliable predictive capabilities for the operational contact and coupling dynamics of refuelling hardware with lab-based hybrid testing is a major achievement. At a time of an industry-wide shift towards virtual system validation and a rapidly expanding unmanned aircraft market, the RPsDT technique offers an important means of laboratory testing to inform design iterations, reduce development time scales and cost and improve safety and reliability prior to flight testing.

Bibliography

[1] Cobham plc - mission systems. http://www.cobham.com/mission-systems/. Online; accessed: 2017-09-25.

[2] RK Nangia. Operations and aircraft design towards greener civil aviation using air-to-air refuelling. *The Aeronautical Journal*, 110(1113):705–721, 2006.

[3] RK Nangia. Unmanned air-to-air refuelling success. *Professional Engineering*, 20(22):13, 20017.

[4] Astraea. https://www.uavs.org/ASTRAEA. Accessed: 2017-09-25.

[5] Cobham and University of Bristol progress Autonomous Air to Air Refuelling Research. http://astraea.aero/news-2/cobham-and-university-of.html. Accessed: 2014-07-27.

[6] U.S Air Force. Early mid-air refueling. http://www.af.mil/News/Photos/igphoto/2000594100/. Online; accessed: 2017-10-24.

[7] U.S Air Force. F-35 Aircraft AF-4 Australian KC-30 Tanker Test. http://www.af.mil/News/Photos/igphoto/2001296618/. Online; accessed 2017-10-24.

[8] U.S Air Force. Boeing KC-135R Stratotanker with Mk32B refueling pods by Cobham. https://en.wikipedia.org/wiki/Aerial_refueling#/media/File:Boeing_KC-135R_Multipoint_Refueling.JPEG. Online; accessed 2017-10-24.

[9] Richard K Smith. Seventy-five years of inflight refueling. *Air Force History and Museums Program*, 1998.

[10] Christopher Bolkcom. Air force aerial refueling methods: flying boom versus hose-and-drogue. LIBRARY OF CONGRESS WASHINGTON DC CONGRESSIONAL RESEARCH SERVICE, 2006.

[11] Peter R. Thomas, Ujjar Bhandari, Steve Bullock, Thomas S. Richardson, and Jonathan Luke du Bois. Advances in air to air refuelling. *Progress in Aerospace Sciences*, Jul 2014.

[12] Cobham plc - Mission System. Hose-Drum Units and Wing Air Refuelling Pods. `http://www.cobham.com/mission-systems/air-to-air-refuelling/hose-and-drogue-systems/wing-air-refuelling-pods/`. Online; accessed 2014-11-15.

[13] Cobham plc - Mission System. Refuelling Drogues. `http://www.cobham.com/mission-systems/air-to-air-refuelling/hose-and-drogue-systems/refuelling-drogues/`. Online; accessed 2017-10-24.

[14] U.S Navy. Tornado GR4 refueling from the drogue of an RAF VC10 tanker over Iraq. `https://en.wikipedia.org/wiki/Aerial_refueling#/media/File:GR4_VC10.jpg`. Online; accessed 2017-10-24.

[15] Cobham plc - Mission System. Refuelling Probes. `http://www.cobham.com/mission-systems/air-to-air-refuelling/hose-and-drogue-systems/refuelling-probes/`. Online; accessed 2017-10-24.

[16] G Gilardi and I Sharf. Literature survey of contact dynamics modelling. *Mechanism and machine theory*, 37(10):1213–1239, 2002.

[17] John C Vassberg, David T Yeh, Andrew J Blair, and Jacob M Evert. Numerical simulations of kc-10 wing-mount aerial refueling hose-drogue dynamics with a reel take-up system. In *21st applied aerodynamics conference*, volume 26. Orlando, Florida, 2003.

[18] William Ribbens, Frank Saggio, Rodney Wierenga, and Mike Feldmann. Dynamic modeling of an aerial refueling hose & drogue system. In *25th AIAA Applied Aerodynamics Conference*, page 3802, 2007.

[19] Kapseong Ro and James W Kamman. Modeling and simulation of hose-paradrogue aerial refueling systems. *Journal of guidance, control, and dynamics*, 33(1):53–63, 2010.

[20] Kapseong Ro, Taeseung Kuk, and James W Kamman. Dynamics and control of hose-drogue refueling systems during coupling. *Journal of Guidance, Control, and Dynamics*, 34(6):1694–1708, 2011.

[21] U.S. Department of Defense. *PERFORMANCE SPECIFICATION: COUPLINGS, REGULATED, AERIAL PRESSURE REFUELING TYPE MA-2, TYPE MA-3 AND TYPE MA-4.* Number MIL-PRF-81975C. January 2008.

[22] Jonathan Luke du Bois, Peter Thomas, Steve Bullock, Ujjar Bhandari, and Thomas Richardson. Control methodologies for relative motion reproduction in a robotic hybrid test simulation of aerial refuelling. In *AIAA guidance, navigation, and control conference, Minneapolis, MN, USA*, 2012.

[23] J.L. du Bois, P.R. Thomas, and T.S. Richardson. Development of a relative motion facility for simulations of autonomous air to air refuelling. In *Aerospace Conference, 2012 IEEE*, pages 1–12, Big Sky, MT, March 2012.

[24] Carol Martínez, Thomas Richardson, Peter Thomas, Jonathan Luke du Bois, and Pascual Campoy. A vision-based strategy for autonomous aerial refueling tasks. *Robotics and Autonomous Systems*, 61(8):876–895, Aug 2013.

[25] Jonathan L Du Bois, Peter Newell, Steve Bullock, Peter Thomas, and Thomas Richardson. Vision based closed-loop control systems for satellite rendezvous with model-in-the-loop validation and testing. In *23rd International Symposium on Space Flight Dynamics*. Jet Propulsion Laboratory, Pasadena, California, USA, 2012.

[26] Jonathan Luke du Bois, Branislav Titurus, and NAJ Lieven. Transfer dynamics cancellation in real-time dynamic substructuring. In *ISMA2010 international conference on noise and vibration engineering, Leuven, Belgium*, pages 1891–1914, 2010.

[27] Jonathan L du Bois. A strategy for improving performance in real time hybrid testing. In *Dynamics of Civil Structures, Volume 4*, pages 219–225. Springer, 2014.

[28] J-C Piedboeuf, J De Carufel, Farhad Aghili, and Erick Dupuis. Task verification facility for the canadian special purpose dextrous manipulator. In *Robotics and Automation, 1999. Proceedings. 1999 IEEE International Conference on*, volume 2, pages 1077–1083. IEEE, 1999.

[29] Farhad Aghili and J-C Piedbœuf. Hardware-in-loop simulation of robots interacting with environment via algebraic differential equation. In *Intelligent Robots and Systems, 2000.(IROS 2000). Proceedings. 2000 IEEE/RSJ International Conference on*, volume 3, pages 1590–1596. IEEE, 2000.

[30] JC Piedboeuf, F Aghili, M Doyon, Y Gonthier, E Martin, and WH Zhu. Emulation of space robot through hardware-in-the-loop simulation. In *Proc. of the 6th Int. Symposium on Artificial Intelligence and Robotics & Automation in Space: i-SAIRAS*, pages 18–22, 2001.

[31] Farhad Aghili and J-C Piedboeuf. Contact dynamics emulation for hardware-in-loop simulation of robots interacting with environment. In *Robotics and Automation, 2002. Proceedings. ICRA'02. IEEE International Conference on*, volume 1, pages 523–529. IEEE, 2002.

[32] Victor Saouma and Mettupalayam Sivaselvan. *Hybrid simulation: theory, implementation and applications*. CRC Press, 2008.

[33] Kiriakos Athanasas and Ian Dear. Validation of complex vehicle systems of prototype vehicles. *IEEE Transactions on Vehicular Technology*, 53(6):1835–1846, 2004.

[34] Herbert Hanselmann. Advances in desktop hardware-in-the-loop simulation. Technical report, SAE Technical Paper, 1997.

[35] Peter Terwiesch, Thomas Keller, and Erich Scheiben. Rail vehicle control system integration testing using digital hardware-in-the-loop simulation. *IEEE Transactions on Control Systems Technology*, 7(3):352–362, 1999.

[36] Jace L Allen. Implementation of hil testing systems for aerospace ecus. Technical report, SAE Technical Paper, 2005.

[37] MI Wallace, DJ Wagg, SA Neild, P Bunniss, NAJ Lieven, and AJ Crewe. Testing coupled rotor blade–lag damper vibration using real-time dynamic substructuring. *Journal of Sound and Vibration*, 307(3):737–754, 2007.

[38] Hao Yan, Junwei Han, Zhizhong Tong, and Hongren Li. Hybrid realtime simulation of the space docking process. In *Artificial Reality and Telexistence–Workshops, 2006. ICAT'06. 16th International Conference on*, pages 323–327. IEEE, 2006.

[39] Hiroshi Kawabe, Eiichi Inohira, Takashi Kubota, and Masaru Uchiyama. Analytical and experimental evaluation of impact dynamics on a high-speed zero g motion simulator. In *Intelligent Robots and Systems, 2001. Proceedings. 2001 IEEE/RSJ International Conference on*, volume 4, pages 1870–1875. IEEE, 2001.

[40] M Zapateiro, HR Karimi, N Luo, and BF Spencer. Real-time hybrid testing of semiactive control strategies for vibration reduction in a structure with mr damper. *Structural Control and Health Monitoring*, 17(4):427–451, 2010.

[41] Sung-Ho Hwang, Seung-Jin Heo, Hong-Seok Kim, and Kyo-Il Lee. Vehicle dynamic analysis and evaluation of continuously controlled semi-active suspensions using hardware-in-the-loop simulation. *Vehicle System Dynamics*, 27(5-6):423–434, 1997.

[42] DC Batterbee and ND Sims. Hardware-in-the-loop simulation of magnetorheological dampers for vehicle suspension systems. *Proceedings of the Institution of Mechanical Engineers, Part I: Journal of Systems and Control Engineering*, 221(2):265–278, 2007.

[43] WE Misselhorn, NJ Theron, and PS Els. Investigation of hardware-in-the-loop for use in suspension development. *Vehicle System Dynamics*, 44(1):65–81, 2006.

[44] Seung Tae Cha, Qiuwei Wu, Arne Hejde Nielsen, Jacob Østergaard, and In Kwon Park. Real-time hardware-in-the-loop (hil) testing for power electronics controllers. In *Power and Energy Engineering Conference (APPEEC), 2012 Asia-Pacific*, pages 1–6. IEEE, 2012.

[45] Bin Lu, Xin Wu, Hernan Figueroa, and Antonello Monti. A low-cost real-time hardware-in-the-loop testing approach of power electronics controls. *IEEE Transactions on Industrial Electronics*, 54(2):919–931, 2007.

[46] AGCO Fendt HiL Test Bench. `https://www.speedgoat.com/user-stories/speedgoat-user-stories/agco-fendt`. Accessed: 2017-10-16.

[47] Christof Ebert and Capers Jones. Embedded software: Facts, figures, and future. *Computer*, 42(4), 2009.

[48] AP Darby, A Blakeborough, and MS Williams. Improved control algorithm for real-time substructure testing. *Earthquake engineering & structural dynamics*, 30(3):431–448, 2001.

[49] Jonathan L du Bois. A strategy for improving performance in real time hybrid testing. In *Dynamics of Civil Structures, Volume 4*, pages 219–225. Springer, 2014.

[50] Cheng Chen and James M Ricles. Real-time hybrid testing using an unconditionally stable explicit integration algorithm. In *Structures Congress 2008: Crossing Borders*, pages 1–10, 2008.

[51] Cheng Chen, James M Ricles, Thomas M Marullo, and Oya Mercan. Real-time hybrid testing using the unconditionally stable explicit cr integration algorithm. *Earthquake Engineering & Structural Dynamics*, 38(1):23–44, 2009.

[52] Herbert Schuette and Peter Waeltermann. Hardware-in-the-loop testing of vehicle dynamics controllers–a technical survey. Technical report, SAE Technical Paper, 2005.

[53] Pini Gurfil and Itzik Klein. Stabilizing the explicit euler integration of stiff and undamped linear systems. *Journal of Guidance Control and Dynamics*, 30(6):1659, 2007.

[54] John Charles Butcher. *The numerical analysis of ordinary differential equations: Runge-Kutta and general linear methods*. Wiley-Interscience, 1987.

[55] MS Williams and A Blakeborough. Laboratory testing of structures under dynamic loads: an introductory review. *Philosophical Transactions of the Royal Society of London A: Mathematical, Physical and Engineering Sciences*, 359(1786):1651–1669, 2001.

[56] Andrew R Plummer. Model-in-the-loop testing. *Proceedings of the Institution of Mechanical Engineers, Part I: Journal of Systems and Control Engineering*, 220(3):183–199, 2006.

[57] YN Kyrychko, KB Blyuss, A Gonzalez-Buelga, SJ Hogan, and DJ Wagg. Real-time dynamic substructuring in a coupled oscillator–pendulum system. In *Proceedings of the Royal Society of London A: Mathematical, Physical and Engineering Sciences*, volume 462, pages 1271–1294. The Royal Society, 2006.

[58] Stephen A Mahin and Pui-shum B Shing. Pseudodynamic method for seismic testing. *Journal of Structural Engineering*, 111(7):1482–1503, 1985.

[59] Motohiko Hakuno, Masatoshi Shidawara, and Tsukasa Hara. Dynamic destructive test of a cantilever beam, controlled by an analog-computer. In *Proceedings of the Japan Society of Civil Engineers*, volume 1969, pages 1–9. Japan Society of Civil Engineers, 1969. in Japanese.

[60] Koichi Takanashi, Kuniaki Udagawa, Matsutaro Seki, Tsuneo Okada, and Hisashi Tanaka. Nonlinear earthquake response analysis of structures by a computer-actuator on-line system. *Bulletin of Earthquake Resistant Structure Research Center*, 8:1–17, 1975.

[61] K Takanashi, K Udagawa, and H Tanaka. Earthquake response analysis of steel frames by computer-actuator on-line system. In *Proceedings of the 5th Japan Earthquake Engineering Symposium*, pages 1321–1328. Architecture Institute of Japan (AIJ), 1978.

[62] K Takanashi, K Udagawa, M Seki, and H Tanaka. Seismic failure analysis of structures by computer-pulsator on-line system. *Bulletin of Earthquake Resistant Structure Research Center, Institute of Industrial Science, University of Tokyo*, 11:13–25, 1974. in Japanese.

[63] Koichi Takanashi and Masayoshi Nakashima. Japanese activities on on-line testing. *Journal of Engineering Mechanics*, 113(7):1014–1032, 1987.

[64] P Benson Shing, Masayoshi Nakashima, and Oreste S Bursi. Application of pseudodynamic test method to structural research. *Earthquake spectra*, 12(1):29–56, 1996.

[65] P Pegon and AV Pinto. Pseudo-dynamic testing with substructuring at the elsa laboratory. *Earthquake engineering & structural dynamics*, 29(7):905–925, 2000.

[66] Pui-Shumi B Shing and Stephen A Mahin. Rate-of-loading effects on pseudodynamic tests. *Journal of Structural Engineering*, 114(11):2403–2420, 1988.

[67] Erhard Krempl. Relaxation behavior and modeling. *International journal of Plasticity*, 17(10):1419–1436, 2001.

[68] K Takanashi and K Ohi. Earthquake response analysis of steel structures by rapid computer-actuator on-line system,(1) a progress report, trial system and dynamic response of steel beams. *Bull. Earthquake Resistant Struct. Research Center (ERS)*, (16):103–109, 1983.

[69] Georges Magonette. Development and application of large–scale continuous pseudo–dynamic testing techniques. *Philosophical Transactions of the Royal Society of London A: Mathematical, Physical and Engineering Sciences*, 359(1786):1771–1799, 2001.

[70] E Watanabe, T Kitada, S Kunitomo, and K Nagata. Parallel pseudodynamic seismic loading test on elevated bridge system through the internet. In *The Eight East Asia-Pacific Conference on Structural Engineering and Construction*, 2001.

[71] Gilberto Mosqueda, Bozidar Stojadinovic, and Stephen A Mahin. Geographically distributed continuous hybrid simulation. In *Proceedings of the 13th World Conference on Earthquake Engineering*, 2004.

[72] AR Plummer. Control techniques for structural testing: a review. *Proceedings of the Institution of Mechanical Engineers, Part I: Journal of Systems and Control Engineering*, 221(2):139–169, 2007.

[73] T. Horiuchi, M. Inoue, T. Konno, and Y. Namita. Real-time hybrid experimental system with actuator delay compensation and its application to a piping system with energy absorber. *Earthquake Engineering & Structural Dynamics*, 28(10):1121–1141, 1999.

[74] PA Bonnet, MS Williams, and A Blakeborough. Compensation of actuator dynamics in real-time hybrid tests. *Proceedings of the Institution of Mechanical Engineers, Part I: Journal of Systems and Control Engineering*, 221(2):251–264, 2007.

[75] Cheng Chen and James M Ricles. Analysis of actuator delay compensation methods for real-time testing. *Engineering Structures*, 31(11):2643–2655, 2009.

[76] Mehmet N Sahinkaya, Pengfei Wang, and Sam Akehurst. Causal inversion of non-minimum-phase systems for hardware-in-the-loop transmission testing. *Proceedings of the Institution of Mechanical Engineers, Part I: Journal of Systems and Control Engineering*, 227(3):298–307, 2013.

[77] MI Wallace, DJ Wagg, and SA Neild. An adaptive polynomial based forward prediction algorithm for multi-actuator real-time dynamic substructuring. *Proceedings of the Royal Society A: Mathematical, Physical and Engineering Science*, 461(2064):3807, 2005.

[78] DP Stoten and RA Hyde. Adaptive control of dynamically substructured systems: the single-input single-output case. *Proceedings of the Institution of Mechanical Engineers, Part I: Journal of Systems and Control Engineering*, 220(2):63–79, 2006.

[79] CN Lim, SA Neild, DP Stoten, D Drury, and CA Taylor. Adaptive control strategy for dynamic substructuring tests. *Journal of Engineering Mechanics*, 133(8):864–873, 2007.

[80] G Li, DP Stoten, and J-Y Tu. Model predictive control of dynamically substructured systems with application to a servohydraulically actuated mechanical plant. *IET Control Theory & Applications*, 4(2):253–264, 2010.

[81] Guang Li, Guido Herrmann, David P Stoten, Jiaying Tu, and Matthew C Turner. Application of robust antiwindup techniques to dynamically substructured systems. *IEEE/ASME Transactions on Mechatronics*, 18(1):263–272, 2013.

[82] Ou Ma, Angel Flores-Abad, and Toralf Boge. Use of industrial robots for hardware-in-the-loop simulation of satellite rendezvous and docking. *Acta Astronautica*, 81(1):335–347, 2012.

[83] Neville Hogan. Impedance control: An approach to manipulation. In *American Control Conference, 1984*, pages 304–313. IEEE, 1984.

[84] Romeo Ortega, Arjan J Van Der Schaft, Iven Mareels, and Bernhard Maschke. Putting energy back in control. *Control Systems, IEEE*, 21(2):18–33, 2001.

[85] Günter Schreiber, Andreas Stemmer, and Rainer Bischoff. The fast research interface for the kuka lightweight robot. In *IEEE Workshop on Innovative Robot Control Architectures for Demanding (Research) Applications How to Modify and Enhance Commercial Controllers (ICRA 2010)*, pages 15–21, 2010.

[86] Milad Geravand, Fabrizio Flacco, and Alessandro De Luca. Human-robot physical interaction and collaboration using an industrial robot with a closed control architecture. In *Robotics and Automation (ICRA), 2013 IEEE International Conference on*, pages 4000–4007. IEEE, 2013.

[87] Rainer Krenn and B Schaefer. Limitations of hardware-in-the-loop simulations of space robotics dynamics using industrial robots. *EUROPEAN SPACE AGENCY-PUBLICATIONS-ESA SP*, 440:681–686, 1999.

[88] Anders Blomdell, Isolde Dressler, Klas Nilsson, and Anders Robertsson. Flexible application development and high-performance motion control based on external sensing and reconfiguration of abb industrial robot controllers. In *IEEE International Conference on Robotics and Automation, 2010*, pages 62–66, 2010.

[89] Anders Blomdell, Gunnar Bolmsjo, Torgny Brogardh, Per Cederberg, Mats Isaksson, Rolf Johansson, Mathias Haage, Klas Nilsson, Magnus Olsson, Tomas Olsson, et al. Extending an industrial robot controller: implementation and applications of a fast open sensor interface. *IEEE Robotics & Automation Magazine*, 12(3):85–94, 2005.

[90] Mario Bolien, Pejman Iravani, and Jonathan Luke du Bois. Toward Robotic Pseudodynamic Testing for Hybrid Simulations of Air-to-Air Refueling. *IEEE/ASME Transactions on Mechatronics*, 22(2):1004–1013, 2017.

[91] Philippe Gerum. Xenomai-implementing a rtos emulation framework on gnu/linux. *White Paper, www.Xenomai.org*, pages 1–12, 2004.

[92] Philippe Gerum. Life with adeos. *White paper, Available: http://www. xenomai. org/documentation/xenomai-2.3/pdf/Life-with-Adeos-rev-B. pdf*, 2005.

[93] Jan Kiszka and Bernardo Wagner. RTnet-a flexible hard real-time networking framework. In *Emerging Technologies and Factory Automation, 2005. ETFA 2005. 10th IEEE Conference on*, volume 1, pages 8–pp. IEEE, 2005.

[94] Richard P Paul and Hong Zhang. Computationally efficient kinematics for manipulators with spherical wrists based on the homogeneous transformation representation. *The International Journal of Robotics Research*, 5(2):32–44, 1986.

[95] MB Leahy, LM Nugent, George N Saridis, and Kimon P Valavanis. Efficient puma manipulator jacobian calculation and inversion. *Journal of Field Robotics*, 4(2):185–197, 1987.

[96] Ken Shoemake. Animating rotation with quaternion curves. In *ACM SIGGRAPH computer graphics*, volume 19, pages 245–254. ACM, 1985.

[97] Zheng Hong Zhu and Shake A Meguid. Elastodynamic analysis of aerial refueling hose using curved beam element. *AIAA journal*, 44(6):1317, 2006.

[98] Mario Bolien, Pejman Iravani, and Jonathan Luke Du Bois. Robotic pseudodynamic testing (rpsdt) of contact-impact scenarios. In *Conference Towards Autonomous Robotic Systems*, pages 50–55. Springer, 2015.

Appendix A

Delay-Induced Energy Gain in Real-Time Hybrid Testing

The manifestation of actuator delay as 'negative damping' in RTHT has been widely stated in the literature. The following sections aim to provide a simple assessment of the effects of actuator delay on a simple hybrid test using only energy based considerations. The analysis is in parts similar to that performed by Horiuchi [73].

Let's consider a hybrid test of a 2nd order mass-spring-damper system that is solely compromised by actuator delay. Assume that the test is setup to include the mass in the numerical substructure while the experimental substructure consists of a spring-damper element with no further inertia. For simplicity, further assume that all elements in the tests are perfect, i.e. the stiffness element k is linear, the viscous damping coefficient c has constant properties, noise is not introduced at any point and a perfect sensor provides exact and instantaneous force feed back measurements to the numerical substructure which in turn performs an instantaneous exact integration of the motion equations to produce the next reference commands. An ideal transfer system would reproduce/track this demand perfectly, however, here the actuator delay is the only compromise to the test.

Lets recall from Fourier's theorem, that any actuator command can be represented as the superposition of a series of sinusoids with different frequencies and phase shifts. Following on from this, we can investigate the effect of an actuator delay in a hybrid test by considering in isolation a pure sinusoidal position command $x_c = Asin(\omega t)$ of arbitrary amplitude A and frequency ω that is tracked with an actuator dead-time t_d. Expressing the commanded and actual position of the actuator as $x_c(t)$ and $x_a(t)$ respectively it is

clear that for the spring element the reaction force fed back to the simulation takes the form of $F_r = kx_c$ and $F_r = kx_a$ for the perfect zero-delay and the delayed case respectively. Also note, that time functions of commanded and actual actuator positions are given as follows:

$$X_c(t) = A\sin(\omega t) \qquad \dot{X}_c(t) = v(t) = A\omega cos(\omega t) \tag{A.1}$$

$$X_a(t) = A\sin(\omega(t - t_d)) = A\sin(\omega t - \omega t_d) \qquad \dot{X}_a(t) = A\omega\cos(\omega t - \omega t_d) \tag{A.2}$$

It is then possible to independently quantify the contributions of spring and damper element to the energy level of the hybrid test over one period of the command signal. In the following, this is done on a case-by-case basis considering both the zero-delay and the delayed option.

Energy change due to damping element - zero delay

The energy dissipated by the damper element over one period of the sinusoid is:

$$\begin{aligned}
W_d &= \oint F_d dx = \oint -cvdx \\
&= \int_0^T -cv(t)\frac{dx}{dt}dt = 2\int_0^{T/2=\pi/\omega} -cv^2(t)dt \\
&= 2\int_0^{\pi/\omega} -cA^2\omega^2 cos^2(\omega t)dt \qquad \text{using} \quad cos(2x) = 2cos^2(x) - 1 \\
&= 2\int_0^{\pi/\omega} -\frac{1}{2}cA^2\omega^2\left[cos(2\omega t) + 1\right]dt = -cA^2\omega^2\int_0^{\pi/\omega} cos(2\omega t) + 1dt \\
&= -cA^2\omega^2\left[\frac{sin(2\omega t)}{2\omega} + t\right]_0^{\pi/\omega} = -cA^2\omega^2\frac{\pi}{\omega} \\
&= -\pi cA^2\omega
\end{aligned} \tag{A.3}$$

The energy is dissipative as indicated by the negative sign. Energy dissipation per cycle is constant for a command signal of constant frequency and amplitude. This is to be expected.

Energy change due to damping element - constant delay

The energy W_d dissipated by the damper element over one period of the sinusoid is:

$$
\begin{aligned}
W_d &= \oint F_d dx = \oint -cvdx \\
&= \int_0^T -c\dot{x}_a(t)\frac{dx_c(t)}{dt}dt = -c\int_0^T A\omega cos(\omega t - \omega t_d)A\omega cos(\omega t)dt \\
&= -cA^2\omega^2 \int_0^T cos(\omega t - \omega t_d)cos(\omega t)dt \\
&\qquad \text{using} \quad cos(a-b) = cos(a)cos(b) + sin(a)sin(b) \\
&= -cA^2\omega^2 \int_0^T \left[cos(\omega t)cos(\omega t_d) + sin(\omega t)sin(\omega t_d)\right] cos(\omega t) \\
&= -cA^2\omega^2 \left[\int_0^T cos(\omega t_d)cos^2(\omega t)dt + \int_0^T sin(\omega t_d)sin(\omega t)cos(\omega t)dt\right] \\
&= -cA^2\omega^2 cos(\omega t_d)\int_0^T cos^2(\omega t)dt \quad - cA^2\omega^2 sin(\omega t_d)\int_0^T sin(\omega t)cos(\omega t)dt \\
&\quad \text{using} \quad cos(2a) = cos^2(a) - 1 \qquad \text{and letting} \quad u = sin(\omega t) \quad \frac{du}{dt} = \omega cos(\omega t) \quad dt = \frac{du}{\omega cos(\omega t)} \\
&= -cA^2\omega^2 cos(\omega t_d)\int_0^T \frac{1}{2}\left(cos(2\omega t) + 1\right)dt \quad - cA^2\omega^2 sin(\omega t_d)\int_0^T \frac{1}{\omega}udu \\
&= -\frac{1}{2}cA^2\omega^2 cos(\omega t_d)\int_0^T cos(2\omega t) + 1dt \quad - cA^2\omega sin(\omega t_d)\int_0^T udu \\
&= -\frac{1}{2}cA^2\omega^2 cos(\omega t_d)\left[\frac{sin(2\omega t)}{2\omega} + t\right]_0^{T=\frac{2\pi}{\omega}} \quad - cA^2\omega sin(\omega t_d)\left[\frac{1}{2}sin^2(\omega t)\right]_0^{T=\frac{2\pi}{\omega}} \\
&= -\frac{1}{2}cA^2\omega^2 cos(\omega t_d)\left[\frac{sin(4\pi)}{2\omega} + \frac{2\pi}{\omega} - 0\right] \quad - \frac{1}{2}cA^2\omega sin(\omega t_d)\left[sin(2\pi)\right] \\
&= -\frac{1}{2}cA^2\omega^2\left[\frac{2\pi}{\omega}\right]cos(\omega t_d) = -\pi c\omega A^2 cos(\omega t_d)
\end{aligned}
\tag{A.4}
$$

The energy is dissipative as indicated by the negative sign and increasing the delay will reduce the energy dissipation, *i.e* increase the energy level in the simulation.

Energy change due to stiffness element - zero-delay

This should not contribute to a change of energy of the hybrid simulation. The work W_k done by the spring over one cycle is

$$\begin{aligned} W_k &= \oint -F_x dx = \oint -kx(t)dx = \int_0^T -kx(t)\frac{dx}{dt}dt \\ &= -\int_0^T kAsin(\omega t)A\omega cos(\omega t)dt = -kA^2\omega \int_0^T sin(\omega t)cos(\omega t)dt \\ &\qquad \text{letting} \quad u = sin(\omega t) \quad \frac{du}{dt} = \omega cos(\omega t) \quad dt = \frac{du}{\omega cos(\omega t)} \\ &= -kA^2\omega \int_0^T \frac{1}{\omega}ucos(\omega t)\frac{du}{cos(\omega t)} = -kA^2 \int_0^T udu \\ &= -kA^2 \left[\frac{1}{2}u^2\right]_0^{T=-\frac{2\pi}{\omega}} = -\frac{1}{2}kA^2 \left[sin(\omega t)\right]_0^{\frac{2\pi}{\omega}} = 0 \end{aligned} \tag{A.5}$$

Hence, a perfect spring does not influence the system energy in hybrid test with zero actuator delay. As expected!

Energy change due to stiffness element - constant delay

Energy gain per cycle due to stiffness element with constant-delay transfer system. Note that the reaction force gets integrated and opposes the actuator force. Simulation assumes that the actuator instantly reached the demanded position, however, its response is delayed. In turn the reaction force from the physical substructure does not correspond to the demanded position and velocity but to the delayed position and velocity. This obviously adversely affects the validity and stability of the simulation. The work balance over one cycle is

$$
\begin{aligned}
W_{kd} &= \oint -F_{k_d} dx = \oint -k x_d(t) dx = -\int_0^T k x_d(t) \frac{dx_c(t)}{dt} dt \\
&= -\int_0^T kA sin(\omega t - \omega t_d) A\omega cos(\omega t) dt = -kA^2\omega \int_0^T sin(\omega t - \omega t_d) cos(\omega t) dt \\
&\qquad \text{using} \quad sin(a-b) = sin(a)sin(b) - cos(a)sin(b) \\
&= -kA^2\omega \int_0^T \left[sin(\omega t) sin(\omega t_d) - cos(\omega t) sin(\omega t_d) \right] cos(\omega t) dt \\
&= -kA^2\omega \left[\int_0^T sin(\omega t_d) sin(\omega t) cos(\omega t) dt - \int_0^T sin(\omega t_d) cos^2(\omega t) dt \right] \\
&= -kA^2\omega sin(\omega t_d) \left[\int_0^T sin(\omega t) cos(\omega t) dt - \int_0^T cos^2(\omega t) dt \right] \\
&\qquad \text{using} \quad sin(2a) = 2sin(a)cos(a) \quad \text{and} \quad cos(2a) = 2cos^2(a) - 1 \qquad \text{(A.6)} \\
&= -kA^2\omega sin(\omega t_d) \left[\int_0^T \frac{1}{2} sin(2\omega t) dt - \int_0^T \frac{1}{2} \left[cos(2\omega t) + 1 \right] dt \right] \\
&= -\frac{1}{2} kA^2\omega sin(\omega t_d) \left[\int_0^{T=\frac{2\pi}{\omega}} sin(2\omega t) dt - \int_0^{T=\frac{2\pi}{\omega}} cos(2\omega t) + 1 dt \right] \\
&= -\frac{1}{2} kA^2\omega sin(\omega t_d) \left[\left[\frac{-cos(2\omega t)}{2\omega} \right]_0^{\frac{2\pi}{\omega}} - \left[\frac{sin(2\omega t)}{2\omega} + t \right]_0^{\frac{2\pi}{\omega}} \right] \\
&= -\frac{1}{2} kA^2\omega sin(\omega t_d) \left[\left[\frac{-cos(4\pi)}{2\omega} - \frac{-1}{2\omega} \right] - \left[\frac{sin(4\pi)}{2\omega} + \frac{2\pi}{\omega} - 0 \right] \right] \\
&= -\frac{1}{2} kA^2\omega sin(\omega t_d) \left[\left[\frac{-1}{2\omega} + \frac{1}{2\omega} \right] - \left[\frac{2\pi}{\omega} \right] \right] \\
&= +\pi kA^2 sin(\omega t_d)
\end{aligned}
$$

The expression above states the energy gained per period of a sinusoidal command signal of frequency ωt for a fixed transfer system delay of t_d. Clearly increasing delay increases the energy balance of the simulation.

Summary

The outcome from all cases is tabulated below. Note that for typical time delays in the order of $10ms$ and systems with low natural frequencies the product wt_d is small. In such a case, the energy added per period due to the spring element in the constant delay case may be simplified to the term $+\pi kA^2\omega t_d$ while the expression for the dissipative energy of the damping element of the constant delay case reduces to the same expression obtained for the zero delay case, *i.e* $-\pi c\omega A^2$. Note that interesting observations can be made if both expressions are equated at the critical point where the energy gain outbalances the inherent damping in the system causing the response to grow unbounded as shown in Eq. A.7. Here, the equation states that for a constant actuator delay t_d and system/ specimen stiffness k a damping coefficient of at least $c = kt_d$ is needed to keep the system theoretically stable.

	zero delay	constant delay
Stiffness	0	$+\pi kA^2 sin(\omega t_d)$
Damping	$-\pi cA^2\omega$	$-\pi c\omega A^2 cos(\omega t_d)$

Table A.1: Summary of spring and damper effects on energy balance in hybrid tests for zero-delay and delayed actuator response.

$$\begin{aligned} W_k - W_d &= 0 \\ +\pi kA^2\omega t_d - \pi c\omega A^2 &= 0 \\ +\pi kA^2\omega t_d &= +\pi c\omega A^2 \\ c &= +kt_d \end{aligned} \tag{A.7}$$

Conversely, one may arise at the idea that delay in a hybrid test manifests as 'negative damping' (as Horiuchi put it [73]). This is the result of a direct comparison between the nominal energy gain of the spring element and energy loss of the damper as shown in Eq. A.8:

$$\begin{aligned} +\pi kA^2\omega t_d &= -\pi c\omega A^2 \\ c &= -kt_d \end{aligned} \tag{A.8}$$

Appendix B

Differentiation of Algebraic Constraint Equations

Starting from the constraint definition in Equation 3.43 (restated below for convenience), where all variables are functions of time,

$$\boldsymbol{p_k} \boldsymbol{p_k} = l_k^2 \tag{B.1}$$

and noting that:

$$\boldsymbol{p_k} = \boldsymbol{r_k} - \boldsymbol{r_j} = -l_k \boldsymbol{n_{k_x}} \tag{B.2}$$

Then, differentiating once gives:

$$\dot{\boldsymbol{p}}_{\boldsymbol{k}} = \boldsymbol{v_k} - \boldsymbol{v_j} = -\dot{l}_k \boldsymbol{n_{k_x}} - l_k \dot{\boldsymbol{n}}_{\boldsymbol{k_x}} \tag{B.3}$$

And differentiating a second time gives:

$$\begin{aligned} \ddot{\boldsymbol{p}}_{\boldsymbol{k}} &= \boldsymbol{a_k} - \boldsymbol{a_j} = -\ddot{l}_k \boldsymbol{n_{k_x}} - \dot{l}_k \dot{\boldsymbol{n}}_{\boldsymbol{k_x}} - \dot{l}_k \dot{\boldsymbol{n}}_{\boldsymbol{k_x}} - l_k \ddot{\boldsymbol{n}}_{\boldsymbol{k_x}} \\ \ddot{\boldsymbol{p}}_{\boldsymbol{k}} &= \boldsymbol{a_k} - \boldsymbol{a_j} = -\ddot{l}_k \boldsymbol{n_{k_x}} - 2\dot{l}_k \dot{\boldsymbol{n}}_{\boldsymbol{k_x}} - l_k \ddot{\boldsymbol{n}}_{\boldsymbol{k_x}} \end{aligned} \tag{B.4}$$

Differentiating the constraint definition in Equation B.1 yields:

$$2\boldsymbol{p_k} \dot{\boldsymbol{p}}_{\boldsymbol{k}} = 2 l_k \dot{l}_k \tag{B.5}$$

and substituting the expressions from Equation B.2 and Equation B.3 while accounting for the fact that $\boldsymbol{n}_{\boldsymbol{k}_x}\boldsymbol{n}_{\boldsymbol{k}_x} = 1$ yields:

$$\begin{aligned}
2\left[-l_k\boldsymbol{n}_{\boldsymbol{k}_x}\right]\left[-\dot{l}_k\boldsymbol{n}_{\boldsymbol{k}_x} - l_k\dot{\boldsymbol{n}}_{\boldsymbol{k}_x}\right] &= 2l_k\dot{l}_k \\
2l_k\dot{l}_k\boldsymbol{n}_{\boldsymbol{k}_x}\boldsymbol{n}_{\boldsymbol{k}_x} + 2l_k^2\boldsymbol{n}_{\boldsymbol{k}_x}\dot{\boldsymbol{n}}_{\boldsymbol{k}_x} &= 2l_k\dot{l}_k \\
2l_k\dot{l}_k + 2l_k^2\boldsymbol{n}_{\boldsymbol{k}_x}\dot{\boldsymbol{n}}_{\boldsymbol{k}_x} &= 2l_k\dot{l}_k \\
2l_k^2 n_k\dot{\boldsymbol{n}}_{\boldsymbol{k}_x} &= 0 \\
l_k^2\boldsymbol{n}_{\boldsymbol{k}_x}\dot{\boldsymbol{n}}_{\boldsymbol{k}_x} &= 0
\end{aligned} \tag{B.6}$$

Taking the derivative of the above equation yields:

$$\begin{aligned}
\frac{d}{dt}\left[l_k^2\boldsymbol{n}_{\boldsymbol{k}_x}\dot{\boldsymbol{n}}_{\boldsymbol{k}_x}\right] &= \frac{d}{dt}\left[0\right] \\
2l_k\dot{l}_k\boldsymbol{n}_{\boldsymbol{k}_x}\dot{\boldsymbol{n}}_{\boldsymbol{k}_x} + l_k^2\dot{\boldsymbol{n}}_{\boldsymbol{k}_x}^2 + l_k^2\boldsymbol{n}_{\boldsymbol{k}_x}\ddot{\boldsymbol{n}}_{\boldsymbol{k}_x} &= 0 \\
2\dot{l}_k\boldsymbol{n}_{\boldsymbol{k}_x}\dot{\boldsymbol{n}}_{\boldsymbol{k}_x} + l_k\dot{\boldsymbol{n}}_{\boldsymbol{k}_x}^2 + l_k\boldsymbol{n}_{\boldsymbol{k}_x}\ddot{\boldsymbol{n}}_{\boldsymbol{k}_x} &= 0
\end{aligned} \tag{B.7}$$

Noting the similarity between Equation B.7 and the expression $-\ddot{\boldsymbol{p}}_{\boldsymbol{k}} = \ddot{l}_k\boldsymbol{n}_{\boldsymbol{k}_x} + 2\dot{l}_k\dot{\boldsymbol{n}}_{\boldsymbol{k}_x} + l_k\ddot{\boldsymbol{n}}_{\boldsymbol{k}_x}$ from Equation B.4, we will add $\ddot{l}_k\boldsymbol{n}_{\boldsymbol{k}_x}\boldsymbol{n}_{\boldsymbol{k}_x}$ to both sides of Equation B.7 and factorise subsequently:

$$\begin{aligned}
2\dot{l}_k\boldsymbol{n}_{\boldsymbol{k}_x}\dot{\boldsymbol{n}}_{\boldsymbol{k}_x} + \ddot{l}_k\boldsymbol{n}_{\boldsymbol{k}_x}\boldsymbol{n}_{\boldsymbol{k}_x} + l_k\boldsymbol{n}_{\boldsymbol{k}_x}\ddot{\boldsymbol{n}}_{\boldsymbol{k}_x} &= \ddot{l}_k\boldsymbol{n}_{\boldsymbol{k}_x}\boldsymbol{n}_{\boldsymbol{k}_x} - l_k\dot{\boldsymbol{n}}_{\boldsymbol{k}_x}^2 \\
\left[\ddot{l}_k\boldsymbol{n}_{\boldsymbol{k}_x} + 2\dot{l}_k\dot{\boldsymbol{n}}_{\boldsymbol{k}_x} + l_k\ddot{\boldsymbol{n}}_{\boldsymbol{k}_x}\right]\boldsymbol{n}_{\boldsymbol{k}_x} &= \ddot{l}_k\boldsymbol{n}_{\boldsymbol{k}_x}\boldsymbol{n}_{\boldsymbol{k}_x} - l_k\dot{\boldsymbol{n}}_{\boldsymbol{k}_x}^2 \\
-\ddot{\boldsymbol{p}}_{\boldsymbol{k}}\boldsymbol{n}_{\boldsymbol{k}_x} &= \ddot{l}_k - l_k\dot{\boldsymbol{n}}_{\boldsymbol{k}_x}^2 \\
\ddot{\boldsymbol{p}}_{\boldsymbol{k}}\boldsymbol{n}_{\boldsymbol{k}_x} &= l_k\dot{\boldsymbol{n}}_{\boldsymbol{k}_x}^2 - \ddot{l}_k
\end{aligned} \tag{B.8}$$

And finally given that $\ddot{\boldsymbol{p}}_{\boldsymbol{k}} = \boldsymbol{a}_{\boldsymbol{k}} - \boldsymbol{a}_{\boldsymbol{j}}$ (Equation B.4), the following expression is obtained for the second derivative of the constraint equation:

$$\left(\boldsymbol{a}_{\boldsymbol{k}} - \boldsymbol{a}_{\boldsymbol{j}}\right)\boldsymbol{n}_{\boldsymbol{k}_x} = l_k\dot{\boldsymbol{n}}_{\boldsymbol{k}_x}^2 - \ddot{l}_k \tag{B.9}$$

Further note that for a link of constant length this reduces to the expression given in [19]:

$$\left(\boldsymbol{a}_{\boldsymbol{k}} - \boldsymbol{a}_{\boldsymbol{j}}\right)\boldsymbol{n}_{\boldsymbol{k}_x} = l_k\dot{\boldsymbol{n}}_{\boldsymbol{k}_x}^2 \tag{B.10}$$

Appendix C

Full Scale Validation Tests - Supplementary Material

The validation of the RPsDT method with full scale refuelling hardware was performed by comparing a full speed contact scenario with a RPsDT reproduction as outlined in Chapter 5. A rig was designed based on the schematic shown in Figure C.1 and full speed contact scenarios were performed at a variety of contact points, strike angles and contact speeds. Fundamentally, the rig design was motivated by the setup used for the impact and endurance tests as per MIL-PRF-81975C [21] but included a variety of deliberate modifications to increase the system complexity (by incorporating non-linear visco-elastic bungee cords) and to enable more repeatable testing (using controlled robotic actuation).

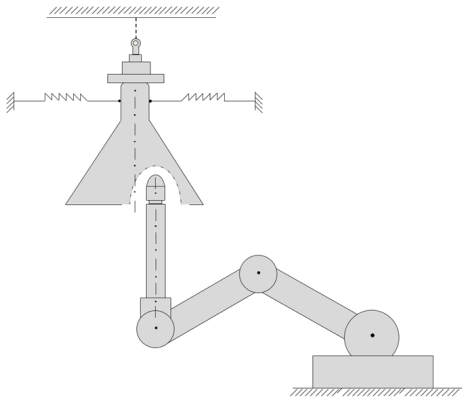

Figure C.1: Schematic of experimental set-up for full speed contact tests.

C.0.1 Motion Profiles

To perform a contact scenario the probe was manoeuvred to a pre-contact position under the drogue from where it was accelerated along a straight path (in the direction of the probe's line of symmetry) to strike the drogue at a predefined angle and contact point. To this end, the motion profile consisted of an acceleration phase (amounting to the first $150mm$ of the path) followed by a constant speed phase (over a length of $180mm$) and a deceleration phase of $150mm$. For all tests, the point of initial contact was reached $180mm$ from the pre-contact position, *i.e* $30mm$ into the constant speed phase. Subsequently, the robot was kept stationary for a settling period of 2 seconds before it slowly returned to its original position. The underlying motion profiles for the contact scenarios presented in Chapter 5 (contact speeds of $1000mm/s$ and strike angles of $0deg$, $15deg$ and $35deg$) are shown in Figure C.2, Figure C.3 and Figure C.4 respectively. Good robot tracking accuracy to sub-millimetre level and negligible contact disturbances can be reported for all cases.

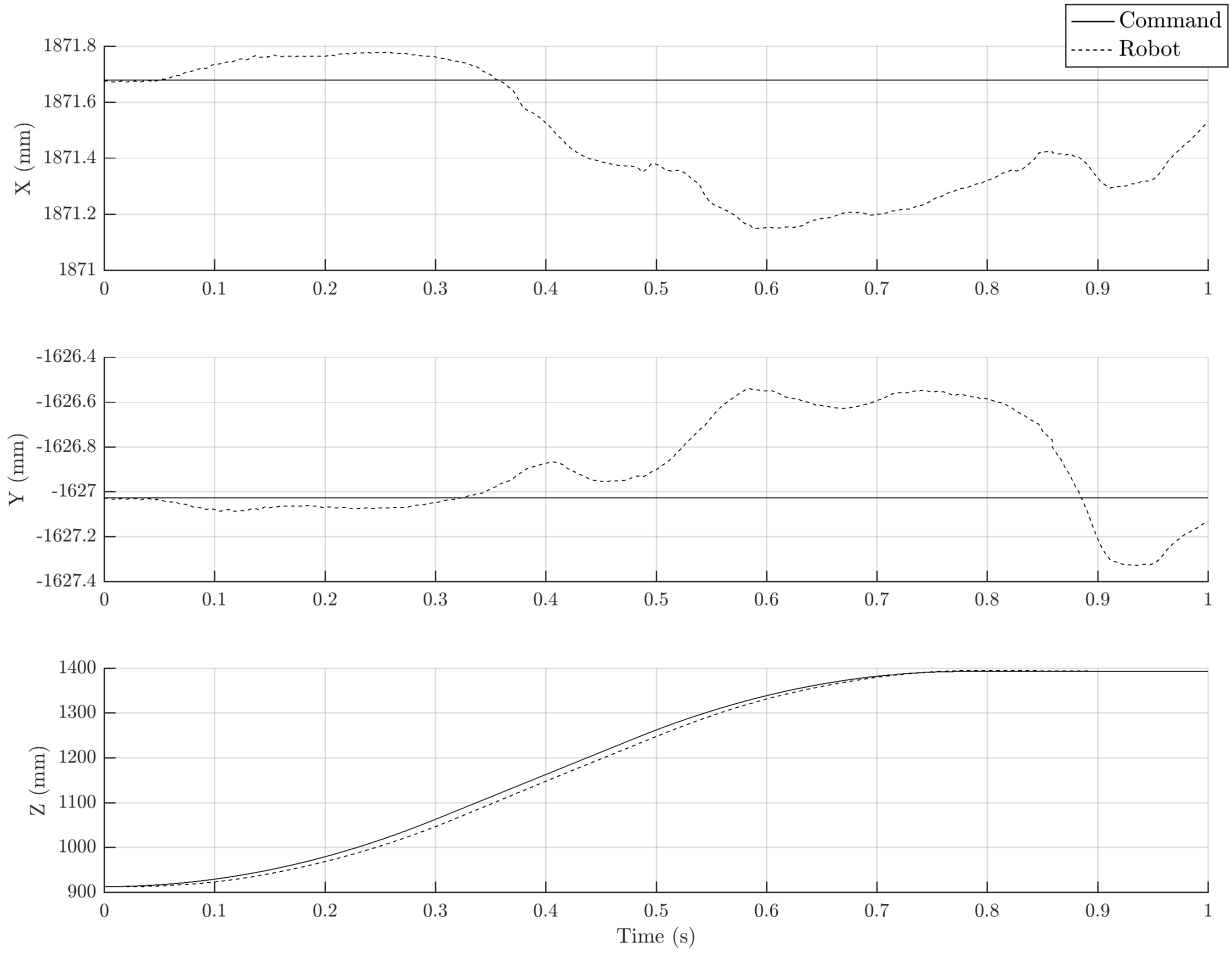

Figure C.2: Contact motion profiles and robot tracking for contact case V1000A0 (1000mm/s and 0deg strike angle). All coordinates are shown in the robot's base frame.

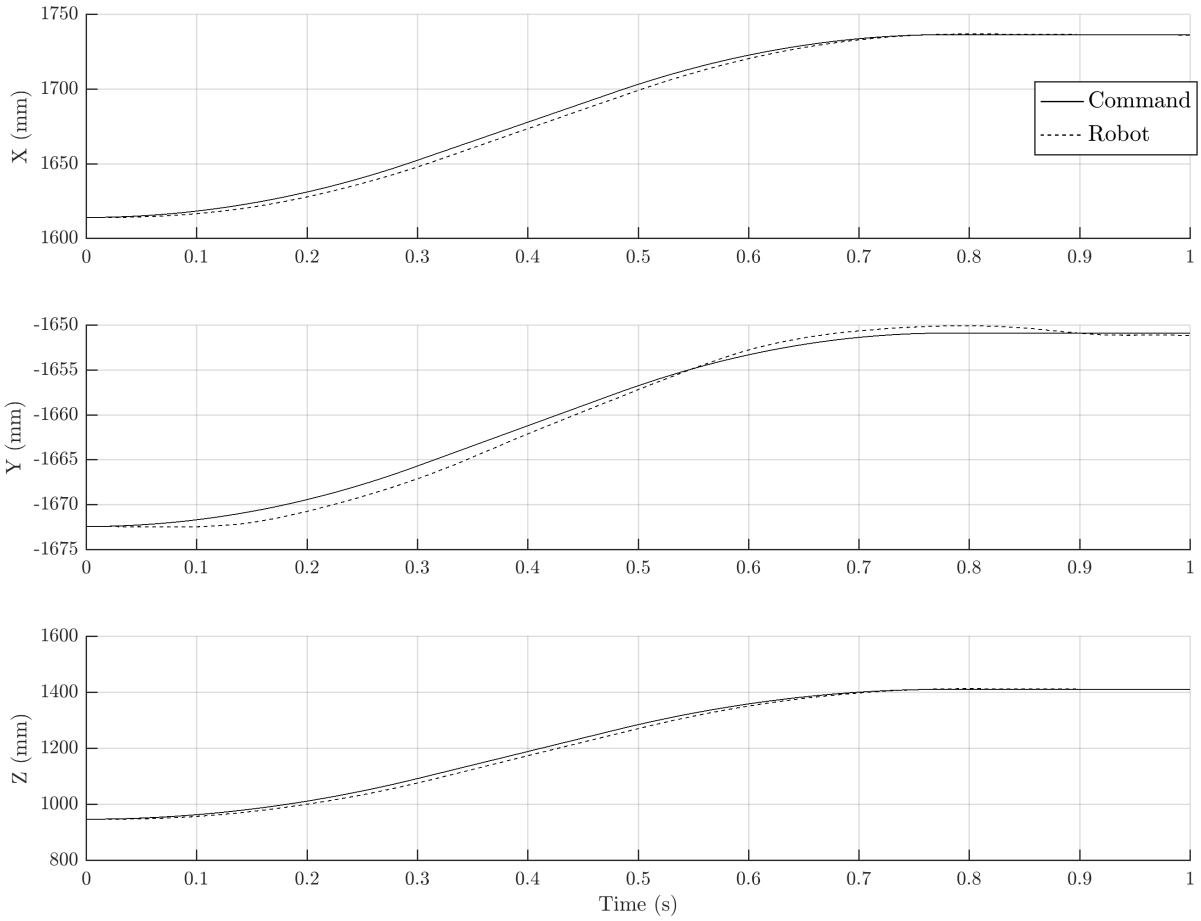

Figure C.3: Contact motion profiles and robot tracking for contact case V1000A15 (1000mm/s and 15deg strike angle). All coordinates are shown in the robot's base frame.

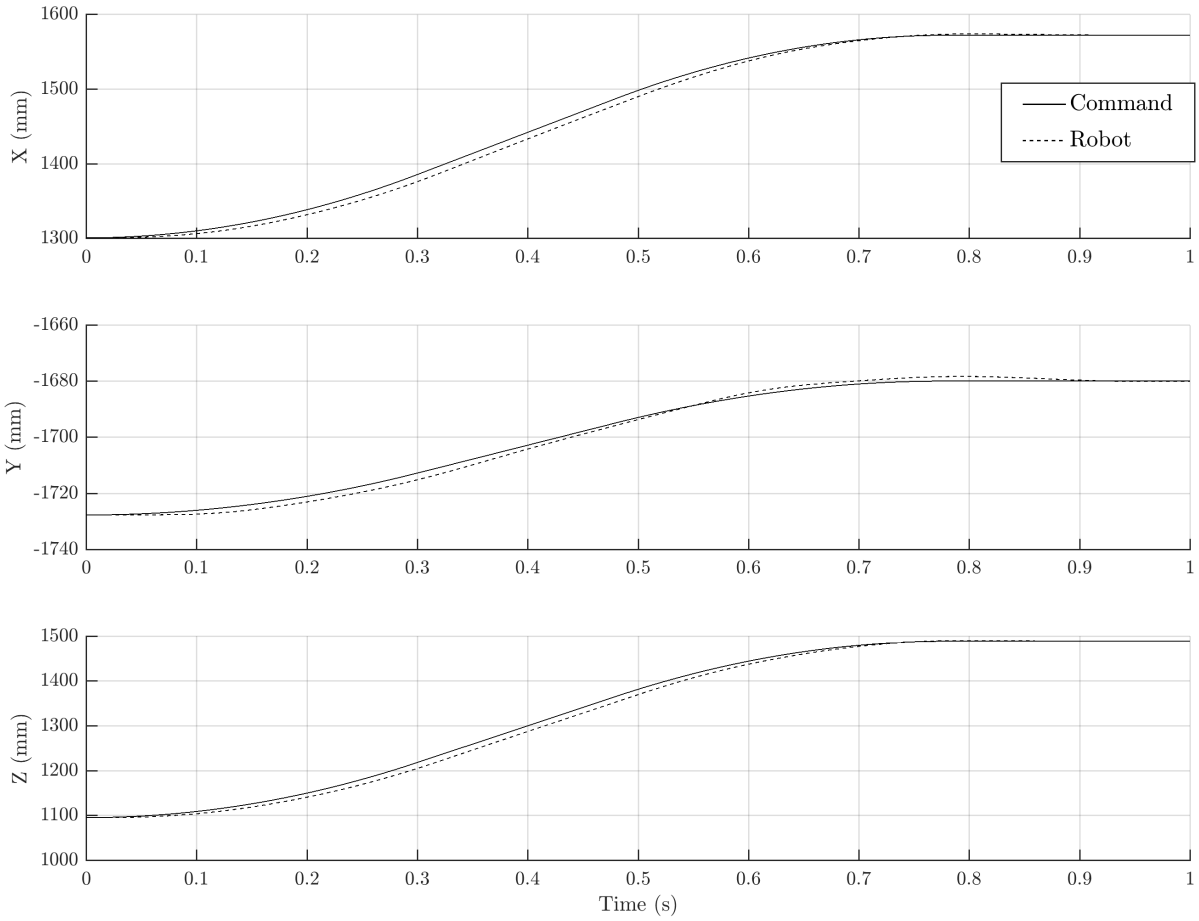

Figure C.4: Contact motion profiles and robot tracking for contact case V1000A15 (1000mm/s and 35deg strike angle). All coordinates are shown in the robot's base frame.

C.0.2 Experimental Setup & Instrumentation

Pictures of the experimental setup of the rig in the robot cell are shown in Figure C.5. The drogue was suspended off a scaffold tower using a static rope and the robot positioned underneath. The location of the reaction mass, attachment points of the bungees and the setup of the high speed motion tracking system are clearly marked. The vision system tracked the reflective markers on the drogue to record its contact perturbations and was used to measure the rig geometry for the model generation in a subsequent step. Masking tape was applied to metallic components in order to reduce the reflectivity and interference with the tracking system. The cable conduit guiding the strain gauge leads to the signal conditioning and DAQ system is also clearly visible in Figure C.5.

The location of the strain gauges on the drogue ribs are highlighted in Figure C.6a). Note that a total of 64 gauges have been applied to the top and side of the 32 ribs on the basket (*i.e* two gauges per rib) to measure the radial and lateral strains induced by the contact events. The excitation directions for radial bending and lateral flexure are shown in Figure C.6b) and C.6c) respectively.

The signal conditioning and data acquisition equipment was placed on a lab trolley to the side of the robot cell as shown in Figure C.7. Bespoke conditioning boxes were employed including provisions for low pass filtering of the strain data with a 10kHz cut-off frequency. Network switches belonging to the 'OptiTrack' motion capture system and a bespoke interface box including a power supply unit with over-voltage protection for the ATI 6DOF force/torque sensor and break out connections for access to the raw sensor channels via a DSUB 37 connector are also clearly visible. The data acquisition and processing at runtime for both, the force/torque sensor and the strain gauges was performed on two CompactRIOs (also shown in Figure C.7). A picture of the operator desk outside the cell is shown in Figure C.8.

C.0.3 RPsDT Reproduction

For the RPsDT reproduction of the full speed contact scenarios a model of the rig was created and coupled to a robot controlled contact test as shown in Figure C.9. The robots pseudo-dynamically reproduced the relative motion of probe and drogue in each time step to acquire the contact force. Subsequently, this was fed back to the simulation of the rig which in turn computed the next drogue position and orientation. The cycle then repeated in this manner.

The structure of the underlying rig model is schematically illustrated in Figure C.10. As shown, the rope was modelled as a series of interconnected spherical joints with small masses and the bungees were represented by prismatic joints with spherical joint attachment points. Contact forces and torques were applied at the drogue's connecting flange via a 6 DOF joint located in parallel with the rope.

The individual model parameters were first estimated experimentally and then fine tuned in a constraint optimisation. The mass of the drogue assembly and its COG were identified by suspending the drogue at known positions off two load cells as shown in Figure C.12. Estimates for the drogue's inertias could then be obtained by treating the drogue as a simple pendulum with a lumped mass concentrated at the drogue's COG. These estimates could be fine tuned in a second step by taking into account the drogue's swing phase when released from different positions as discussed below.

The bungee response was characterised manually by stretching the bungee cord with a load cell attached to its end as shown in Figure C.11a). Throughout these tests, the motion capture system was used to record the precise extension imposed onto the bungee cords. The characteristics could then be incorporated into the model based on look-up functions as shown in Figure C.11b) which defined the actuation profile of the respective prismatic joints.

Once parametrised with the estimates identified above, a two stage constraint parameter optimisation was performed to fine tune the model. In a first step, the drogue's rotational inertia was fine tuned and the damping on the rotational axes of the 6DOF joint identified by optimisation. To this end, the free swing phase of the drogue when released from different positions was experimentally recorded with the motion tracking system. A constraint optimisation algorithm ('fmincon') was then employed to minimise the error norm between the experimentally recorded swing phase of the unconstrained drogue (no bungees attached) and the swing phase computed by the model when released from various initial conditions (see Figure C.13a)).

In a second step (see Figure C.13b)), the procedure was repeated for the constraint swing phase (drogue constrained by bungees). This time, the bungee damping and steady state extensions were left subject to optimisation and once more, the error norm between the experimentally recorded swing phase of the constrained drogue and the model when released from various initial conditions was minimised. Comparisons of the final optimisation results are shown in Figures C.14 C.15 C.17 C.17 respectively. Here, the experimental and modelled swing phases (with bungees attached) are compared for drogue releases from four different initial conditions (drogue was pulled to each rig corner and released to swing diagonally across to the opposite rig corner). For all cases, the non-linear dynamics were well reproduced and a good match of the oscillation frequencies obtained. Minor steady state offsets exist and were also reflected in the validation data in Chapter 5. These are the result of the cable conduit and strain gauges leads (pulling the drogue to one corner and tilting it in steady state) which were not accounted for in the model.

a)

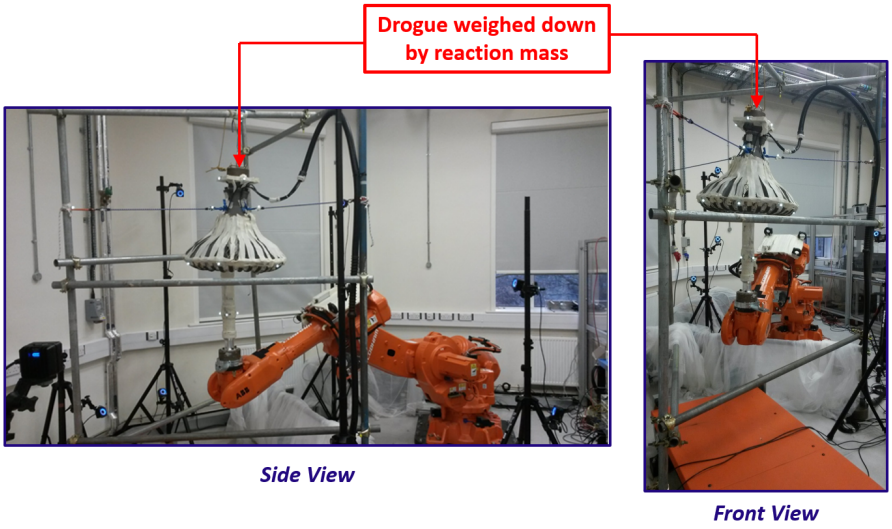

b)

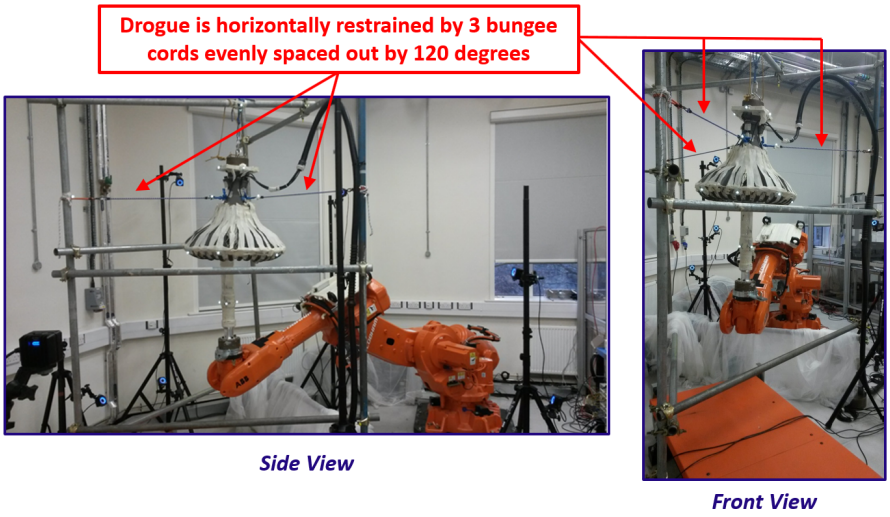

c)

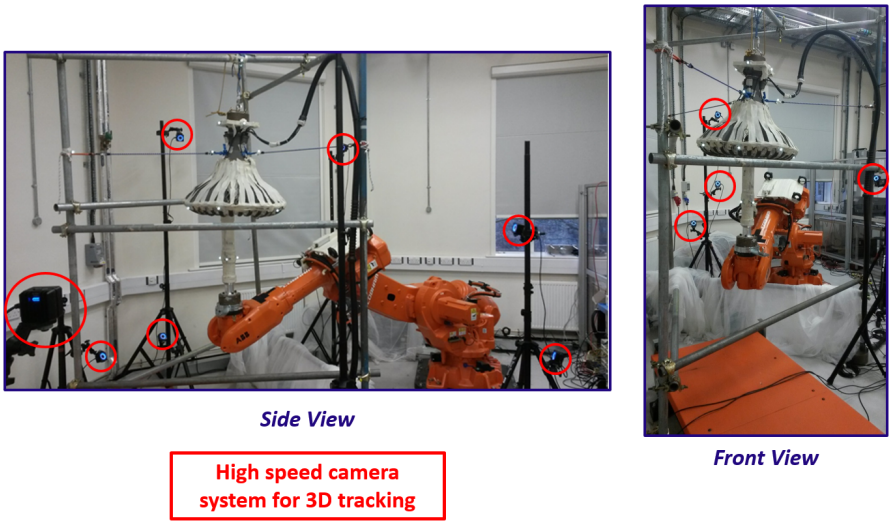

Figure C.5: Front and side view of experimental setup in robot workspace showing a) location of reaction mass b) bungee attachment points c) high speed motion capture system.

a)

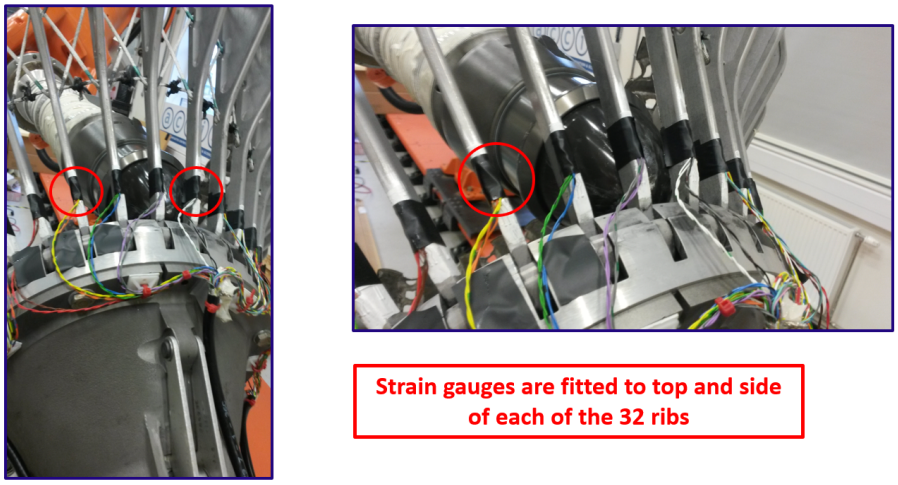

b)

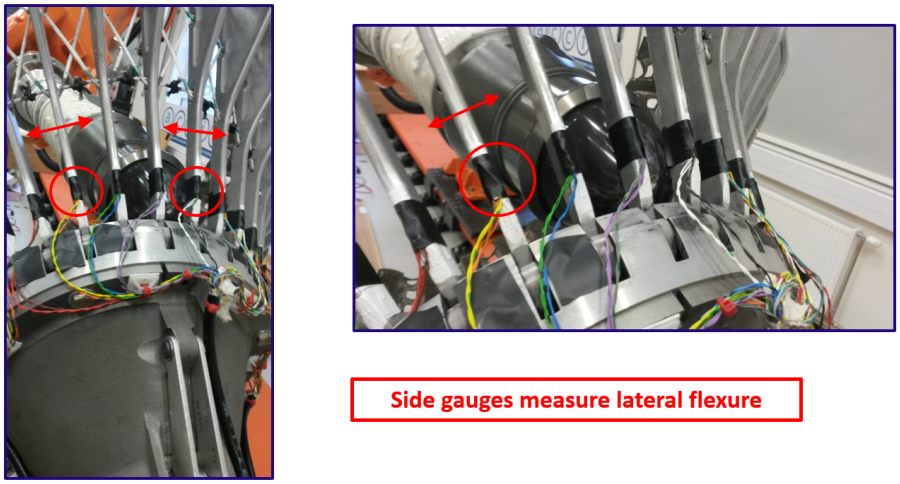

c)

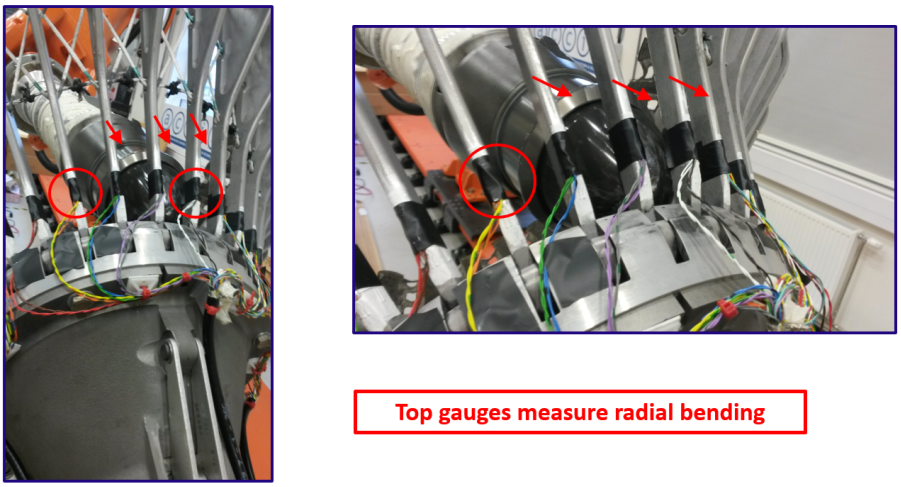

Figure C.6: Drogue instrumentation with strain gauges showing rib attachment points to measure radial bending and lateral flexure upon impact.

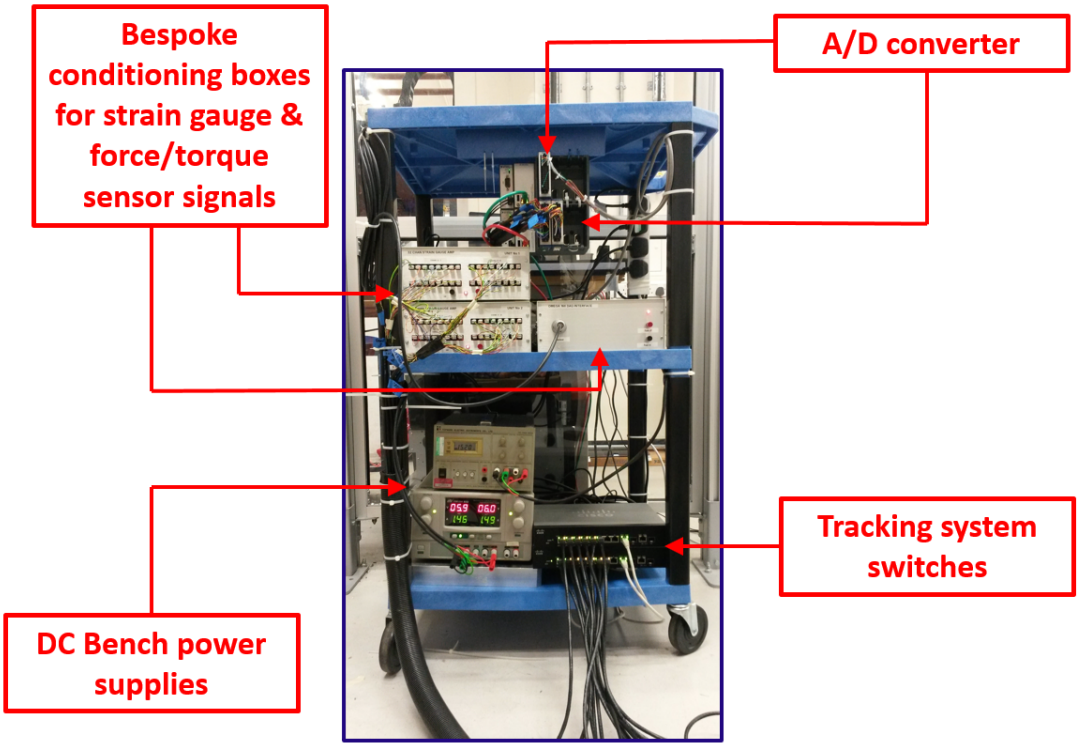

Figure C.7: Signal conditioning and data acquisition systems.

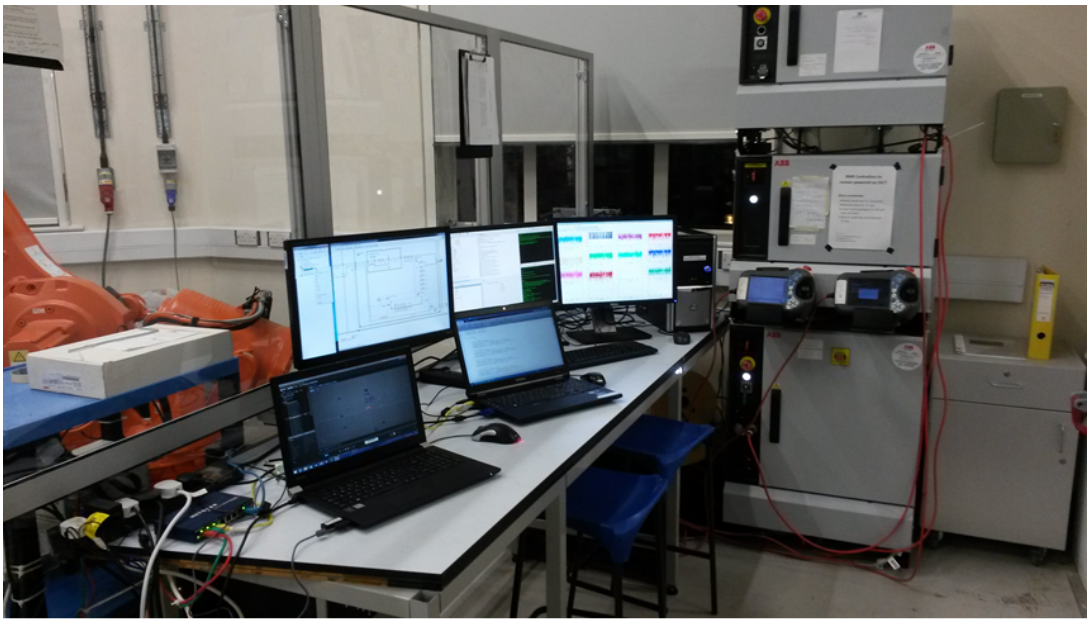

Figure C.8: Operator desk outside robot cell.

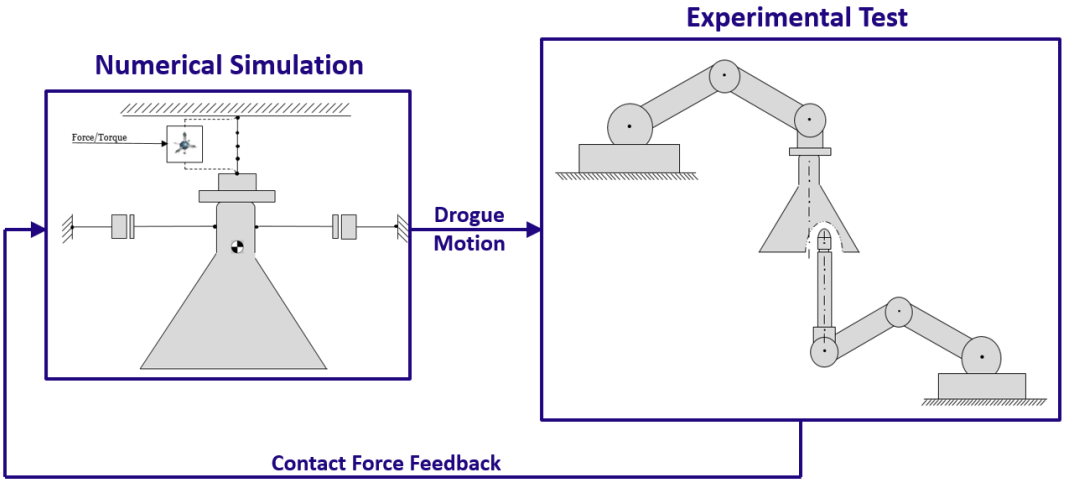

Figure C.9: Schematic of RPsDT validation test reproduction.

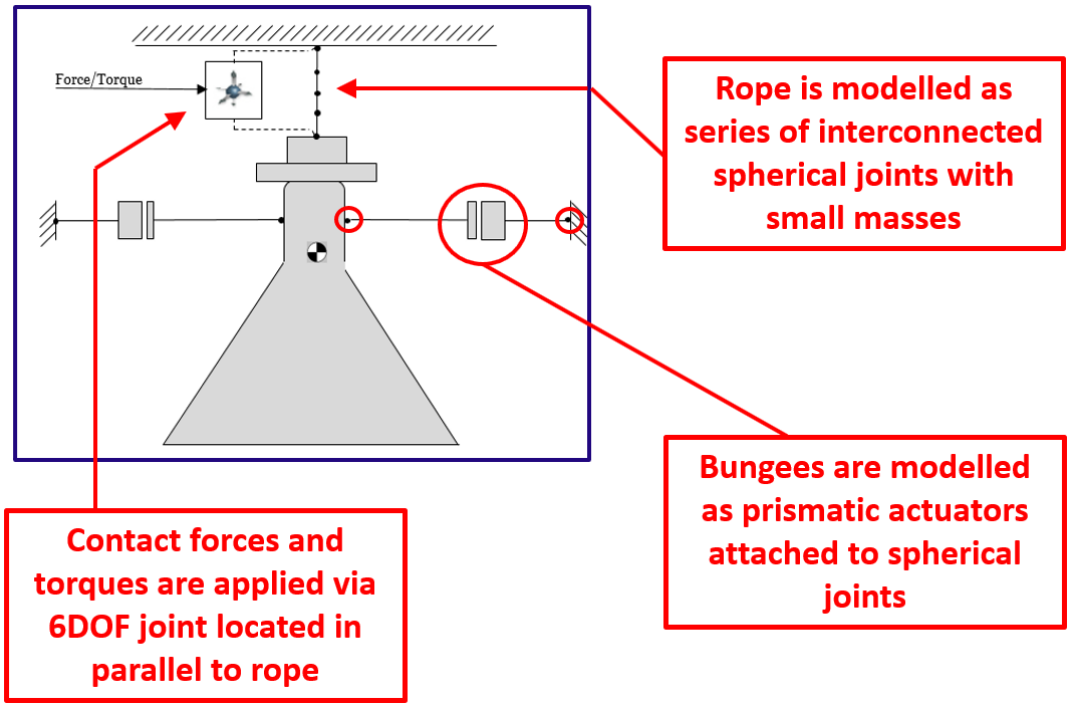

Figure C.10: Structure of numerical model for validation tests.

a)

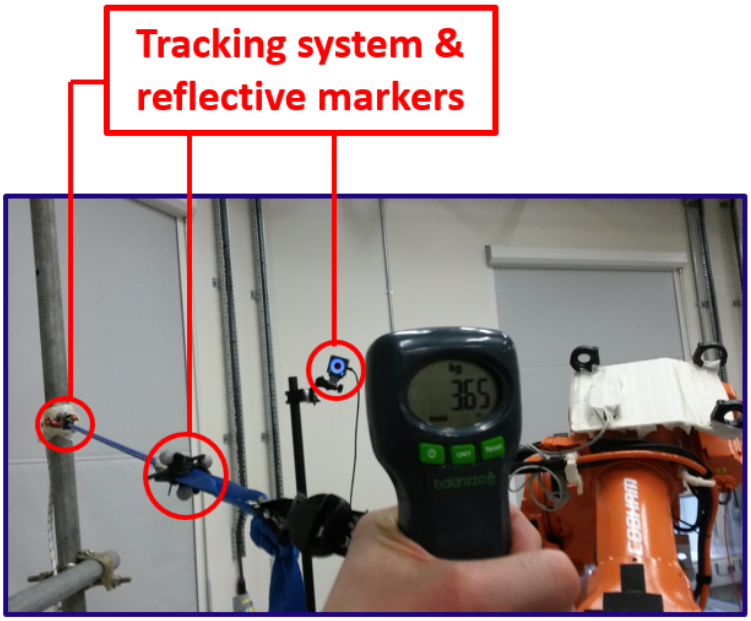

b)

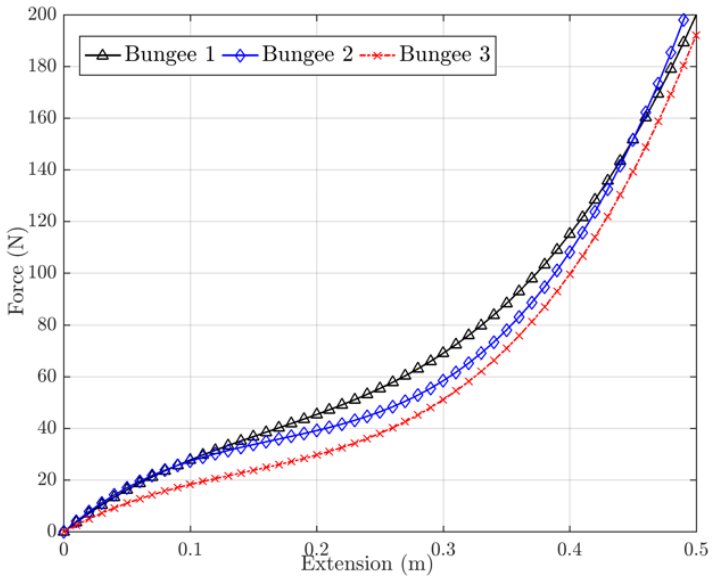

Figure C.11: a) Experimental identification of bungee stiffness characteristics using reflective markers and tracking system to measure bungee extension. b) Look-up functions for stiffness characteristics obtained for all three bungee cords.

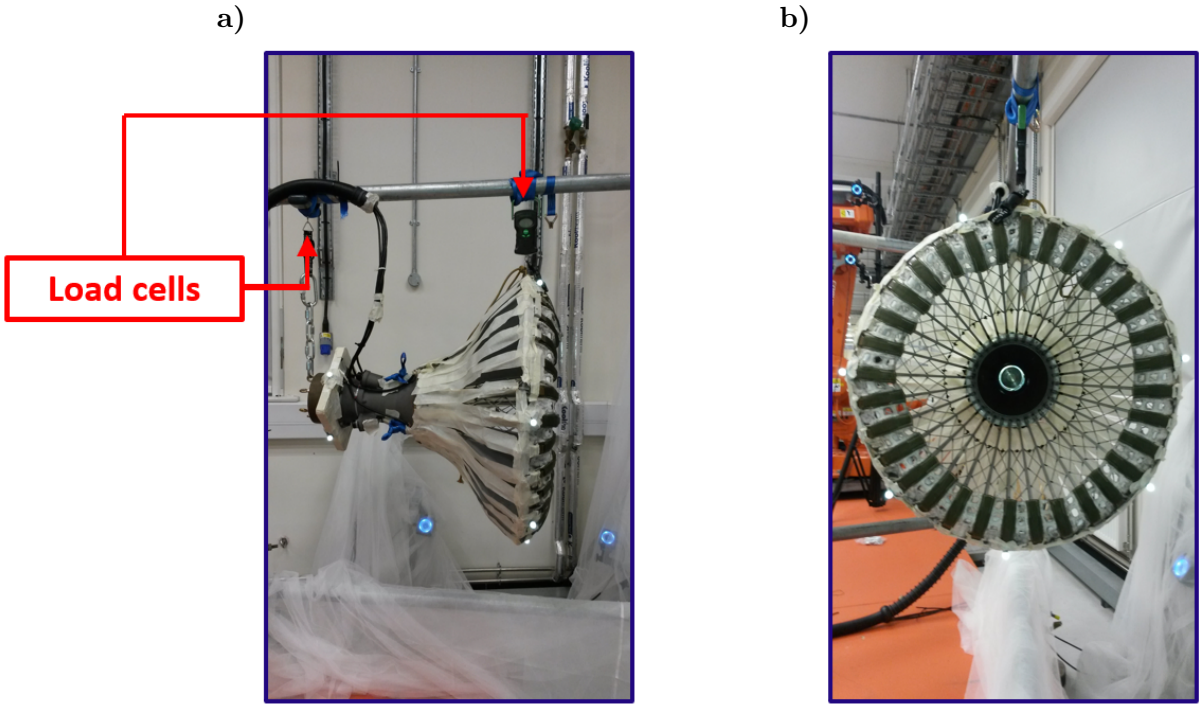

Figure C.12: Estimation of drogue centre of gravity. The drogue assembly is suspended off load cells at known positions for identification of its weight and centre of mass a) Side view. b) Front view.

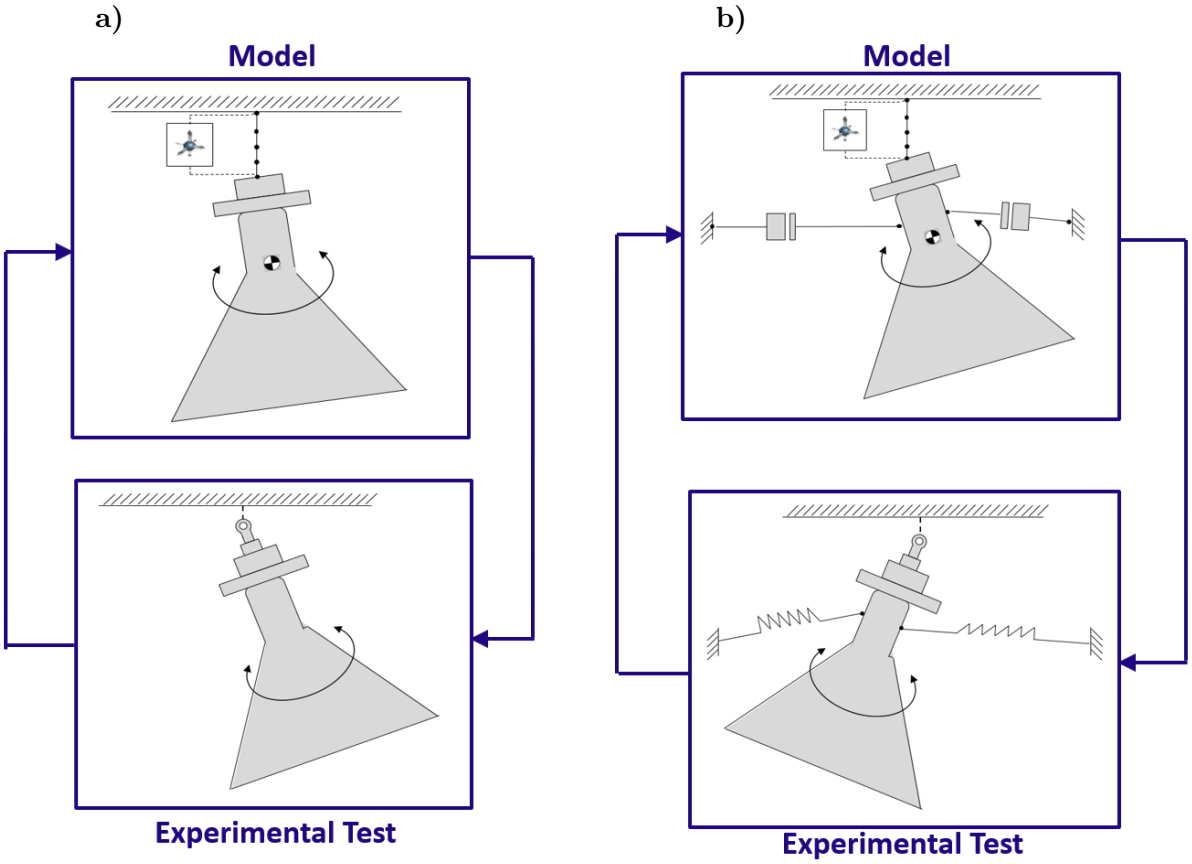

Figure C.13: Two-stage constraint optimisation of model parameters. a) Optimisation of inertia and rope friction parameters using free swing phase. b) Optimisation of initial bungee extension and viscous damping parameters using swing phases with bungees connected.

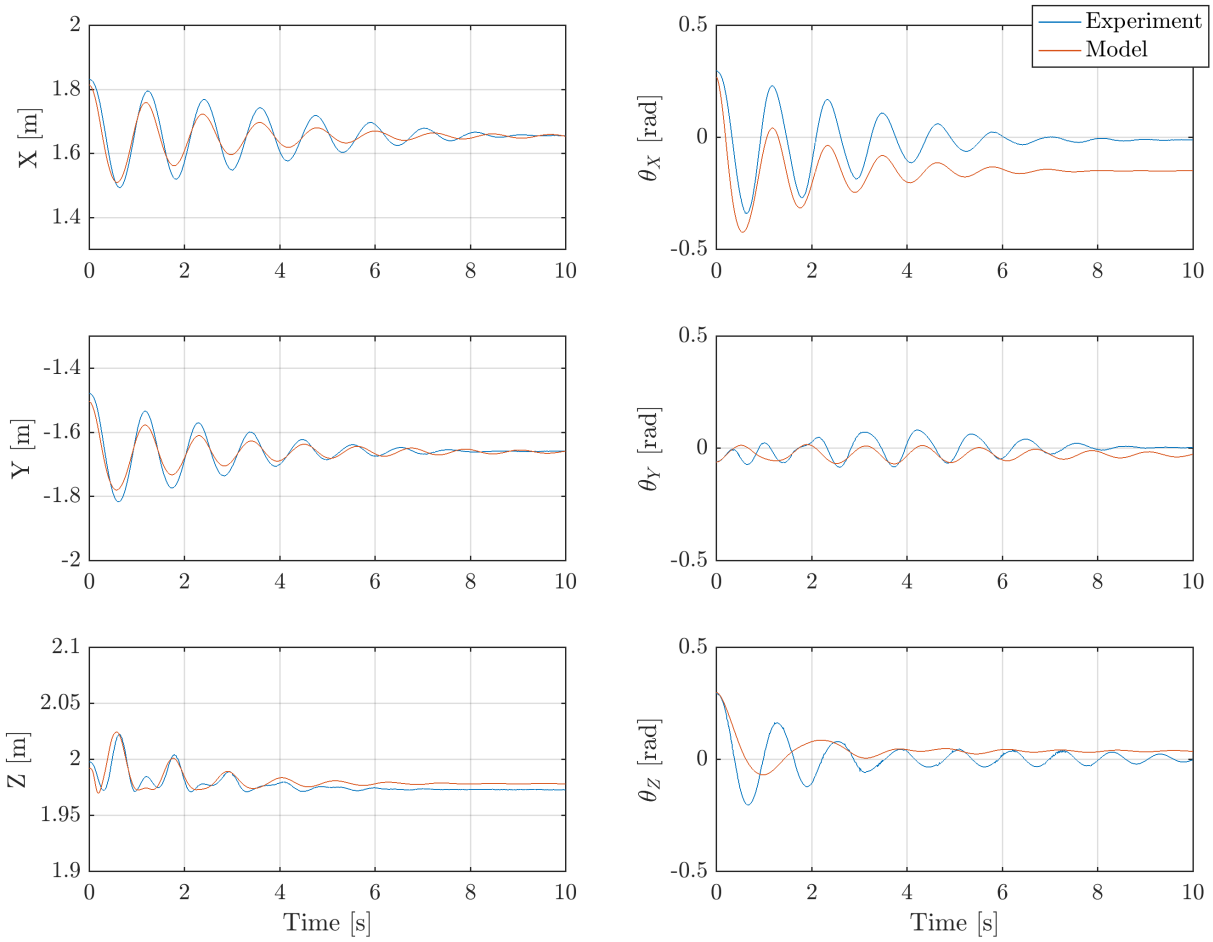

Figure C.14: Comparison of experimental and model swing phase when released from initial condition 1.

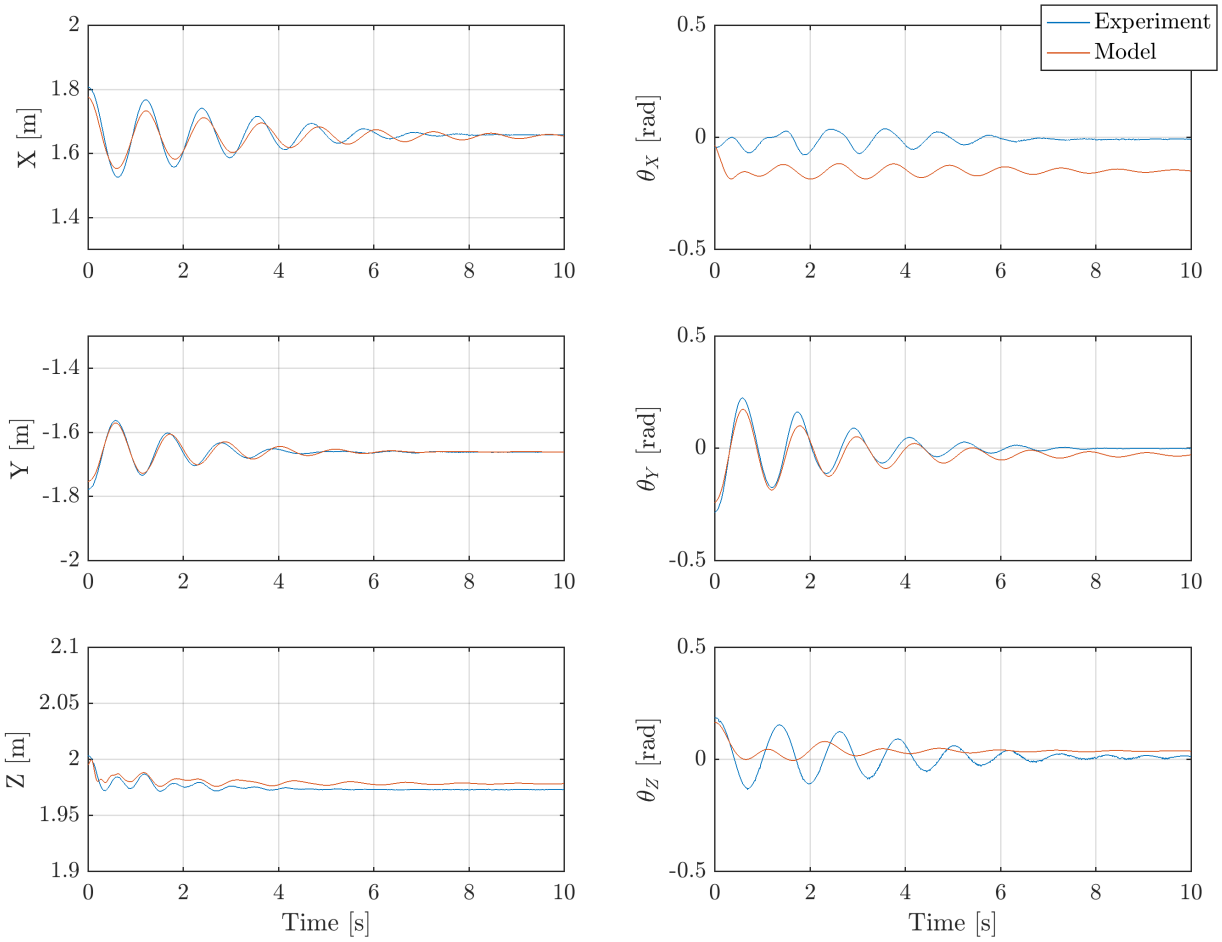

Figure C.15: Comparison of experimental and model swing phase when released from initial condition 2.

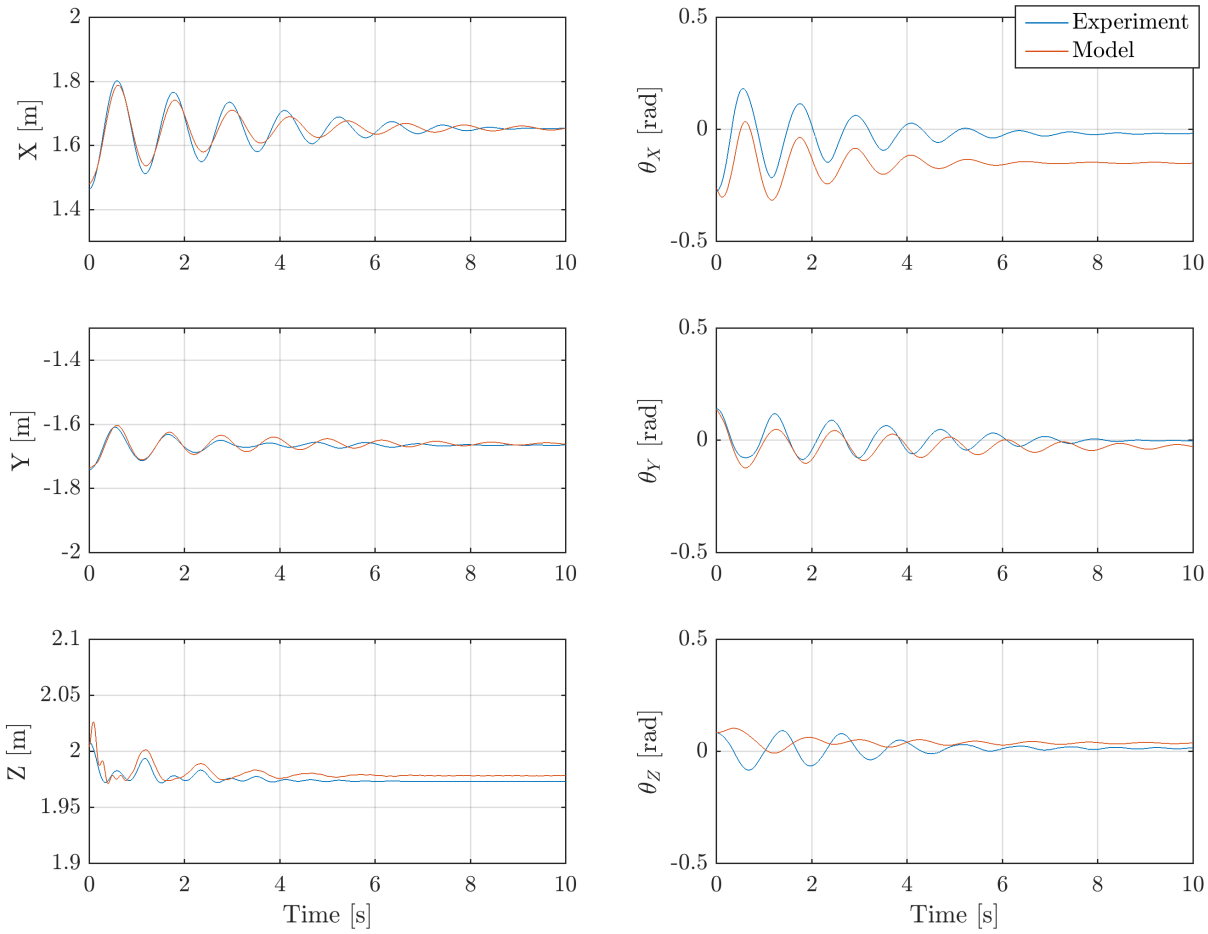

Figure C.16: Comparison of experimental and model swing phase when released from initial condition 3.

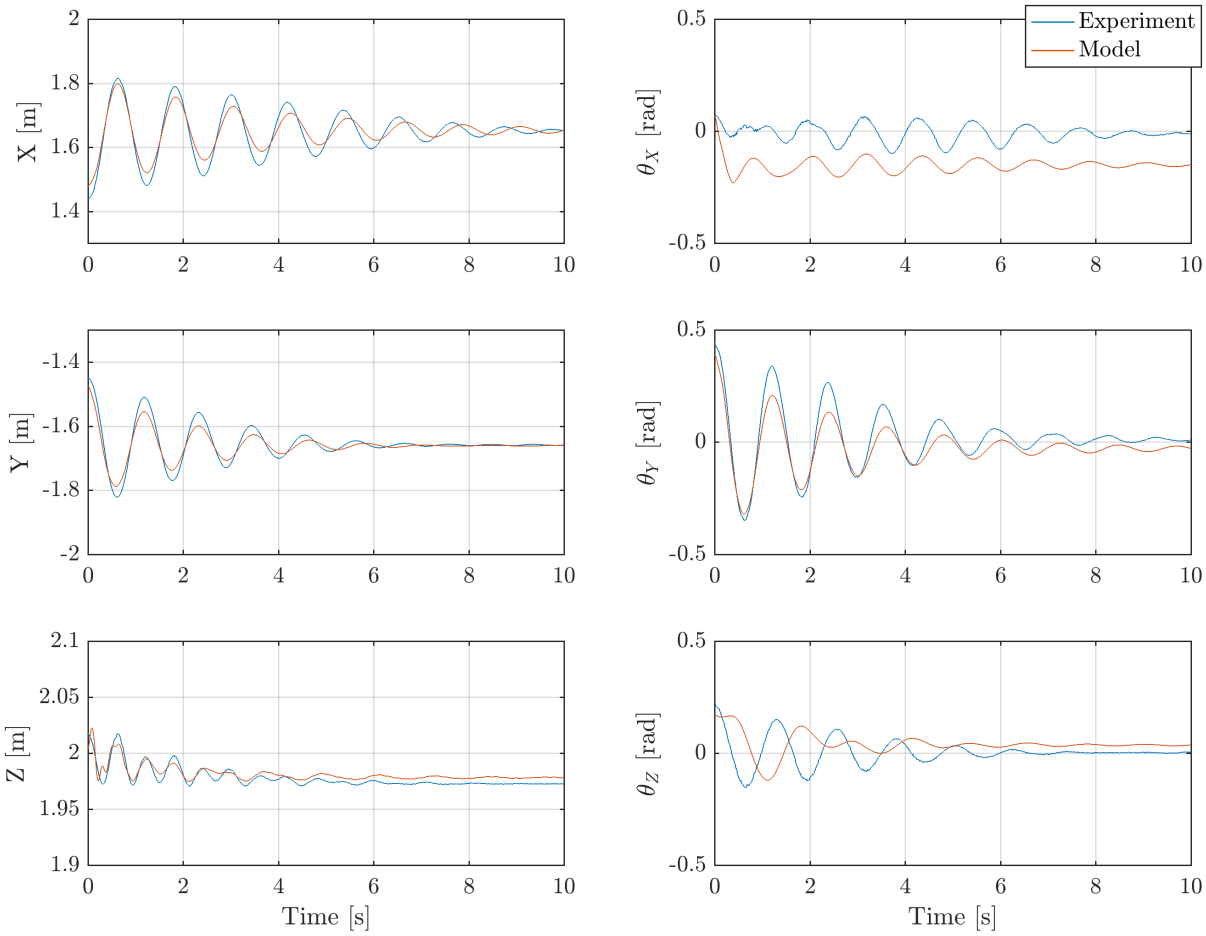

Figure C.17: Comparison of experimental and model swing phase when released from initial condition 4.